Predicting the Oxidation/Corrosion Performance of Structural Alloys in Supercritical CO_2

Final Technical Report

Reporting Period: 10/01/14-9/31/17

Principle Authors:
John Shingledecker
Steven Kung
Ian Wright

Issue Date: December 2017

DE-FE0024120

Submitting Organization:
Electric Power Research Institute
1300 West W.T. Harris Blvd.
Charlotte, NC 28262 USA

Other Contributing Organizations:

Det Norske Veritas USA, Inc
5777 Frantz Road
Dublin, OH 43017

Oak Ridge National Laboratory
One Bethel Valley Rd
Oak Ridge, TN 37831

Wright HT Inc.
8976 E. 35th Ave
Denver, CO 80238

Disclaimer

Abstract

This project was the first research to address oxidation of alloys under supercritical CO_2 conditions relevant to a semi-open Allam Cycle system. The levels of impurities expected in the CO_2 for typical operation were determined by thermodynamic and mass balance calculations, and a test rig was assembled and used to run corrosion tests at temperatures from 650 to 750°C in CO_2 at 200 bar for up to 5,000h, with and without impurities. Oxidation rates were measured for seven alloys representing high-strength ferritic steels, standard austenitic steels, and Ni-based alloys with higher-temperature capabilities. The very thin, protective scales formed on the high-temperature alloys provided significant challenges in characterization and thickness measurement. The rates of mass gain and scale thickening were possibly slower when oxidizing impurities were present in the sCO_2, and the scale morphologies formed on the ferritic and austenitic steels were consistent with expectations, and similar to those formed in high-pressure steam, with some potential influences of C. Some surface hardening (possibly due to carbon uptake) was identified in ferritic steels Grade 91 and VM12, and appeared more severe in commercially-pure CO_2. Hardening was also observed in austenitic steel TP304H, but that in HR3C appeared anomalous, probably the result of work-hardening from specimen preparation. No hardening was found in Ni-base alloys IN617 and IN740H. An existing EPRI Oxide Exfoliation Model was modified for this application and used to evaluate the potential impact of the scales grown in sCO_2 on service lifetimes in compact heat exchanger designs. Results suggested that reduction in flow area by simple oxide growth as well as by accumulation of exfoliated scale may have a major effect on the design of small-channel heat exchangers. In addition, the specific oxidation behavior of each alloy strongly influences the relationship of channel wall thickness to service lifetime.

Table of Contents

Executive Summary

The objective of this cross-cutting materials project was to provide computational predictions of the performance of structural alloys in supercritical CO_2 in severe operating environments at high temperatures. This objective was accomplished through short (300-1,000 hour) and limited long-term (5,000hour), isothermal laboratory testing of structural candidate alloys that are candidates for construction of components that contact the working fluid in supercritical CO_2 power cycles at high temperatures (>700°C) and pressures (200bar and higher), and the modification of an existing mathematical model for oxide growth and exfoliation. Overall the project was successful in identifying key candidate materials for use in these cycles, and modeling clearly showed that the temperature use limitations will be based on a combination of the materials performance and the specific design features in small channel complex heat exchangers. Also, new areas for additional study such as carburization, scale characterization, and additional testing were identified.

Specifically, this project was the first research to address oxidation of alloys under supercritical CO_2 conditions relevant to a semi-open Allam Cycle system. The levels of impurities expected in the CO_2 for typical operation were determined by thermodynamic and mass balance calculations, and a test rig was assembled and used to run corrosion tests at temperatures from 650 to 750°C in CO_2 at 200 bar for up to 5,000h, with and without impurities. Oxidation rates were measured for seven alloys representing high-strength ferritic steels, standard austenitic steels, and Ni-based alloys with higher-temperature capabilities. The selection of materials was based on a review of literature, the assembled team's experience, and discussion with technology vendors. It was found that the very thin, protective scales formed on the high-temperature alloys provided significant challenges in characterization and thickness measurement. The rates of mass gain and scale thickening were possibly slower when oxidizing impurities were present in the sCO_2, and the scale morphologies formed on the ferritic and austenitic steels were consistent with expectations, and similar to those formed in high-pressure steam, with some potential influences of C. Some surface hardening (possibly due to carbon uptake) was identified in ferritic steels Grade 91 and VM12, and appeared more severe in commercially-pure CO_2. Hardening was also observed in austenitic steel TP304H, but that in HR3C appeared anomalous, probably the result of work-hardening from specimen preparation. No hardening was found in Ni-base alloys IN617 and IN740H.

An existing EPRI Oxide Exfoliation Model was modified for this application and used to evaluate the potential impact of the scales grown in sCO_2 on service lifetimes in compact heat exchanger designs. Only oxidation and corrosion were considered in this work; failure modes due to creep, creep-fatigue, joining and fabrication processes, etc. were beyond the scope of this work. Four scenarios were considered in the performance of small channel heat exchangers: change in pressure drop due to oxide thickening, time to rapid oxidation due to exhaustion of a chromium reservoir, time to reach a critical thickness for oxide exfoliation, and a threshold for blockage due to exfoliation. Results suggested that reduction in flow area by simple oxide growth as well as by accumulation of exfoliated scale may have a major effect on the design of small-channel heat exchangers. In addition, the specific oxidation behavior of each alloy strongly influences the relationship of channel wall thickness to service lifetime. Specific equations, where applicable, are provided in the report for use in such evaluations by other technologists, researchers, and designers.

1 Accomplishments

Chapter 2 of this report contains the background on materials selection, test condition selection, experimental procedures, results, and discussion. As this was the first, to the author's knowledge, study specific potential oxidation and corrosion challenges under conditions in a direct fossil-fuel fired supercritical CO_2 (sCO_2) applied, via modeling, to compact (small channel) heat-exchangers, a number of notable accomplishments were made during the course of the study as follows:

- Impurities, likely to be present in supercritical CO_2 under the conditions experienced in a natural gas-fired, semi-open Allam Cycle system, were determined through calculations involving thermodynamic and mass balance considerations.
- An experimental rig was modified to supply the desired environment at 200 bar and up to 750°C, and its operation verified by two shakedown tests before successfully completing the planned corrosion exposures.
- The accumulated experience of the project team, along with discussions with manufacturers of small-channel heat exchangers, was used to select seven commercially-available alloys as potential candidates for operation in sCO_2 up to 750°C.
- An existing Oxide Exfoliation Model developed by EPRI for application in steam boilers was modified to incorporate the characteristics of sCO_2 and specifics of the proposed design and operating parameters of small-channel heat exchangers.
- Specimens were produced from the selected alloys and exposed in two shakedown tests, three 1,000h tests at 650, 700, and 750°C, and in a 5,000h test at 700°C. The oxidation kinetics were measured, and the oxide scales developed characterized to provide input for oxidation rate algorithms for use by the EPRI Oxide Exfoliation Model.
- The resulting oxidation kinetics and characteristics of the scale morphologies were compared with those from exposure in high-pressure steam (expected to provide oxidation behavior more akin to sCO_2 than oxidation in air). Similarities identified suggested that the mechanisms of scale failure employed in the EPRI Oxide Exfoliation Model would be applicable to sCO_2.
- Difficulties in measuring scale thicknesses and properly characterizing the scale morphologies formed on some high-temperature alloys prevented the generation of acceptable scale thickness-based algorithms for those alloys. Data from exposures in high-pressure steam were obtained and substituted where appropriate for modeling purposes.
- Micro-hardness measurements provided indications of possible C uptake in two ferritic steels and possibly an austenitic steel. Attempts to find suitable analytical tools in future research to provide verification, and microstructural explanations, are highly desirable.
- Experience of carburization attack during exposure to sCO_2 in gas-cooled nuclear reactors was examined to determine characteristic effects on oxidation kinetic and scale morphologies.
- Output from the EPRI Oxide Exfoliation Model provided significant guidance on the potential effects of oxide growth in small-channel heat exchangers.
- Results suggested that reduction in flow area by simple oxide growth and by accumulation of exfoliated scale could have a major influence on design considerations. In addition, the specifics of the oxidation behavior of each alloy could also strongly influence the relationship of channel wall thickness to service lifetime.

2 Summary of Research

2.1 Overview

To achieve the project objective of developing a model to predict the performance of structural alloys in supercritical CO_2 a multi-task project was undertaken. Initial activities included a review of the current status of materials for use in contact with supercritical CO_2 at high temperatures in order to identify the structural alloys with potential for use in the highest-temperature components of the proposed systems. This effort included discussions with vendors and technologists on the likely compositions of CO_2 present in their proposed cycles to provide focus for the experimental work. Based on this review a short list of seven materials was selected for study, and samples were obtained. In addition, a study was made to determine the most appropriate types and levels of impurities to be added to the supercritical CO_2 to appropriately simulate the conditions expected in the proposed power cycles.

Experimental exposures were conducted in an existing high-temperature, high-pressure corrosion test rig that was reconfigured to generate supercritical CO_2 at conditions of 600-750°C and 200 bar, and to accommodate the required alloy specimens. The ability of the test rig to achieve the desired conditions and to operate safely for the required test durations was evaluated during two 300-hour 'shakedown' runs. Specimens of three alloys were included in these tests to evaluate procedures for handling and post-test characterization. Following modifications and refinements suggested by the results of the shakedown runs, a series of exposures up to 1,000h was run at 650, 700, and 750°C using all seven candidate alloys, followed by a final test up to 5,000h at 700°C in which a few additional specimens taken from prototype heat exchanger components were included. Results of the post-test analyses are reported in the following.

In a parallel effort, examination of the state of understanding of the types of oxide scales formed in high-pressure steam, including their rates of growth, their detailed morphologies and modes of failure, was conducted to provide a basis for comparison with those formed in sCO_2. This information was used to provide guidance for adapting an existing model for predicting scale growth and failure (including potential for tube blockage due to exfoliated scale) that had been developed for the conditions prevailing inside the highest-temperature heat exchanger tubes in conventional steam power plants. After appropriate modification to accommodate the peculiar properties of sCO_2 and specific features of proposed sCO_2 recuperators, the model was exercised to predict the oxidation/corrosion rates of the various alloy candidates in long-term service (up to 100,000h and 700°C) to provide a scientifically-based approach to alloy selection for use in supercritical CO_2.

2.2: Materials Selection, Production of Specimens, and Selection of Impurities in sCO_2 Fluid

The use of supercritical carbon dioxide (sCO_2) as the working fluid in a closed Brayton power cycles is comparable to the use of high excess air combustion gases in open air-Brayton power cycles

and supercritical steam in modern Rankin power cycles. The power cycles employing sCO_2 are expected to result in an increase in overall cycle efficiency, as well as a reduction in the size of plant required for a given power output. This change is possible, in part, because of the significantly higher density of sCO_2 compared to combustion gases, air, or steam, which leads to higher airfoil loadings and lower pressure ratios across the turbine. Since a large fraction of the energy entering the turbine in the sCO_2 cycle is in the form of recuperated heat (from the turbine exhaust), the key to realizing a practical, high energy-density power plant based on sCO_2 Brayton cycles is the use of compact recuperative and fired heat exchanger designs capable of operation at the temperatures and pressures required to attain the desired overall efficiency.

Standard plate-and-tube heat exchanger designs generally are expected to be too large (costly) for efficient operation under the pressures and temperatures of proposed sCO_2 power cycles. As a result, attention has been focused on compact designs based on plate matrix, checkerboard, and printed circuit configurations [1]. In addition to the general lack of experience with compatibility of typical high-temperature alloys with high-pressure, high-temperature sCO_2 over long times, some of the design features of these types of heat exchangers introduce complications in terms of issues such as fabrication. Some of the unknowns are the ability to attain the expected alloy properties in the thin alloy sections often required in such heat exchangers, and the compatibility of fabrication processes (especially joining) with the complex shapes involved.

2.2.1 — Select Materials

Typically, the first consideration when selecting alloys to be used for pressure-boundary applications such as heat exchanger tubing and shells is that the alloy candidates must have the requisite strength characteristics at the intended service conditions, principally temperature and pressure. A major consideration is a minimum level of creep strength at the proposed operating temperature, based on the strength levels permitted by the ASME Boiler and Pressure Vessel (B&PV) Code. Other major factors, in typical practical order of priority to the engineer, are: availability of the alloys in the desired forms; fabricability (especially compatibility with conventional welding practices); cost; and adequate resistance to corrosion by the working fluids. When contemplating working fluids and environments for which little experience of service behavior is available, the latter factor may assume greater importance, given that generating sufficient data for confident life prediction often is a lengthy process.

Operation of equipment for the generation of electric power places a high priority on the ability of the chosen materials to perform in a predictable manner over the intended plant lifetime, particularly with respect to maintenance of strength and resistance to loss of vessel wall thickness. The desire for ever increasing efficiency of conventional electric utility plants has driven the trend for increasing operating steam temperatures and pressures, which in turn has required operating conventional alloys closer to their maximum capabilities as well as development and introduction of modified or new alloys. An inevitable consequence of increased operating temperatures has been an acceleration in the rate of growth of the protective oxide scales normally formed on the alloys, such that for currently-used alloys the thickness of scales formed after extended operating campaigns may be such that sufficient scale exfoliation may be triggered on subsequent plant start-up or cool down to

cause blockage of the (typically) 2.7 cm (1.1 in) ID superheater tubes. Forced outages of plant from this cause have been an increasing feature in recent years. Remedial measures have included modification of operating practice to induce controlled, non-blocking scale exfoliation events (after each of which the deposits must be removed), imposition of temperature limits for a given alloy so that the critical scale thickness for exfoliation is not reached before the next scheduled outage, or the introduction alloys that form slower-growing oxides either through surface treatments or compositional modifications.

Since the flow passages in some of the advanced heat exchanger designs intended for use in sCO_2 cycles will be significantly smaller than typical in boiler superheater tubes, knowledge of the oxide scale growth rate and failure behaviors of the alloys chosen for their construction becomes an important factor in the overall alloy selection process.

A similar exercise in alloy selection was conducted for advanced ultra-supercritical (A-USC) steam power cycles [2], and provides an excellent template for comparable sCO_2 power cycles. The maximum working fluid conditions in the US efforts in A-USC cycles are 760°C and 350 bar. An alloy creep strength criterion of 100 MPa for 10^5h was set, and a preference for thin-walled heat exchanger tubing (in order to minimize thermal fatigue concerns) fixed the use-temperature limit for each alloy. The net effect on selection from alloys that currently meet the ASME B&PV code for pressure vessel service was that ferritic steels were limited to ~620°C, austenitic steels to 690°C, and solid solution-strengthened Ni-based alloys to approximately 720°C. The intended maximum service conditions therefore required the introduction of precipitation-strengthened nickel-based alloys for the first time in steam boilers. This effort entailed qualification of recently-developed alloys Inconel 740/740H and Haynes 282 (see Table 2.2.1-1), and resulted in a successful B&PV Code case for Inconel 740H (ASME CC2702) [3]. These higher-strength alloys provide advantages at lower temperatures in terms of reduced material usage from the ability to use thinner wall sizes, hence reduced susceptibility to thermal-mechanical fatigue.

Alloy selection for sCO_2 recuperative or fired heat-exchanger designs may or may not follow the same logic as used for A-USC boilers. The approach will depend on how the pressure boundary is considered in specific designs. For example, in a printed circuit heat exchanger the heat transfer surfaces form the actual pressure boundary, while in designs such as a brazed plate and fin, much of the surface is not subject to ASME code rules because only the heat exchanger casing is a true pressure boundary. Thus, there is a wider range of materials to choose from compared to the A-USC case, since alloys that have excellent resistance to oxidation at high temperatures but lower strength than the precipitation-strengthened nickel-based alloys may be considered. The following criteria were used to select a list of 5-7 alloys for use in this study:

- The alloys must be commercially-available alloys so that the results are useful to manufacturers.
- Ability to achieve some of the intended target temperature conditions based on experience in, for instance, steam generators.
- Ability to obtain representative samples of the selected materials.

- Ability to compare experimental results to experience in steam service (oxidation rates and oxide scale morphologies).
- Active interest in the materials on the part of heat-exchanger manufacturers.
- Alloy cost (in terms of being cost-competitive as well as cost-effective).

Table 2.2.1-1
Nominal compositions of alloys mentioned in the text.

Alloy	Nominal Composition, wt%											
	Fe	Ni	Co	Cr	Mo	Nb	Al	Ti	Mn	Si	C	Other
Grade 91 (T91)	Bal	<0.43	0.01	9	1.0	0.08	<0.01	<0.01			1.05	
T92	Bal	<0.4	0.01	9	0.5	0.07	<0.05	<0.01			1.0	
VM12	Bal	0.25	1.6	11.5	0.3	0.05	0.02			0.5	0.12	1.5W
Crofer 22H	Bal			22		0.6				0.4	0.03	2W, La
TP304H	Bal	9		19					2	0.75	0.07	
TP316	Bal	14		18	3				2	1	0.08	
TP347	Bal	11		18				0.01	2	0.75	0.08	Nb+Ti
TP310/310HCbN/HR3C	Bal	20		25		0.4			2	0.75	0.07	
ATI 20-25+Nb	Bal	25		22	1.5	0.2		0.04	1.0	0.42	0.02	
S304H	Bal	8.9	0.1	19	0.13	0.05			0.44	0.13	0.08	
Sanicro 25	Bal	25	1.5	22.5		0.5			0.5	0.2	0.01	3.6W, 3Cu
Incoloy 800H	Bal	33		21			0.4	0.4			0.08	
HR120	Bal	37.6		25	0.28	0.6	0.1		0.73	0.24	0.06	0.5W
IN617		Bal	13	22	9		1.1				0.1	
IN625		Bal		22	9					3.7		
IN740H		Bal	20	24.5	0.1	1.5	1.35	1.35		0.15	0.03	
HA214	3.5	Bal		16			4.3		0.17	0.08	0.05	Zr, Y
HA224	27.5	Bal	2	20				3.8		0.3	0.05	Zr
HA230	1.2	Bal	0.14	22	1.2	0.02	0.33		0.5	0.37	0.09	14W
HA282		Bal	10	20	8.5		1.5	2.1		0.15	0.06	

Inquiries were made to heat exchanger vendors, and discussions were held with research groups involved in materials testing in sCO_2 (Oak Ridge National Laboratory, University of Wisconsin) to build a more complete understanding of perceived materials challenges and the goals of ongoing research. In particular, discussions were held with two commercial sCO_2 heat-exchanger manufacturers, Heatric and Brayton Energy, to collect information on alloys and fabrication processes under active consideration for specific components. A brief summary of the components, alloys, and manufacturing processes pursued by these vendors is given below.

2.2.1.A - Heatric

Heatric specializes in printed-circuit heat exchangers, and uses a diffusion-bonding process to fabricate heat exchangers that have intricate flow patterns and channels. For this process, the nickel-based alloy, Alloy 617 (Table 2.2.1-1), has been fully qualified for commercial applications. Based on Heatric's experience, Alloy 617 offers better manufacturability than Alloy 230 for block components. The diffusion-bonding process requires a specific (proprietary) bonding/post-bonding heat treatment that is difficult to perform for large and complex heat exchangers. In addition, post-bonding quenching

is required, which limits the size of the blocks that can be fabricated. This and subsequent heat-treatments, such as those required for precipitation-strengthened (age-hardenable) alloys such as Inconel 740H or Haynes 282, are an important consideration in these designs. Alternative alloys that have been examined for the highest-temperature heat-exchanger applications include HR120 and Sanicro25, but to date Heatric has not explored the use of any age-hardenable nickel-based alloys. From the mechanical strength standpoint, heat exchangers for sCO_2 applications will be built to the ASME B&PV Code standards.

For stainless steels, Types 304, 316, and 347 have been qualified as candidate materials for molten-salt heat-exchanger applications, and are now available commercially. Limited field experience suggests that Type 316 may be less desirable for this application than the other materials.

The potential for blockage in small-channel heat exchangers also was discussed. Based on Heatric's experience, the propensity for blockage in small channels is highly dependent on the particle velocity and size. A high flow-velocity increases shear of the fluid at the walls, thus improving wall cleaning and reducing fouling. The current guidelines for particle sizes for minimizing blockage are that, with an upstream strainer, a particle hydraulic diameter 1/3 or less compared to the channel diameter is recommended for small channels. These guidelines are based on the results of a study performed by Sydney University (30 years ago) using 200 μm particles flowing through heat exchanger channels, and has been used by industry with good experience. Heatric indicated that this may be a conservative rule, but without better data and more study it is their general approach for most applications.

In addition to high-temperature oxidation, carburization may be a concern for heat-exchanger alloys in sCO_2 under certain operating conditions. However, this concern has not been extensively investigated. Beyond channel blockage from solid particles resulting from high-temperature corrosion (oxidation and perhaps carburization), no other degradation mechanisms are currently known to be of concern for alloys exposed to these sCO_2 environments. Experience of stress corrosion cracking (SCC) has been reported in some applications handling sCO_2, but such conditions are not considered to apply to high-temperature sCO_2 components. It was acknowledged that there is a need for better understanding and for modeling of the operating conditions likely to lead to carburization in sCO_2 applications. Due to a lack of access to laboratory facilities and test loops, Heatric was interested in working with EPRI and other R&D organizations to perform component tests for its heat exchangers.

2.2.1.B - Brayton Energy LLC

Brayton Energy LLC is a system designer and integrator. Its heat exchanger designs incorporate extended surface areas, and generally the hottest components are under the lowest stress. On the high-pressure side of a structural heat exchanger cell, the service environments usually are expected to be essentially pure CO_2, whereas on the outer, low-pressure side the CO_2 may contain moisture as an impurity. One concern is that the presence of moisture may lead to accelerated oxidation rates of alloys that form chromia-based scales (chromia can be further oxidized to a volatile species at the highest temperatures envisioned). Therefore, where hot, humid CO_2 is to be handled (considered by Brayton Energy to be the most corrosive condition), the gas pass may be fabricated from an alumina-forming alloy that possesses higher oxidation resistance.

Brayton Energy is currently investigating Ni brazing and transient liquid-phase (TLP) diffusion bonding as options for joining heat-exchanger cells. Compositions of the fillets formed by either method will be Ni-Cr with intermetallic compounds from melting-temperature depressants, mainly Si, P, and B. Trials of various processes for joining were in progress when contact first was made, and the possibility of including samples from those trials in the laboratory testing planned in this project was considered. Brayton Energy expressed concern about the lack of data on the performance of the braze alloys in sCO_2 environments.

Brayton Energy has some involvement with the oxy/gas-fired Allam (open) Cycle system that employs sCO_2 [5], in which the maximum temperature and pressure experienced by the heat exchanger components are 775°C and 300 bar, respectively, while the maximum sustained temperature typically is about 750°C. Figure 2.2.1-1 shows a simplified flow diagram of an open oxy/gas-fired Allam Cycle. Apparently, there is some uncertainty about the availability of suitable

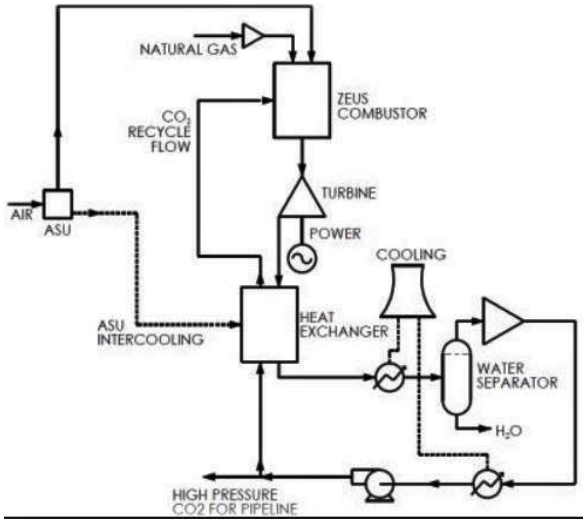

Figure 2.2.1-1 – Flow Diagram of Oxy/gas-Fired Allam sCO_2 Cycle

commercial materials to support the fabrication of the hot section components required. The candidate alloys currently considered for the hottest sections are IN625, IN617, HR214, and HR224 (see Table 2.2.1-1). At lower temperatures, alloy HR120 is potentially an option for component fabrication. The alloy ATI 20-25+Nb also was considered be a lower-cost option for the lower-temperature components. As mentioned earlier, the creep resistance of the alloys will be an important consideration for determining the applicability of these alloys in system design for the Allam Cycle.

2.2.1.C - Other Alloys

Further discussions with industry and the research community suggested that most of the compact designs of interest incorporate approaches used by either Heatric or Brayton Energy; alloys such as Inconel 625 and Incoloy 800H were considered candidates for those heat exchangers. A review of available literature (Section 2 .4) identified some alloys for inclusion this study to provide some

communality with other studies. Key alloys that already have been exposed to sCO_2 in other test programs include Grade 91, TP316, Incoloy 800H, and IN740H.

Of this list, there are extensive steam oxidation data for Grade 91 (service and laboratory) and IN740H (laboratory only). TP316 and Incoloy 800H were considered to be of less interest due to lower strength (most of the studies of these alloys in sCO_2 were focused on low-temperature nuclear application applications, which are not of direct relevance to a transformational fossil system). Thus, for the initial testing, three representative alloys were chosen: Grade 91, TP304H, and IN740H.

2.2.1.D - Summary

Based on (1) discussions with heat-exchanger manufacturers, (2) inquiries with other research institutions, (3) review of available literature data, and (4) EPRI's experience with A-USC power cycles, a compilation of possible candidate materials for use in sCO_2 heat exchangers was assembled, as shown in Table 2.2.1-2. All of the alloys listed are available commercially, and most have ASME B&PV Code approval; some general comments on the current standings of these materials also are provided. Of these alloys, seven were chosen for evaluation in the planned long-term testing in this project (Sections 2.3.3 and 2.3.4). These alloys are highlighted in blue in Table 2.2.1-2, and consist of representative ferritic steels (Grade 91, VM12, and Crofer 22H), austenitic steels (TP304H and 310HCbN (HR3C)], and Ni-based alloys (IN617 and IN740H).

Table 2.2.1-2: Commercially-available alloys (alloys shown in blue were evaluated in this project).

Alloy Class	Alloy	ASME Code Approval	Advantages	Limitations	Lit. data in sCO_2	Plant experience in steam (EPRI database)	Chosen for shake-down test?	Consider for long-term testing
Ferritic steels (lowest cost, but will have temp. limitations)	Grade 91	Yes	Lowest cost	Potential for carburization, temperature limit in sCO_2 unknown	X	X	X	X
	T92	Yes				X		
	VM12	Yes	Improved oxidation resistance compared to T91/T92					X
	Crofer 22H	No	Highly oxidation-resistant ferritic steel (used in fuel cells)	Low strength at 700°C, not suitable for pressure boundary (ASME Code)				X
Stainless steels and austenitic alloys	TP316H	Yes	Supply chain, industrial steam experience	Scale exfoliation concerns based on supercritical steam experience	X			
	TP304H	Yes				X	X	X
	TP347H	Yes				X		
	S304H	Yes	Higher strength than other 18Cr steels			X		
	20/25+Nb	Yes*	Highest strength for austenitic stainless steel					

	HR3C (310HCbN)	**Yes**	Highest oxidation resistance of stainless steels			**X**		**X**
	Incoloy 800H	**Yes**		Low strength for high cost	**X**			
	HR120	**Yes****						**X**
Nickel-based alloys	**IN625**	**Yes*****	Short-term studies suggest acceptable oxidation rates	Expensive	**X**			**X**
	HA230	**Yes**		May not be suitable for printed-circuit designs	**X**			
	IN617	**Yes**		Expensive	**X**			**X**
	IN740H	**Yes**	Best strength for a nickel-based alloy	May be limited due to heat-treatment requirement for some designs	**X**		**X**	**X**
	HA282	No			**X**			
	HA214	No	Alumina former	Low strength; fabrication				

**ASME Code Case 2581 (NF709) is equivalent to 20/25+Nb*
*** Permitted for ASME Section VIII-1 but not Section I*
**** ASME restricts use temperature of Alloy 625 in Section I to 593°C (1100°F)*

2.2.2 — Produce Test Specimens

The materials available from EPRI's inventory that were used on this project are as follows:

- Ferritic steels: Grade 91 (T91), VM12 (obtained for this project), Crofer 22H (obtained for this project).
- Stainless steels: TP304H and HR3C.
- Nickel-based alloys: IN617, IN740H.

The actual compositions of these alloys are listed in Table 2.2.2-1. Eight coupons of each of three alloys: Grade 91, TP304H, and IN740H, were required for the 300-hour shakedown test in Section 2.3.1.B and exposure in CO_2 with controlled levels of additions in Section 2.3.2.B.

Additionally, samples of components from commercial compact heat exchangers were obtained from two heat-exchanger manufacturers for inclusion in the 5,000-hour long-term confirmatory test (Section 2.3.4). These components were made from several alloys, including TP347H, TP304/304L, HA230, IN625, and FeCrAl. The small flow channels in these components were created by 'sandwiching' thin, corrugated foil between two separator plates, using either a brazing or diffusion-bonding process. Coupons cut from these components were included in the 5,000-hour confirmatory test (Section 2.3.4).

Table 2.2.2-1
Actual chemical compositions of the seven alloys used in this study.

Element	Grade 91/T91	VM12	Crofer 22H	TP304H	HR3C	IN617	IN740H
Al	0.01	0.01	0.01	<0.01	0.01	1.13	1.33
B	0.002	0.004	<0.001	0.001	0.001	0.002	0.001
Ce	-	-	-	<0.01	<0.01	<0.01	<0.01
Ca	<0.01	<0.01	<0.01	-	-	-	-
Co	0.02	1.47	0.02	0.22	0.08	11.44	20.28
Cr	8.39	11.2	22.71	18.42	25.13	22.19	24.53
Cu	0.09	0.08	0.01	0.18	0.03	0.03	0.01
Fe	-	-	-	70.33	52.39	1.55	0.12
La	<0.01	<0.01	0.06	-	-	-	-
Mn	0.44	0.39	0.43	1.8	1.19	0.09	0.26
Mo	0.93	0.36	0.01	0.22	0.1	9.5	0.32
Nb	0.06	0.03	0.5	0.01	0.44	0.06	1.49
Ni	0.13	0.36	0.26	8.13	19.85	53.31	50.04
P	0.014	0.015	0.018	0.028	0.015	<0.002	<0.002
Si	0.24	0.41	0.29	0.48	0.4	0.08	0.15
Sn	0.01	<0.01	<0.01	<0.01	<0.01	<0.01	<0.01
Ta	<0.01	<0.01	<0.01	<0.01	<0.01	<0.01	<0.01
Ti	<0.01	<0.01	0.08	<0.01	<0.01	0.35	1.36
V	0.18	0.2	0.02	0.05	0.05	0.03	0.01
W	0.15	1.6	1.9	0.01	<0.01	0.13	<0.01
Zr	<0.01	<0.01	<0.01	<0.01	<0.01	<0.01	0.02
As	0.0038	0.0029	0.0019	0.0025	0.0021	0.0002	<0.0001
Bi	<0.00001	<0.00001	<0.00001	0.0008	0.00006	0.00007	0.00017
Pb	0.00005	<0.00001	0.00007	-	-	-	-
Sb	0.00077	0.00041	0.0001	-	-	-	-
C	0.08	0.12	0.004	0.043	0.066	0.091	0.024
S	0.001	0.001	0.002	0.002	0.001	<0.001	0.002
O	0.0032	0.0037	0.0032	0.0032	0.0016	0.0005	0.0006
N	0.0447	0.0359	0.017	0.0604	0.238	0.0065	0.004

2.2.3 — Select Type and Concentrations of Impurities in sCO_2 Fluid

To facilitate the decision on potential impurities in sCO_2 for semi-open and open systems, a review was made of articles published concerning such cycles, and discussions were conducted with cycle developers. Table 2.2.3-1 shows an overview of the information obtained. Whereas some impurities (for example, hydrocarbons) are listed as 'near zero,' it is expected that some hydrocarbon contamination may build up in closed cycles if volatilization of turbine bearing and/or seal lubricant were to occur (dependent on turbine design). The available information was used to estimate the maximum impurities for an open-cycle fossil system burning a coal-derived synthetic gas. Such a system represents a transformational opportunity for future fossil energy systems.

2.2.3.A - Calculations for Impurities in sCO_2

In contrast to the relatively pure sCO_2 working fluid anticipated for indirect-fired closed sCO_2 Brayton cycles, the direct oxy/gas-fired semi-closed Brayton power cycle working fluid will routinely contain a number of contaminants derived from the fuel and oxygen flows to the combustor, and produced in the flame. These contaminants will flow through the combustor, turbine and low-pressure side of the power cycle, and some will be actively removed prior to compression (see Figure 2.2.3-1). Other contaminants will increase in concentration and be removed in the stream that bleeds CO_2 produced by combustion of the carbonaceous fuel. The major contaminants in sCO_2 are:

- H_2O – water vapor is produced during combustion of hydrocarbon fuels. This contaminant largely will be removed from the circulating sCO_2 by condensation in the compressor inlet cooler/condenser. The working fluid will enter the compressor saturated with water at the temperature of the cooler/condenser exit.
- O_2 – some level of excess oxygen will be required for complete combustion. Oxygen will leave the circulation loop only in the bleed CO_2 stream.
- N_2 – nitrogen will enter the loop in trace amounts in both the fuel gas stream and the oxygen stream. Small amounts of the N_2 will be converted to NO_x in the flame. Nitrogen will leave the circulation loop only in the bleed CO_2 stream.
- Ar – argon will enter the loop as a trace in the oxygen stream. Argon will leave the circulation loop only in the bleed CO_2 stream.
- NO_x – very small amounts of NO_x will be produced in the flame. If the "lead chamber" process (see below) is employed on the low-pressure working-fluid stream, essentially all the NO_x produced will be converted to nitric acid and removed by the aqueous condensate collected in the compressor inlet cooler/condenser. Otherwise, the NO_x will leave the circulation loop only in the bleed CO_2 stream.
- SO_x – any sulfur entering with the fuel will be converted to SO_2/SO_3 in the flame. If the "lead chamber" process (see below) is employed on the low-pressure working fluid stream, nearly all of the SO_2 in the working fluid will be converted to SO_3 and removed as sulfuric acid in the aqueous condensate collected in the compressor inlet cooler/condenser. Otherwise, the SO_2 will leave the circulation loop only in the bleed CO_2 stream.
- HCl – chloride in the fuel gas will be converted to hydrogen chloride in the flame. The HCl will be removed into the aqueous condensate collected at the compressor inlet cooler/condenser.

Table 2.2.3-1

Overview of proposed sCO_2 cycles, temperatures, and working fluid conditions.

Name	Proposer/ Developer	Type (Open/ Closed)	Description	Approx Size (MW)	Thermal Resource	High-Temperature Heat Exchanger Design			Impurities		
						Max T (°C)	Max P (MPa)	sCO_2 Purity	H_2O	Hydro carbons	Others
Novel Air/sCO_2	Peregrine Turbine Tech LLC	Closed	Proposed combination air/sCO_2	66	Nat Gas	750	26.7	High	Near zero	Near zero	
Simple Brayton Test System	Bechtel Marine	Closed	Operating test facility	0.1	Electric heaters	300	16.5	High	Near zero	Near zero	
Test Facility	SwRI	Closed	Test facility (in design)	1				High	Near zero	Near zero	
RCBC Test Facility	Sandia	Closed	Operating test facility (recompression Brayton cycle)	0.2	Electric heaters	538	13.8	High	Near zero	Near zero	
Thermafficient Systems	Echogen Power Systems	Closed	Heat recovery system (in commercialization)	10	Waste heat	485	23.3	High	Near zero	Near zero	
Korean PGSRF	Generic	Closed	Nuclear	150	Nuclear	545	20	High	Near zero	Near zero	
NREL/Sunshot	Generic	Closed	CSP	150	Sun	700	≈30	High	Near zero	Near zero	
Nuclear (Na) w/Brayton	Argonne National Lab	Closed	Sodium reactor with sCO_2 Brayton		Nuclear	500		High	Near zero	Near zero	
ZEPS	GTI	Closed	Oxy-PFBC	676	Coal/ petcoke/ biomass	700	27.6	High	Near zero	Near zero	
Allam Cycle	NET Power	Open	Full-scale module	285	Natural gas/coal syngas	1150	30	95%	2%	Low	O_2=1%, Ar=1%, NO_x=0.2 ppbm SO_2=1 ppbm
	NET Power	Open	Natural Gas Pilot plant	20	natural gas	1150	30	95%	2%	low	O_2=1%, Ar=1%,
	8 Rivers Capital	Open	oxy-coal syngas	285	coal syngas	1150	30				
SCOT	Aerojet Rocketdyne	Open	Proposed design		Natural gas/coal syngas	<1350					

Notes: highlighted projects represent the only field facilities in operation at the time that enquires were made. Max temperature for open cycles is the reported combustor temperature, not in the heat exchangers which likely will be near 700°C.

An estimate of contaminant levels can be made for a prototype Allam Cycle using information published in the patent [4]. The recycle sCO_2 flow is approximately 35 times the molar flow of methane. Using this ratio, adjusted for a constant LHV input to the cycle, a simple 'mass balance' can be used to estimate working fluid contaminant levels for two fueling scenarios:

1. Methane-fueling – This is the cleanest case and represents the lower limits of contaminants that might be expected in the working fluid.
2. Cooled, raw coal syngas-fueling – This is the case which gives upper limits to HCl and SO_x in the working fluid. This approach is taken in the expectation that overall efficiency might be

maximized by removing SO_x and NO_x from the Brayton cycle working fluid, rather than in the coal gasification island. A reactor employing the 'lead chamber' process treats the contaminated working fluid upstream of the inlet cooler/condenser [5]. In this process SO_x is converted to H_2SO_4 and NO_x is converted to HNO_3. These acids are highly soluble in water and dissolve in the condensate collected by the compressor inlet cooler/condenser.

The fuel composition used for the coal syngas case is a model composition developed from data previously published by US-DOE [6] for gasification of a 2.7% sulfur, 0.3% chlorine Illinois bituminous coal and is indicated in Table 2.2.3-2, as is a model composition for merchant oxygen. The resulting working fluid compositions for the two cases are given in Table 2.2.3-3. For each fuel case, two working fluid compositions are shown: (1) the recirculating sCO_2 at the combustor inlet, and (2) the products of combustion entering the gas turbine.

Table 2.2.3-2
Composition of model fuels and model oxidant.

Species	Composition (mole%)		
	Methane	Cooled raw coal syngas	Oxygen
CH_4	100	1.0	
CO		39.0	
H_2		28.3	
CO_2		8.0	
H_2O		20.0	
N_2+Ar		2.0	0.5
H_2S		0.9	
HCl		0.02	
O_2			99.5
LHV	912 BTU/scf	218 BTU/scf	

Table 2.2.3-3
Estimated working fluid composition.

Component	Composition (mole%)			
Fuel Stream	Methane		Cooled Raw Coal Syngas	
	Combustor Inlet	Turbine Inlet	Combustor inlet	Turbine Inlet
CO_2	95	90	90	85
H_2O	250 ppm	5	250 ppm	5
N_2+Ar	1	1	9	9
O_2	4	4	1	1
HCl				20 ppm
SO_2				1000 ppm

Notes to Table 2.2.3-3:

- *The higher concentration of N_2+Ar in the coal syngas-fueled case is due to the elevated nitrogen content of the syngas.*
- *The reduced oxygen content for the coal syngas-fueled case is largely explained by higher CO_2 bleed rates due to the elevated CO_2 content of the fuel gas. A secondary effect is the reduced oxygen required (per unit LHV) to burn syngas compared to methane.*
- *H_2O concentrations at the combustor inlet are calculated to be those associated with saturated gas at 38°C and 275 bar total gas pressure.*
- *There are no reliable reports of excess oxygen required to avoid carbon monoxide in the products of combustion at the very high combustor pressures associated with the Allam Cycle. This calculation assumes 2% excess oxygen feed to the combustor. Oxygen concentrations in the working fluid will rise and fall with the excess oxygen required.*
- *There are no reliable reports of NO_x production at the high pressures associated with the direct-fired Brayton power cycle. NO_x levels likely will be low due to the comparatively low firing temperatures anticipated (1150°C) and the low nitrogen concentrations (compared to air-firing in combustion turbines).*

To further validate the gas compositions derived from simple mass balances and listed in Table 2.2.3-3, detailed thermodynamic calculations were performed using commercial software, *HSC Chemistry 8*. In the thermodynamic treatments, both mass balance and Gibbs energy minimization were considered simultaneously. Therefore, chemical species were redistributed through reactions to allow the system to reach the lowest Gibbs energy state (i.e., equilibrium). Such redistribution is especially important for corrosive species of interest, which typically are minor in concentration and cannot be estimated by using mass balances alone. In these thermodynamic treatments, the same fuel compositions for methane and syngas shown in Table 2.2.3-3 were used, and the calculations were carried out with 2% excess O_2 in the combustion gas at 700°C and 200 bar.

Results of the thermodynamic calculations, summarized in Table 2.2.3-4, show the concentrations of the selected species of interest present in the combustor prior to dilution by the recycled CO_2. Noticeably, the concentration of CO_2 from the syngas is much higher than that of methane, while the moisture content from the syngas is significantly lower than that of methane. Such differences are attributed to the high hydrogen content of methane (as CH_4). From the standpoint of high-temperature corrosion, the combustion gas from syngas contains much higher concentrations of HCl and SO_2 (969 ppm and 8,500 ppm, respectively) than that from methane (0 and 1 ppm, respectively).

Once the combustion gas is diluted with recycled CO_2 that has been scrubbed by an upstream condenser, the concentrations of HCl and SO_2 (as well as the moisture content) in the working fluid entering the gas turbine are significantly reduced. Based on these calculations, the only meaningful amounts of impurities present in the O_2/methane-fired sCO_2 Allam Cycle at the turbine inlet are O_2 and H_2O, which are approximately 3.6 and 5.3 mole%, respectively. These impurity concentrations are similar to those shown in Table 2.2.3-3 determined from a simple mass balance.

Table 2.2.3-4
Equilibrium concentrations of selected species produced from the combustor of an O_2-fired sCO_2 Allam Cycle (in mole%).

Species	Methane	Syngas
CO_2	33.8	62.9
HCl	nil	0.0969
H_2O	65.6	33.7
O_2	1.31	1.48
N_2+Ar	0.33	0.9
NO_x	nil	0.0025
SO_2	0.0001	0.85

For the O_2/syngas-fired sCO_2 Allam Cycle, meaningful amounts of HCl and SO_2 also exist in the working fluid as impurities at the turbine inlet, along with O_2 and H_2O. The HCl and SO_2 concentrations were calculated to be approximately 100 and 1,000 ppm in sCO_2, respectively. The SO_2 concentration of 1,000 ppm from the thermodynamic calculations is identical to that shown in Table 2.2.3-3 from a mass balance. However, a much higher concentration of HCl is calculated for the syngas-fired Allam Cycle than that in Table 2.2.3-3.

In early commercialization of the sCO_2 Allam power cycle, a semi-open O_2/NG (methane)-fired system is likely the most economical and attractive. As demonstrated by the thermodynamic calculations above, the resulting sCO_2 working fluid from firing methane possesses a lower corrosion potential, thus potentially allowing lower-cost materials to be used.

Consequently, it was decided that the focus of the laboratory testing for more extensive materials evaluation (Section 2.3) should be the impact of O_2 and H_2O as impurities produced from a semi-open O_2/NG-fired sCO_2 Allam Cycle.

2.2.3.B - Summary for Impurities in sCO_2

Based on (1) a review of available data in the literature, (2) the desire to maximize cycle efficiency for a future transformational fossil power system, and (3) the potential for these impurities to impact on corrosion, the following ranges of impurities are anticipated for burning different fuels and will be explored:

- H_2O: 2-5%
- O_2: 1-4%
- SO_2: 100-1000 ppm
- HCl: 0-100 ppm

With the aid of thermodynamic calculations, a better determination of the impurity concentrations was accomplished for burning syngas and methane. From these results it was decided that the focus of initial short-term (300 hours) corrosion tests (Sections 2.3.1.B and 2.3.2.B) should be

to compare the corrosion performance of alloys exposed to relatively pure sCO_2, and sCO_2 with impurity concentrations from using methane.

2.2.4 — References Cited in Section 2.2

1. R. Le Pierres, D. Southall, and S. Osborne, "Impact of mechanical design issues on printed circuit heat exchangers," Supercritical CO_2 Power Cycle Resource Center (2014).
2. R. Viswanathan, J.F. Henry, J. Tanzosh, G. Stanko, J.P. Shingledecker, and B. Vitalis, "U.S. program on materials technology for USC power plants," *Proc. Advances in Materials Technology for Fossil Power Plants*, Hilton Head Island, R. Viswanathan, D. Gandy, and K. Coleman, Eds., ASM (2005).
3. J.P. Shingledecker and I.G. Wright, "Evaluation of the Materials Technology Required for a 760°C Power Steam Boiler," pp. 107-120 in *Proc. 8th Liege Conf. on Materials for Advanced Power Engineering 2006,* Forschungszentrum Jülich GmbH (2006).
4. *System and Method for High-Efficiency Power Generation Using a Carbon Dioxide Circulating Working Fluid*, US Patent 2011/0179799 A1, July 28, 2011.
5. R.J. Allam, et al., "High efficiency and low cost of electricity generation from fossil fuels while eliminating atmospheric emissions, including carbon dioxide," *Energy Procedia*, 37, 1135–1149 (2013).
6. *Cost and Performance for Fossil Energy Plants, Volume 1: Bituminous Coal and Natural Gas to Electricity,* DOE/NETL-2010/1397, Revision 2a (September 2013).

2.3 Laboratory Oxidation/Corrosion Testing and Analysis of Exposed Test Specimens

2.3.1— Assemble Corrosion Test Rig and Conduct 300-h Shakedown Tests

2.3.1.A- Facility Overview

2.3.1.A.1 - Assembly of Test Rig

An existing high-temperature, high-pressure corrosion test chamber and flow loop were modified to perform exposures to CO_2 at a pressure of 200 bar and temperatures up to 750°C. A schematic diagram of the test system is shown in Figure 2.3.1-1. The major system components consisted of a custom-built reaction chamber; a high-pressure pneumatic-powered gas booster pump; a water injection pump; and a furnace. The overall test facility and safety considerations included the following features:

1) A designated laboratory facility equipped with appropriately-sized exhaust;
2) A CO_2 sensor and building monitor (in the event of a rapid release of CO_2);
3) A private entrance door; and
4) A video camera.

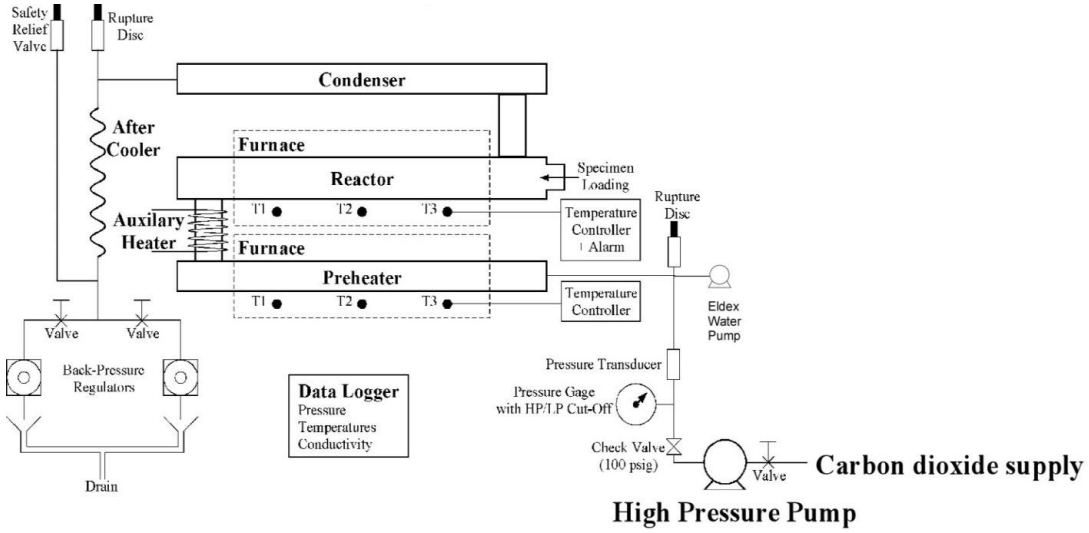

Figure 2.3.1-1. Diagram of the high-pressure corrosion test rig.

Figure 2.3.1-2 illustrates the flow loop and the location of the CO_2 alarm system, air inlet fans, and video camera. The laboratory space can be replenished with fresh air six times per minute using a dedicated exhaust that is vented directly to outside. The CO_2 sensor is shown in detail in Figure 2.3.1-3.

2.3.1.A.2 - Reaction Chamber

The reaction chamber was a single isobaric volume fabricated from alloy HA230 with three distinct temperature zones. As shown in Figure 2.3.1-1, the temperatures were measured on the

outside surfaces of the reaction chamber during testing. The temperature of the preheater furnace was set at 440°C.

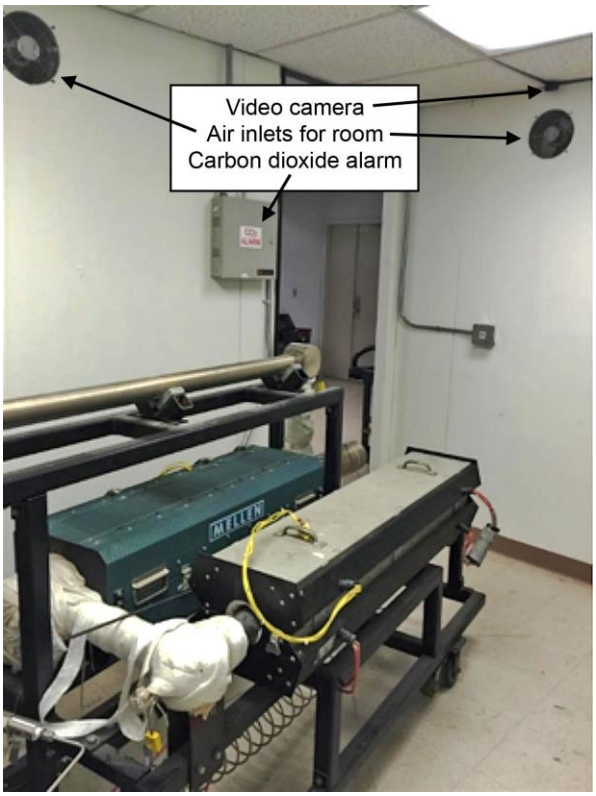

Figure 2.3.1-2 – Overall view of the test rig.

Figure 2.3.1-3 - Details of the CO_2 sensor used.

The lowest temperature measured at the preheater inlet was 220°C (outside the furnace vestibule), and the coldest portion of the gas inlet tubing (TP316L austenitic steel) leading to the gas preheater (Alloy 230) was 175°C. The temperatures of the retort (between the preheater furnace and

the condenser inlet) were above 300°C at all times, excluding the specimen loading port which was maintained at 175°C by air-cooling to protect its Teflon seal. The lowest temperature of the condenser (including the TP316L outlet tubing) was 130°C. The desired temperature profile along the retort was maintained by external heating, conduction, and convection. The working zone where the specimens were exposed was well controlled by the external furnace.

2.3.1.A.3 - Pressure Control

The pressure of the CO_2 was controlled by solenoid valves and a pressure-relief valve. The specification of the solenoid valves (rated at a maximum allowable working pressure of 689 bar) is shown in Figure 2.3.1-4. When not powered by direct current the solenoid valves remain open. Bump tests were performed while high-pressure nitrogen was introduced into the solenoid control valves, and during an initial shake-down test each valve successfully stopped the flow of nitrogen at a pressure differential of 276 bar. The pressure and temperature sensing equipment were calibrated according to DNV GL Laboratory Standard Operating Procedures and Testing Protocols. A hydrostatic pressure test was carried out successfully under nitrogen for 24h at 241 bar with no pressure drop.

Figure 2.3.1-4 – Specification of the solenoid valve model used to control the inlet and outlet pressures.

2.3.1.A.4 - Temperature Control

The temperature of the zone in which the specimens were located was well controlled by the external furnace, and the temperature profile along the retort was maintained by external heating, conduction, and convection. The length of the isothermal working zone of the furnace at 760°C was approximately 356 mm, and the temperature accuracy was expected to be +/-5.5°C. At the target test temperature of 760°C the sealing flange of the specimen insertion port remained at approximately 80°C, allowing the use of a PTFE gasket for the flange. DuPont Kalrez® seals also were procured as a

higher-performance alternative for use if needed. A temperature profile of the furnace determined in air at atmospheric pressure is shown in Figure 2.3.1-5.

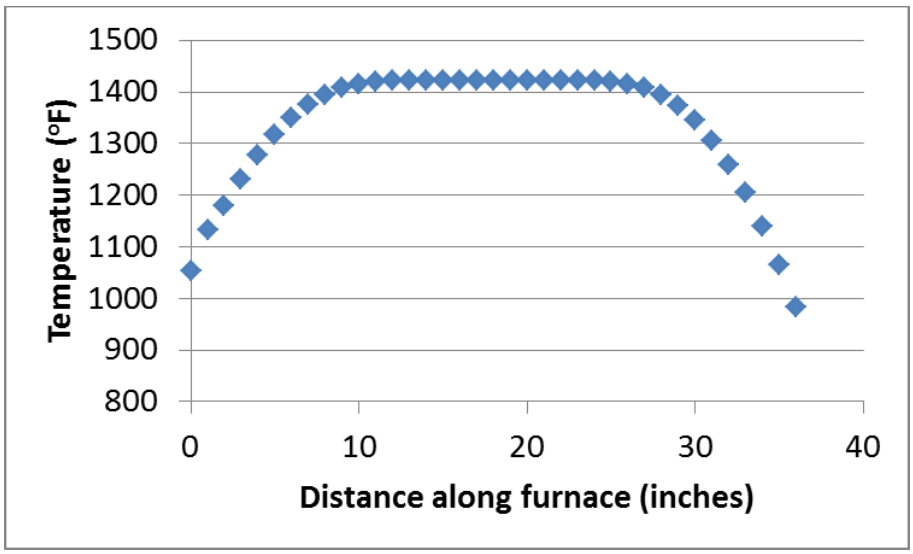

Figure 2.3.1-5 - Temperature profile of the furnace through the working zone.

As indicated in Figure 2.3.1-1 temperatures were measured on the outside surfaces of the retort during testing. The temperature of the preheater furnace was set at 440°C, and the system pressure was 200 bar. The lowest temperature measured at the preheater inlet (Alloy HA230), outside of the furnace vestibule, was 220°C. The coldest portion of the gas inlet tubing (TP316L) leading to the preheater was 175°C. The retort temperatures between the preheater furnace and the condenser inlet, excluding the specimen loading port, were above 300°C at all times. The specimen loading port was maintained at 175°C by air-cooling to protect the Teflon® seal. The lowest temperature of the condenser, including the outlet tubing, was 130°C.

2.3.1.A.5 - Computer Control

A computer-based interface was used to control the test apparatus, and an example of an image captured on the computer screen is shown in Figure 2.3.1-6. The test pressure was changed using 'switches' on the computer software interface that controlled the solenoid valves. All temperature and pressure sensors throughout the test facility were connected to the data acquisition system. The pressure and temperature data also were recorded on a computer during each test. Images from the video camera were visible on the computer monitor and recorded continuously (a room image was taken every 3 seconds) throughout the shakedown testing.

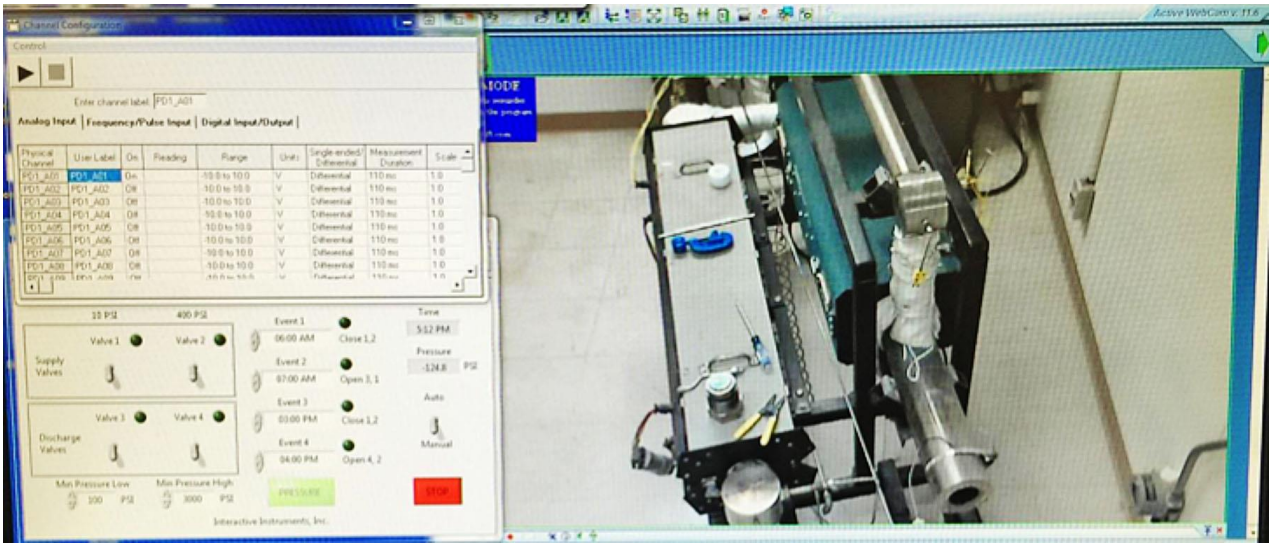

Figure 2.3.1-6 - Overview of the computer-based control system, data acquisition, and output of monitoring video camera.

2.3.1.A.6 - Specimen Preparation and Evaluation Procedures

Test specimens of dimensions 2.54 x 2.54 x 3.2 mm were machined from all alloys by the EPRI machine shop. The weight and dimensions of each of the alloy specimens were measured prior to the test. For exposure specimens were placed in vertical slots in a specimen tray (made of Alloy IN625), as shown in Figure 2.3.1-7), so that when loaded in the retort one of the main surfaces of each specimen faced the gas flow.

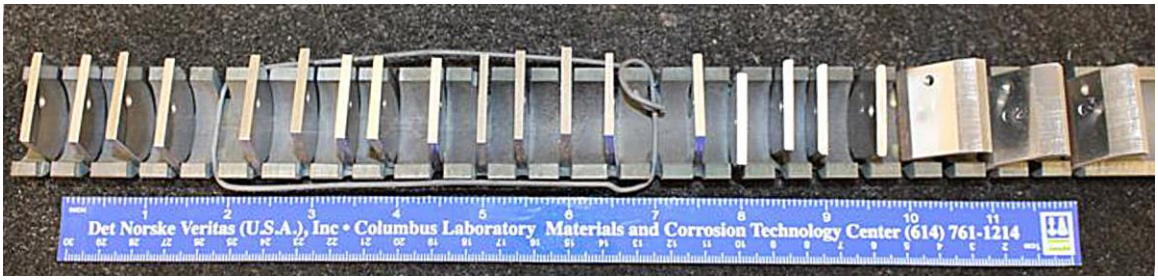

Figure 2.3.1-7 – Example of alloy specimens and tray used for high-temperature exposures.

After exposure, specimens were reweighed, then sectioned along the centerline using a precision-cutting, diamond wafer blade operated at a very slow speed. One of the resulting pieces of each specimen was mounted vertically in conductive epoxy, ground to remove approximately 3 mm of the material from one end, then polished with 0.5-µm diamond paste and finished using a 0.1-µm colloidal suspension of silica. The mounted and polished cross sections were examined using an optical microscope and a scanning electron microscope (SEM) in secondary electron (SE) and backscattered electron (BSE) modes. The SEM was equipped with energy-dispersive X-ray spectrometers (EDS) to allow elemental analysis via spot measurements, mapping, or line scans. Initial examination determined the locations of the interfaces between the layers in the scales, and the thicknesses of each layer (and total thickness) were measured at three locations on the polished cross-section of each

specimen using an inverted optical microscope. Ten measurements were made at each location at 400x magnification, resulting in a total of thirty measurements for each cross-section.

Where very thin oxides were formed (as on alloys HR3C, IN617, and IN740H) thickness measurement using optical microscopy was considered to be imprecise, so that those scales were examined by SEM/BES/EDS using an Olympus image analysis system at magnifications up to 2,500x. As a reference, specimens of TP304H (for which thickness measurements were available using optical means) were included in these measurements.

Etching was used to detect the presence of carburization attack in the ferritic steels. Polished cross sections were swabbed with 10% oxalic acid, or with Kalling's solution, and/or etched electrolytically using 4% Nital.

Microhardness measurements also were made to infer the presence of carburization in the alloys. The measurement procedure used a standard Vickers indenter with a 1 kg load, operated with a 10 sec dwell time.

2.3.1.B – Initial Shakedown Testing in Commercial-Grade CO_2 at 200 bar and 700°C

A shake-down run of approximately 300h duration using commercial-grade (CG) purity CO_2 at 200 bar and 700°C was conducted to allow adjustments to be made to the equipment, operating procedures, and test conditions. Following completion of the test and evaluation of operating experience and results, any required adjustments to the equipment, operating procedures, and test conditions were made before the start of the second shakedown test (Section 2.3.2.B).

Standard specimens of three alloys were included in this test: ferritic steel Grade 91, austenitic steel TP304H, and Ni-base alloy Inconel 740H (compositions shown in Table 2.2.2-1). Following exposure, evaluation involved visual examination, measurement of mass gain/loss and, after sectioning and metallographic polishing, measurement of the thicknesses of oxide scales formed. Finally, cross sections were subjected to microhardness testing and etching to detect signs of carburization. The mass gain results for each alloy are summarized in Table 2.3.1-1.

Table 2.3.1-1
Alloy mass gain results after exposure at 700°C for 300h to commercial-grade purity CO_2 at 200 bar.

Alloy	Specimen #	Mass gain (mg/cm^2)
Grade 91	1	7.66
	2	8.82
	3	7.63
TP304H	1	0.28
	2	0.17
	3	0.24
N740H	1	0.19
	2	0.21
	3	0.23

Figure 2.3.1-8 shows optical micrographs of a metallographically-polished and etched cross section of a representative specimen of Grade 91 after exposure for 300h. The scale formed was relatively uniform in thickness and featureless, but appeared to consist of two (or three layers). Etching revealed a dark-appearing zone along the alloy-scale interface, suggestive of the presence of a zone of carburization. Hardness measurements indicated that the dark-appearing region was noticeably harder than the alloy matrix (Table 2.3.1-2).

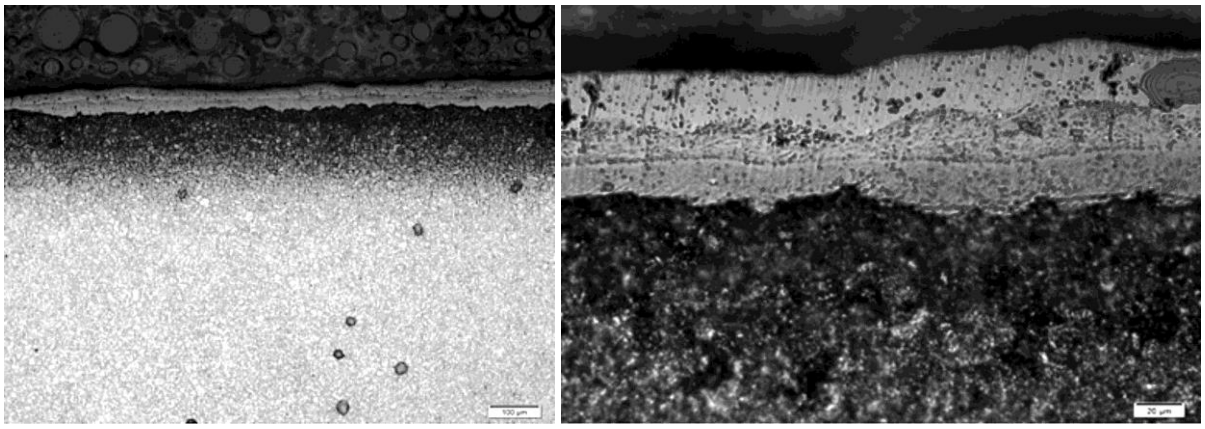

Figure 2.3.1-8 - Optical micrographs of metallographically-polished and etched cross-section of ferritic steel Grade 91 after exposure at 700°C for 300h to commercial-grade purity CO_2 at 200 bar (etched by swabbing using Kalling's etchant).

Table 2.3.1-2
Vickers hardness measurements of Grade 91 as a function of depth, following exposure at 700°C for 300h to commercial-grade purity CO_2 at 200 bar.

Distance from alloy-oxide interface (µm)	Hardness (Vickers)
83	297
167	321
271	251
417	234
625	224

An SEM/BSE image of the same polished cross-section is shown in Figure 2.3.1-9. This suggests that the approximately 60 µm-thick scale was comprised of three layers, rather than the two-layered structure typically found on this alloy after exposure in HP steam [1]. Elemental maps for elements C, O, S, V, Cr, Mn, Fe, and Cu were generated from the cross-section of the scale using SEM/EDS, and are shown in Figure 2.3.1-10. The maps for Cr, Fe, and O clearly indicate the presence of four layers with different Fe+Cr combinations: a Cr-rich inner layer (L1 in Figure 2.3.1-9), an Fe-rich (Cr-free) outermost layer, and two thinner, intermediate layers containing Fe and Cr, with the innermost indicating a lower Cr content than the outer. The Mn map shows a similar distribution to the Cr map, with a lower level of Mn in the innermost 'intermediate' layer. The presence of Cu was considered to have resulted from

contamination during the specimen preparation process, and measures were taken to prevent its recurrence in future tests.

Figure 2.3.1-11 is a composite of the elemental maps superimposed on the SEM/BSE image, and clearly shows the boundaries separating the different layers of oxide, suggesting that the overall structure consisted of two sets of Fe-rich and Cr-rich oxides. The innermost Cr-containing layer appeared to be the expected Fe-Cr spinel layer (L1), while the next layer (an 'intermediate' layer from Figure 2.3.1-10) appeared to be magnetite that had a structure more like that of L1 than the usually columnar-grained structure of the expected magnetite layer (L2) [1]. Next was a thin, Cr-rich layer, while the outmost thicker, Fe-rich layer resembled the expected L2.

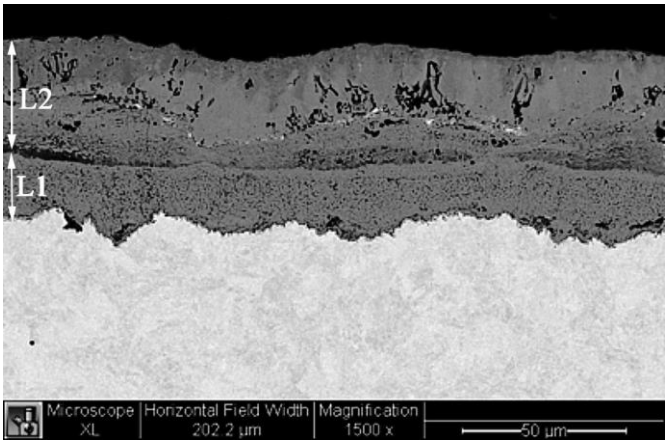

Figure 2.3.1-9 – SEM micrograph of metallographically-polished cross-section of Grade 91 after exposure to commercial-grade purity CO_2 for 300h at 700°C and 200 bar.

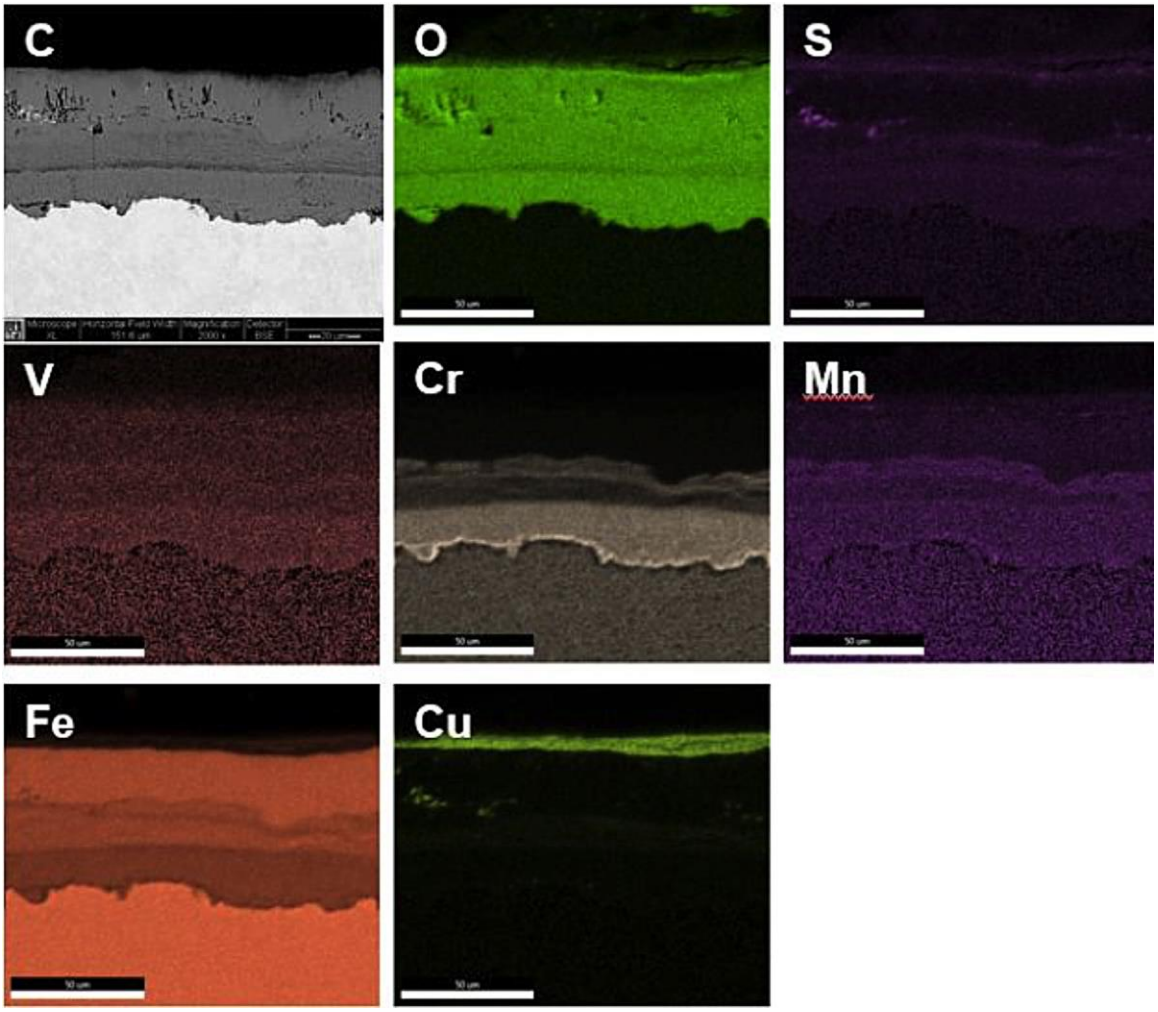

Figure 2.3.1-10 – SEM/EDS elemental maps of the scale formed on Grade 91 after exposure to commercial-grade purity CO_2 for 300h at 700°C and 200 bar.

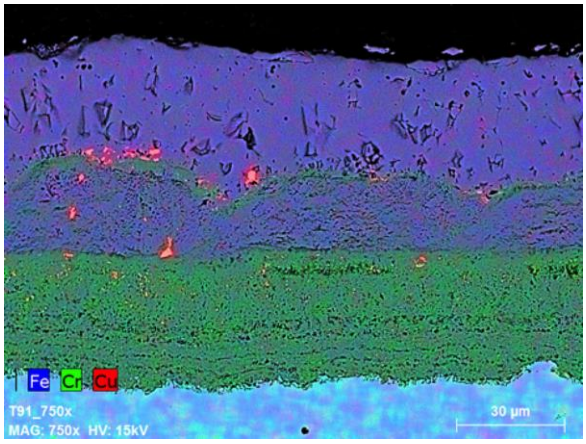

Figure 2.3.1-11 - EDS maps for Fe (blue), Cr (green) and Cu (red) superimposed on an SEM/BSE image of a cross-section of scale formed on Grade 91 after exposure to commercial-grade purity CO_2 for 300h at 700°C and 200 bar.

An EDS line-scan for Fe, Cr, and O across the thickness of the oxide scale, shown in Figure 2.3.1-12, confirms that the inner layer was equivalent to an Fe-Cr spinel layer (L1) and the outermost layer to an essentially Cr-free magnetite layer (L2), both typically formed in steam. The innermost 'intermediate' layer contained Cr at a level between those of L1 and L2, while a higher of Cr was present in the outermost 'intermediate' layer.

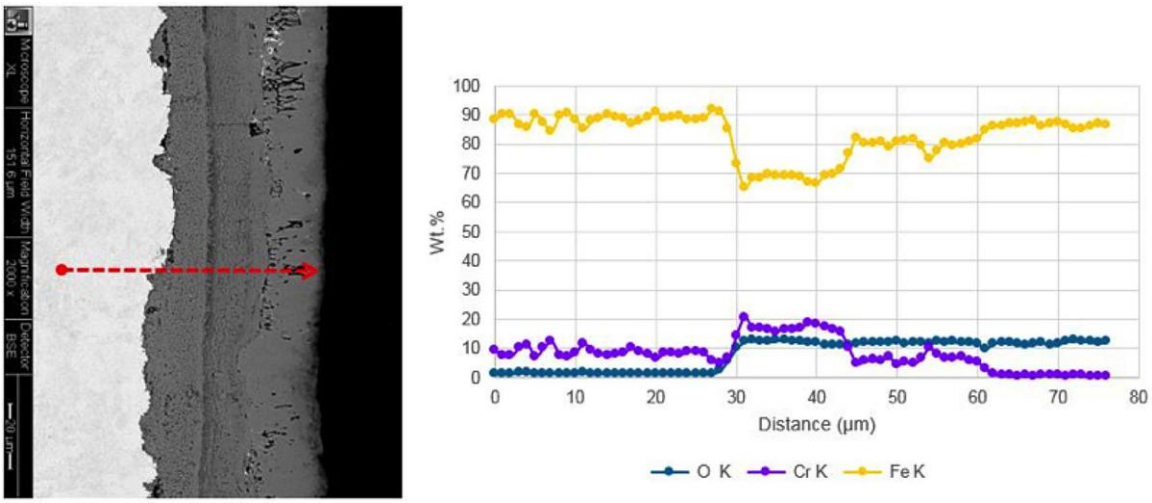

Figure 2.3.1-12 - EDS line scan for O, Cr, and Fe through a metallographically-polished cross-section of Grade 91 after exposure to commercial-grade purity CO_2 for 300h at 700°C and 200 bar.

From thermodynamic considerations growth of an Fe-rich oxide ('intermediate' layer) beneath an (apparently) continuous Fe-Cr-containing oxide is unlikely to have occurred during steady-state oxidation. A possible alternative explanation is that the scale that formed originally consisted of the two layers expected from experience in steam (L1 and L2), and at some point during the test exposure separation occurred near the interface of those layers, allowing access of the ambient gas. Subsequent re-exposure resulted in growth of a new magnetite layer (L2) along the original L1-L2 interface beneath a portion of the original L1. Subsequent scale growth presumably involved thickening of L1 and the new magnetite layer. Such interruption in scale growth likely would have required a significant thermal cycle. Fluctuations in the exposure conditions were in fact detected during this shakedown test, and apparently were associated with a major pressure cycle experienced after approximately 24h of operation. Explanation for the apparent decoration with Cu of the interfaces between L1, L2, and the intermediate layers (Figure 2.3.1-11) is not available at this time.

The approach for measuring the thicknesses of the scales formed is demonstrated in Figure 2.3.1-13. Measurements were made at 50 µm intervals along the selected length of scale using optical microscopy at 200x magnification. For these initial measurements it was assumed that the scale comprised two main layers: an inner layer (L1) as indicated in Figure 2.3.1-9, and an outer layer (L2) comprising the remainder of the scale thickness (that is, all of thickness of the 'original' and 'new' magnetite layers). The presence of the thin, 'intermediate' spinel layer was ignored. The length of scale from which measurements were made is shown in Figure 2.3.1-13 as a horizontal pink line, and the actual measurements locations as white lines.

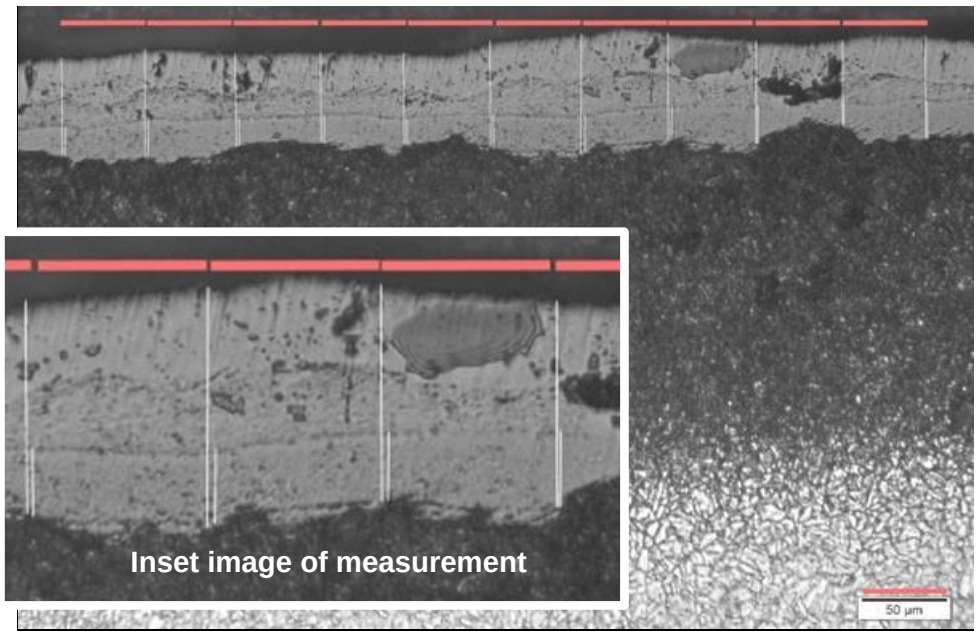

Figure 2.3.1-13 – Optical micrograph of metallographically-polished cross-section of Grade 91 showing locations (vertical white lines) and intervals (horizontal pink lines) where thickness measurements were made after 300h exposure to commercial-grade purity CO_2 at 700°C and 200 bar.

The measured total and inner layer (L1) thicknesses are summarized in a box and whisker plot (or 'box plot') shown in Figure 2.3.1-14. Box plots demonstrate the degree of uniformity of scale thickness by simultaneously providing the mean value (solid diamond), median value (horizontal line inside the box), second and third quartiles (top and bottom of the box), and minimum and maximum readings (the positive and negative bars or 'whiskers' attached to the boxes). A small, compact box with short whiskers signifies uniform scale thicknesses, whereas a large box with long whiskers represents much more varied scale thicknesses along the specimen surface. In this case the thickness of the inner layer ranged from 15 to 23 µm with a median value of 20 µm (average thickness 19 µm), and the total scale thickness ranged from 50 to 71 µm (median value 61 µm; average thickness 60 µm). These readings suggest relative layer thicknesses of L1/L2 = 0.5, significantly lower than the value of ≈1 typically found in steam-grown scales (and possibly unduly influenced by an interruption in test conditions during this shakedown run.

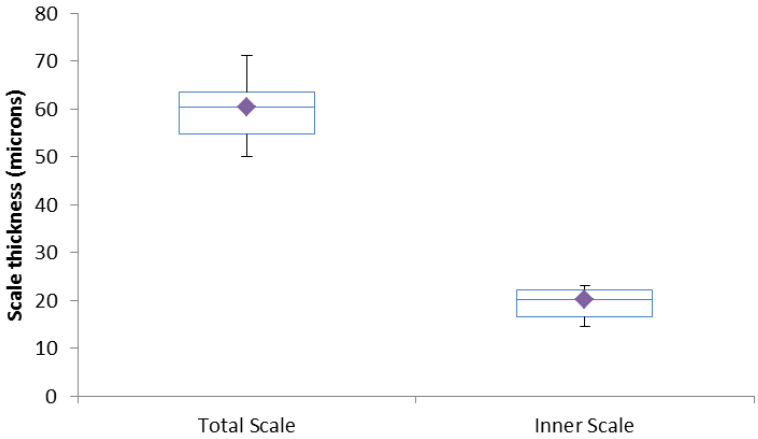

Figure 2.3.1-14 – Box plot of oxide layer thicknesses formed on Grade 91 after exposure to commercial-grade purity CO_2 during a 300h shakedown run at 700°C and 200 bar.

The other alloy specimens exposed in the shakedown test, austenitic steel TP304H and nickel-base alloy IN740H, exhibited lower mass gains and much thinner scales than alloy Grade 91. Etched cross-sections of these alloys, shown at low magnification in Figures 2.3.1-15 and 2.3.1-16, respectively, indicated no evidence of obvious carburization near the specimen surfaces.

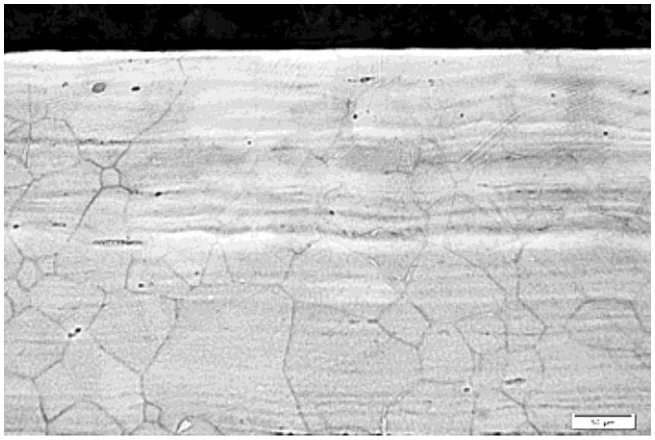

Figure 2.3.1-15 - Optical micrograph of a metallographically-polished cross section TP304H after exposure to commercial-grade purity CO_2 for 300h at 700°C and 200 bar (etched by swabbing with Kalling's etchant).

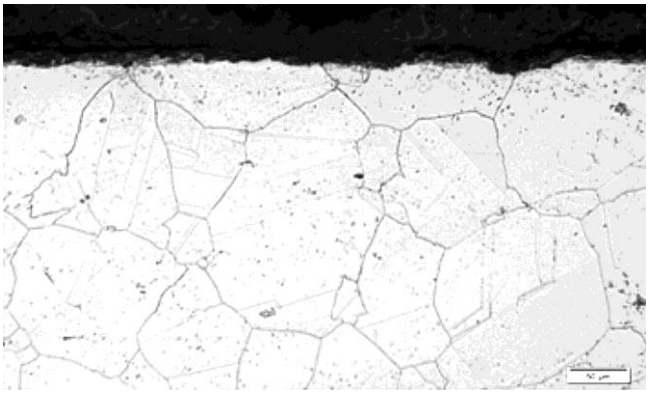

Figure 2.3.1-16 - Optical micrograph of a metallographically-polished cross section IN740H after exposure to commercial-grade purity CO_2 for 300h at 700°C and 200 bar (etched by swabbing with Kalling's etchant).

A higher-magnification SEM micrograph of the cross section of TP304H, and a corresponding EDS line scan for Fe, Ni, Cr, Mn, and O are shown in Figure 2.3.1-17. The external scale appeared to be uniform in thickness and around 1 µm thick, with significant penetration into the alloy, possibly along alloy grain boundaries. This scale consisted of a main layer enriched in Cr, with possibly a thinner outer layer containing Fe and very little Cr. Ni did not appear to participate in the oxides, while Mn probably was present in any outer, Fe-rich scale.

The surface features on IN740H, Figure 2.3.1-18, suggest that the area examined included significant artifacts from metallographic preparation. The root cause of this apparent surface roughness subsequently was identified and corrective measures instituted.

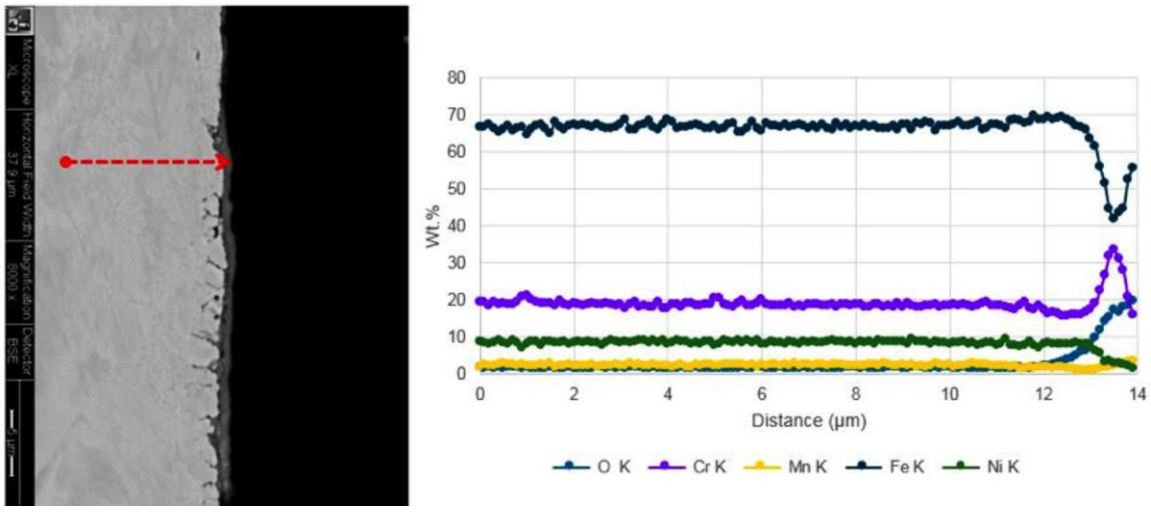

Figure 2.3.1-17 –SEM micrograph and EDS line scan for Fe, Ni, Cr, Mn, and O through a metallographically-polished cross-section of TP304H after exposure to commercial-grade purity CO_2 for 300h at 700°C and 200 bar.

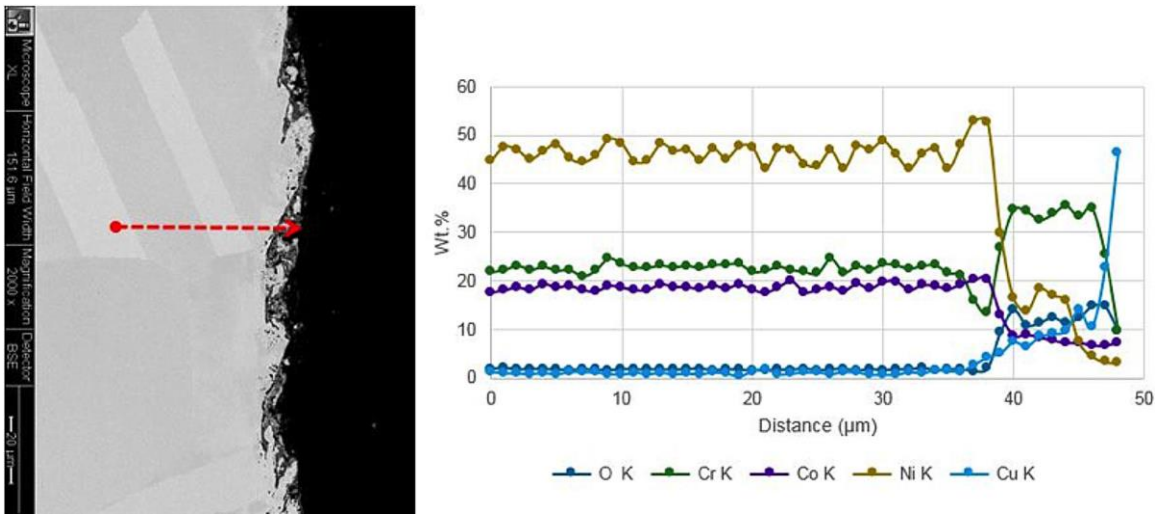

Figure 2.3.1-18 – SEM micrograph and EDS line scan for Ni, Co, Cr, Cu, and O through a metallographically-polished cross-section of IN740H after exposure to commercial-grade purity CO_2 for 300h at 700°C and 200 bar.

Microhardness measurements were performed on these metallographically-polished cross-sections to examine the possibility that carburization had occurred during this shakedown run. An array of 7 x 14 measurements was made in the near-surface regions of the cross-sections using a 100-g indenter, with indentations made approximately 60 µm apart in both directions, as illustrated in Figure 2.3.1-19. Note that the first row of measurements (shown by a horizontal red line) was made at about 60 µm from the alloy-scale interface to avoid any interference from the scale.

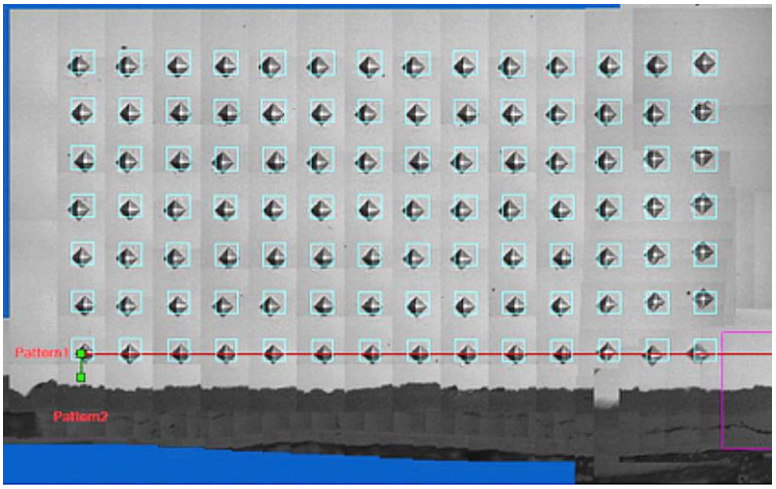

Figure 2.3.1-19 – Optical micrograph of a finished surface after micro-hardness measurements.

These micro-hardness data were used to develop maps of hardness variation near the alloy surfaces, as shown by the example in Figure 2.3.1-20 for Grade 91. The specimen orientation in the figure corresponds to that in Figure 2.3.1-19 (i.e., the alloy-scale interface is at the bottom of the plot). Two sets of maps were made for each alloy as a means of verifying the repeatability and sensitivity of the measurements. For Grade 91 the highest hardness values were found near the alloy-scale

interface, suggesting that carburization probably had occurred during this exposure to sCO_2. Hardness-depth profiles also were plotted, and comparisons with the similar exposure to sCO_2 with oxidizing impurities are presented for all three alloys (Section 2.3.2.B).

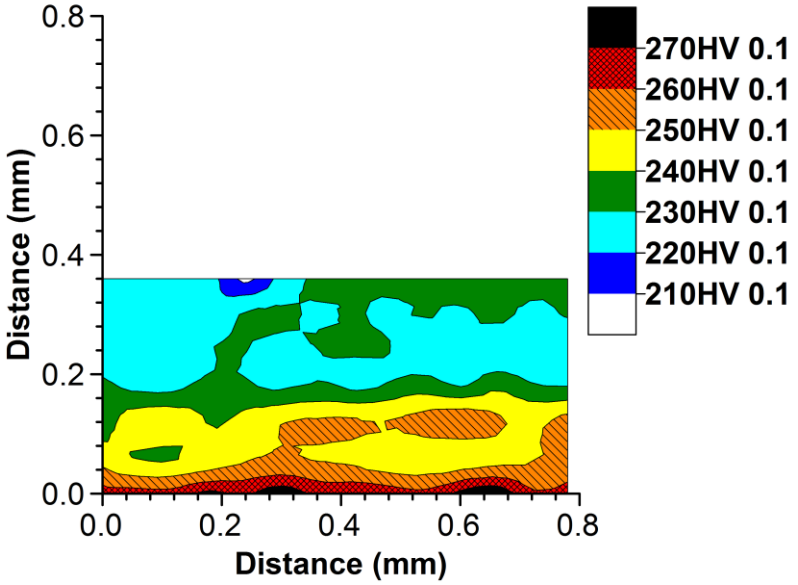

Figure 2.3.1-20 – Hardness map for Grade 91 after exposure to commercial-grade purity CO_2 for 300h at 700°C, showing increased hardness near the alloy-scale interface (at bottom of map).

2.3.2 — Complete Tests to Support Final Decision on CO_2 Composition For Remaining Testing

2.3.2.A – Thermodynamic Modeling

Thermodynamic modeling using OLI software (OLI Studio version 9.2) was carried out to better understand the solubility range of water in sCO_2 as a function of temperature. This modeling work was intended to address a knowledge gap in the propensity of water condensation in the low-temperature zones of the retort system of the test rig. Results of the modeling indicated a change in solubility of H_2O in sCO_2 near 180°C. Figure 2.3.2-1 is a plot of the solubility water in CO_2 containing 3.6 vol% O_2 (expressed in moles of water in the vapor phase) as a function of temperature at 200 bar. The data points from the model are labeled with the moles of water in the vapor space (i.e. the solubility limit) as the temperature decreases. The total amount of water in the system was 1.47 moles, which is equivalent to a molar fraction of 0.123 in the retort under the test conditions. Oxygen had no effect on the solubility of water and was miscible in sCO_2 at all temperatures based on the modeling results.

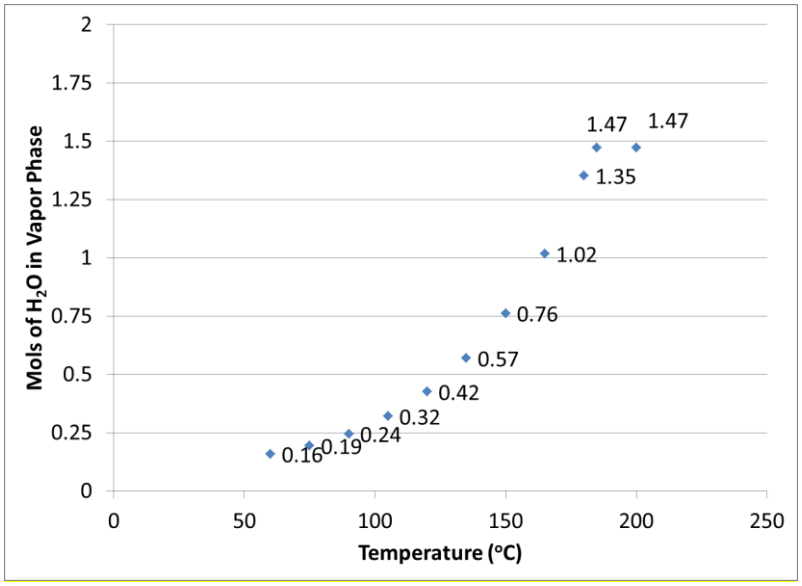

Figure 2.3.2-1 - OLI model results showing the solubility of 5.3 vol.% water in sCO_2 containing 3.6 vol.% oxygen.

Published results for the solubility of water in sCO_2 as a function of pressure indicate the water solubility to be approximately 0.060 molar fraction at 150°C (Figure 2.3.2-2 [2]), which is consistent with the results shown in Figure 2.3.2-1. It should be noted that Figure 2.3.2-2 also contains data indicating higher solubility [3]. Subsequent examination of a broader body of published data further demonstrated the extent of such scatter, and that discrepancies tended to increase with temperature and pressure. This is illustrated in Figure 2.3.2-3, which compiles modeling results and experimental data on the solubility of water in sCO_2 as a function of pressure at various temperatures. The discrepancies become particularly apparent above 100 bar and 50°C.

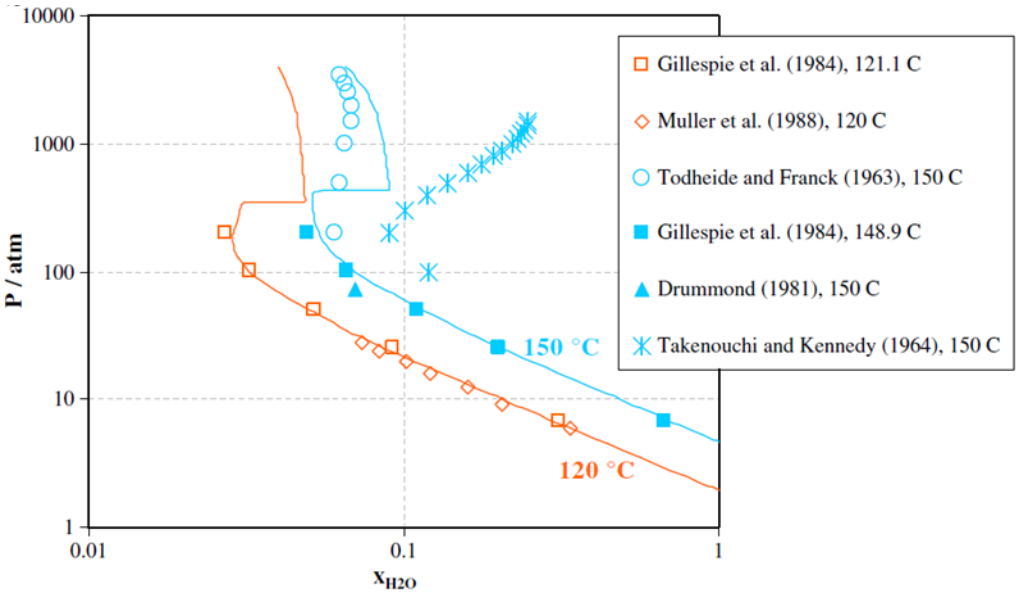

Figure 2.3.2-2 - Modeling results and experimental results reported by Springer et al. [2] for the solubility of water in sCO_2 at 120 and 150°C.

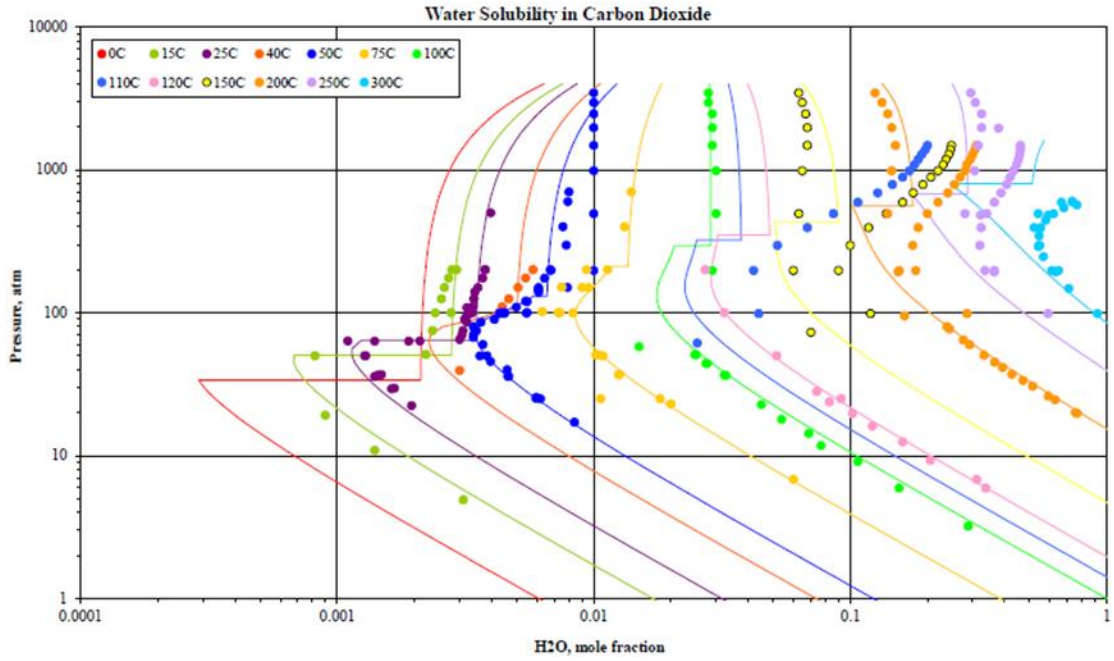

Figure 2.3.2-3 - Modeling and experimental results summarized by Springer, et al. [2] for the solubility of water in sCO_2 at different temperatures.

The results of OLI modeling from this study showed that the concentration of moisture in the test report might be reduced due to water condensation, although the exact amount is not known. As mentioned above, the lowest temperature measured in the retort system was about 130°C. Therefore, it is reasonable to assume a reduction of water concentration in the vapor phase of nearly fifty percent may be possible at this lowest temperature.

The practical impact of possible variation in the water solubility is considered to be very small for the current project, as the total amount of oxygen consumed by the alloy specimens exposed at 700°C was calculated to be negligible. The source of oxygen contributing to the oxidation of alloys in this study included H_2O, CO_2, and O_2. To estimate the amount of O_2 consumed by the formation of oxide scales on the alloy specimens, it was assumed that the scales formed on all iron-based alloys consisted of a spinel inner layer and a magnetite outer layer of equal thickness. The actual mass gains and scale thicknesses measured on the exposed alloys from this study (Section 2.3.1.B) were used to estimate the O_2 consumption. The contribution to O_2 depletion by oxidation of the reaction chamber body itself was ignored on the basis that 1) as it is constructed entirely with Alloy HA230 which possesses excellent oxidation resistance, and 2) a protective scale already was present on its surfaces from previous testing, so that the rate of subsequent oxide growth would be very slow.

The calculated results for O_2 consumption are summarized in Table 2.3.2-1. These indicate that the total oxygen consumption in the test system was on the order of 0.0062 mole during a 1,000-h exposure of specimens of the four less oxidation-resistant alloys: Grade 91, VM12, Crofer 22H, and TP304H (Section 2.3.1.B). This amount of O_2 consumption was negligible compared to the initial gas

composition of approximately 9.5 moles CO_2, 1 mole of O_2, and 1.47 moles of H_2O. Therefore, even if the water concentration in the vapor phase was reduced by half due to condensation in the low-temperature section of the test system, oxidation of the alloys investigated in this study was unlikely to be affected. Nevertheless, during testing the actual concentration of H_2O existing at the location of the specimens in the reaction chamber would have been lower than the 5.3 vol.% intended initially.

Table 2.3.2-1
Calculated O_2 consumption (in mole) by alloy specimens based on measured mass gains and scale thicknesses.

Exposure Period (h)	Grade 91	VM12	Crofer 22H	TP304H
300	0.00124	0.000334	0.000183	0.000121
600	0.00130	0.000297	0.000270	0.000139
1000	0.00139	0.000375	0.000322	0.000144
Total O_2 per alloy	**0.00393**	**0.001001**	**0.000775**	**0.000493**

While minor amounts of sulfur species might be present in sCO_2 (depending on the fuel source and cycle configuration), such impurities were not included in this test because they would not be expected to be present in quantities sufficient to cause corrosion concerns for natural gas-fired systems. The sulfur species also would introduce complications to the understanding of the impact of dominant impurities on the corrosion mechanism(s). Furthermore, the inclusion of sulfur species would have required the current test rig to be relocated to a different laboratory space due to safety concerns for accidental release of sulfur-containing gases. Based on past experience in high-temperature and -pressure tests involving sulfur-containing gases, there existed the possibility that the exit line of the test rigs would become plugged by the corrosion products during operation, leading to significant operational and scheduling issues.

2.3.2.B - Modified Test Procedures

Carbon dioxide containing oxygen was obtained in the form of a certified mixed gas cylinder. System start-up procedure was as follows:

i) The retort pressure was raised to the mixed gas cylinder pressure, which typically was near 55 bar (800 psi).
ii) The furnaces controlling the preheater and working zone were activated, and the system temperature was allowed to equilibrate for approximately 8h after the set points were reached.
iii) Liquid water was added to the retort at room temperature; the volume of added water was determined on a molar basis based on the final mixture.
iv) The system pressure was brought to the test pressure (200 bar) using the CO_2-O_2 mixed gas cylinder and a high-pressure gas booster pump.

2.3.2.C - Shakedown Testing Using CO_2 With Controlled Additions at 200 bar and 700°C

A 2nd 300-hour shakedown run was made using basically the same conditions as the first but with CO_2 containing specific levels of impurities determined in Section 2.3.2.A, instead of commercial-grade purity CO_2. The specific gas mixture chosen for this test was:

- O_2: 3.6 vol%
- H_2O: 5.3 vol%
- CO_2: balance

Overall, the mass gains of the three alloys exposed in this test were consistently lower than in sCO_2 of commercial grade (CG) purity, as indicated in Table 2.3.2-2, in which the mass gains for each

Table 2.3.2-2
Mass gain of alloys exposed at 700℃ for 300h to commercial-grade purity (CG) CO_2 (Section 2.3.1.B) and CO_2 containing 3.6 vol.% O_2 and 5.3 vol.% H_2O (Section 2.3.2.B) and 200 bar.

Alloy	Specimen #	Mass Gain (mg/cm^2)	
		CG Purity CO_2 (1.2.3.1.B)	CO_2 + Controlled Impurities (1.2.3.2.B)
Grade 91	1	7.66	2.96
	2	8.82	2.76
	3	7.63	2.66
		Avg. = 8.04	Avg. = 2.79
TP304H	1	0.28	0.08
	2	0.17	0.08
	3	0.24	0.06
		Avg. = 0.23	Avg. = 0.07
IN740H	1	0.19	0.09
	2	0.21	0.04
	3	0.23	0.07
		Avg. = 0.21	Avg. = 0.07

alloy are the average of three specimens. In two instances during this 2nd shakedown test the system pressure decreased by approximately 14 bar (200 psig) due to a slow release of the mixed gas at a valve seal. It was considered that this minor pressure drop was unlikely to have caused a significant change in oxidation kinetics and weigh gains; the furnace temperature was well controlled at 700°C. Therefore, the differences in mass gain between the two shakedown tests were considered to reflect differences due to the gaseous environments.

The SEM micrograph shown in Figure 2.3.2-4 of a cross section of the scale formed on Grade 91 ferritic steel after 300h at 700°C in this environment suggests an essentially double-layered structure, with a value of L1/L2 much closer to 1 than found after the 300h shakedown test in CG purity CO_2. There was some indication of a banded structure in the inner layer, which also appeared to have a fine, highly-porous structure. In contrast, the outer layer appeared quite dense but otherwise featureless.

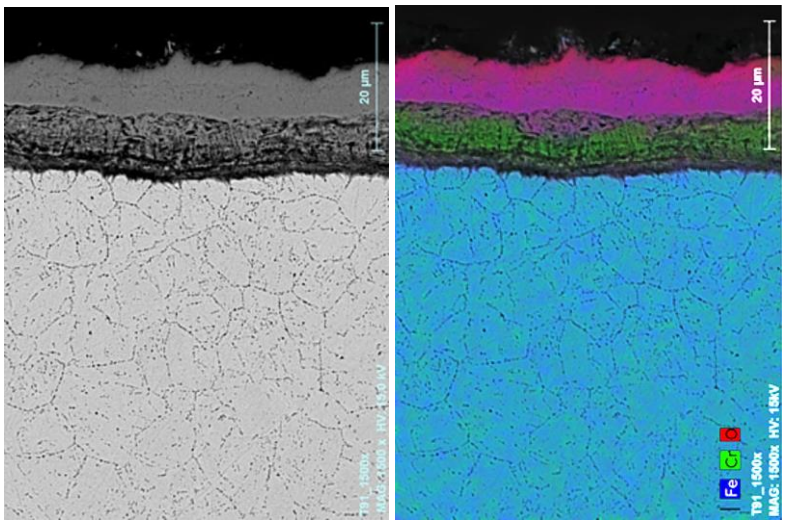

Figure 2.3.2-4 - SEM micrograph and EDS map overlay of a metallographically-polished cross section of alloy Grade 91 after exposure for 300h to CO_2 containing 3.6 vol.% O_2 and 5.3 vol.% H_2O at 700°C and 200 bar.

The overlaid EDS map in Figure 2.3.2-4 for Fe, Cr, and O further inferred the presence of two layers of distinctly different compositions (with Cr essentially confined to the inner oxide layer) as in steam-formed scales, but also suggested that the inner oxide layer was not as uniform in thickness and composition as suggested by the SEM image. Some regions present in the main inner layer adjacent to the interface with the main outer layer had a distinctly higher Fe content. No further clues were found to explain these features.

Micro-hardness measurements made in the surface regions of this specimen are displayed as a hardness map in Figure 2.3.2-5. The region very close to the alloy-scale interface (bottom of figure) clearly exhibited higher hardness values, but these were confined to a zone approximately 20 µm thick. Beyond that region the hardness quickly returned to levels similar to the base metal. Assuming that such hardening was attributable to carburization, the depth of carburization (hence the amount of

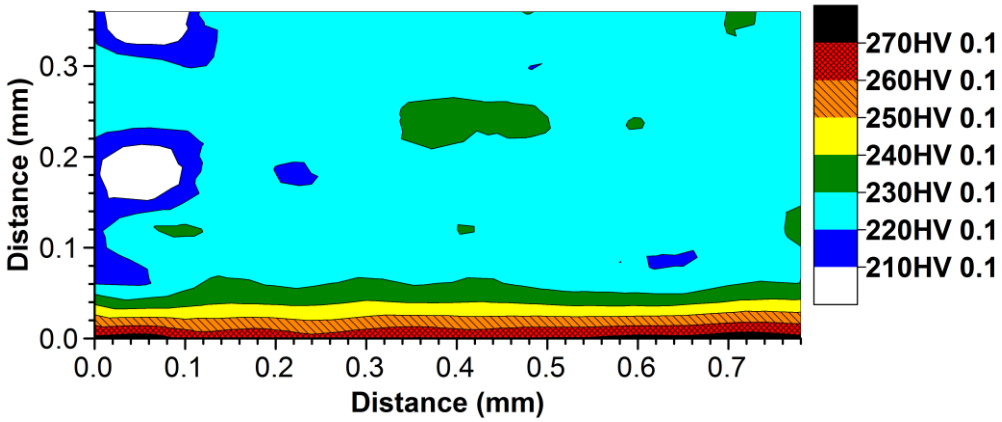

Figure 2.3.2-5 – Micro-hardness map for Grade 91 after exposure to CO_2 containing 3.6 vol.% O_2 and 5.3 vol.% H_2O for 300h at 200 bar and 700°C.

carbon pickup) was significantly lower in this test in sCO_2 with oxidizing additions than that in CG purity sCO_2 (Figure 2.3.1-20).

Hardness profiles for the specimens of Grade 91 exposed in the two shakedown test environments (Sections 2.3.1.B and 2.3.2.B) are compared in Figure 2.3.2-6. At each location, the entire row of 14 hardness data points (as shown in Figure 2.3.1-19) was analyzed statistically, and the data scattering and mean values were determined and are indicated in the plot. In both cases, a significant increase in hardness (to 265-271 HV, compared to the bulk alloy level of 218-227 HV) was measured immediately beneath the alloy-scale interface, after which the profile after exposure to CG purity CO_2 indicated increased hardness extending to a depth of approximately 300 µm from the alloy-oxide interface, whereas in CO_2 with controlled (oxidizing) impurities increased hardness appeared to be confined to within 60 µm of the alloy surface.

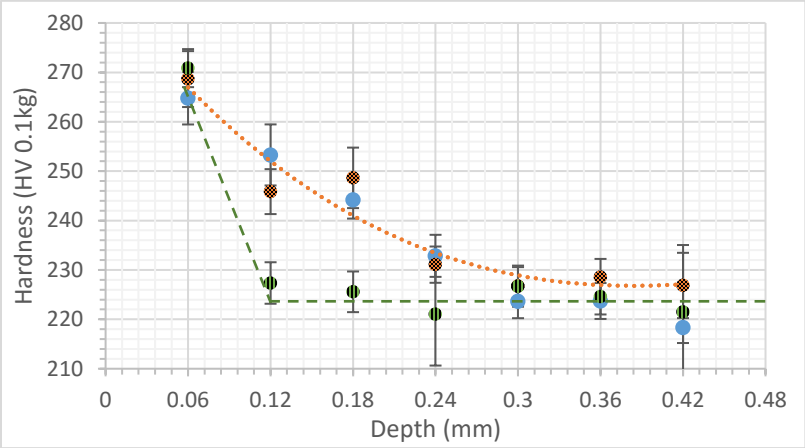

Figure 2.3.2-6 – Hardness profiles of Grade 91 after exposure at 700°C for 300h to CG purity CO_2 at 200 bar (red and blue symbols), and CO_2 containing 3.6 vol.% O_2 and 5.3 vol.% H_2O at 200 bar (green symbols). Measurements were started at 60 µm from the alloy-oxide interface.

Alloy TP304H formed a scale approximately 1 µm thick after exposure for 300h in this test (Figure 2.3.2-7); localized oxidation along alloy grain boundaries at the alloy surface also was evident. The yellow box and locations marked in green in this micrograph denote points where EDS analyses were performed. Those EDS results revealed the Cr content near the alloy surface and grain boundaries to be approximately 20 wt%, suggesting that Cr had not been depleted significantly due to oxidation during the relatively short exposure.

Figure 2.3.2-8 shows a micro-hardness map generated from this metallographically-polished cross section of TP304H. The map contours indicate that significant hardening (carburization) had occurred. Comparison of the hardness-depth profile with that from the test in commercial-grade purity sCO_2, Figure 2.3.2-9, illustrates the magnitude of the increase in hardness after exposure in this

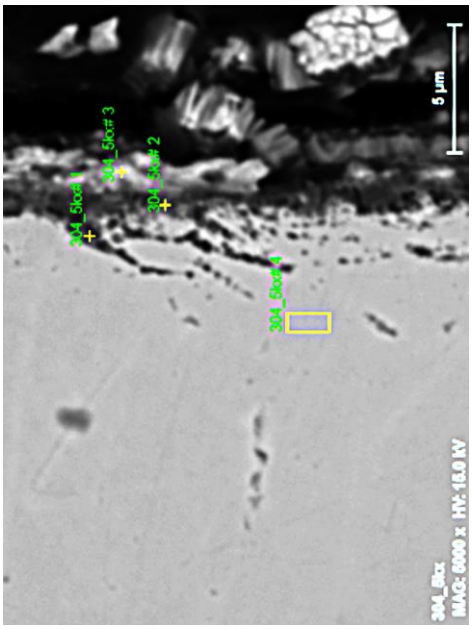

Figure 2.3.2-7 - SEM micrograph of a metallographically-polished cross-section of TP304H after exposure at 700°C for 300h in CO_2 containing 3.6 vol.% O_2 and 5.3 vol.% H_2O at 200 bar.

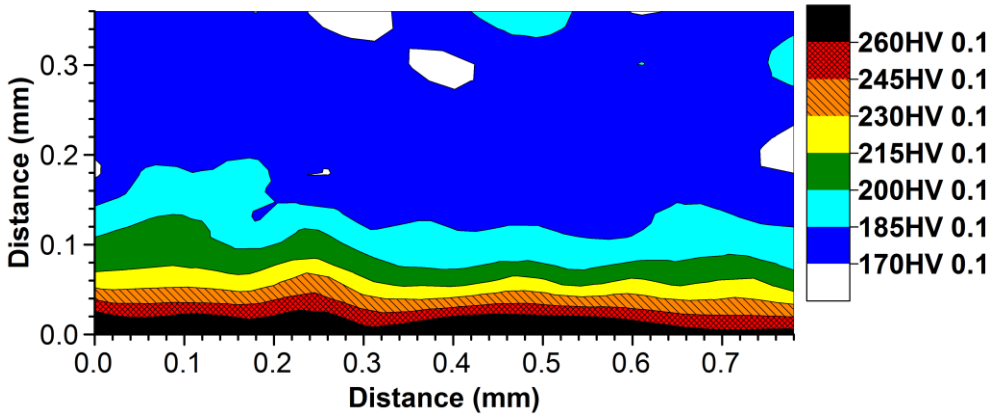

Figure 2.3.2-8 – Microhardness map for TP304H after at 700°C for 300h in CO_2 containing 3.6 vol.% O_2 and 5.3 vol.% H_2O at 200 bar.

Oxidizing environment. In fact, increased hardness was measured to a depth greater than in Grade 91 after the same test. That such a carburized band in this alloy was not observed after exposure to CG purity CO_2 is surprising, since it would be reasonable to expect more severe carburization in that test conducted with a gas mixture having a lower oxygen partial pressure.

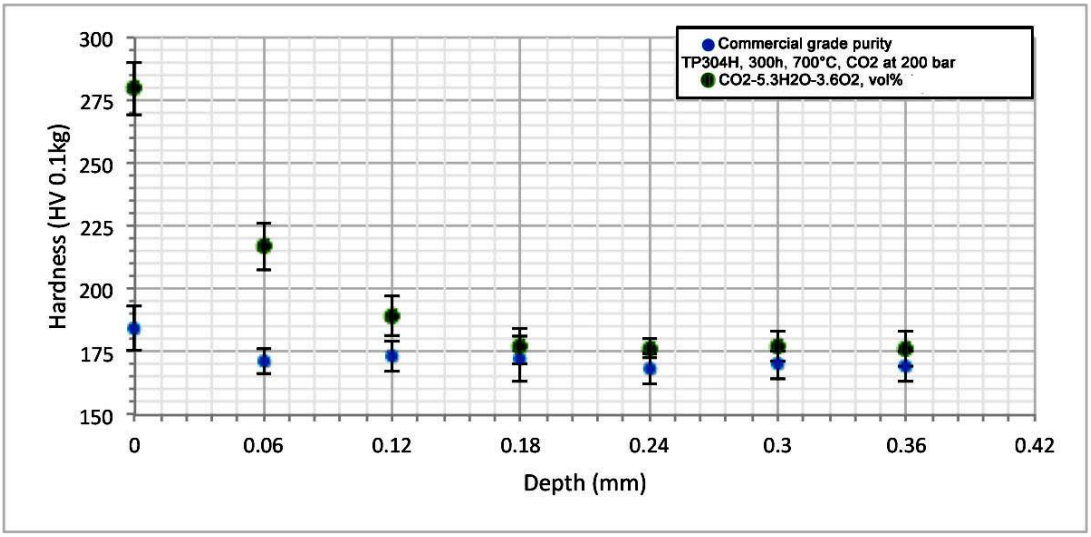

Figure 2.3.2-9 – Comparison of hardness profiles of TP304H after exposure at 700°C for 300h to CG purity CO_2 at 200 bar (blue symbols), and CO_2 containing 3.6 vol.% O_2 and 5.3 vol.% H_2O at 200 bar (green symbols).

No evidence of increased surface hardness was found in IN740H after exposure in this test (see hardness map in Figure 2.3.2-10). Comparison of the hardness-depth profile after 300h at 700°C with that after exposure to CG-purity CO_2 (Figure 2.3.2-11) indicates that while neither suggest that any hardening has taken place, the overall level of hardness was substantially lower after exposure to sCO_2 containing oxidizing impurities. Superior carburization resistance is expected from Ni-based alloys, especially those with relatively high Cr contents.

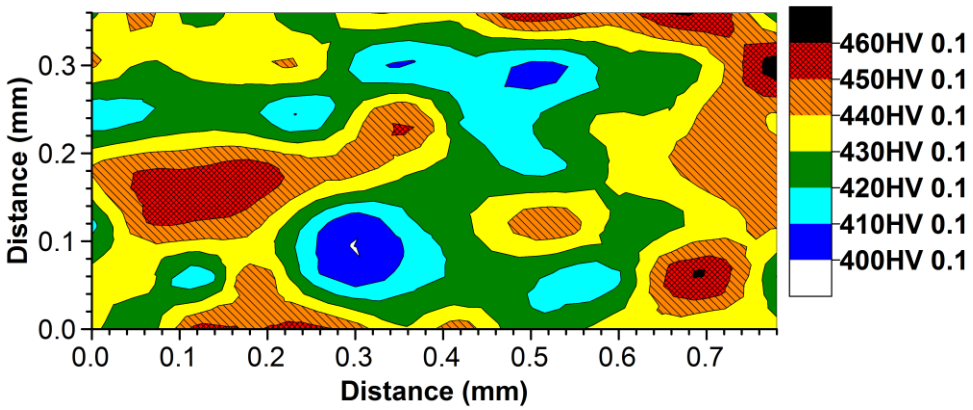

Figure 2.3.2-10 – Microhardness map for IN740H after exposure at 700°C for 300h in CO_2 containing 3.6 vol.% O_2 and 5.3 vol.% H_2O at 200 bar.

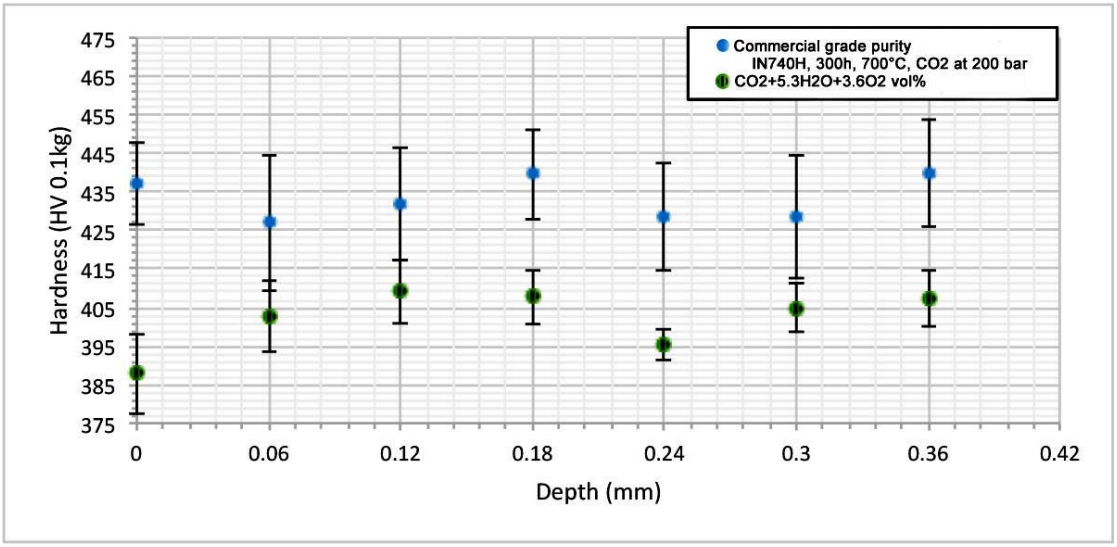

Figure 2.3.2-11 – Comparison of hardness profiles of IN740H after exposure at 700°C for 300h to CG purity CO_2 at 200 bar (blue symbols), and CO_2 containing 3.6 vol.% O_2 and 5.3 vol.% H_2O at 200 bar (green symbols).

2.3.3 — Perform High-Pressure Oxidation/Corrosion Tests

The following tests were performed for a total exposure time of 1,000h at 700, 650, and 750°C using CO_2 containing 3.6 vol.% O_2 and 5.3 vol.% H_2O at 200 bar. In this section the mass gain results after all three exposures are presented, while results of characterization of the scale morphologies are presented in Section 2.3.5.

2.3.3.A - Exposure for up to 1,000h at 700°C in CO_2 containing 3.6 vol.% O_2 and 5.3 vol.% H_2O at 200 bar

In the first 1,000-hour laboratory test, triplicate specimens of the seven candidate alloys (Section 2.2) were exposed for intervals of 280, 560, and 1,000h. During this exposure, specimens were removed from the test rig for inspection and weighing after the planned exposure intervals, and at each such interval one specimen of each alloy was removed for destructive examination. After removal, specimens were sectioned, mounted, and metallographically polished for further examination, as described earlier. The thicknesses of the scales formed were measured on the mounted cross sections using optical microscopy and SEM/EDS, and on some alloys microhardness measurements were made to estimate the extent of any carburization. Results of these characterization efforts are reported in Section 2.3.5.

Table 2.3.3-1 provides a comparison of the mass gains after nominally 300h with those for the three alloys from the shakedown tests. Note that the mass gains for the shakedown tests were the average values of three specimens of each alloy, whereas the data from this test (Section 2.3.3.A) were derived from only one specimen of each alloy. The results from both tests in CO_2 with controlled additions (Sections 2.3.2.B and 2.3.3.A) were not consistent except that the austenitic steel TP304H and Ni-based alloy IN740H exhibited much less mass gain than the ferritic steel, possibly reflecting upsets and other shortcomings in the shakedown test (Section 2.3.1.B) that were rectified before undertaking the longer-term testing (Section 2.3.3.A). Given these caveats, comparison of the results from 300-h tests with CG-purity CO_2 (Section 2.3.1.B) and CO_2 with controlled oxidizing impurities

Table 2.3.3-1
Comparison of mass gains (mg/cm^2) after exposure for 300h at 700°C and 200 bar to CO_2 of CG purity, and CO_2 with controlled additions.

Alloy	Shakedown (2.3.1.B)	Shakedown (2.3.2.B)	Standard Test (2.3.3.A)
	CG Purity CO_2	*CO_2 + 3.6 vol% O_2 and 5.3 vol% H_2O*	
	300h	*300h*	*280h*
Grade 91	8.04	2.79	8.32
VM12	—	—	2.24
Crofer 22H	—	—	1.23
TP304H	0.23	0.07	0.81
HR3C	—	—	0.18
IN740H	0.21	0.07	0.02
IN617	—	—	NA

(Section 2.3.3.A) suggests little effect on the ferritic steel when oxidizing additions are made to CO_2, but an obvious reduction in mass gain for austenitic steel TP304H and Ni-based alloy IN740H. The resulting alloy mass gains after full exposure to the conditions of this test are summarized in Table 2.3.3-2.

Table 2.3.3-2
Mass gains after exposure at 700°C to CO_2 with controlled additions at 200 bar.

Alloy	Mass Gain, mg/cm²		
	280h	560h	1,000h
Grade 91	8.32	8.73	9.34
VM12	2.24	1.99	2.51
Crofer 22H	1.23	1.81	2.16
TP304H	0.81	0.93	0.96
HR3C	0.18	0.15	0.16
IN740H	0.02	0.04	0.05
IN617	0	0	0

These data also are plotted in Figure 2.3.3-1 as a function of exposure time, and as parabolic plots to illustrate the consistency of the results. Surprisingly, alloy Crofer 22H, which registered lower mass gains than VM12 up to 1,000h, exhibited a higher oxidation rate (slope of curve) in this test, despite its much higher Cr content (22.7 wt% compared to 11.2 wt% for VM12). Possible mitigating factors are that VM12 has (i) a higher Si content (0.41 vs 0.29 wt%) that may have promoted protective scale formation; (ii) lower levels of strong carbide-forming elements Nb and Ti (0.03 and <0.01, respectively compared to 0.5 and 0.08 respectively in Crofer 22H); and (iii) a higher initial C content (0.12 vs 0.004 wt%), hence potentially a lower susceptibility to carburization attack.

Parabolic rate constants derived from the slopes of the curves in the parabolic plot for exposures up to 1,000h are listed in Table 2.3.3-3.

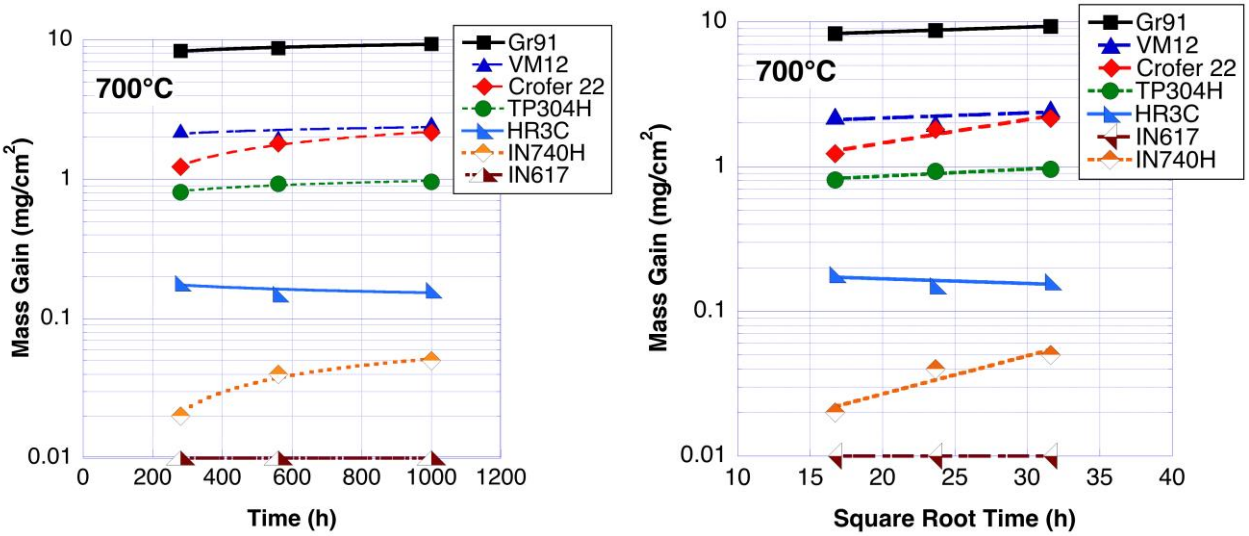

Figure 2.3.3-1 – Mass gains and parabolic plots for all alloys exposed up to 1,000h at 700°C in CO_2 containing 3.6 vol.% O_2 and 5.3 vol.% H_2O at 200 bar.

Table 2.3.3-3
Parabolic rate constants for exposure at 700°C for up to 1,000h in CO_2 with controlled additions at 200 bar.

Alloy	Slope of Parabolic Plot			k_p g^2/cm^4s
	y mg/cm^2	*x* $mg/cm^2h^{0.5}$	R^2	
Grade 91	7.147	0.069	1.00	6.56E-13
VM12	1.784	0.019	0.31	5.17E-14
Crofer 22	0.245	0.06200	0.97	5.34E-13
TP304H	0.662	0.00992	0.87	1.37E-14
HR3C	0.194	-(0.00128)	0.39	-(2.27E-16)
IN740H	-0.011	0.00200	0.95	5.53E-16
IN617				NA

2.3.3.B - Exposure for up to 1,000h at 650°C in CO_2 containing 3.6 vol.% O_2 and 5.3 vol.% H_2O at 200 bar

In this test interruptions were made after 300, 628, and 1,000 h, at which times one specimen of each alloy was removed from test and mounted and polished for further examination, as described earlier. Results of characterization of the scale morphologies are reported in Section 2.3.5.

The mass gains of the exposed alloys are summarized in Table 2.3.3-4, and are plotted in Figure 2.3.3-2 as a function of exposure time. The mass gain measured for alloy Grade 91 (8.4 wt% Cr, 0.24 wt% Si) after 1,000h was a factor of 5 higher than that of VM12 (11.2 wt% Cr, 0.41 wt% Si). As at 700°C the mass gains for Crofer 22H were noticeably higher than for VM12. The austenitic alloys HR3C, IN740H, and IN617 are expected to form protective oxide scales, and exhibited very small mass gains in this test.

Table 2.3.3-4
Mass gains after exposure at 650°C to CO_2 with controlled additions at 200 bar.

Alloy	Mass Gain, mg/cm^2		
	300h	628h	1,000h
Grade 91	4.01	4.19	4.35
VM12	0.14	0.20	0.87
Crofer 22H	0.44	0.74	1.38
TP304H	0.15	0.30	0.40
HR3C	0.07	0.10	0.15
IN740H	0.05	0.07	0.04
IN617	NA	NA	NA

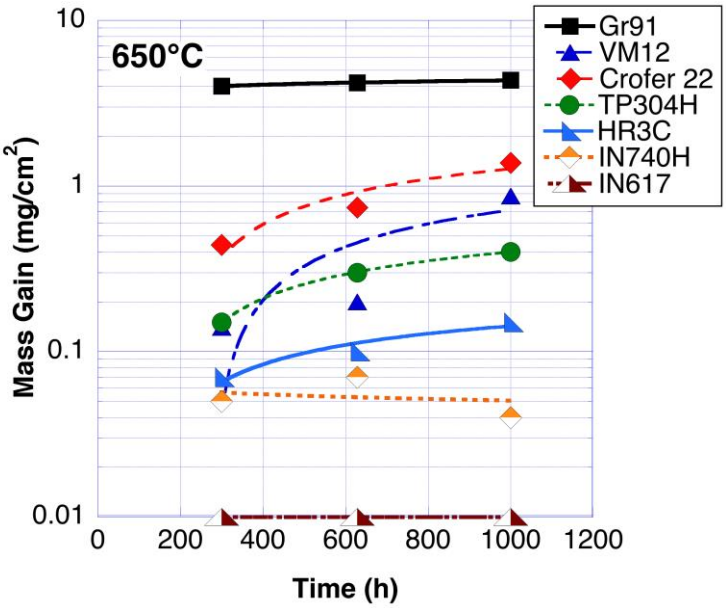

Figure 2.3.3-2 – Mass gains of alloys exposed at 650°C to CO_2 containing 3.6 vol.% O_2 and 5.3 vol.% H_2O at 200 bar.

A parabolic plot for these data is shown in Figure 2.3.3-3, and the parabolic rate constants are listed in Table 2.3.3-5. Curiously, the slope of the curve for Grade 91 was significantly lower than for the other ferritic steels VM12 and Crofer 22H, resulting a lower calculated parabolic rate constant.

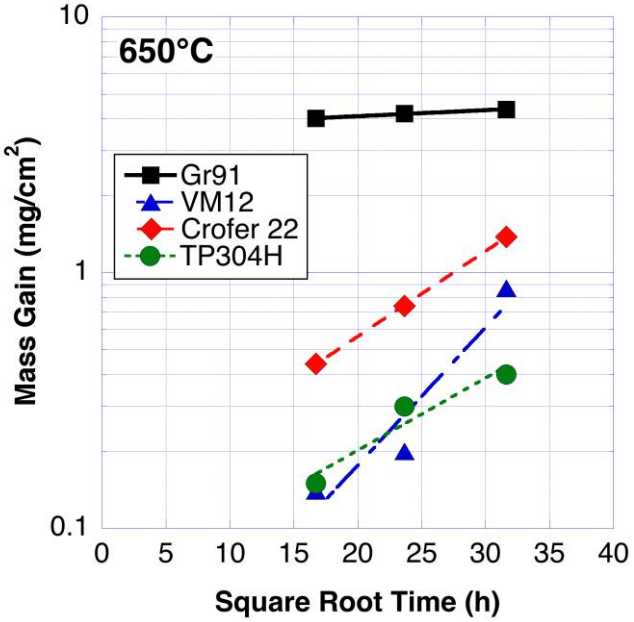

Figure 2.3.3-3 – Parabolic plots for ferritic and austenitic steels exposed at 650°C to CO_2 containing 3.6 vol.% O_2 and 5.3 vol.% H_2O at 200 bar.

Table 2.3.3-5
Parabolic rate constants for exposure at 650°C to CO_2 with controlled additions at 200 bar.

Alloy	Slope of Parabolic Plot			k_p g^2/cm^4s
	y mg/cm^2	*x* $mg/cm^2h^{0.5}$	R^2	
Grade 91	3.637	0.023	0.99	7.20E-14
VM12	-0.794	0.050	0.84	3.46E-13
Crofer 22	-0.67	0.06356	0.97	5.61E-13
TP304H	-0.117	0.01669	0.98	3.87E-14
HR3C	-0.029	0.00540	0.99	4.04E-15
IN740H	-0.071	-(0.00075)	0.13	-(7.76E-17)
IN617	NA	NA	NA	NA

2.3.3.C - Exposure at 750°C for up to 1,000h in CO_2 containing 3.6 vol.% O_2 and 5.3 vol.% H_2O at 200 bar

This test was interrupted after 300, 628, and 1,000 h, and one specimen of each alloy was removed from test at those intervals. After completion of the exposures, specimens were sectioned, mounted, and metallographically polished for subsequent examination. Results of those characterization efforts are reported in Section 2.3.5.

The mass gains are summarized in Table 2.3.3-6, and plotted in Figure 2.3.3-4 as a function of exposure time. Overall, the mass gains decreased with increasing alloy Cr content. Figure 2.3.3-5 is a parabolic plot of these data, and parabolic rate constants derived from the slopes of the curves are listed in Table 2.3.3-7.

Table 2.3.3-6
Mass gains after exposure at 750°C to CO_2 with controlled additions at 200 bar.

Alloy	Mass Gain, mg/cm^2		
	300h	628h	1,000h
Grade 91	7.6	10.6	11.2
VM12	2.5	4.5	5.0
Crofer 22H	1.8	2.7	3.4
TP304H	0.8	1.3	1.4
HR3C	0.2	0.3	0.3
IN740H	0.1	0.04	0.04
IN617	0.03	NA	NA

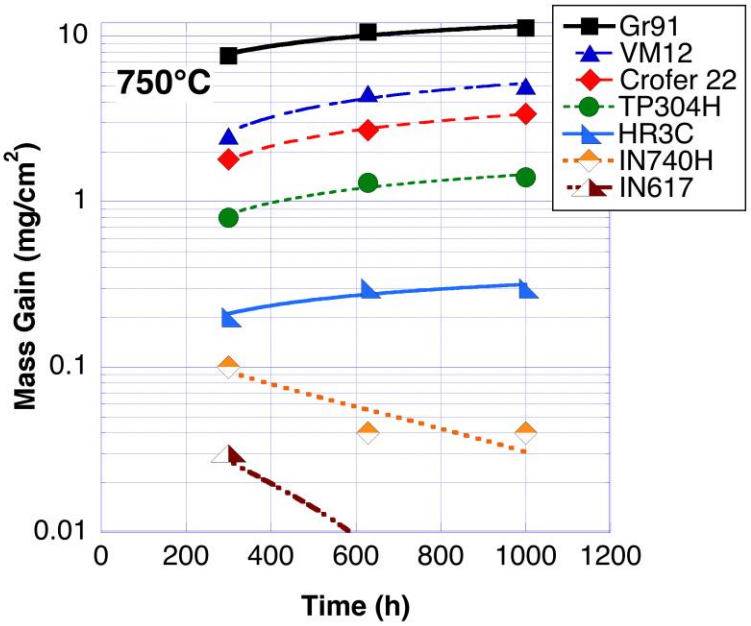

Figure 2.3.3-4 – Mass gains of alloys exposed and 750°C to CO_2 containing 3.6 vol.% O_2 and 5.3 vol.% H_2O at 200 bar.

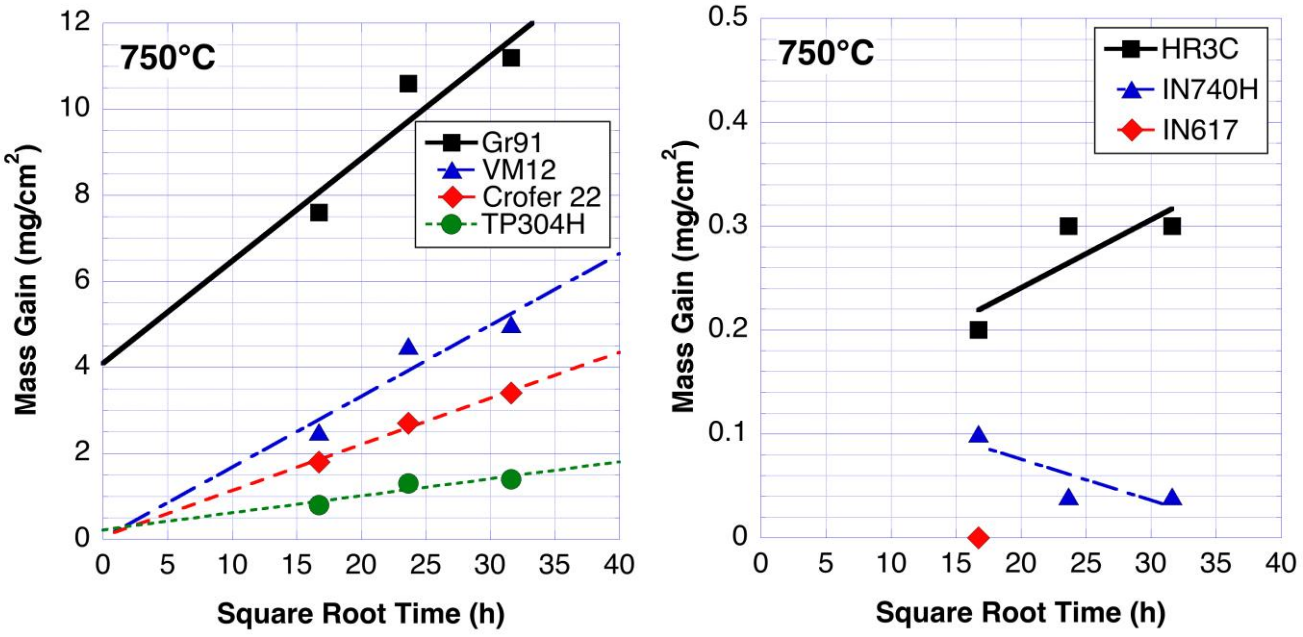

Figure 2.3.3-5 – Parabolic plots for alloys exposed at 750°C to CO_2 containing 3.6 vol.% O_2 and 5.3 vol.% H_2O at 200 bar.

Table 2.3.3-7
Parabolic rate constants for exposure at 750°C to CO_2 with controlled additions at 200 bar.

Alloy	Slope of Parabolic Plot			k_p g^2/cm^4s
	y mg/cm^2	*x* $mg/cm^2h^{0.5}$	R^2	
Grade 91	4.094	0.238	0.84	7.85E-12
VM12	0.031	0.165	0.87	3.80E-12
Crofer 22H	0.065	0.10698	0.99	1.59E-12
TP304H	0.216	0.03962	0.84	2.18E-13
HR3C	0.109	0.00655	0.71	5.96E-15
IN740H	0.154	-(0.00393)	0.71	-(2.15E-15)
IN617	NA	NA	NA	NA

2.3.4 — Complete Long-Term 5,000-h Confirmatory Testing

A long-term (up to 5,000h) confirmatory test was conducted at 700°C and 200 bar using CO_2 with controlled additions of 3.6 vol.% O_2 and 5.3 vol.% H_2O. Included in this test were triplicate specimens of each of the seven alloys exposed in the prior 1,000h tests (Section 2.3.3). Actual alloy compositions are listed in Table 2.2.2-1. During the course of this exposure, specimens were inspected and weighed at intermediate times of 1,000 and 3,500h, and at each inspection one specimen of each alloy was removed for destructive evaluation

In addition to the candidate alloys, testing included specimens extracted from components from commercial compact heat exchangers intended for application in sCO_2 Brayton power cycle plants. An example of such a component is shown in Figure 2.3.4-1, and illustrates the complex structure of the flow passages formed using corrugated foils sandwiched between parallel plates and bonded. In this example the nominal thicknesses of the foils and plates were 0.01 mm and 0.25 mm, respectively. The arrows in Figure 2.3.4-1 show the center channel being used by the hot gas flanked by cold gas channels.

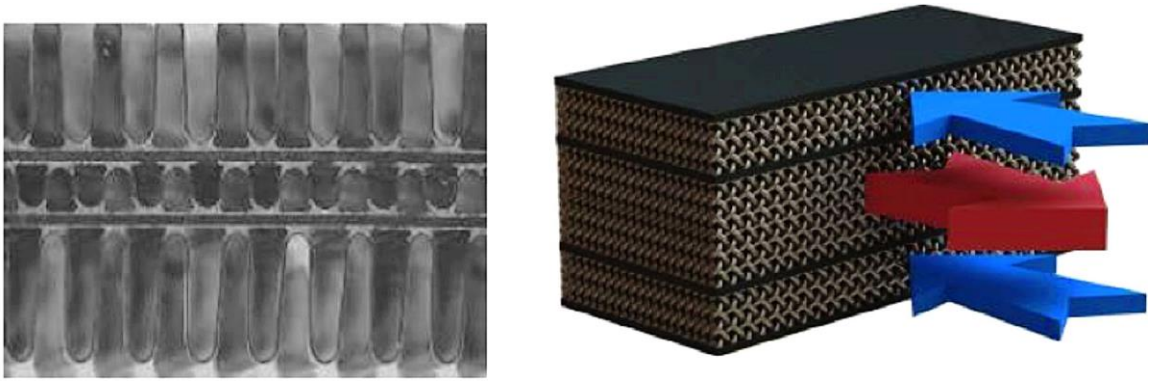

Figure 2.3.4-1 – Sample of a component from a compact heat exchanger (Manufacturer A) obtained for evaluation in the 5,000-h confirmatory test.

The sample components obtained from Manufacturer A were fabricated from:

- Ni-based alloy HA230
- Ni-based alloy IN625
- Austenitic steel TP347H

In addition, a sample of a component constructed from a ferritic FeCrAl alloy and fabricated by brazing was provided by this manufacturer.

Manufacturer B provided samples of components that consisted of sections from compact heat exchangers made from TP304/304L austenitic steels fabricated by brazing and diffusion-bonding processes. Specimens cut from these components are shown in Figure 2.3.4-2. The specimens produced were exposed along with standard alloy test specimens in trays fabricated from Alloy HA230. Figure 2.3.4-3 illustrates the assembly of specimens in such trays. The locations in the trays vacated by standard specimens removed after the first 1,000h exposure were filled by specimens cut from

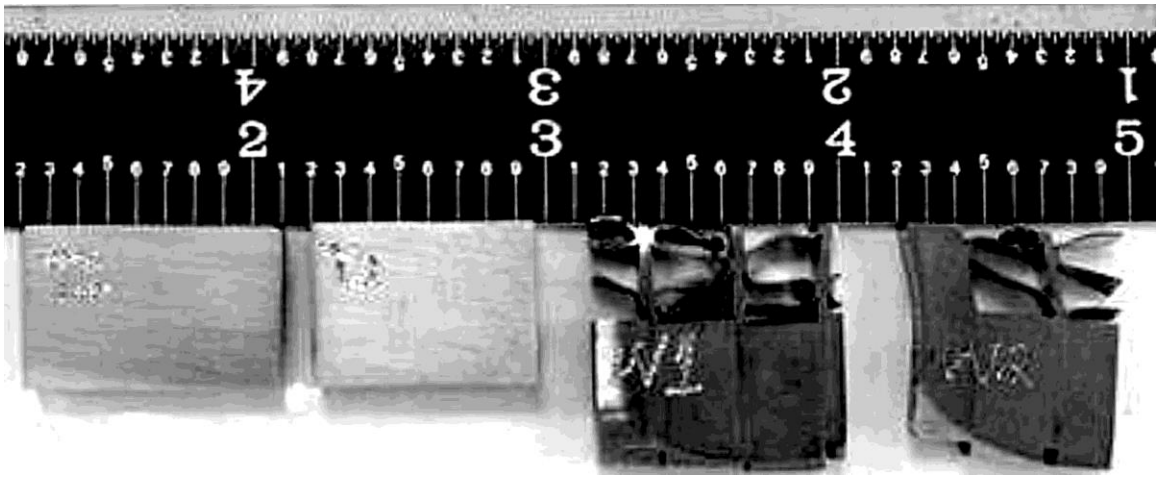

Figure 2.3.4-2 - Specimens (at RHS) cut from brazed and diffusion-bonded TP304/304L austenitic steel components provided by Manufacturer B, shown alongside standard alloy specimens before test exposure.

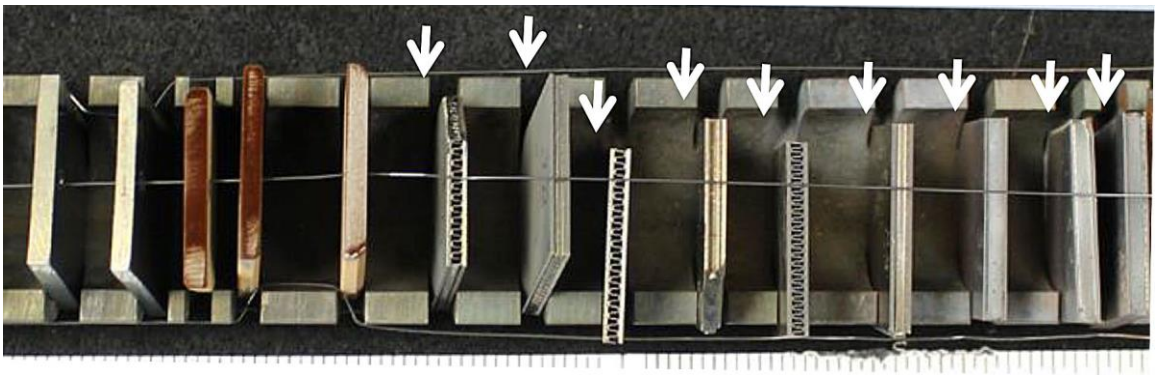

(a)

(b)

Figure 2.3.4-3 - Close-up views of trays containing specimens after test exposure: (a) specimens from heat exchanger samples from Manufacturer A are indicated by arrows; and (b) the arrow indicates a specimen from Manufacturer B.

samples of heat exchanger components. These new test specimens were removed after intervals of 2,500 and 5,000h (counting from the beginning of the test). The exposure schedules for the various specimens tested are summarized in Table 2.3.4-1.

Table 2.3.4-1
Summary of exposures schedules for standard alloy and component-derived specimens.

Alloy	Exposure Time (kh)
Grade 91	1, 3.5, 5
VM 12	1, 3.5, 5
Crofer 22	1, 3.5, 5
TP304H	1, 3.5, 5
HR3C	1, 3.5, 5
IN740H	1, 3.5, 5
IN617	1, 3.5, 5
IN625 microchannel (Manuf A)	1, 2.5, 3.5, 4, 5
HA230 microchannel (Manuf A)	1, 2.5, 3.5, 4, 5
TP347H microchannel (Manuf A)	1, 2.5, 3.5, 4, 5
FeCrAl (#17) (Manuf A)	2.5, 4
FeCrAl (#18) (Manuf A)	2.5, 4
Mesh (Manuf B)	2.5, 4
Brazed monolithic (Manuf B)	2.5, 4

After removal from test at the completion of the scheduled exposures specimens were photographed, and macro images of specimen surfaces are compiled in Appendix C. These include representative images of specimens from heat exchanger components that were exposed in this test. Oxides formed on those specimens appeared to be adherent in all cases, and no scale spallation from the external surfaces was evident. While the heat exchanger-derived specimens were not included in subsequent characterization efforts, the samples were archived for possible detailed examination at a later date.

The standard alloy specimens were sectioned, mounted, and metallographically polished for subsequent characterization of the oxide scales formed. Results of those characterization efforts are reported in Section 2.3.6.

The mass gains for the standard alloy specimens are summarized in Table 2.3.4-2. Note the inclusion of three new alloys: TP347, IN625, and HA230 to gain comparative data for the specimens made from actual heat exchanger components also included in this test. Table 2.3.4-2 includes the mass gains recorded for these same alloys exposed to an earlier 1,000-hour, 700°C test (Section 2.3.3.A) in the same modified CO_2 environment, and those results can be seen to be in reasonable agreement. Although total mass gains also were measured for the specimens made from heat exchanger components, no unit mass gains (mg/cm^2) were calculated due to the inability to measure the surface areas of the complex channel structures that were exposed.

Table 2.3.4-2
Mass gains of alloys after exposure at 700°C for up to 5,000h to CO_2 containing 3.6 vol.% O_2 and 5.3 vol.% H_2O (in mg/cm^2).

Alloy	1,000h (2.3.3A)*	5,000-h Confirmatory Test (2.3.4)		
		1,000h	3,500h	5,000h
Grade 91	9.3	8.9	13.9	15.4
VM 12	2.5	3.4	7.2	9.4
Crofer 22H	2.2	1.9	3.5	4.4
TP304H	1.0	0.8	1.7	2.2
TP347H	NA	0.2	2.2	2.5
HR3C	0.2	0.1	0.2	0.1
IN740H	0.1	0.04	0.02	0.1
IN617	NA	-0.04	-0.1	-0.1
IN625	NA	0.09	0.15	0.15
HA230	NA	0.1	0.14	0.13

* see Table 2.3.3-2

The mass gains of the exposed standard alloy specimens are plotted as a function of time, along with the data from the earlier 1,000h test (Table 2.3.3-2) in Figure 2.3.4-4. The trends for each alloy appear to be consistent. Figure 2.3.4-5 shows parabolic plots for these same data, and the parabolic rate constants derived are listed in Table 2.3.4-3.

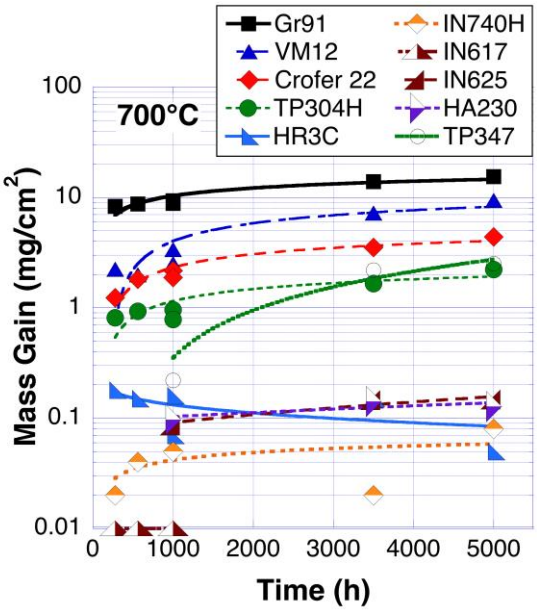

Figure 2.3.4-4 – Mass gains as a function of time after exposure at 700°C for up to 5,000h in CO_2 containing 3.6 vol.% O_2 and 5.3 vol.% H_2O and 200 bar.

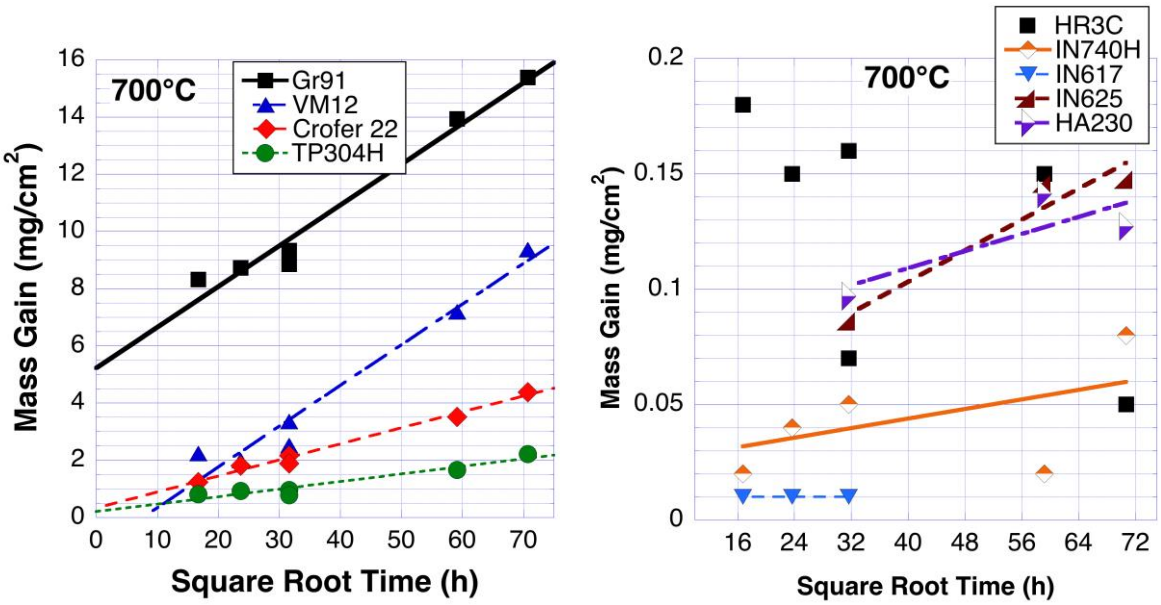

Figure 2.3.4-5 – Mass-based parabolic plots for alloys after exposure at 700°C for up to 5,000h in CO_2 containing 3.6 vol.% O_2 and 5.3 vol.% H_2O and 200 bar.

Table 2.3.4-3
Mass-based parabolic rate constants for exposure at 700°C for up to 5,000h in CO_2 containing 3.6 vol.% O_2 and 5.3 vol.% H_2O at 200 bar.

Alloy	Slope of Parabolic Plot			k_p g^2/cm^4s
	y mg/cm^2	*x* $mg/cm^2h^{0.5}$	R^2	
Grade 91	5.2	0.14	0.97	2.82E-12
VM12	-1.1	0.14	0.96	2.82E-12
Crofer 22	0.32	0.06	0.99	4.36E-13
TP304H	0.20	0.03	0.92	9.64E-14
TP347H[a]	-1.6	0.06	0.97	5.17E-13
HR3C	0.18	-(0.001)	0.35	-(3.04E-16)
IN740H	0.01	0.001	0.91	1.34E-16
IN617[b]	NA	NA	NA	NA
IN625[a]	0.04	0.002	0.93	3.92E-16
HA230[a]	0.07	0.001	0.67	1.19E-16

a: exposed in SubTask 2.3.4 only.
b: alloy exhibited no mass gain, or loss at all times.

2.3.5 — Characterize and Analyze Exposed Test Specimens

2.3.5.A - Specimens from long-term (1,000h) test at 700°C in CO_2 containing 3.6 vol.% O_2 and 5.3 vol.% H_2O at 200 bar (Section 2.3.3.A).

Figure 2.3.5-1 shows optical micrographs of representative areas of the scales formed on the ferritic alloys Grade 91, VM12, and Crofer 22H after 560h of exposure in this test. The locations at which scale thickness measurements were made are indicated on the micrographs as red lines. Note that while the inner oxide layers (L1) were readily identified, on alloys Grade 91 and VM12 the 'outer' layer clearly consisted of two phases, with the darker-appearing phase (in optical micrographs) being magnetite, and the lighter-appearing phase haematite. Since haematite typically grows at the expense of the magnetite layer in such scales [1], the outer layer (L2) was considered to consist of magnetite + haematite. Whereas only some 25% of the thickness of L2 on Grade 91 had been converted to haematite, this oxide comprised more than 50% of the thickness of L2 on VM12, while in the case of Crofer 22H there was very little magnetite remaining in L2. By analogy with scales grown on these alloys in high-pressure steam, the appearance and thickening of haematite at the outer surface of L2 (initially magnetite) is taken as an indication of the decreasing rate of outward transport of Fe ions as the Cr content of L1 increased with increased alloy Cr content, and with time for all these alloys [1].

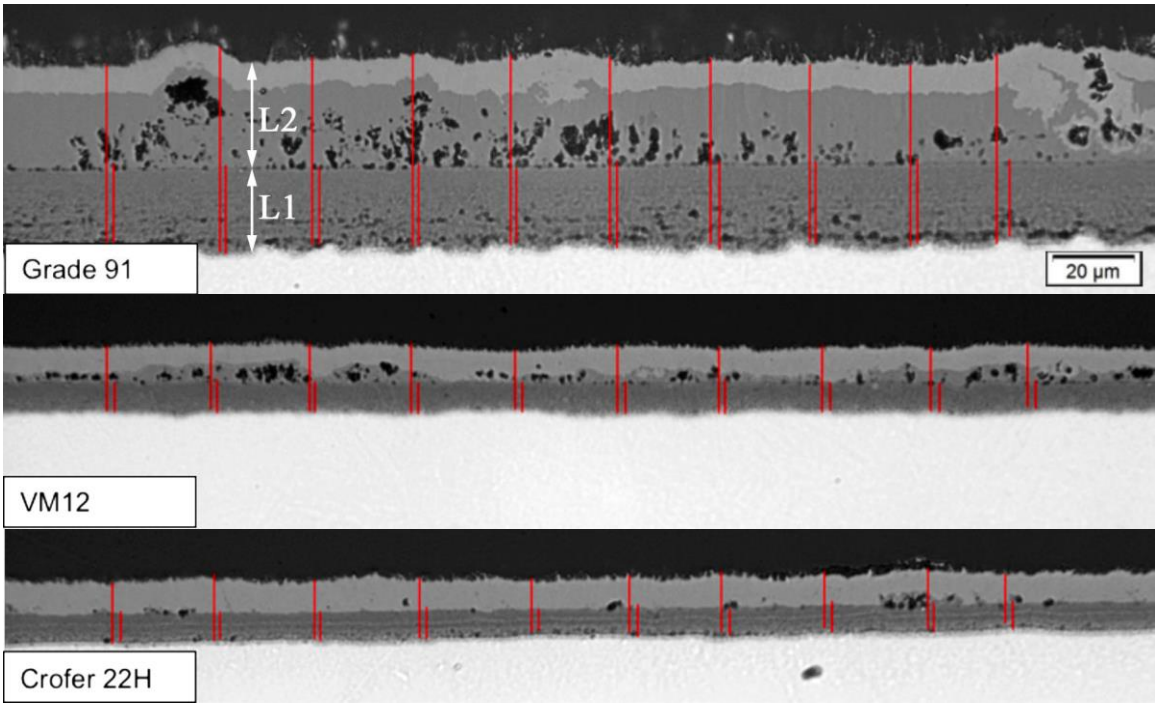

Figure 2.3.5-1 –Optical micrographs of metallographically-polished cross-sections showing oxide scales formed on Grade 91, VM12, and Crofer 22H after exposure at 700°C for 560h in CO_2 containing 3.6 vol.% O_2 and 5.3 vol.% H_2O at 200 bar. Red bars indicated locations where thickness measurements were made.

The resulting values for scale thicknesses formed on these alloys (as well as TP304H) after exposures of 280, 560, and 1,000h are compiled in Figure 2.3.5-2 as box plots. For each alloy, the thickness of the full scale and those of the inner and outer layers of oxide (where these could be identified) are plotted in that order. Clearly, alloy Grade 91 formed the thickest scales after all three exposure times. In addition, the thickness of the inner oxide layer formed on Grade 91 became extremely variable after 1,000h, whereas both layers on the other three alloys maintained reasonably uniform thicknesses. The thicknesses of the scale formed on the high-temperature (HT) alloys HR3C, IN617, and IN740H were too thin to be measured accurately by the techniques available.

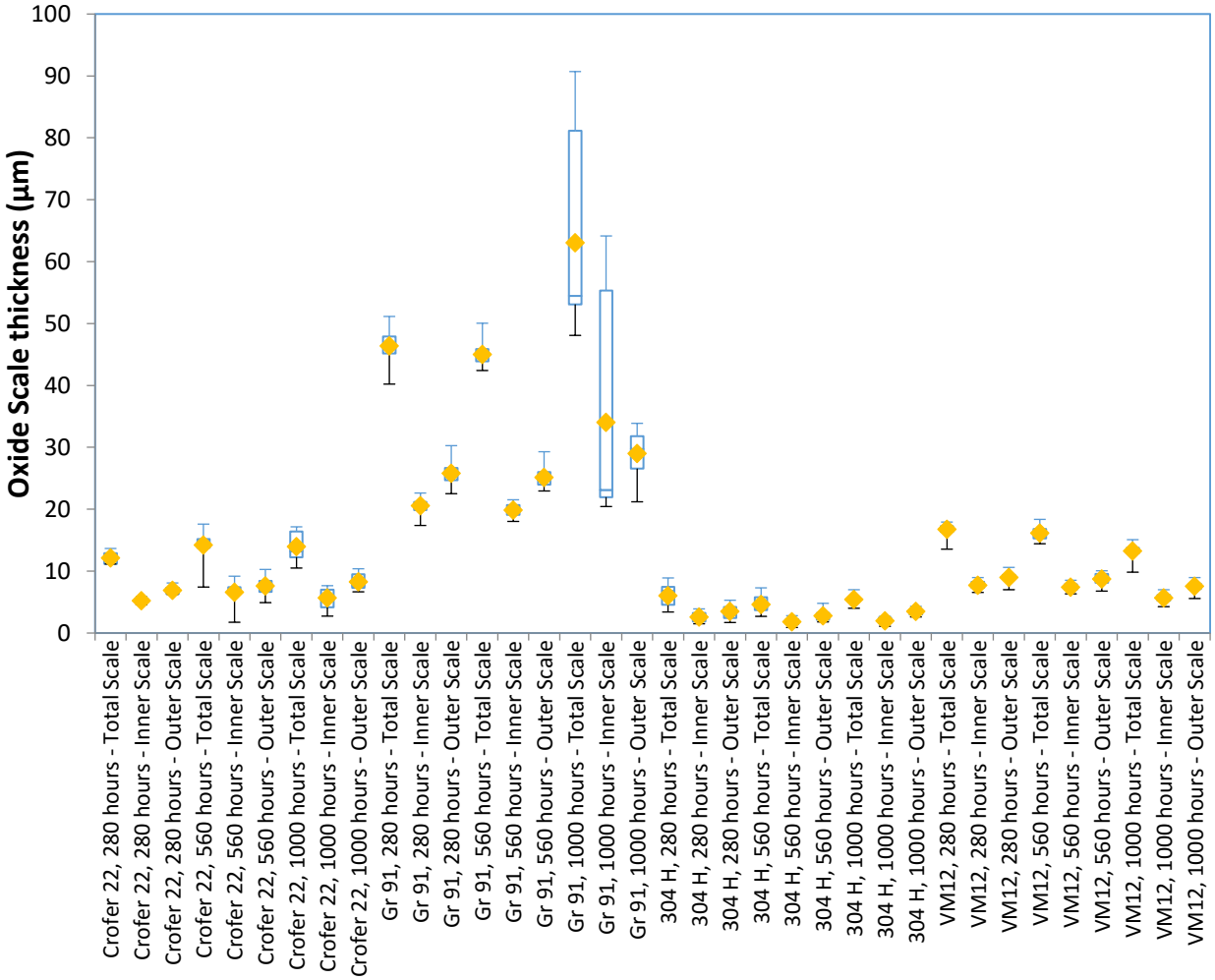

Figure 2.3.5-2 – Comparison of oxide thicknesses for Grade 91, Crofer 22H, VM12, and TP304H as a function of time after exposure at 700°C for up to 1,000h in CO_2 containing 3.6 vol.% O_2 and 5.3 vol.% H_2O at 200 bar (SubTask 2.3.3A).

Parabolic plots of these data (using total scale thicknesses) are shown in Figure 2.3.5-3. Scale thickness-based parabolic rate constants derived from the slopes of the curves are listed in Table 2.3.5-1.

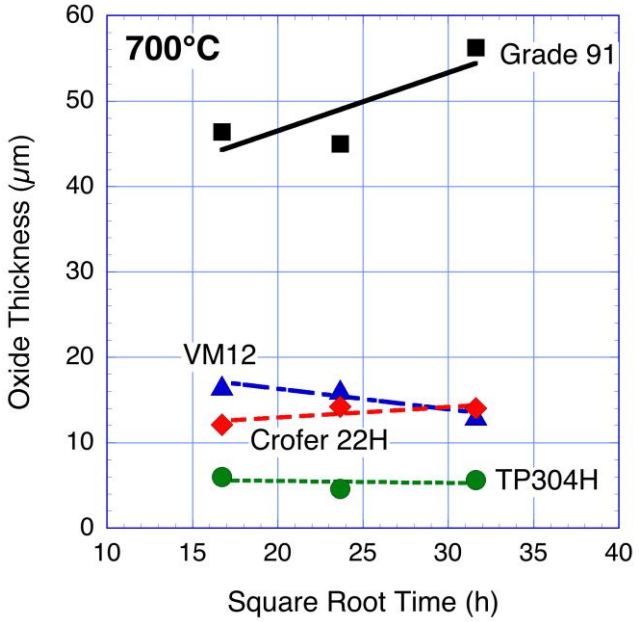

Figure 2.3.5-3 – Parabolic plots for total scale thicknesses after exposure at 700°C for up to 1,000h in CO_2 containing 3.6 vol.% O_2 and 5.3 vol.% H_2O at 200 bar.

Table 2.3.5-1
Total scale thickness-based parabolic rate constants for alloys exposed at 700°C for up to 1,000h in CO_2 containing 3.6 vol.% O_2 and 5.3 vol.% H_2O at 200 bar.

Alloy	k_p, μm²/h	R^2
Grade 91	2.3×10^{-1}	0.68
VM12	$-(2.9 \times 10^{-2})$	0.88
Crofer 22H	$7.7E \times 10^{-3}$	0.63
TP304H	$-(2.4E \times 10^{-4})$	0.80

The thicknesses of the inner and outer oxide layers formed in these tests are further compared in Figures 2.3.5-4 and 2.3.5-5. For all alloys shown except Grade 91 there was a tendency for the thickness of the outer oxide layer to be greater than that of the corresponding inner oxide layer. For Grade 91 the thicknesses of both layers became increasingly variable after 1,000h, with the greatest variability shown by the inner layer. These data are summarized in Table 2.3.5-2.

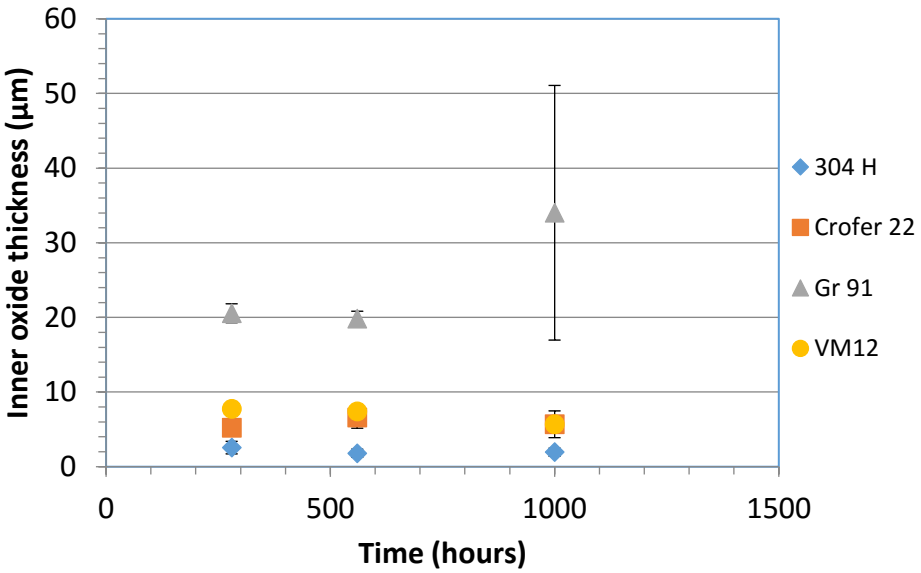

Figure 2.3.5-4 – Comparison of inner oxide layer thicknesses for Grade 91, VM12, Crofer 22H, and 304H as a function of time after exposure at 700°C for up to 1,000h in CO_2 containing 3.6 vol.% O_2 and 5.3 vol.% H_2O and 200 bar.

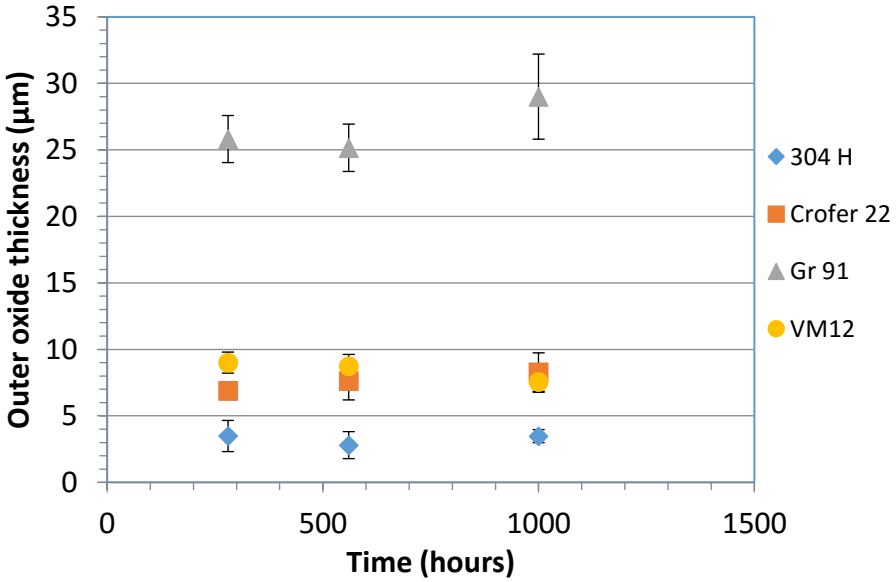

Figure 2.3.5-5 – Comparison of outer oxide layer thicknesses for Grade 91, Crofer 22H, VM12, and 304H as a function of time after exposure at 700°C for up to 1,000h in CO_2 containing 3.6 vol.% O_2 and 5.3 vol.% H_2O and 200 bar.

Table 2.3.5-2
Trend with time of the relative thicknesses of oxide layers formed after exposure at 700°C for up to 1,000h in CO_2 containing 3.6 vol.% O_2 and 5.3 vol.% H_2O at 200 bar.

Alloy	Ratio, L1/L2		
	280h	560h	1,000h
Grade 91	0.8	0.8	1.2
VM 12	0.8	0.8	0.7
Crofer 22H	0.7	0.9	0.8
TP304H	0.7	0.5	0.5
HR3C	NA	NA	NA
IN740H	NA	NA	NA
IN617	NA	NA	NA

Figure 2.3.5-6 shows examples of elemental maps for Fe, Cr, and O superimposed on SEM/BSE images of metallographically-polished cross sections of scales formed after 1,000h on Grade 91, VM12, Crofer 22H, and TP304H. Two major oxide layers having different compositions can be identified on each alloy, with the inner layer (L1) containing Cr and the outer layer (L2) being predominantly iron oxide. In VM12 a definite zone of precipitates (internal oxidation zone, IOZ) also was evident in the alloy immediately beneath L1. An exception to this apparently simple arrangement is alloy Grade 91, which exhibited a layer (or possibly several layers) of Cr-containing oxide located in the inner part of L2. A similar structure noted after the 300h, 700°C shake-down run (Figure 2.3.1-9) in CG purity CO_2 at 200 bar was attributed to a disruption in test conditions, but no such upset was recorded during this test. The frequency with which scale thicknesses measurements were made along the specimen surfaces is demonstrated on a representative SEM micrograph of TP304H shown in Figure 2.3.5-7.

Only submicron-thick oxide scales were observed on cross-sections of HT alloys HR3C, IN617, and IN740H after exposure in this test, consistent with the very small mass gains reported in Table 2.3.3-2. As a result, attempts were made (with limited success) to measure the thicknesses of these scales using an SEM/BES image analysis system at magnifications up to 2,500x. As a means of providing reference points, specimens of alloy TP304H were included in these measurements. EDS analyses of these same cross-sections of scales did not provide any systematic information; slight enrichment of Ni was found at some locations along the surface of IN740H, suggesting possible localized depletion of Cr due to the formation of a chromia scale. No obvious Cr depletion was detected at the surfaces of alloys HR3C or IN617.

A microhardness map and corresponding profile for Grade 91 after exposure in this test for 1,000h are shown in Figures 2.3.5-8 and 2.3.5-9 respectively. The wide distribution of areas with elevated hardness (shown in yellow, pink, and red) in Figure 2.3.5-8 suggests that some hardening/carburization has occurred. The hardness profile (Figure 2.3.5-9) indicates a level of near-surface hardness similar to that found after 300h exposure to the (nominally) same test conditions in (Figure 2.3.2-6), but that hardening after exposure for 1,000h in this test was present to a depth of 350+ μm, significantly beyond the depth measured after the 300-h exposure. These results also indicate that the increased surface harness was not caused by cold work introduced by machining and

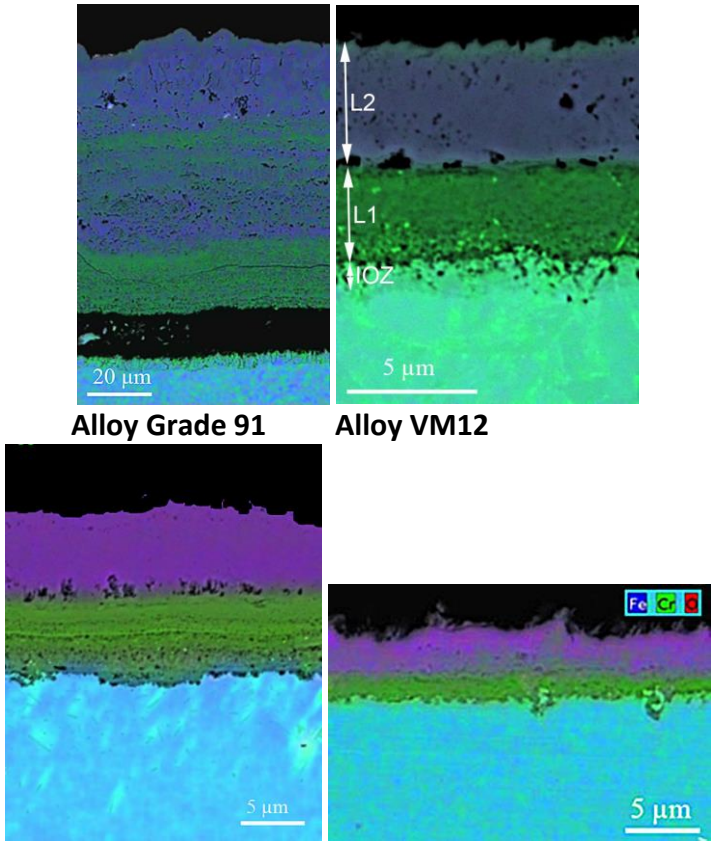

Alloy Grade 91 Alloy VM12

Alloy Crofer 22H Alloy TP304H

Figure 2.3.5-6 –SEM/BSE micrographs of metallographically-polished cross sections with superimposed EDS maps for alloys Grade 91, VM12, Crofer 22H, and TP304H after exposure at 700°C for 1,000h in CO_2 containing 3.6 vol.% O_2 and 5.3 vol.% H_2O at 200 bar.

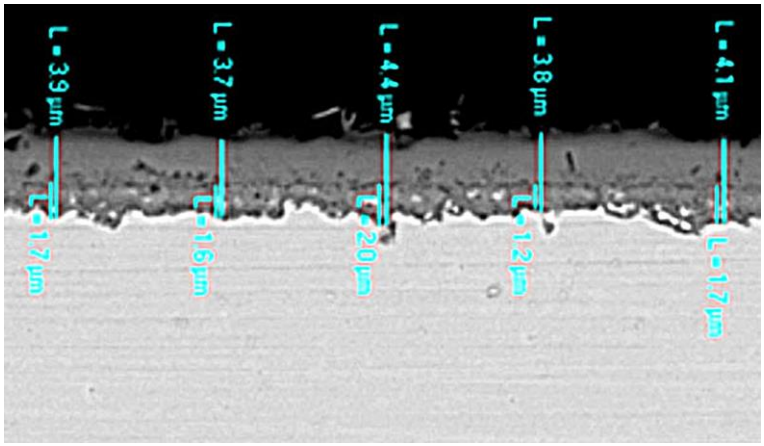

Figure 2.3.5-7 – SEM micrograph of a metallographically-polished cross-section of the oxide scale formed on TP304H after exposure at 700°C for 560h in CO_2 containing 3.6 vol.% O_2 and 5.3 vol.% H_2O at 200 bar, showing locations at which scale thickness measurements were made.

polishing during specimen preparation, since increasing exposure time from 300 to 1,000h at 700°C would have significantly reduced any such cold work effects.

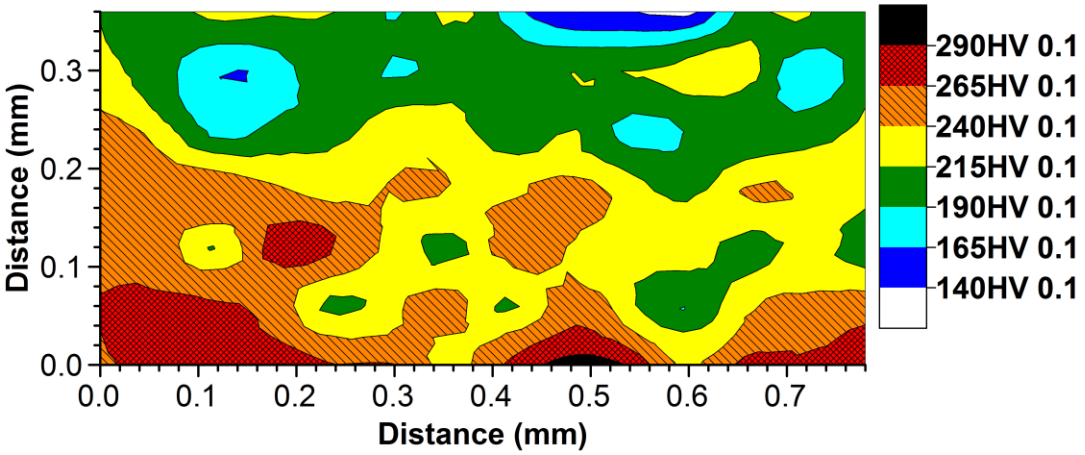

Figure 2.3.5-8 – Hardness distribution in the surface of Grade 91 (alloy-oxide interface is located at Distance = 0.0) after exposure at 700°C for 1,000h in CO_2 containing 3.6 vol.% O_2 and 5.3 vol.% H_2O at 200 bar.

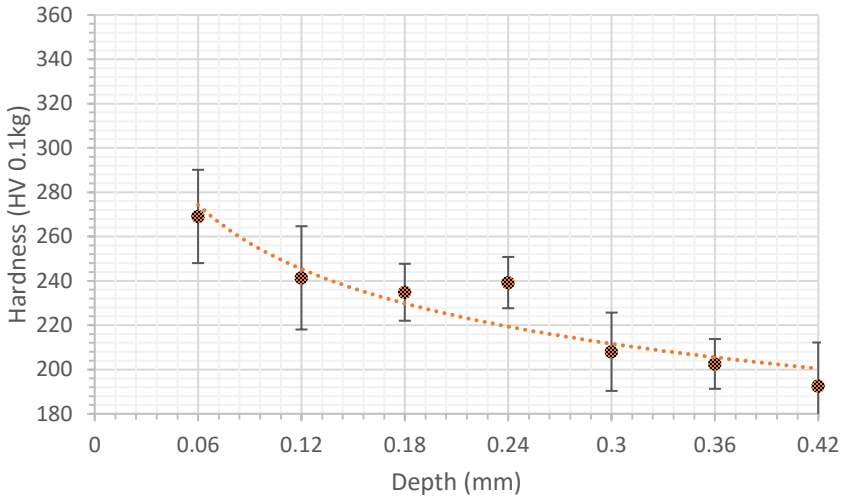

Figure 2.3.5-9 – Microhardness profile for Grade 91 after exposure at 700°C for 1,000h in CO_2 containing 3.6 vol.% O_2 and 5.3 vol.% H_2O at 200 bar.

Figures 2.3.5-10 and 2.3.5-11 show a hardness map and corresponding hardness depth profile, respectively, for alloy VM12 after exposure in this test for 1,000h. An increase in surface hardness is apparent, extending to a depth of possibly 100 µm. In addition, the maximum subsurface hardness was greater than that measured for Grade 91 (315 vs 270 HV), as was the baseline hardness of the alloy.

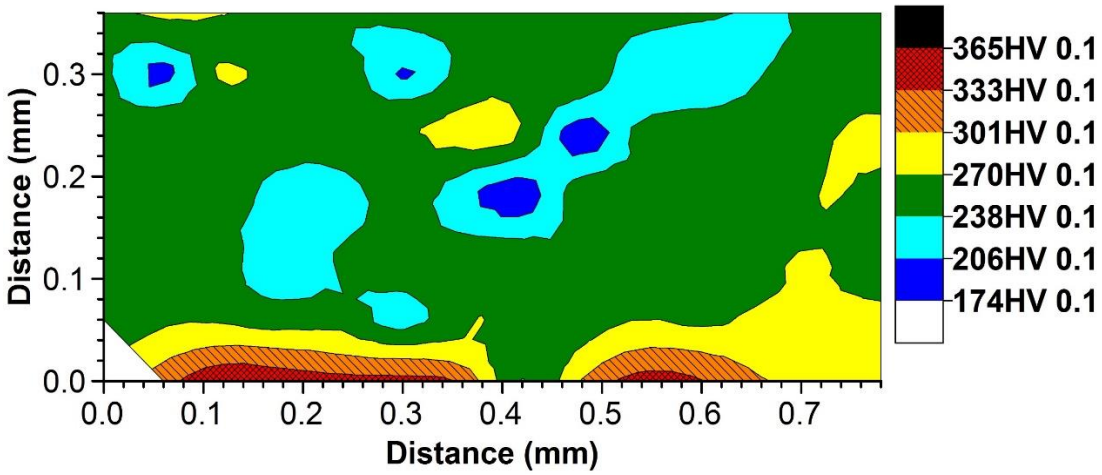

Figure 2.3.5-10 – Microhardness map beneath the alloy-oxide interface (Distance = 0.0) on alloy VM12 after exposure at 700°C for 1,000h in CO_2 containing 3.6 vol.% O_2 and 5.3 vol.% H_2O at 200 bar.

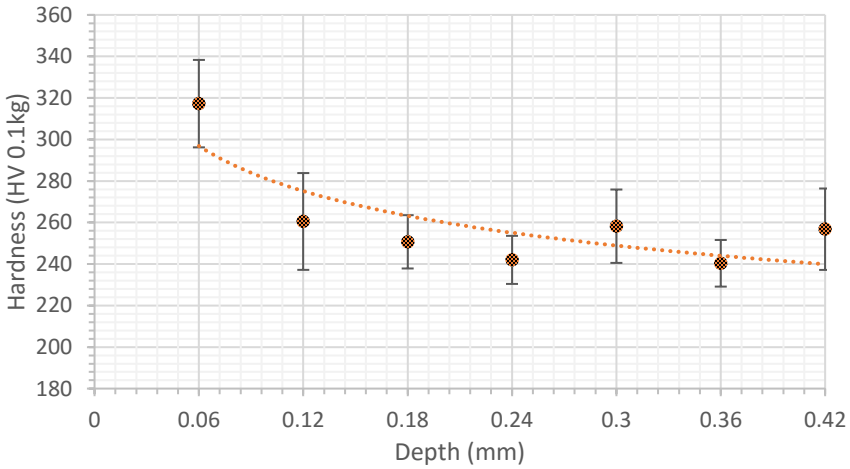

Figure 2.3.5-11 – Microhardness profile for alloy VM12 after exposure at 700°C for 1,000h in CO_2 containing 3.6 vol.% O_2 and 5.3 vol.% H_2O at 200 bar.

Figures 2.3.5-12 and 2.3.5-13 show a micro-hardness map and profile, respectively, for Crofer 22H after exposure for 1,000h in this test. Little evidence of hardening is apparent, at least to the maximum depth to which measurements were made. This alloy was not exposed in the earlier 300h tests (Section 2.3.2.B).

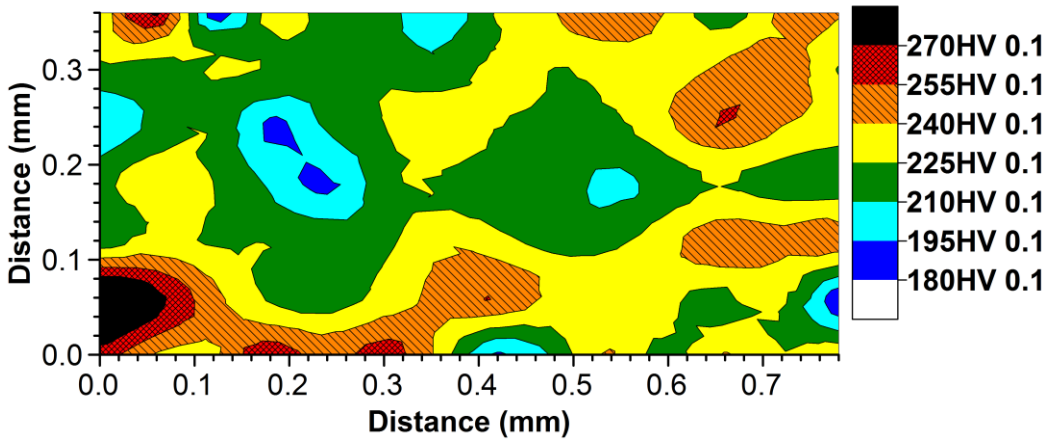

Figure 2.3.5-12 – Microhardness map for Crofer 22H after exposure at 700°C for 1,000h in CO_2 containing 3.6 vol.% O_2 and 5.3 vol.% H_2O at 200 bar. The alloy-scale interface is at Distance = 0.0.

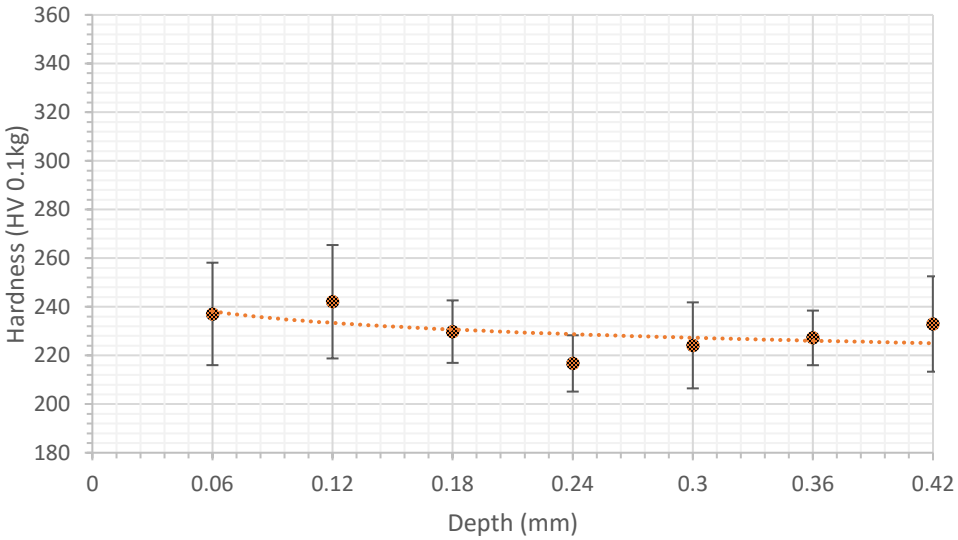

Figure 2.3.5-13 – Microhardness profile for alloy Crofer 22H after exposure at 700°C for 1,000h in CO_2 containing 3.6 vol.% O_2 and 5.3 vol.% H_2O at 200 bar.

Figures 2.3.5-14 and 2.3.5-15 show a micro-hardness map and profile, respectively for austenitic steel TP304H after exposure in this test for 1,000h. As with Crofer 22H, no increase in hardness was apparent in the surface of this alloy. This contrasts sharply with the strong evidence of hardening/ carburization after exposure to nominally the same gas mixture after the second 300h shakedown test at 200 bar and 700°C (Figure 2.3.2-8).

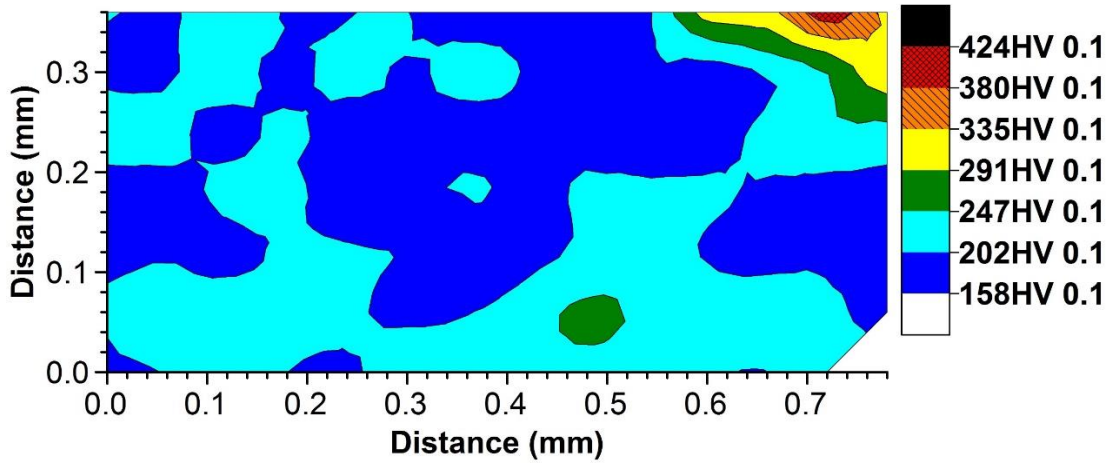

Figure 2.3.5-14 – Microhardness map of TP304H after exposure at 700°C for 1,000h in CO_2 containing 3.6 vol.% O_2 and 5.3 vol.% H_2O at 200 bar. The alloy-scale interface is at Distance = 0.0.

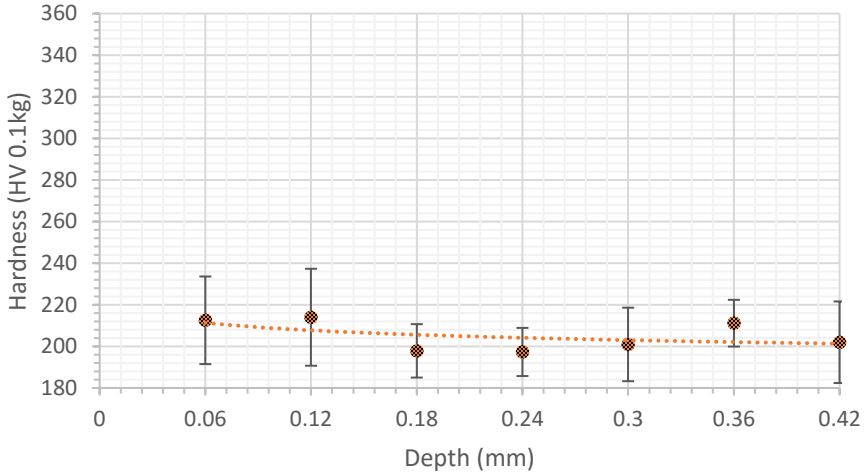

Figure 2.3.5-15 – Microhardness profile of alloy TP304H after exposure at 700°C for 1,000h in CO_2 containing 3.6 vol.% O_2 and 5.3 vol.% H_2O at 200 bar.

A micro-hardness map and hardness profile for alloy HR3C after exposure in this test for 1,000h are shown in Figures 2.3.57-16 and 2.3.5-17, respectively; this hardness profile is presented as a box plot. Increased hardness was measured over a relatively uniform front to a depth of 150-200 µm from the alloy-oxide interface. Given that HR3C is expected to form a chromia scale that is a good barrier to C penetration, the degree of hardening measured after this test was surprising. A possible explanation is that the observed hardening was not due to carburization, since the specimens of this alloy were prepared from samples of boiler tubes removed from a steam boiler and experienced significant cold working.

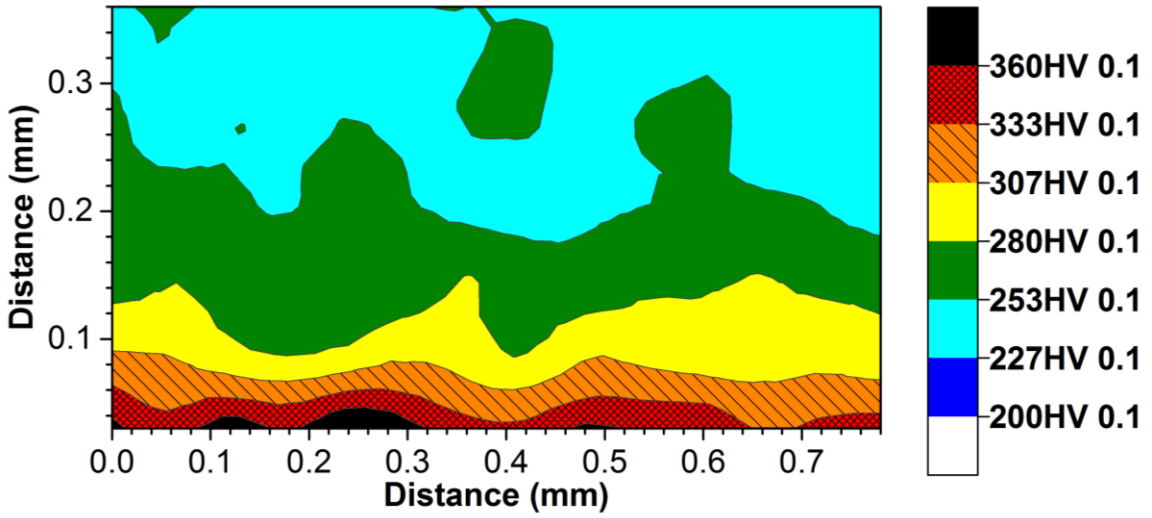

Figure 2.3.5-16 – Microhardness map for alloy HR3C after exposure at 700°C for 1,000h in CO_2 containing 3.6 vol.% O_2 and 5.3 vol.% H_2O at 200 bar.

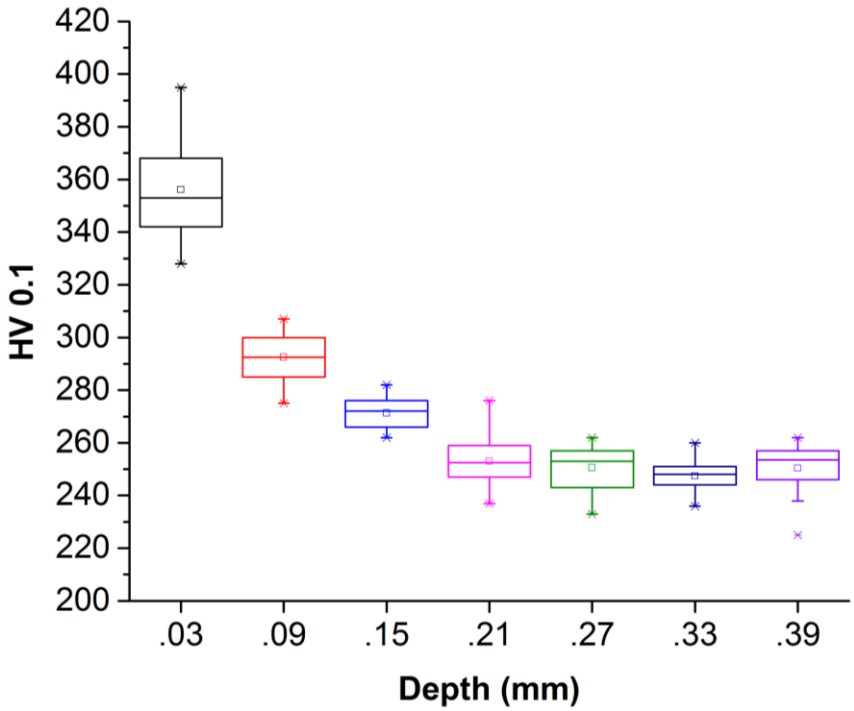

Figure 2.3.5-17 – Microhardness profile of alloy HR3C after exposure at 700°C for 1,000h in CO_2 containing 3.6 vol.% O_2 and 5.3 vol.% H_2O at 200 bar.

Micro-hardness measurements for alloys IN617 and IN740H did not reveal any evidence of hardening or carburization.

2.3.5.B - Specimens from long-term (1,000h) test at 650°C in CO_2 containing 3.6 vol.% O_2 and 5.3 vol.% H_2O at 200 bar (also see Section 2.3.3.B).

Specimens exposed in this test were removed after 300, 628, and 1,000h at 650°C and cross-sections were prepared for examination according to the procedures described for the previous (700°C) test. In addition to the micrographs presented here, others are assembled in Appendix A. As with scales from exposures at the higher temperature of the previous test, those formed on alloys HR3C, IN617, and IN740H were too thin to be determined accurately by the available techniques.

A SEM/BSE micrograph of Grade 91 after 1,000h in this test and a corresponding overlay of EDS maps for Fe, Cr, and O, shown in Figure 2.3.5-18, indicate a very similar scale morphology to that at 700°C. A notable difference is that hematite (which appears darker than magnetite in BSE imaging) occupies more than 66% of the thickness of L2, compared to approximately 25% after 560h at 700°C (Figure 2.3.5.1), presumably reflecting the much slower rate of transport of Fe ions outward at 650°C. In addition, the outer surface of L2 exhibited pronounced needle-like features.

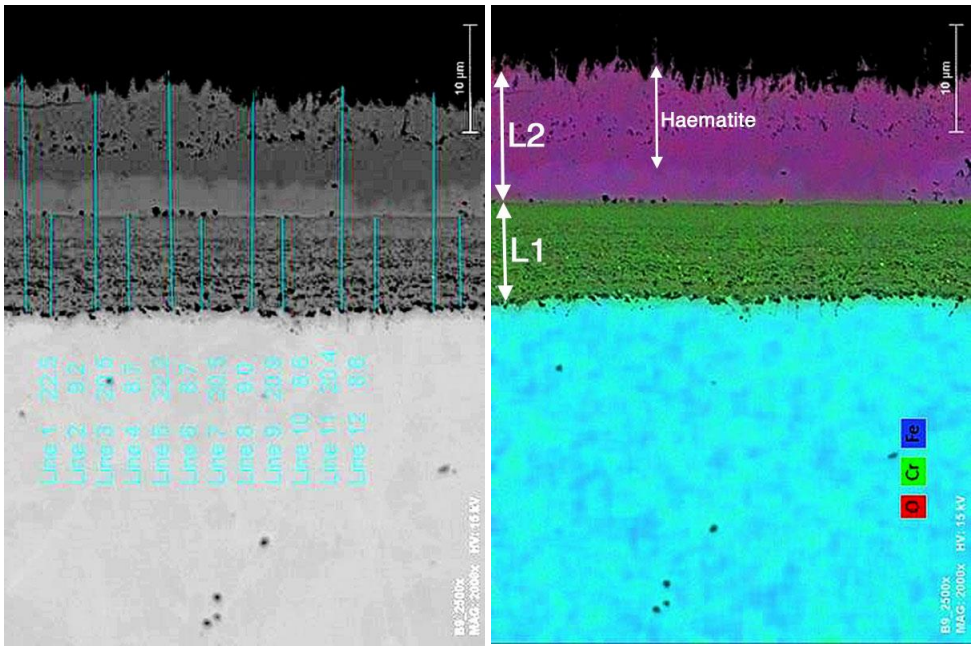

Figure 2.3.5-18 – SEM/BSE micrograph of metallographically-polished cross section of Grade 91 after exposure at 650°C for 1,000h in CO_2 containing 3.6 vol.% O_2 and 5.3 vol.% H_2O at 200 bar, showing locations in which thickness measurements were made, and superimposed EDS maps for Fe, Cr, and O.

The much thinner scale present on VM12 after 628h at 650°C consisted of a continuous and essentially uniformly-thick inner layer of Cr-rich oxide, and an outer, Fe-rich layer that was non-uniform in thickness and composed of coarse, needle-like structures, Figure 2.3.5-19. In addition, there were significant penetrations into the alloy directly beneath the inner oxide layer.

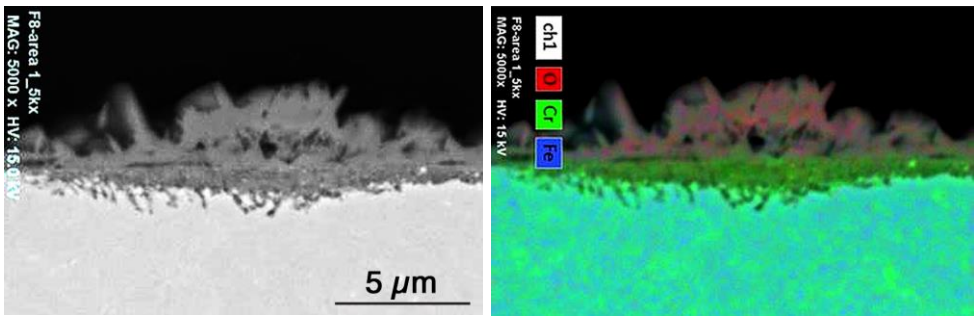

Figure 2.3.5-19 – SEM/BSE micrograph of metallographically-polished cross section of VM12 after exposure at 650°C for 628h in CO_2 containing 3.6 vol.% O_2 and 5.3 vol.% H_2O at 200 bar, and superimposed EDS maps for Fe, Cr, and O.

In contrast, the morphology of the scale formed on Crofer 22H after 1,000h at 650°C resembled that on Grade 91 than the VM12 scale, with two main layers that mostly appeared to be uniformly thick (Figure 2.3.5-20). The layer corresponding to L1 in Grade 91 exhibited a similar banded structure, but there was a continuous and relatively uniformly-thick layer beneath L1 that appeared to have a higher Cr content than L1. No discrete internal precipitates were visible beneath this innermost layer. The appearance of voids along the L1-L2 interface possibly indicated that the rate of outward transport of Fe ions had slowed considerably, presumably as a result of the formation of the basal, Cr-rich layer. Curiously, no structure was apparent in L2 to suggest if it was magnetite or had partially (or fully) converted to hematite.

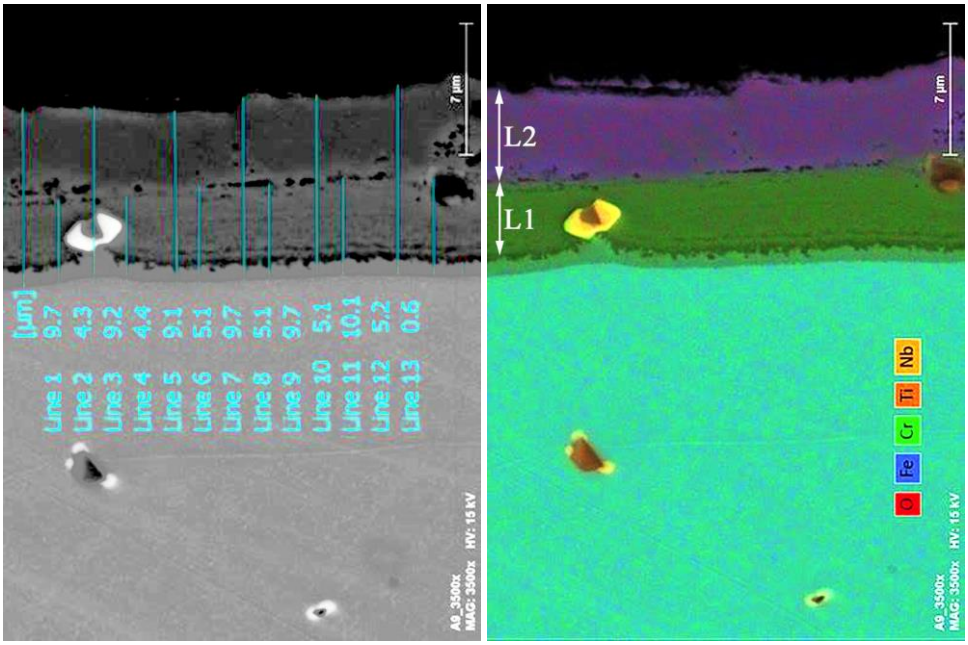

Figure 2.3.5-20 – SEM/BSE micrograph of metallographically-polished cross section of Crofer 22H after exposure at 650°C for 1,000h in CO_2 containing 3.6 vol.% O_2 and 5.3 vol.% H_2O at 200 bar, showing locations in which thickness measurements were made, and superimposed EDS maps for Fe, Cr, O, Ti, and Nb.

After 300h at 650°C the scale on TP304H consisted of two readily-distinguishable layers, both of which were irregular in thickness, as shown in Figure 2.3.5-21. As expected, the inner contained Cr, but the structure of the outer layer resembled than formed on VM12, and consisted of coarse needle-like oxides.

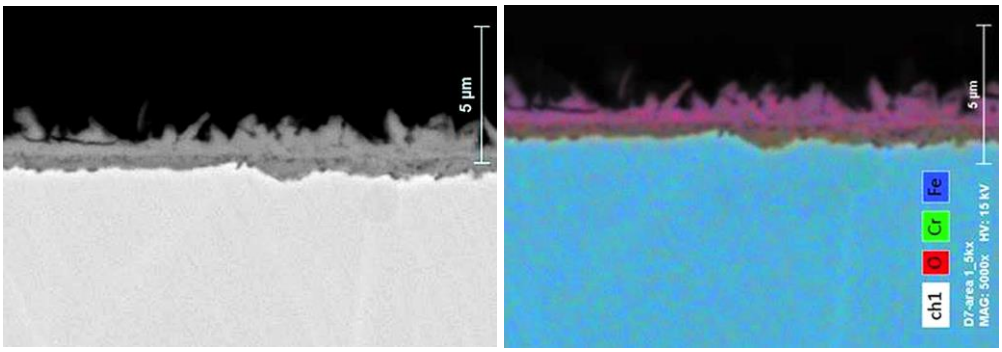

Figure 2.3.5-21 – SEM/BSE micrograph of metallographically-polished cross section of TP304H after exposure at 650°C for 300h in CO_2 containing 3.6 vol.% O_2 and 5.3 vol.% H_2O at 200 bar, showing superimposed EDS maps for Fe, Cr, and O.

A compilation of measured thicknesses of the scales formed on Grade 91, Crofer 22H, and TP304H, shown in Figure 2.3.5-22, suggests considerable variation in the thicknesses of the layers formed on the ferritic steels. In comparison, the thin scales formed on TP304H were relatively uniform.

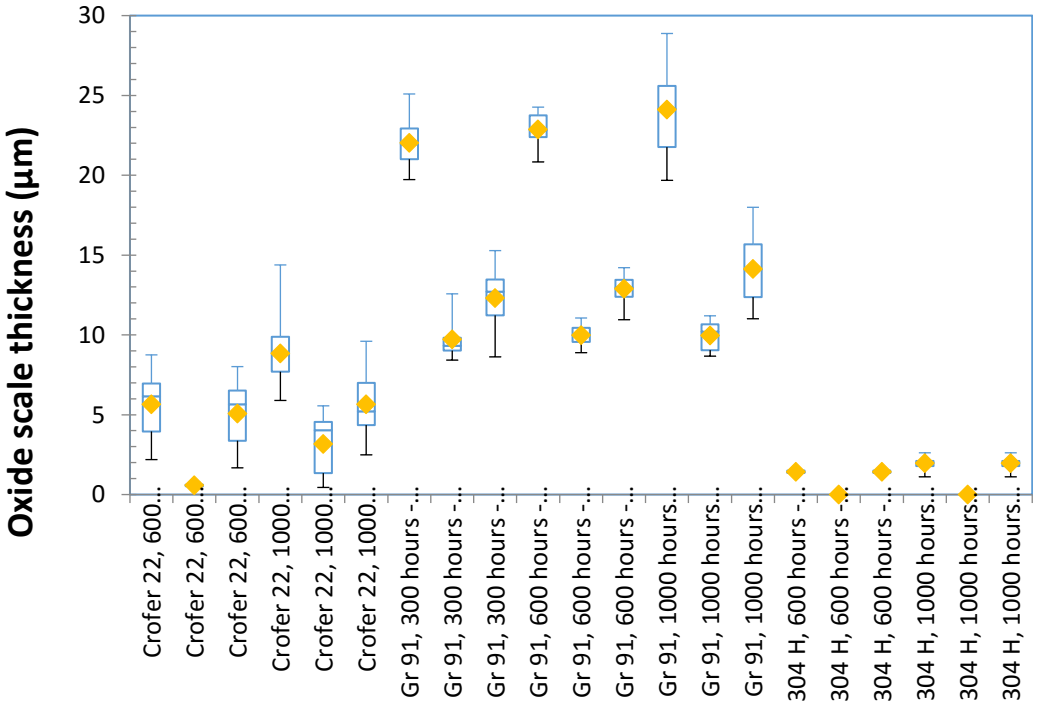

Figure 2.3.5-22 – Comparison of oxide thicknesses formed on alloys Grade 91, Crofer 22H, and TP304H after exposure at 650°C for up to 1,000h in CO_2 containing 3.6 vol.% O_2 and 5.3 vol.% H_2O at 200 bar.

Parabolic plots of these data are shown in Figure 2.3.5-23, and the parabolic rate constants derived from the slopes of the curves are listed in Table 2.3.5-3.

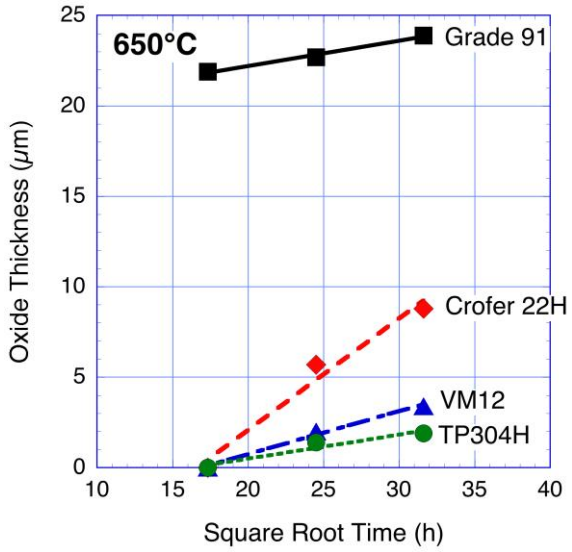

Figure 2.3.5-23 – Parabolic plot for total scale thicknesses formed on ferritic steels and austenitic steel TP304H after exposure at 650°C to CO_2 containing 3.6 vol.% O_2 and 5.3 vol.% H_2O and 200 bar.

Table 2.3.5-3
Total scale thickness-based parabolic rate constants for alloys exposed at 650°C for up to 1,000h in CO_2 containing 3.6 vol.% O_2 and 5.3 vol.% H_2O at 200 bar.

Alloy	k_p, μm²/h	R^2
Grade 91	9.8E x 10^{-3}	0.99
VM12	2.8E x 10^{-2}	0.99
Crofer 22H	1.9Ex 10^{-1}	0.97
TP304H	3.3E x 10^{-3}	0.99

The thicknesses of inner and outer oxide layers are compared in Figures 2.3.5-24 and 2.3.5-25, respectively. Since some layers were too thin to be measured reliably, especially after the shortest exposures, data points for some alloys and conditions are omitted from these Figures. For Grade 91, Crofer 22H, and TP304H the inner layers were notably thinner than the outer after all exposure times. Table 2.3.5-4 compares the trends with time of L1/L2.

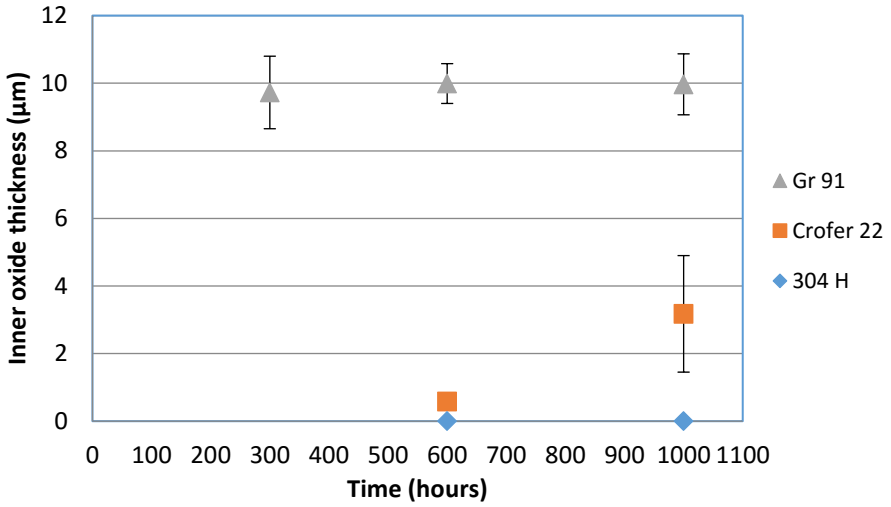

Figure 2.3.5-24 – Comparison of inner oxide layer thicknesses formed on Grade 91, Crofer 22H, and TP304H as a function of time after exposure for up to 1,000h at 650°C to CO_2 containing 3.6 vol.% O_2 and 5.3 vol.% H_2O at 200 bar.

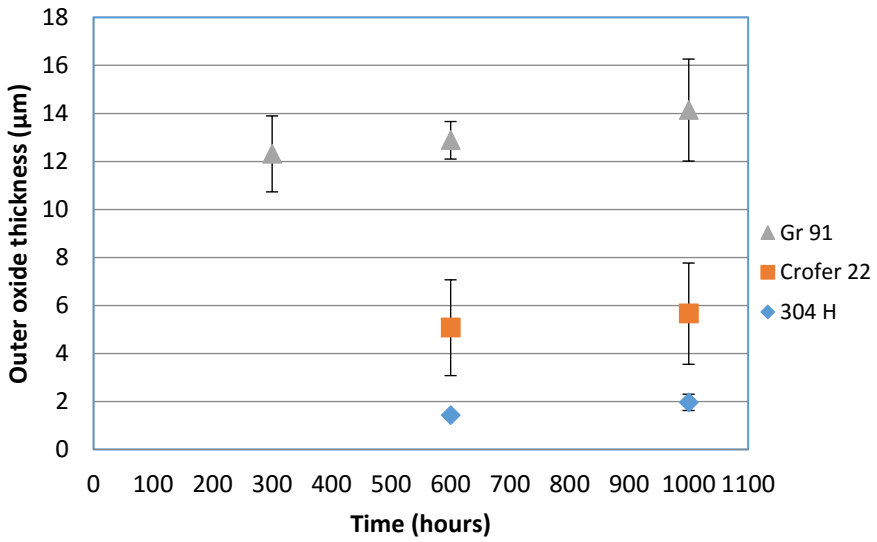

Figure 2.3.5-25– Comparison of outer oxide layer thicknesses formed on Grade 91, Crofer 22H, and TP304H as a function of time after exposure for at 650°C up to 1,000h in CO_2 containing 3.6 vol.% O_2 and 5.3 vol.% H_2O and 200 bar.

Table 2.3.5-4
Trend with time of the relative thicknesses of oxide layers formed after exposure for at 650°C up to 1,000h in CO_2 containing 3.6 vol.% O_2 and 5.3 vol.% H_2O and 200 bar.

Alloy	Ratio, L1/L2		
	300h	600h	1,000h
Grade 91	0.8	0.8	0.7
VM 12	NA	NA	NA
Crofer 22H	NA	0.1	0.6
TP304H	NA	NA	NA
HR3C	NA	NA	NA
IN740H	NA	NA	NA
IN617	NA	NA	NA

2.3.5.C - Specimens from long-term (1,000h) test at 750°C in CO_2 containing 3.6 vol.% O_2 and 5.3 vol.% H_2O at 200 bar (also see Section 2.3.3.C)

The oxide scales formed on Grade 91, VM12, Crofer 22H, and TP304H after exposure for 300, 628, and 1,000h at 750°C in this test were examined by optical and scanning electron microscopy at three locations along metallographically-polished cross sections. In addition to the micrographs presented here, others are assembled in Appendix B. As with specimens exposed at lower temperatures (Sections 2.3.3.A and 2.3.3.B), the scale thicknesses formed on the HT alloys HR3C, IN617, and IN740H after exposure in this test were too thin for accurate measurement using available techniques.

The thick scale formed on Grade 91 at 750°C was quite adherent, Figure 2.3.5-26, and exhibited essentially the same uniformly-thick double-layered structure as seen at the lower temperatures. The structure of L1 again consisted of thin layers oriented parallel to the alloy-L1 interface, and L2 again appeared largely featureless except that approximately 40% of its thickness was occupied by hematite, compared to more than 66% after 1,000h at 650°C. The L1-L2 interface appeared to be free of pores. A feature not observed after exposure at the lower temperatures was the presence of a continuous sublayer of precipitates (IOZ) in the surface of the alloy. It appeared that those precipitates were Cr-rich, and that they were associated with a specific feature of the alloy microstructure.

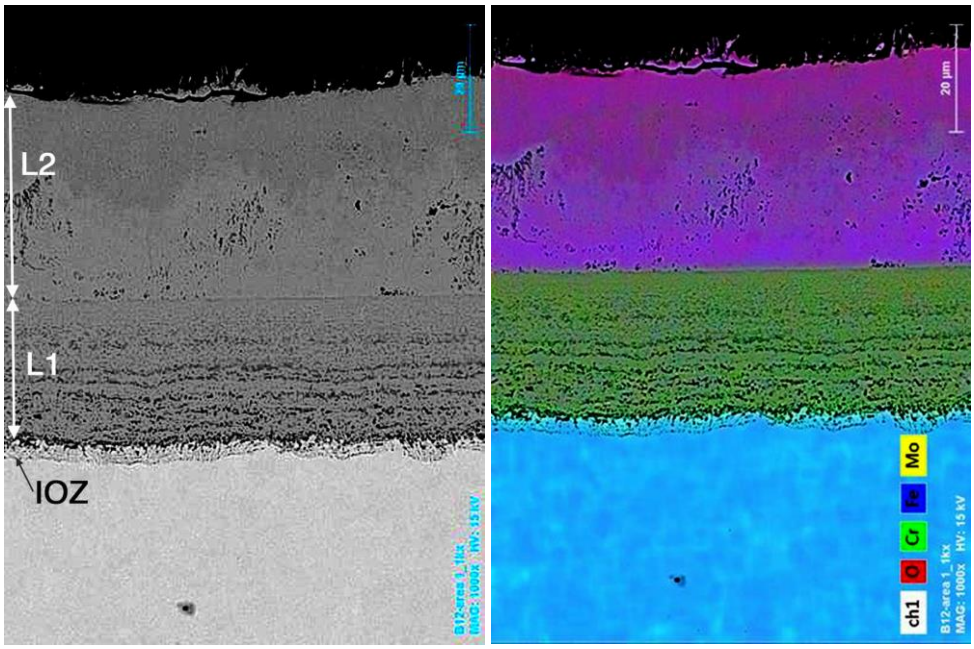

Figure 2.3.5-26 – SEM/BSE micrograph of metallographically-polished cross section of Grade 91 after exposure at 750°C for 1,000h in CO_2 containing 3.6 vol.% O_2 and 5.3 vol.% H_2O at 200 bar, and superimposed EDS maps for Fe, Cr, Mo, and O.

Alloy VM12 also formed a double-layered scale after 1,000h at 750°C, but much thinner than on Grade 91, in which the inner layer was quite uniform in thickness, as shown in Figure 2.3.5-27. The outer surface of the outer layer appeared faceted, with occasional needle-like features. The demarcation between the Cr-containing and Cr-free scale layers indicated in the EDS maps did not appear to coincide with the obvious change in microstructure suggested in the BSE image and decorated by a line of voids. There was a relatively thick IOZ beneath L1; it appeared that inward growth of L1 involved penetration along microstructural features into the IOZ, though no such penetrations extended beyond the IOZ.

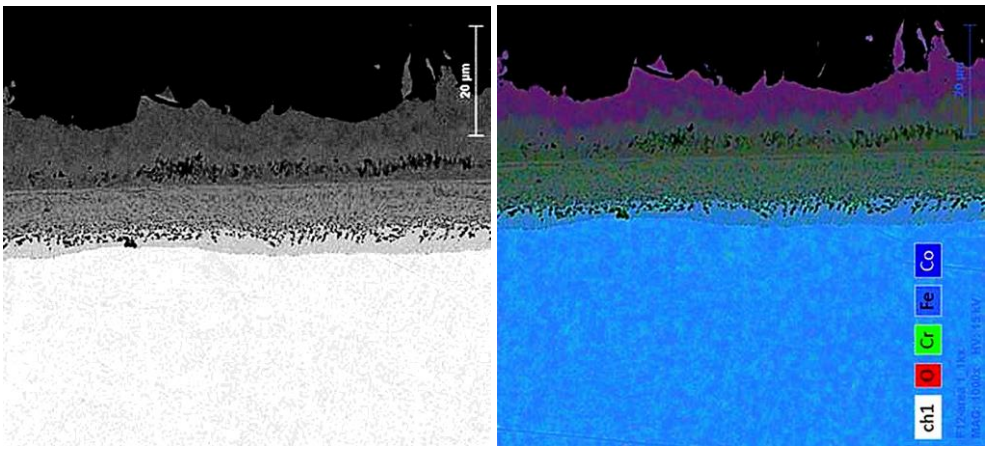

Figure 2.3.5-27 – SEM/BSE micrograph of metallographically-polished cross section of VM12 after exposure at 750°C for 1,000h in CO_2 containing 3.6 vol.% O_2 and 5.3 vol.% H_2O at 200 bar, and superimposed EDS maps for Fe, Cr, and O.

The morphology of the scale formed after 1,000h at 750°C on Crofer 22H was very similar to that on Grade 91, but very much thinner. Both L1 and L2 were uniform in thickness, and an IOZ also was present, Figure 2.3.5-28. Unlike the scale on Grade 91, the structure of L1 did not exhibit any

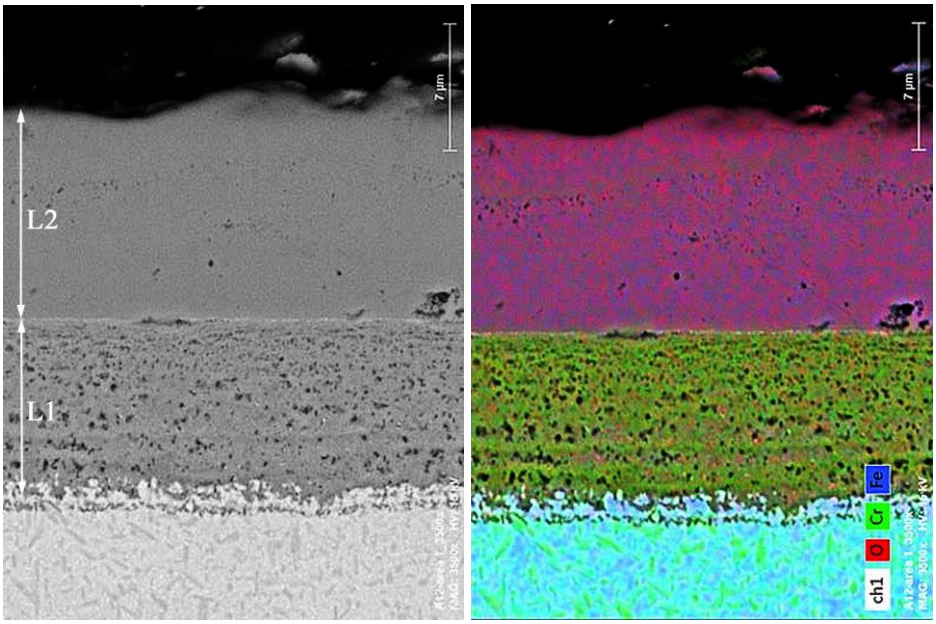

Figure 2.3.5-28 – SEM/BSE micrograph of metallographically-polished cross section of Crofer 22H after exposure at 750°C for 1,000h in CO_2 containing 3.6 vol.% O_2 and 5.3 vol.% H_2O at 200 bar, and superimposed EDS maps for Fe, Cr, O, Ti, and Nb.

pronounced layered or banded features, though it appeared to contain significant distributed fine porosity. L2 was apparently single-phase and featureless, and the L1-L2 interface exhibited only isolated voids or porosity.

The scale morphologies formed on alloy TP304H at 750°C were very similar to those at 700°C: after 1,000h both layers were relatively uniform in thickness, unlike those developed in HP steam (usually at significantly lower temperatures) [1]. The thickness of the inner layer shown in Figure 2.3.5-29 was significantly more uniform than observed at 700°C, and though there are a few penetrations apparently along alloy grain boundaries, no IOZ was apparent. Also, as noted at 700°C, L2 appears featureless and quite unlike the large columnar-grained morphology typical of steam-formed scales.

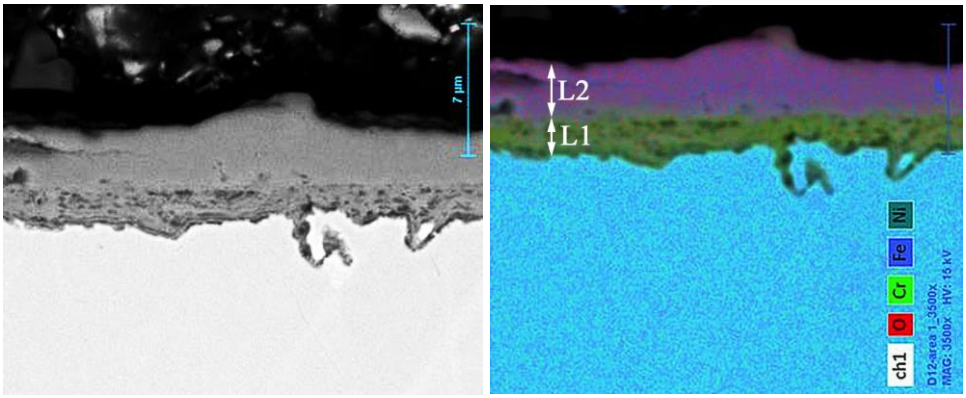

Figure 2.3.5-29 – SEM/BSE micrograph of metallographically-polished cross section of TP304H after exposure at 750°C for 1,000h in CO_2 containing 3.6 vol.% O_2 and 5.3 vol.% H_2O at 200 bar, and showing superimposed EDS maps for Fe, Ni, Cr, and O.

Measurements of scale thicknesses formed on these alloys are presented as box plots in Figure 2.3.5-30. These data also are presented as parabolic plots in Figure 2.3.5-31, and the parabolic rate constants derived from the slopes are summarized in Table 2.3.5-5.

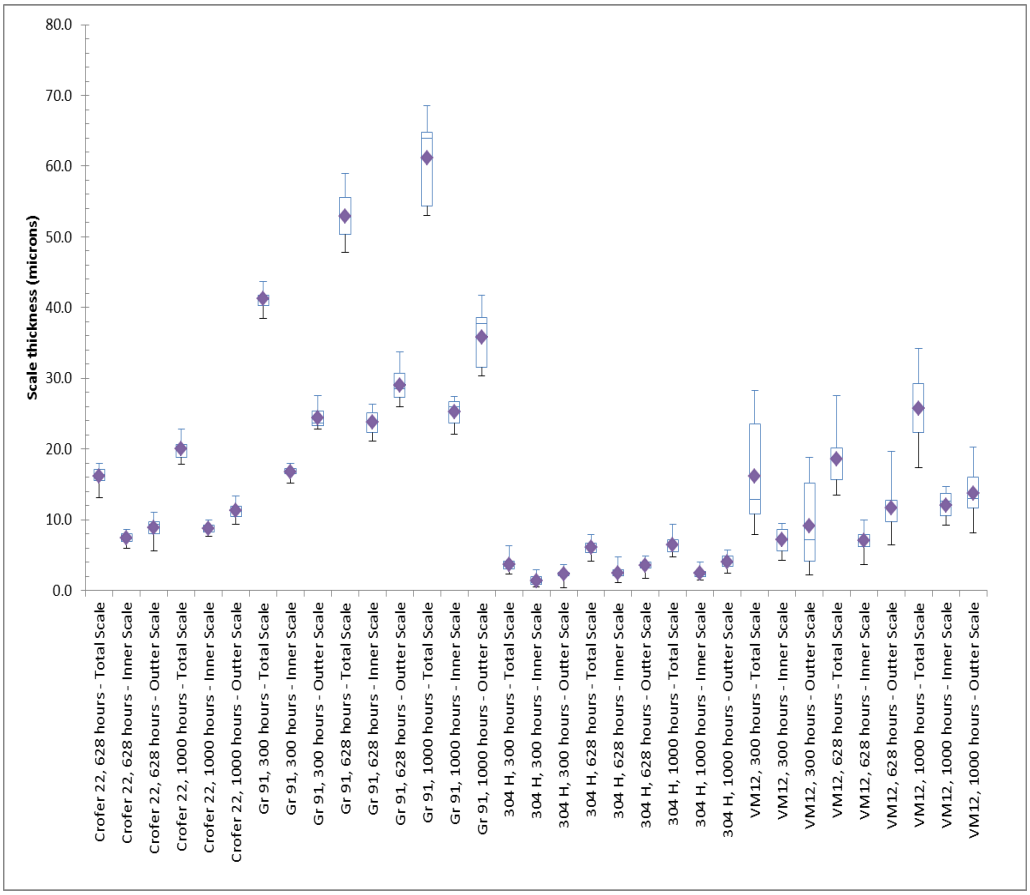

Figure 2.3.5-30 – Comparison of oxide thicknesses formed on Grade 91, VM12, Crofer 22H, and TP304H after exposure at 750°C for up to 1,000h in CO_2 containing 3.6 vol.% O_2 and 5.3 vol.% H_2O at 200 bar.

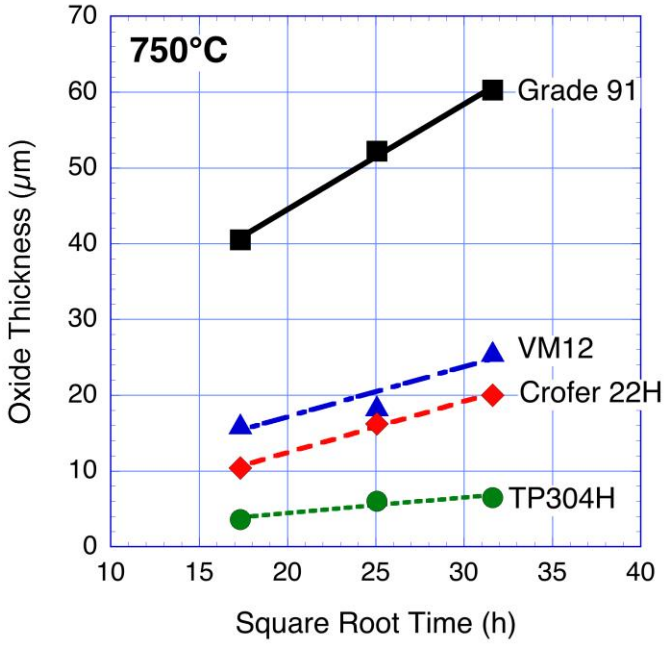

Figure 2.3.5-31 – Total scale thickness-based parabolic plots for ferritic steels and austenitic steel TP304H after exposure at 750°C to CO_2 containing 3.6 vol.% O_2 and 5.3 vol.% H_2O at 200 bar.

Table 2.3.5-5
Total scale thickness-based parabolic rate constants for alloys exposed at 750°C for up to 1,000h in CO_2 containing 3.6 vol.% O_2 and 5.3 vol.% H_2O at 200 bar.

Alloy	k_p, μm²/h	R^2
Grade 91	1.1	0.78
VM12	2.2E x 10^{-1}	0.90
Crofer 22H	2.3E x 10^{-1}	0.99
TP304H	2.2E x 10^{-2}	0.89

Comparison of the thicknesses of the inner and outer oxide layers (Figures 2.3.5-32 and 2.3.5-33, respectively) showed the inner layers formed on all four alloys to be thinner after all exposure times. These ratios are listed in Table 2.3.5-6.

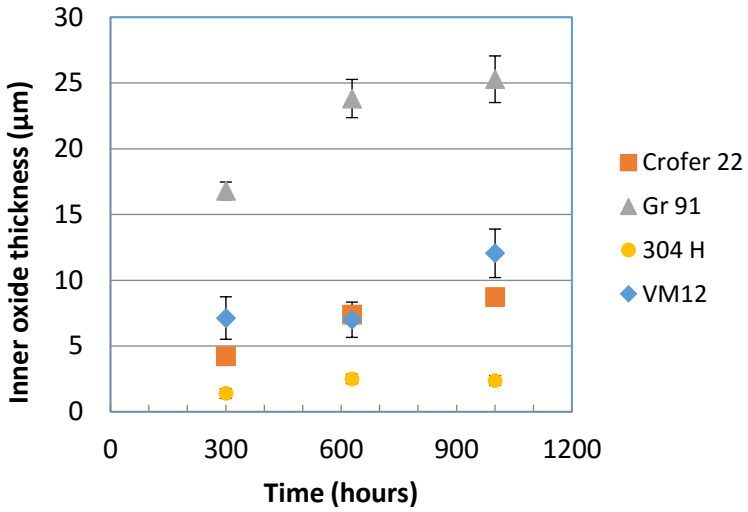

Figure 2.3.5-32 – Comparison of inner oxide layer thicknesses for Grade 91, Crofer 22H, VM12, and TP304H as a function of time during exposure for up to 1,000h at 750°C in CO_2 containing 3.6 vol.% O_2 and 5.3 vol.% H_2O and 200 bar.

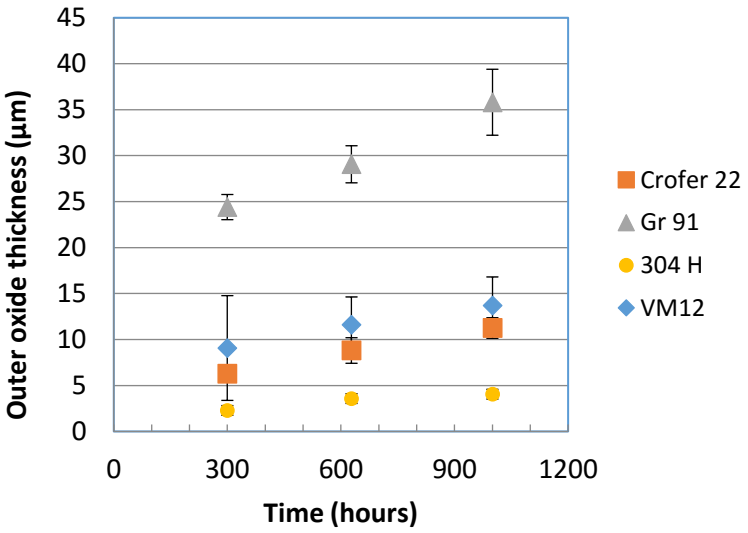

Figure 2.3.5-33 – Comparison of outer oxide layer thicknesses for Grade 91, Crofer 22H, VM12, and TP304H as a function of time during exposure for up to 1,000h at 750°C in CO_2 containing 3.6 vol.% O_2 and 5.3 vol.% H_2O and 200 bar.

Table 2.3.5-6
Trend with time of the relative thicknesses of oxide layers formed after exposure for up to 1,000h at 750°C to CO_2 containing 3.6 vol.% O_2 and 5.3 vol.% H_2O at 200 bar.

Alloy	Ratio, L1/L2		
	300h	600h	1,000h
Grade 91	0.7	0.8	0.7
VM 12	0.8	0.6	0.9
Crofer 22	0.7	0.8	0.8
TP304H	0.6	0.7	0.6
HR3C	NA	NA	NA
IN740H	NA	NA	NA
IN617	NA	NA	NA

2.3.6 — Characterization of Specimens Exposed in the 5,000-h Exposure Test

This test was conducted at 700°C in CO_2 containing 3.6 vol.% O_2 and 5.3 vol.% H_2O at 200 bar. Specimens were removed for inspection and weighing after 1,000, 3,500, and 5,000h, and at each interval one specimen of each alloy was retained for destructive evaluation.

2.3.6.A - Scales formed on Alloy Grade 91

Figure 2.3.6-1 shows backscattered electron images of metallographically-polished cross sections of the oxide scale formed on Grade 91 ferritic steel after exposure at 700°C. As noted earlier, while two main layers readily can be distinguished in the scale, in all cases a large fraction of the thickness of L2 had been converted to hematite, though that fraction appeared to decrease with increasing time (scale thickness). In all cases L1 exhibited a banded (or laminated) structure, with continuous bands running parallel to the L1-alloy interface, and in general appeared to incorporate significant fine porosity. The overall morphology of L1 appeared very similar to that formed on this alloy in HP steam [1]. A thin, continuous and uniformly thick zone of fine particles (IOZ) was present directly beneath L1 after 1,000h, but was either much thinner or absent at longer times. The morphology of L2 was consistent after all exposure times, but did not exhibit the large, columnar-grained structure found after steam exposure. Instead, there was no obvious grain structure evident, and the main feature was distributed porosity (not obviously connected to any grain structure), the level of which increased with increasing time.

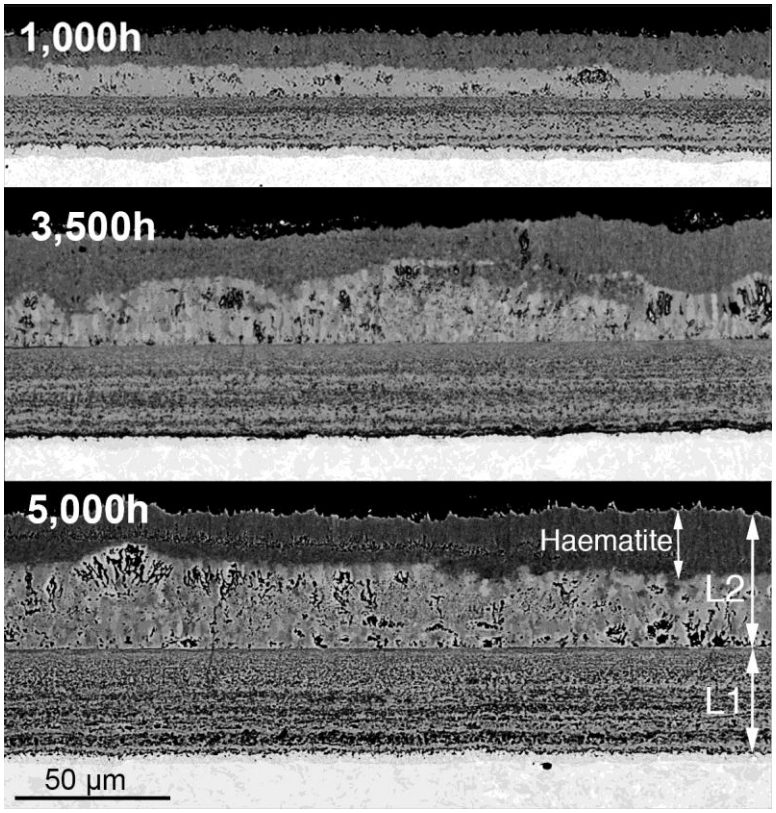

Figure 2.3.6-1 – SEM/BSE images of metallographically-polished cross-sections of Grade 91 showing the oxide scales formed after exposure at 700°C to CO_2 containing 3.6 vol.% O_2 and 5.3 vol.% H_2O at 200 bar.

Typical locations at which scale thickness measurements were made are indicated in Figure 2.3.6-2. The resulting measurements of total oxide thicknesses after 1,000 and 3,500, and 5,000h are summarized in Table 2.3.6-1 and in the box plot shown in Figure 2.3.6-3. These data also are presented as parabolic plots at the end of this section in Figure 2.3.6-23, and the rate constants are summarized in Table 2.3.6-6. As discussed earlier, the outer oxide layer (L2) on Grade 91 was considered to consist of the lighter-appearing (in BSE) region of magnetite plus the darker-appearing hematite. The thicknesses of the inner and outer oxide layers were consistent with the measurements made in the earlier 1,000h test (Section 2.3.3.A) run under the same test conditions (Figures 2.3.5-4 and -5).

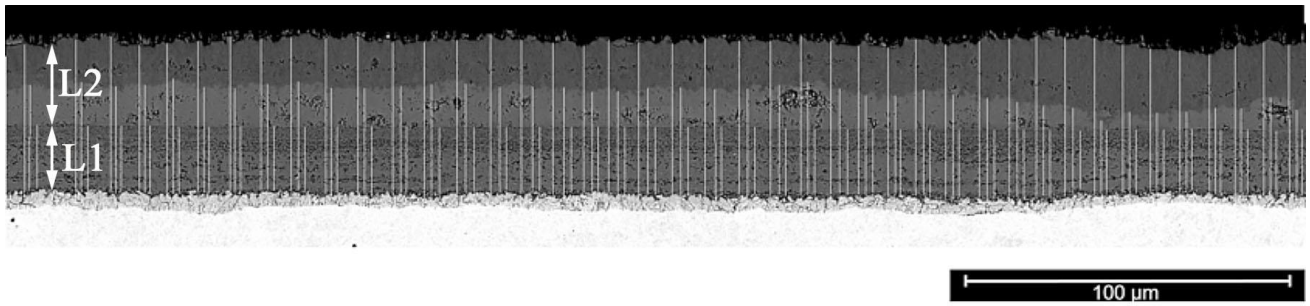

Figure 2.3.6-2 - Backscattered electron image of a metallographically-polished cross-section of Grade 91 oxide scale formed after exposure at 700°C for 1,000h to CO_2 containing 3.6 vol.% O_2 and 5.3 vol.% H_2O at 200 bar, showing the locations at which thickness measurements were made.

Table 2.3.6-1
Summary of total thicknesses of scales formed on alloy Grade 91 after exposure for up to 5,000h at 700°C to CO_2 containing 3.6 vol.% O_2 and 5.3 vol.% H_2O at 200 bar.

Thickness (µm)	Exposure Time (h)		
	1,000	3,500	5,000
Average	47	84	100
Std. Dev.	1.5	3.2	2.2
Min	42	68	93
Max	49	90	105

Similar measurements were made for the thicknesses of the inner and outer oxide layers, and those results are summarized in Table 2.3.6-2. The ratio L1/L2 in the scales on Grade 91 changed little over time, from 0.7 after 1,000h to 0.8 after 5,000h. The thicknesses after 1,000h in this test were consistent with the measurements made in the earlier 1,000h test run under the same test conditions (see Figures 2.3.5-4 and 2.3.5-5).

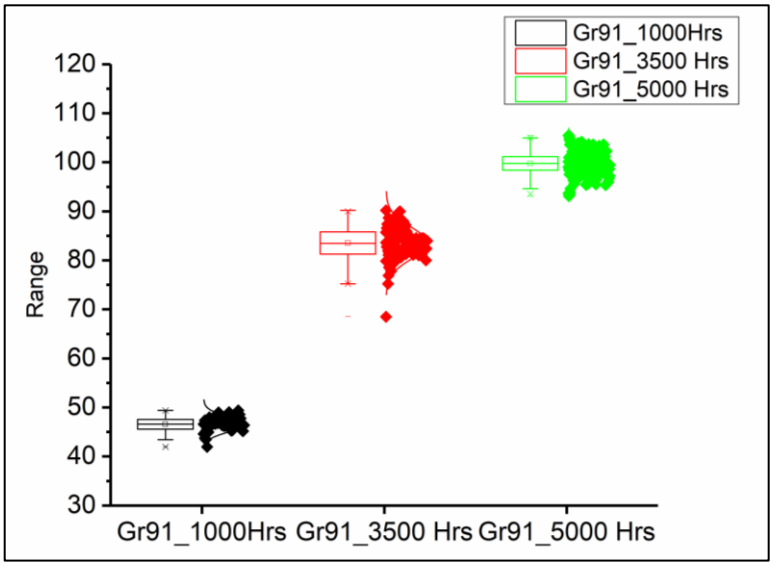

Figure 2.3.6-3 - Box plot showing the total scale thicknesses (in microns) formed on Grade 91 after exposure at 700°C for up to 5,000h in CO_2 containing 3.6 vol.% O_2 and 5.3 vol.% H_2O at 200 bar.

Table 2.3.6-2
Thicknesses of inner and outer oxide layers (in µm) formed on alloys exposed at 700°C for up to 5,000h in CO_2 containing 3.6 vol.% O_2 and 5.3 vol.% H_2O at 200 bar.

Alloy	1,000h			3,500h			5,000h		
	L1	L2	L1/L2	L1	L2	L1/L2	L1	L2	L1/L2
Grade 91	20	27	0.7	94	123	0.8	44	56	0.8
TP304H	2	3	0.7	0.9	1.3	0.8	18-24	26-32	0.7
IN617							0.25-0.4	0.12-0.21	1.6-2.1

Figure 2.3.6-4 shows an SEM/BSE image of a metallographically-polished cross section of an area of scale formed on Grade 91, and EDS elemental maps of the same area for Fe, Cr, and O. The scale had a well-delineated layered structure with a Cr-containing inner layer (L1) and a Cr-free outer layer (L2). The two distinct regions in L2 (which apparently were uniform in thickness) again were assumed to be magnetite (innermost, slightly lower level of O), and hematite. The composition of a sublayer ('partially-oxidized layer' or IOZ) of essentially uniform thickness present between L1 and the alloy was not resolved. Overlaying the elemental distribution maps over the BSE/SEM image, Figure 2.3.6-5, suggested that the composition of the sublayer was similar to that of precipitates in the alloy grain boundaries. Since such grain boundary phases typically are Cr carbides, the inference is that this layer resulted from an accumulation of Cr carbide particles that subsequently were oxidized.

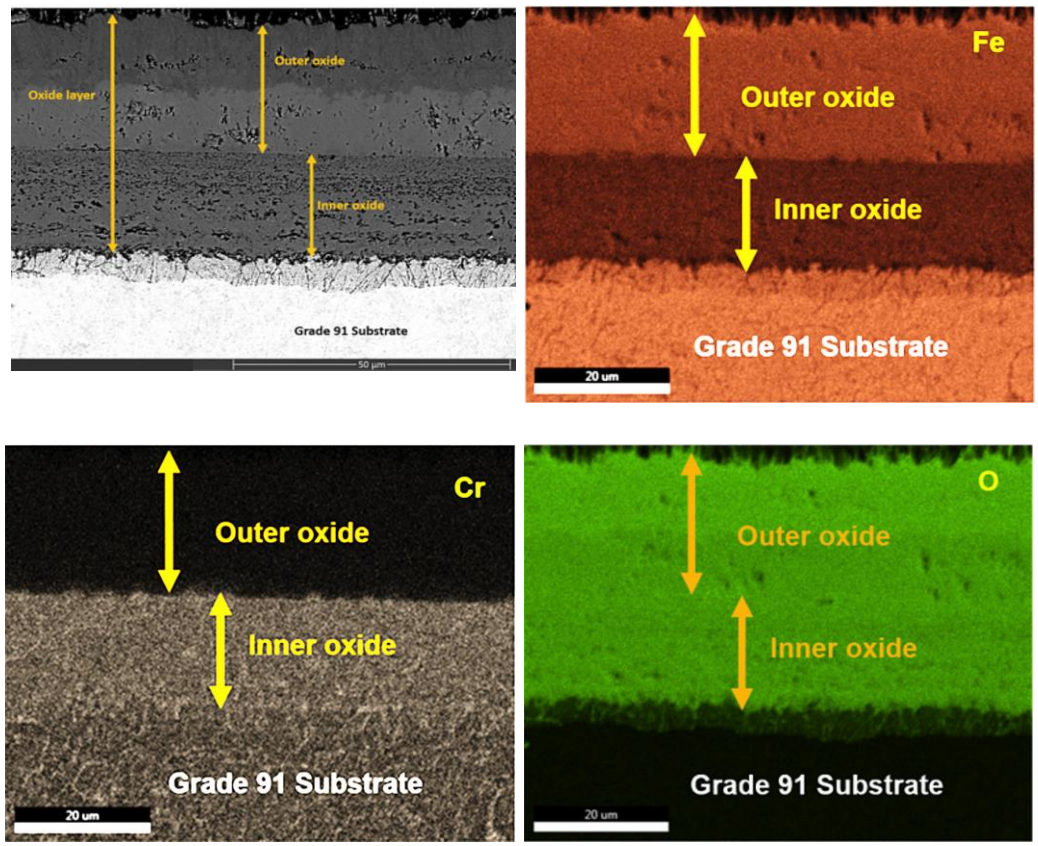

Figure 2.3.6-4 – SEM/BSE image and corresponding EDS maps of the oxide scale formed on Grade 91 at 700°C after 1,000h exposure to CO_2 containing 3.6 vol.% O_2 and 5.3 vol.% H_2O at 200 bar.

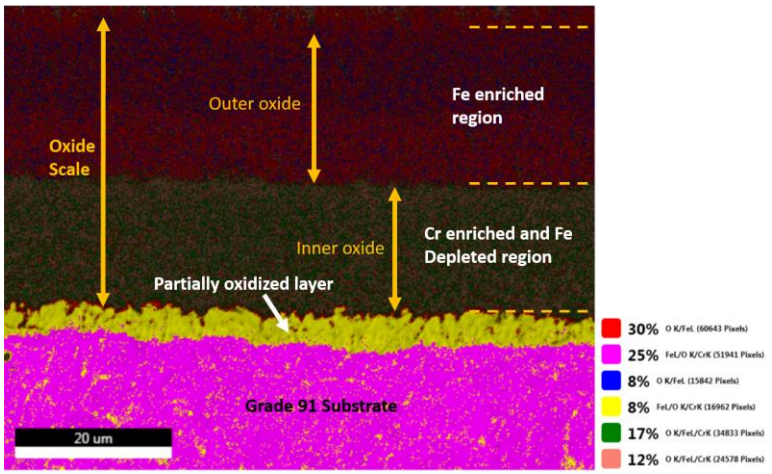

Figure 2.3.6-5 – Elemental distributions overlaid on the SEM/BSE image of Grade 91 from Figure 2.3.6-4 to suggest the possible composition of the scale sublayer ('partially-oxidized layer').

EDS maps for Fe, Cr, and O in the scale formed after 3,500h (Figure 2.3.6-6) showed its morphology to be very similar to that after the 1,000h exposure, but considerably thicker. Areas of Cr

enrichment were apparent in L1, particularly of laminates close to the interface with the alloy, but also in small, dispersed regions. The areas in L2 that appeared as lighter and darker shades of green in the O image delineated a zone of hematite along the outer part of the original magnetite.

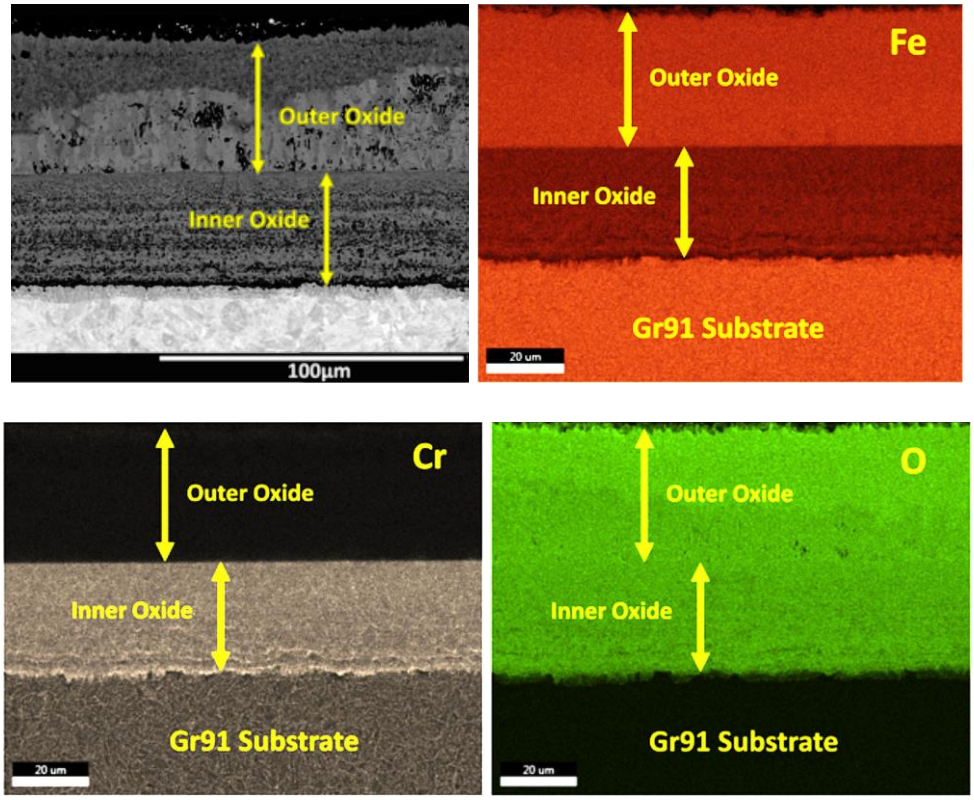

Figure 2.3.6-6 – SEM/BSE image and corresponding EDS maps of the scale formed on Grade 91 after 3,500h exposure at 700°C to CO_2 containing 3.6 vol.% O_2 and 5.3 vol.% H_2O at 200 bar.

Overlaying the elemental distribution maps on the SEM/BSE image, Figure 2.3.6-7, further suggested a layered/laminated structure in L1, with possibly alternating thin layers of Fe-rich and Cr-rich oxide. Such layering was most obvious in the area from the L1-alloy interface to halfway through

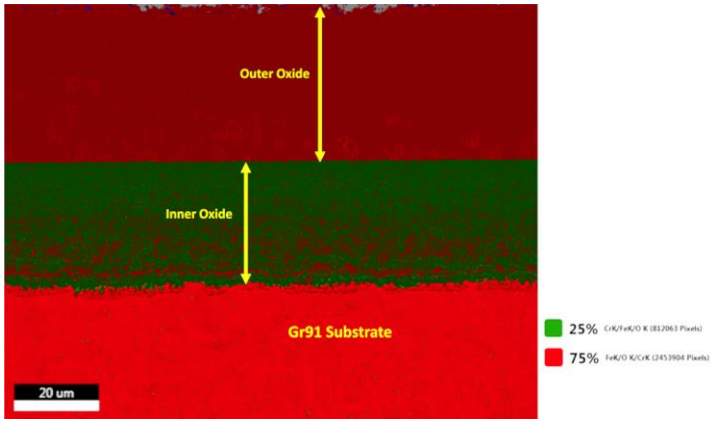

Figure 2.3.6-7 - Elemental distributions overlaid on the SEM/BSE image from Figure 2.3.6-6 to indicate the compositional variation in the oxide layers.

the thickness of the inner layer. This composite map also suggests the presence of Cr-rich precipitates in the alloy directly beneath L1.

2.3.6.B - Scales formed on Alloy TP304H

Figure 2.3.6-8 shows SEM/BSE images of metallographically-polished cross sections of the scales formed on TP304H after 1,000h exposure at 700°C in this test. The locations at which scale thickness measurements were made (40 measurements total at a magnification of 12,000x) are shown in Figure 2.3.6-9. The scale morphology consisted of a two-layered structure commonly reported for this alloy in sCO_2 (and HP steam) in which the thickness of L1 was extremely irregular (reflecting different extents of Cr-enrichment), whereas the thickness of L2 was relatively uniform.

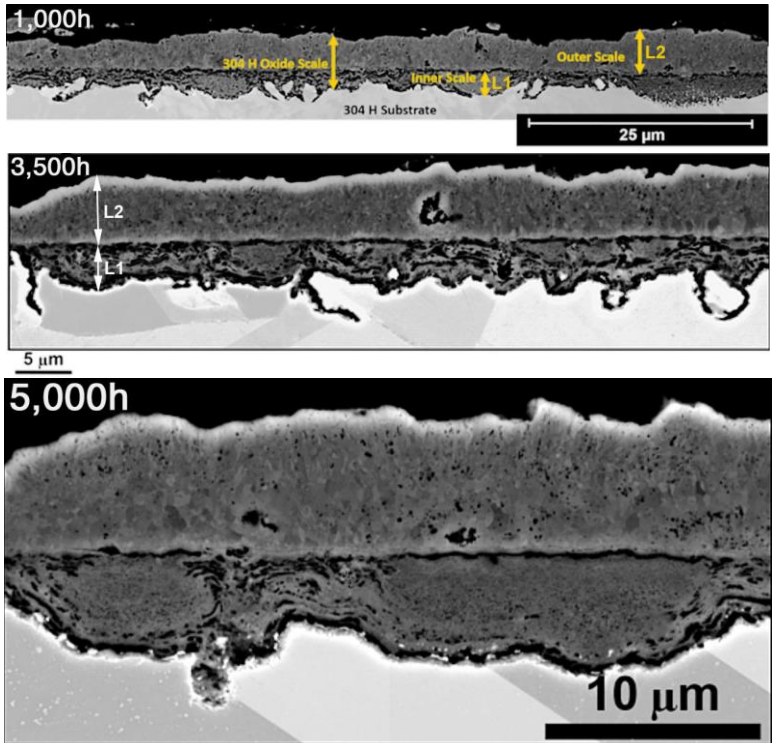

Figure 2.3.6-8 – SEM/BSE images of metallographically-polished cross-sections of TP304H showing the oxide scale formed after exposure for 1,000, 3,500, and 5,000h at 700°C to CO_2 containing 3.6 vol.% O_2 and 5.3 vol.% H_2O at 200 bar.

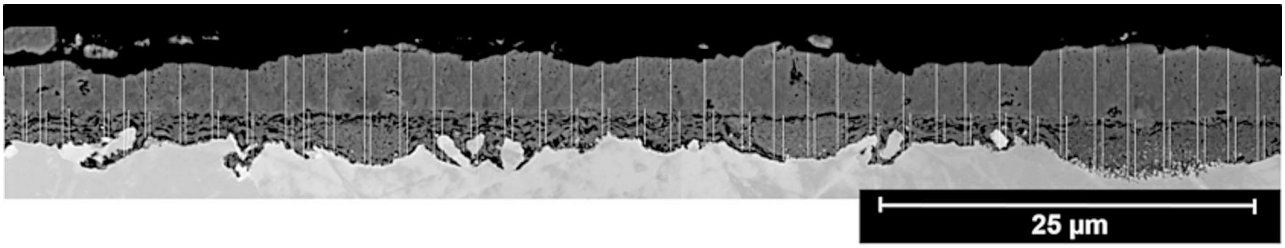

Figure 2.3.6-9 – Locations at which thickness measurements were made on a metallographically-polished cross-section of the oxide scale formed on TP304H after 1,000h at 700°C in CO_2 containing 3.6 vol.% O_2 and 5.3 vol.% H_2O at 200 bar.

The total scale thicknesses measured after exposure at 700°C are summarized in the box plot in Figure 2.3.6-10 and in Table 2.3.6-3. These data also are presented as parabolic plots at the end of this section in Figure 2.3.6-23, and the rate constants are summarized in Table 2.3.6-6.

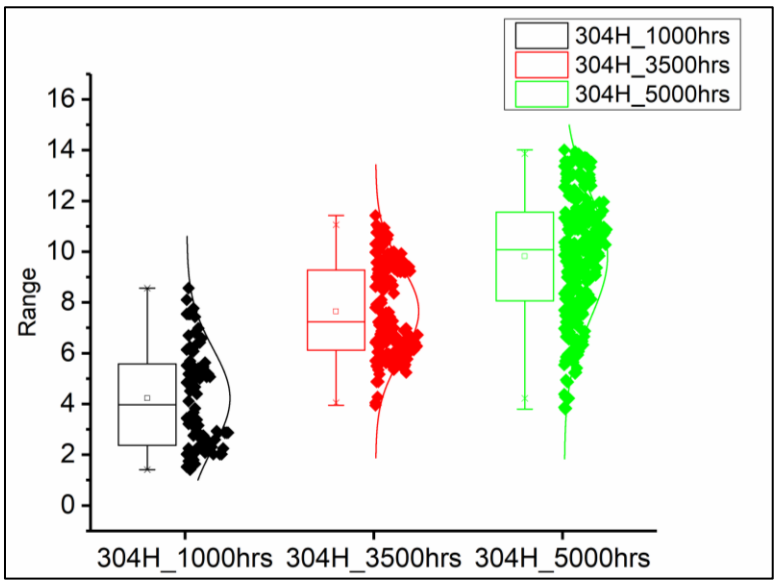

Figure 2.3.6-10 – Summary of total scale thicknesses (in µm) formed on alloy TP304H after exposure for 1,000, 3,500, and 5,000h at 700°C in this test.

Table 2.3.6-3
Summary of total thicknesses of scales formed on alloy TP304H after exposure for up to 5,000h at 700°C to CO_2 containing 3.6 vol.% O_2 and 5.3 vol.% H_2O at 200 bar.

Thickness (µm)	Exposure Time (h)		
	1,000	3,500	5,000
Average	4.2	7.7	9.8
Std. Dev.	2.0	1.8	2.5
Min	1.4	4.0	3.8
Max	8.6	11.4	14.0

Detailed examination of a two-layered nodule present after 1,000h (shown in Figure 2.3.6-11) detected no obvious features such as banding or a definite grain structure in L1, which appeared to consist of particles of oxide intermixed with bright–appearing metallic particles and voids. Further, while in steam-formed scales on this alloy the structure of L2 usually consists of large, columnar grains growing perpendicular to the L1-L2 interface, evidence of a columnar grain structure was present only in the inner third of L2, as shown in Figure 2.3.6-11. Otherwise, this layer consisted mainly of small, equiaxed grains and distributed porosity. A semi-continuous line of voids was present along the L1-L2 interface, just inside L1, was typical of those found in steam-formed scales, in which it represented the plane along which separation of L2 from L1 eventually occurred.

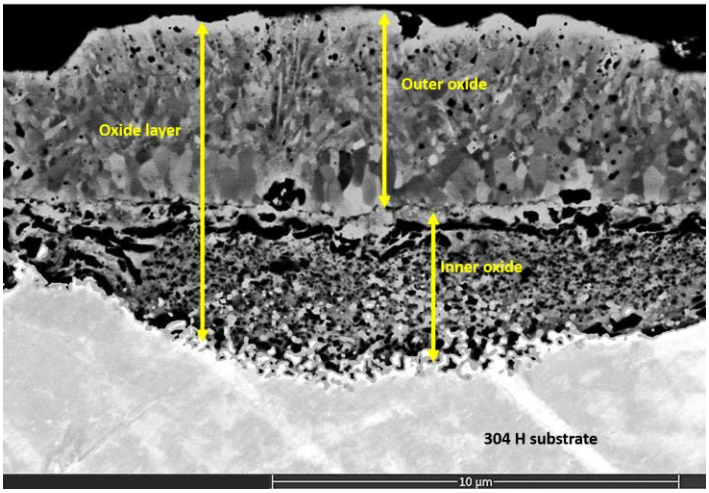

Figure 2.3.6-11 – SEM/BSE image of a scale nodule formed on TP304H after 1,000h at 700°C in CO_2 containing 3.6 vol.% O_2 and 5.3 vol.% H_2O at 200 bar.

EDS maps for Cr, Fe, Ni, and O indicated the expected presence of Cr in L1 and its absence in L2, but in addition there was a thin band along the base of L1 that was enriched in Ni (Figure 2.3.6-12). The non-uniformity of the Cr concentration in L1 suggested the formation of relatively more protective oxide in some areas, as is often observed when the thickness of this layer is extremely non-uniform.

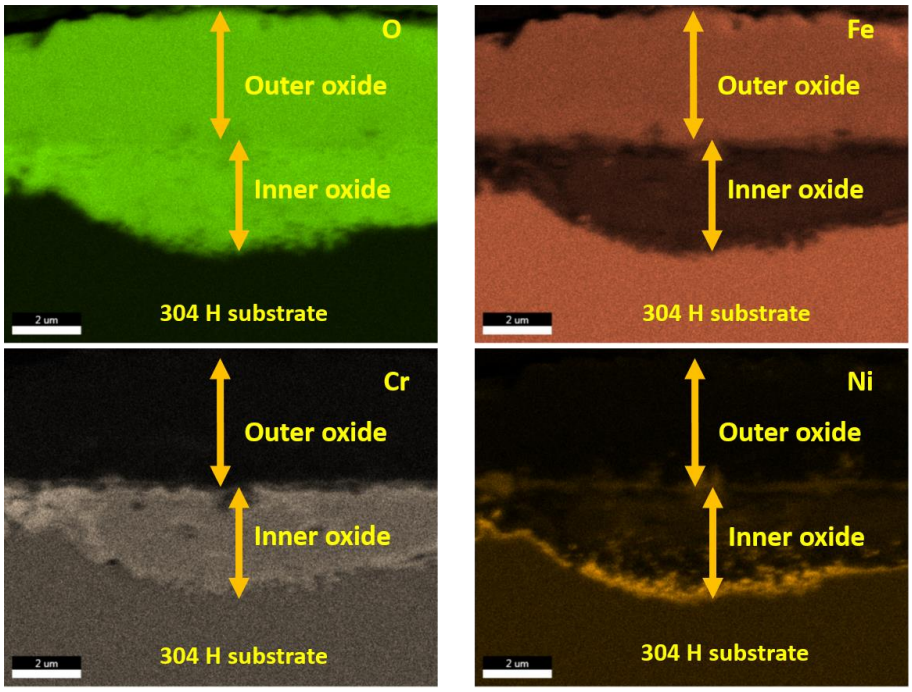

Figure 2.3.6-12 – Distribution of major alloying elements in the nodule of scale formed on TP304H, shown in Figure 2.3.6-11.

Overlaying the elemental distribution maps on the BSE image, as shown in Figure 2.3.6-13, suggested that the structures of L1 and L2 were essentially single-phase, despite their unusual microstructures. The distribution of Ni in L1 also is highlighted by this overlay map: in addition to build-up at the L1-alloy interface, some accumulation of Ni also was indicated along the L1-L2 interface and in particles scattered in L1. During oxidation of austenitic steels such as TP304H in HP steam, Ni typically does not take part in oxide formation but instead is rejected (as metal) near or ahead of the oxidation front. The features shown in Figures 2.3.6-11 and 2.3.6-13 possibly suggest that the process by which L1 formed in sCO_2 with controlled oxidizing impurities was similar to that operating in HP steam.

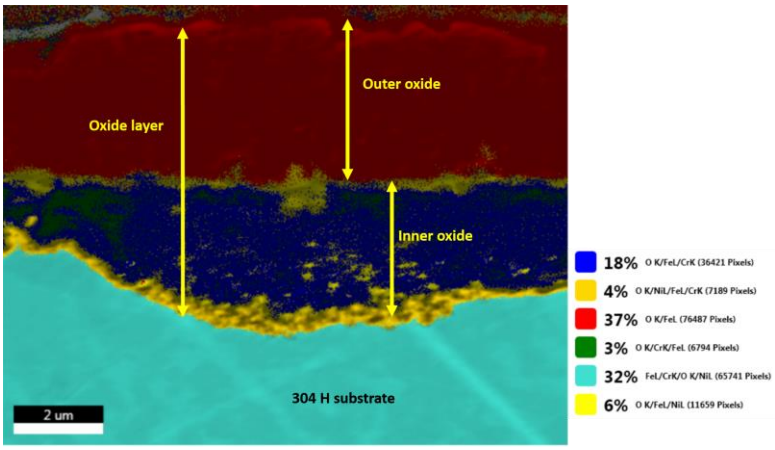

Figure 2.3.6-13 - Elemental distributions overlaid on the SEM/BSE image from Figure 2.3.6-11 to indicate the compositional variation in L1.

An SEM/BSE image and corresponding EDS elemental maps for Fe, Ni, Cr, and O are shown in Figures 2.3.6-14 and 2.3.6-15, respectively for a section of the scale formed after 3,500h. The SEM/BSE image indicates that in addition to its highly non-uniform thickness, in some areas L1 consisted almost entirely of multiple layers. The elemental maps did not provide further discrimination of this scale structure, except that there was some enrichment in Cr along the L1-alloy interface, typical of this type of scale formed in steam. There were no obvious Cr-rich precipitates in the alloy. Areas of enrichment in Ni in L1 appeared to coincide with apparent voids or porosity. The image in Figure 2.3.6-14 also confirmed that the microstructure of L2 consisted almost entirely of small, equiaxed grains, quite different from the large, columnar structures typically found after oxidation in steam. The elemental maps in Figure 2.3.6-15 suggested that L2 was essentially of uniform composition, and most likely was magnetite.

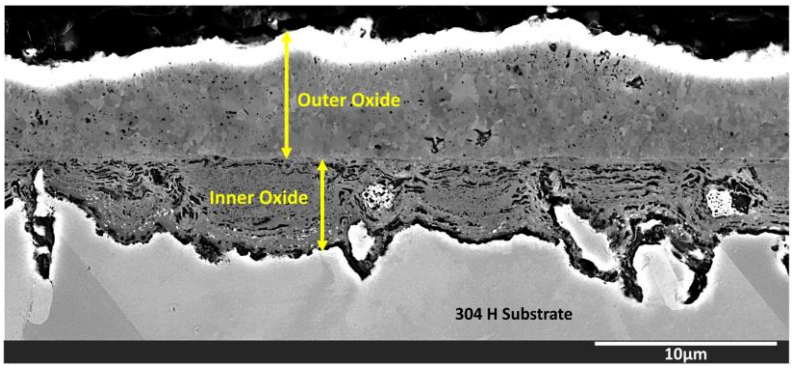

Figure 2.3.6-14 – SEM/BSE image of a metallographically-polished cross section of scale formed on TP304H after exposure in this test for 3,500h at 700°C.

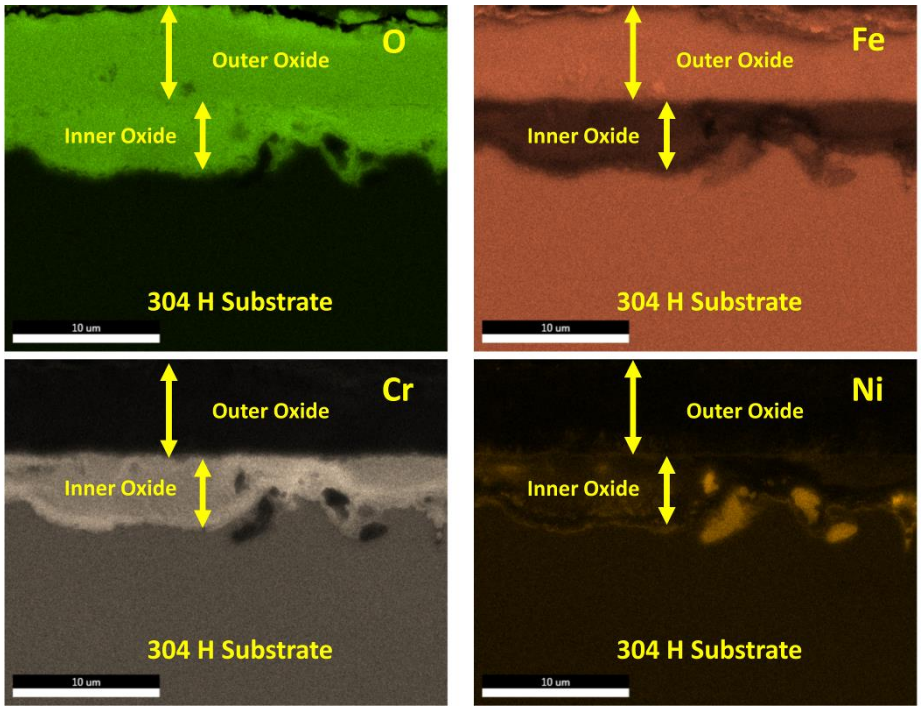

Figure 2.3.6.15 – EDS maps for the metallographically-polished cross section of scale formed on TP304H, shown in Figure 2.3.6-14.

Figure 2.3.6-16 is a composite map of the elemental distribution of Fe, Ni, Cr, and O generated by overlaying individual elemental maps on the corresponding SEM/BSE image. While this confirmed that there were no obvious Cr-rich precipitates in the alloy, there were some small (light green-appearing, possibly Cr-containing) precipitates dispersed in the lower regions of L1. There also appeared to be some fine (apparently Ni-rich) precipitates along the L1-alloy interface, and an almost continuous line of larger Ni-rich precipitates along the L1-L2 interface.

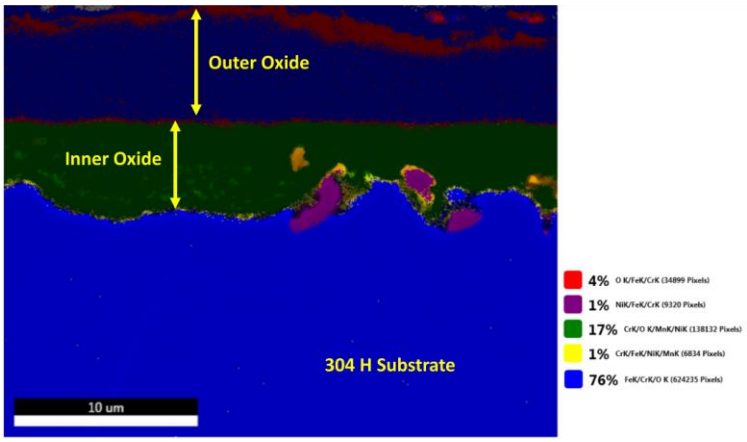

Figure 2.3.6-16 - Elemental distributions overlaid on the SEM/BSE image of a metallographically-polished cross section of TP304H after exposure in this test for 3,500h at 700°C.

2.3.6.C - Scales formed on Alloy IN617

Figure 2.3.6-17 shows an SEM/BSE images of the scales formed on IN617 after 1,000, 3,500, and 5,000h exposure in this test. The images resulted from pioneering use of advanced BSE/EDS/EBSD detection systems on an SEM that became available toward the end of the project. After 1,000h the scale appeared to consist of regions where it was randomly single-layered or double-layered with associated porosity, with occasional larger double-layered nodules (as indicated at the LHS of the figure).

Compared to the apparent scale structure after 1,000h, the scale after 3,500h appeared to be mostly double-layered with a few areas where it was much thinner and consisted of a single layer. Both layers were non-uniform in thickness, with L1 typically thicker than L2. L1 also appeared to contain significant porosity in the form of large voids, whereas L2 appeared to have a columnar-grained structure.

By 5,000h the scale formed on IN617 at 700°C in this test had developed a morphology with features similar (but much thinner) in general form to those typically found on austenitic steels (and observed after 3,500h in this test on IN740H): two layers in which the thickness of L1 was irregular whereas that of L2 was relatively uniform, with a few areas that were thinner and single-layered. In the example shown in Figure 2.3.6-17, L2 appears to consist of columnar grains that span the whole layer thickness. The structure of L1 possibly was fine-grained; it is not known if the voids at the base of

nodular features in L1 and along the L1-L2 interface were real and indicate potential for separation of L2, or were artifacts from specimen preparation.

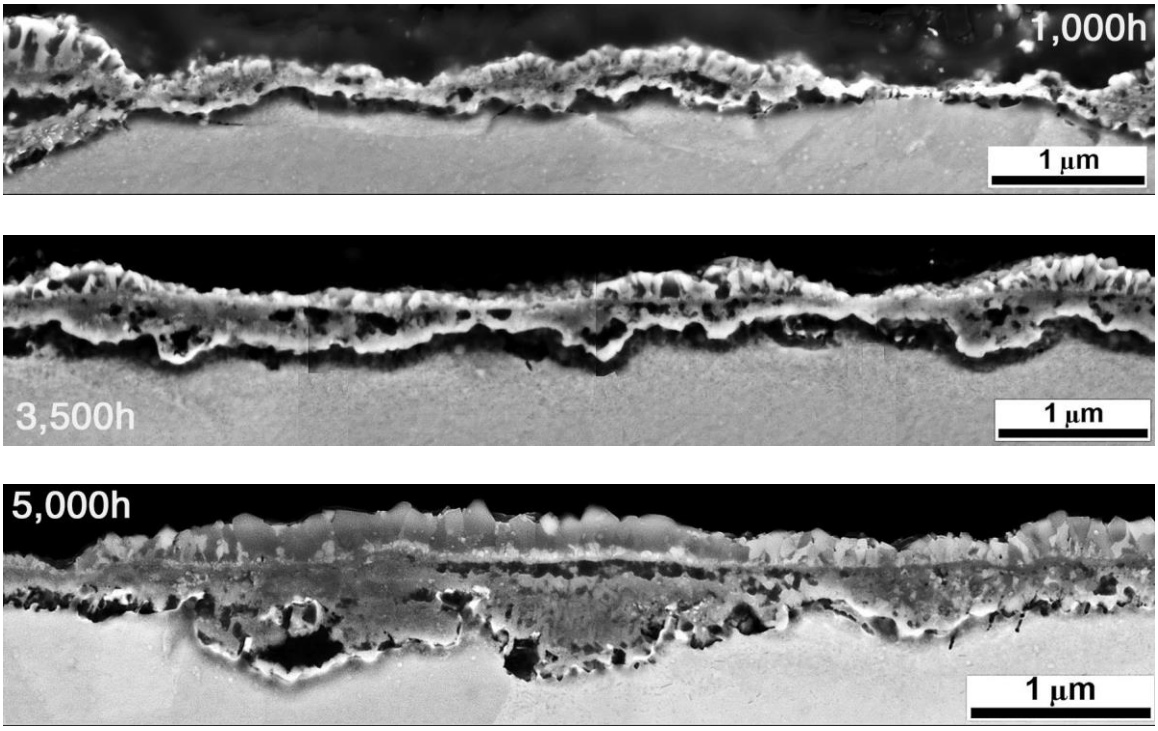

Figure 2.3.6-17 – SEM/BSE images of metallographically-polished cross-sections of IN617 showing the oxide scale formed after exposure up to 5,000h at 700°C in CO_2 containing 3.6 vol.% O_2 and 5.3 vol.% H_2O at 200 bar.

In the absence of prior detailed information or any obvious rigorous approach for systematically determining whether the scale was single- or multilayered, for measurement purposes only the total thickness was considered. The measurements made are summarized in the box plot in Figure 2.3.6-18 and Table 2.3.6-4, which demonstrate the large variability in the thickness of these very thin scales. These data also are presented as parabolic plots at the end of this section in Figure 2.3.6-23, and the rate constants are summarized in Table 2.3.6-6.

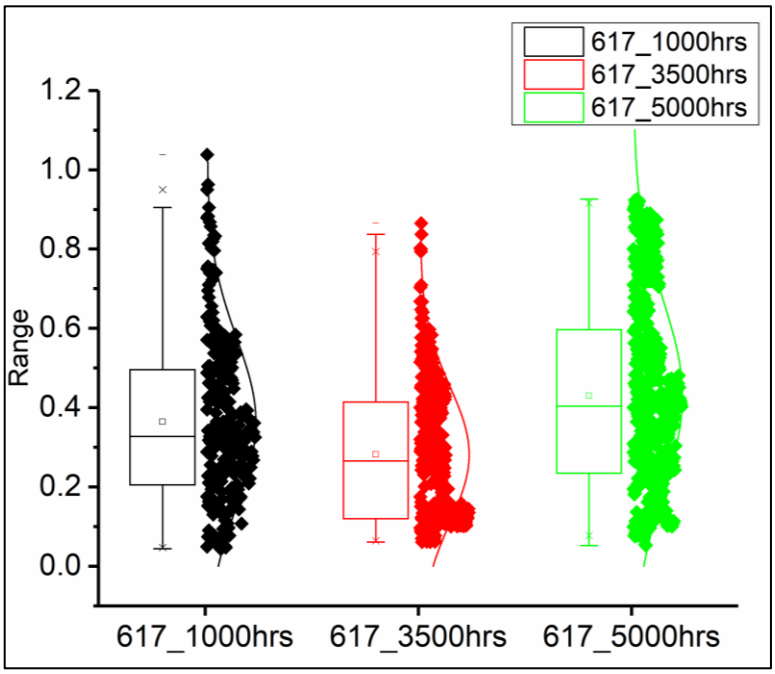

Figure 2.3.6-18 – Summary of total scale thicknesses (in µm) formed on alloy IN617 after exposure for 1,000, 3,500, and 5,000h at 700°C in this test.

Table 2.3.6-4
Summary of total thicknesses of scales formed on alloy IN617 after exposure at 700°C to CO_2 containing 3.6 vol.% O_2 and 5.3 vol.% H_2O at 200 bar.

Thickness (µm)	Exposure Time (h)		
	1,000	3,500	5,000
Average	0.36	0.28	0.43
Std. Dev.	0.21	0.17	0.24
Min	0.04	0.06	0.05
Max	1.04	0.87	0.93

2.3.6.D - Scales formed on Alloy IN740H

Figure 2.3.6-19 shows SEM/BSE images of metallographically-polished cross sections of the scales formed on IN740H after exposure at 700°C for 1,000, 3,500, and 5,000h in this test. After 1,000h the scale appeared to consist of a single layer of oxide that was quite uniform in thickness, with a sublayer of precipitates associated with a specific phase (possibly γ') in the alloy. Such a structure is quite compatible with earlier observations (using lower-resolution optical microscopy) that scales formed on this alloy in HP steam mostly were thin and featureless, with isolated thicker nodules and penetrations into the alloy surface (Figure 2.3.6-20 [4]).

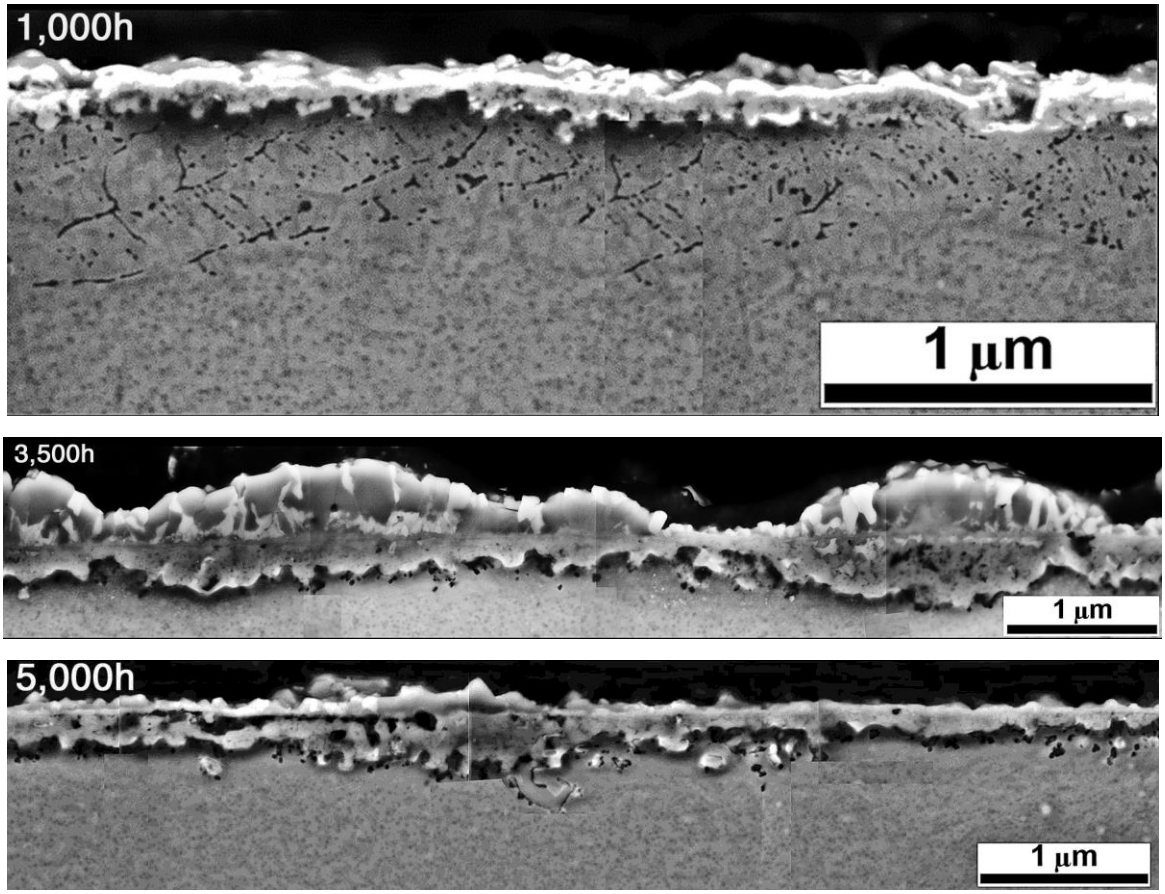

Figure 2.3.6-19 – SEM/BSE images of a metallographically-polished cross-sections of IN740H showing the oxide scale formed after exposures up to 5,000h at 700°C to CO_2 containing 3.6 vol.% O_2 and 5.3 vol.% H_2O at 200 bar.

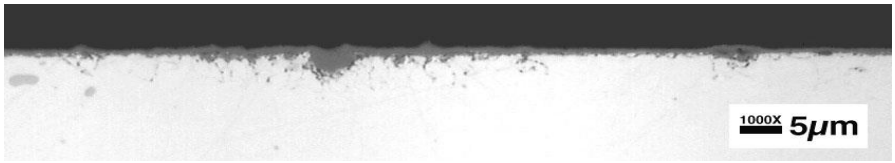

Figure 2.3.6-20 – Optical micrograph of a metallographically-polished cross-section of IN740 after 4,000h at 700°C in steam at 17 bar (4).

The scale formed after 3,500h at 700°C was mostly double-layered, with a few small lengths of scale that were much thinner and single-layered, as indicated in Figure 2.3.6-19. Most regions of L1 appeared to be free of pores and were mostly featureless, whereas L2 had a well-defined columnar-grained structure. It is not known if the much lighter-appearing features in L2 signified a difference in composition, or if the brightness was an artifact of the BSE technique used. Overall, the scale morphology was reminiscent of that formed on austenitic steel TP304H, but on a much finer scale. The

absence of detailed chemical analysis precluded the drawing of further parallels with the mode of development (and failure) of scales formed on TP304H.

After 5,000h the scale appeared thinner than that after 3,500h, and a smaller amount of the scale exhibited a double-layered structure (Figure 2.3.6-19). Where present, the outer layer appeared to be a single grain thick, and there was the suggestion that further development could result in a columnar-grained structure, as found after 3,500h. L1, present either as a single layer or an inner layer, appeared to be featureless and in some areas voids were apparent at the L1-L2 interface.

The measured total scale thicknesses are summarized in the box plot shown in Figure 2.3.6-21, and in Table 2.3.6-5. Comparison of the total scale thicknesses as a function of time illustrates the much greater scatter after 3,500h and its effect on the statistical representation of thicknesses, while a preponderance of data points at 3,500h suggest more communality with the data for the scales formed after 1,000 and 3,500h. These data also are presented as parabolic plots at the end of this section in Figure 2.3.6-23, and the rate constants are summarized in Table 2.3.6-6.

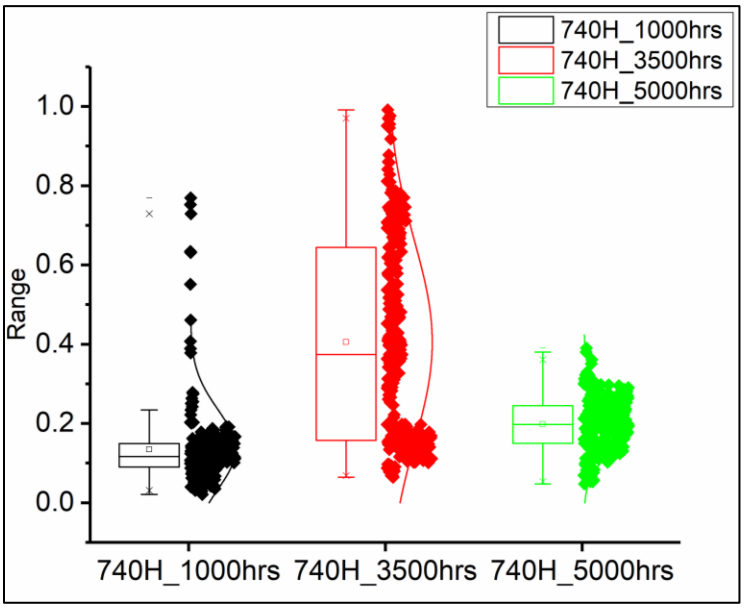

Figure 2.3.6-21 – Summary of total scale thicknesses (in µm) formed on alloy IN740H after exposure for 1,000, 3,500, and 5,000h at 700°C in this test.

Table 2.3.6-5
Summary of total thicknesses of scales formed on alloy IN740H after exposure at 700°C to CO_2 containing 3.6 vol.% O_2 and 5.3 vol.% H_2O at 200 bar.

Thickness (µm)	Exposure Time (h)		
	1,000	3,500	5,000
Average	0.13	0.40	0.20
Std. Dev.	0.10	0.25	0.06
Min	0.02	0.06	0.05
Max	0.77	0.99	0.39

Because of the paucity of scale thickness data for the high-temperature alloy IN740H (and of scale thickness and mass gain data for HR3C and IN617) resulting from difficulties in making physical measurements, the possibility was examined of augmenting those data with thicknesses derived from measured mass gains. Figure 2.3.6-22 is a plot of mass gain against measured total scale thickness for IN740H at 700°C (where both sets of data were obtained from the same specimens). The slope of the straight line drawn through the data points suggests a value of 'apparent density' for the scale of 3.6 gcm^{-3}. Assuming that the scale is solely chromia, this value is somewhat lower than the standard density for massive chromia of 5.22 gcm^{-3} [5], and could be taken to indicate that the thermally-grown scale was approximately 31% porous.

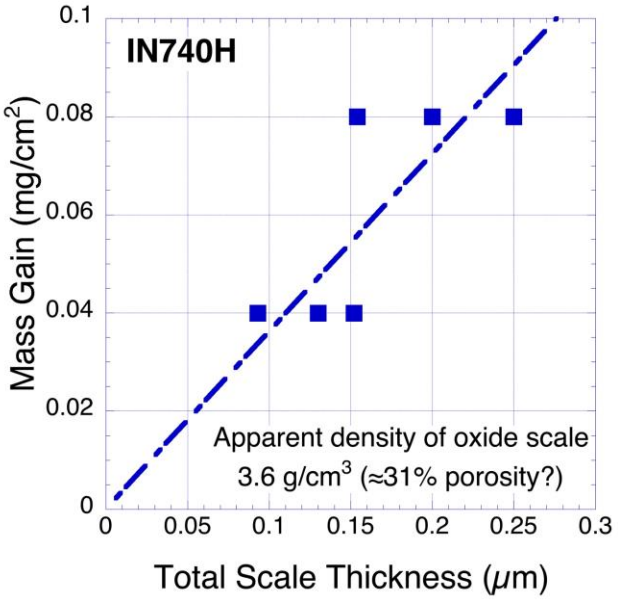

Figure 2.3.6-22 – Mass gain-scale thickness plot for IN740H after exposure at 700°C for up to 5,000h in CO_2 containing 3.6 vol.% O_2 and 5.3 vol.% H_2O and 200 bar.

'Apparent densities' derived similarly for alloys Grade 91 and TP304H were 1.7 gcm^{-3} (68% porosity), and 2.1 gcm^{-3} (59% porosity), respectively. The apparent porosity derived by this approach for Grade 91 appears to be excessively high compared to the 30% porosity obtained for alloy T92 oxidized in steam at 650°C [6]. While measurements of mass gain typically are readily made with high precision, spallation and loss of small amounts of scale during testing and by handling can result in underestimation of the total mass of scale formed, hence in reduced 'apparent densities.'

Nevertheless, the measured mass gains for all three alloys were converted using these apparent density values to scale thicknesses that then were used to augment the actually-measured thicknesses for the purpose of generating values of parabolic rate constants; those plots are shown in Figure 2.3.6-23. Scale thickness-based parabolic rate constants derived from the slopes of the curves are listed in Table 2.3.6-6.

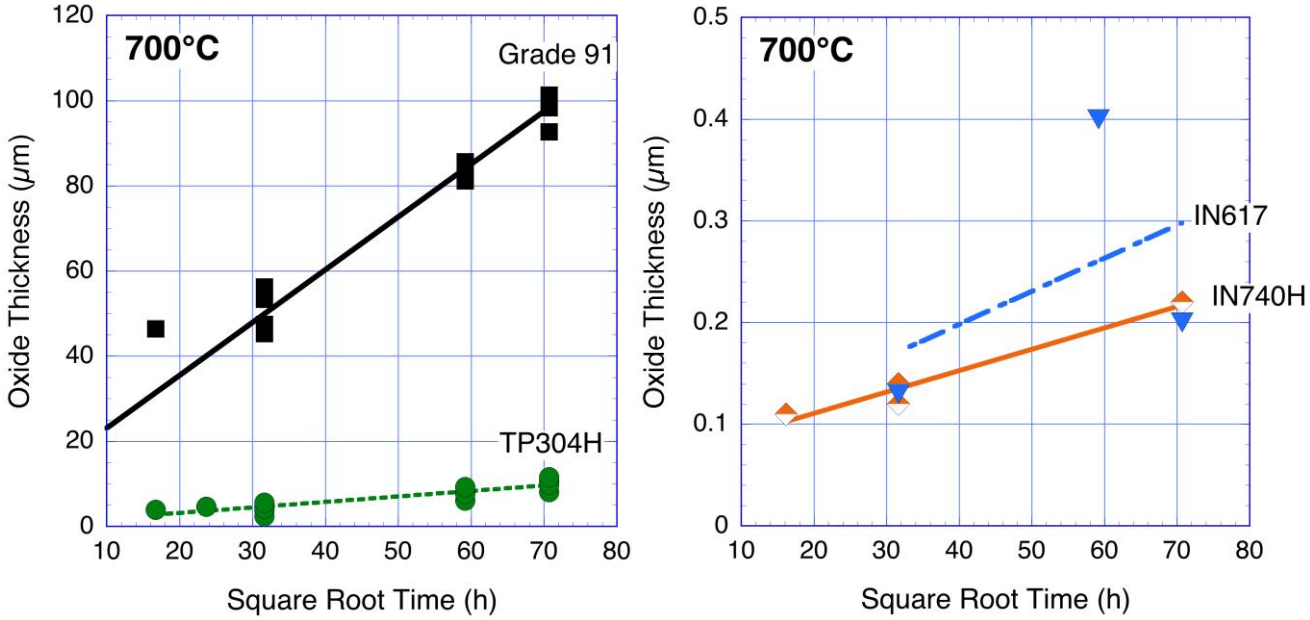

Figure 2.3.6-23 – Parabolic plots for alloys after exposure at 700°C for 5,000h in CO_2 containing 3.6 vol.% O_2 and 5.3 vol.% H_2O at 200 bar.

Table 2.3.6-6
Total scale thickness-based parabolic rate constants for alloys exposed at 700°C for up to 5,000h in CO_2 containing 3.6 vol.% O_2 and 5.3 vol.% H_2O at 200 bar.

Alloy	k_p, μm²/h	R^2
Grade 91	6.3×10^{-1}	0.96
TP304H	6.7×10^{-3}	0.71
IN617	5.3×10^{-6}	0.22
IN740H	2.2×10^{-6}	0.96

2.3.7 — Perform Model Validation Test

This overall project was based on the assumption that the EPRI-ORNL Scale Exfoliation Model [7-9] could, given the availability of relevant input parameters, directly be translated for use in calculations related to heat exchangers handling sCO_2. That modeling approach initially was developed to generate information on scale growth, failure, and extent of scale loss by exfoliation under the conditions prevailing inside superheater tubes in steam boilers. It was recognized that these assumptions would be challenged as actual kinetics data and scale characterization results accumulated from measurements in this and other on-going research on oxidation behavior in sCO_2. It is pertinent to revisit those assumptions in light of new sCO_2 oxidation kinetics and morphological data generated in this program.

Basically, the model requires two main forms of input from oxidation studies:

1. **Oxidation rates** as a function of oxide thickness (d_{ox}) vs time (t) and temperature (T). These are most usefully expressed as an algorithm:

$$d_{ox}^2 = 2.k_{pt}.t$$

where the parabolic oxidation rate constant, $k_{pt} = A_A e^{-Qt/RT}$, A_A is a constant, and Q_t is the activation energy for the oxidation process. The required parameters are readily obtained from measurements of oxide scale thickness as a function of time and temperature: k_{pt} is the slope of a plot of d_{ox} vs $\sqrt{t}$ at a given T, and Q_t can be obtained simply from the slope of a plot of $\ln k_{pt} = \ln A_A - Q_t/RT$.

2. **Morphological data,** which are needed to infer modes of scale growth and failure.

The current model is based on scale morphologies formed in steam, hence the importance of understanding similarities and differences in sCO_2 and steam.

From these requirements it can be seen that mass-based oxidation data are of limited value, even though the bulk of reported oxidation kinetics data is reported as mass gain, and such measurements usually are very accurate. Nevertheless, mass gain data are very useful for providing comparisons with available results from other sources and for examining trends.

A further issue is that for alloys that form very protective (thin) scales, adequate characterization is problematic. In addition, a potential alternative strategy for generating oxide thickness values from mass gains is fraught with uncertainties, especially where the scale involved is not homogeneous or involves layers of different oxides, and not the least because thermally-grown scales usually contain varying and unknown levels of porosity.

2.3.7.A - Relevant Available Information

Based on observations of similarities between the oxide scale morphologies formed on several classes of alloys after exposure in high-pressure (HP) steam and in sCO_2 (discussed in Task 2.4), the extensive available data on oxidation behavior in HP steam can be viewed as a viable starting point for sCO_2 considerations until confirmed or modified as actual data become available. However, there are two areas in particular where it is recognized that assumptions of similarities between oxidation behavior in sCO_2 and HP steam, and between the operation of steam boilers and sCO_2 recuperators, likely will need to be revisited:

a) There is a theoretical expectation as well as historical inferences (and recent discussion) of the participation of C in determining the morphologies of scales formed in sCO_2 [10-13], hence possibly affecting growth kinetics and mode of eventual scale breakdown.

b) Some prototype recuperators associated with proposed power plants based on sCO_2 as the working fluid incorporate novel designs that employ flow passages that are significantly narrower than, for instance, 25 mm OD x 5 mm wall (1 in OD x 0.2 in wall) tubing typically used in power plants based on steam. This feature introduces additional concerns related to effects of scale thickening on reduction in the cross sectional area of flow passages, hence on pressure drops through the heat exchanger. In addition, designs featuring balanced pressure across the

heat transfer boundaries allow the use of very thin walls. Because of the importance of maintaining a certain concentration of Cr in the alloy to ensure the ability to form a protective oxide layer, the reduced total amount of Cr available in thin cross sections raises the concern that, where very high temperatures are involved, the increased rate of oxidation and consumption of this finite Cr reservoir could lead to shorter service lives.

2.3.7.B - New Information

In the following, new data generated in this project for oxidation in sCO_2, together with data from other sources where appropriate, are evaluated and used to derive the oxidation algorithms required by the model. In addition, pertinent similarities and differences among scales grown in sCO_2 and HP steam are evaluated in light of possible modifications to the model.

2.3.7.B.1 - Mass-Based Data

The mass gain data reported in Sections 2.3.3 and 2.3.4 as parabolic plots are combined in Table 2.3.7-1, and plotted on Arrhenius coordinates in Figure 2.3.7-1 to allow determination of the activation energies. Note that two alloys exhibited negative parabolic rates: HR3C at 700°C, and IN740H at 650 and 750°C, precluding determination of values for Q_m. Single data points for alloys IN625 and HA230 from measurements at 700°C also are included, and can be seen to have values very similar to that for IN740H. Mass-based activation energies, Q_m, derived from the slopes of the plots are listed in Table 2.3.7-2.

While the rate of scale growth on Grade 91 ferritic steel (8.39 wt% Cr) was, as expected, considerably faster than on austenitic steel TP304H (18.4 wt% Cr) at 650-750°C, extrapolation to lower temperatures indicated that the oxidation rates would be similar at 600°C. Also surprising was the finding that the actual values of k_{pm} for VM12 (11.2 wt% Cr) were similar or faster than for Grade 91 at 650-700°C; however, the overall temperature-dependence of the oxidation rate was lower, suggesting lower oxidation rates >710°C for VM12 (significantly above the recommended application temperatures for both alloys).

The oxidation behavior of Crofer 22H (22.7 wt% Cr) also was unexpected. This ferritic steel was designed to form a protective chromia scale in oxidizing environments, which should result in oxidation rates slower than TP304H in this temperature range. Although the actual mass gains measured for Crofer 22H were higher than for TP304H at all three temperatures, the temperature dependence of the rates for Crofer 22H was lower. The observation that this alloy exhibited a similar or faster rate of mass gain at 650°C as the lower-Cr ferritics was particularly surprising, given that the temperature-dependence of the diffusion rate of Cr in all three alloys would be expected to be similar.

Table 2.3.7-1
Summary of mass-based parabolic rate constants (k_{pm}) for exposure to CO_2 containing 3.6 vol.% O_2 and 5.3 vol.% H_2O at 200 bar at 650-750°C.

Alloy	650°C		700°C		750°C	
	k_{pm} ($g^2cm^{-4}s^{-1}$)	R^2	k_{pm} ($g^2cm^{-4}s^{-1}$)	R^2	k_{pm} ($g^2cm^{-4}s^{-1}$)	R^2
Grade 91	7.20×10^{-14}	0.99	2.82×10^{-12}	0.97	7.85×10^{-12}	0.84
VM12	3.46×10^{-13}	0.84	2.82×10^{-12}	0.96	3.80E x 10^{-12}	0.87
Crofer 22	5.61×10^{-13}	0.97	4.36E x 10^{-13}	0.99	1.59E x 10^{-12}	0.99
TP304H	3.87×10^{-14}	0.98	9.64×10^{-14}	0.92	2.18E x 10^{-13}	0.84
TP347H			5.17×10^{-13}	0.97		
HR3C	4.04×10^{-15}	0.99	-(3.04E x 10^{-}	0.35	5.96E x 10^{-15}	0.71
IN617	NA		NA		NA	
IN740H	-(7.76×10^{-17})	0.13	1.34E x 10^{-16}	0.91	-(2.15E x 10^{-15})	0.71
IN625			3.92E x 10^{-16}	0.93		
HA230			1.19×10^{-16}	0.67		

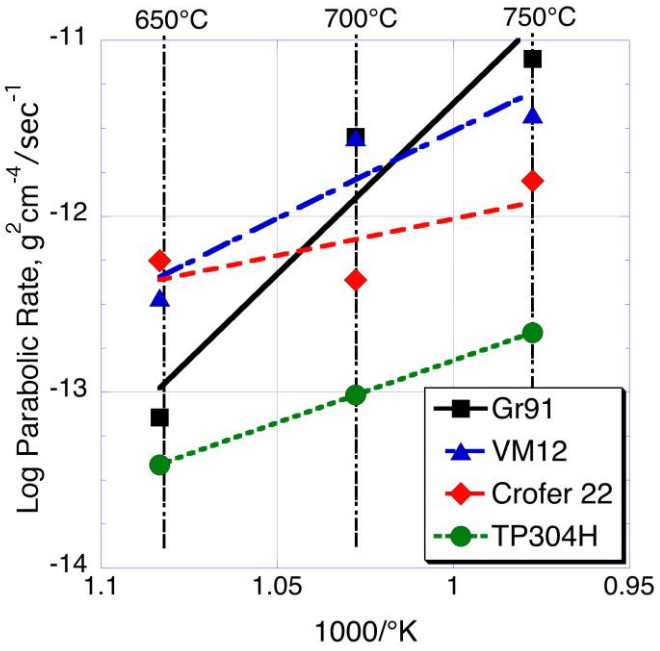

Figure 2.3.7-1 – Arrhenius plot for mass-based oxidation kinetics measured for the candidate alloys after exposure at 650-750°C to CO_2 containing 3.6 vol.% O_2 and 5.3 vol.% H_2O at 200 bar.

Table 2.3.7-2
Activation energies from mass-based oxidation kinetics for exposure at 650-750°C to CO_2 containing 3.6 vol.% O_2 and 5.3 vol.% H_2O at 200 bar.

Alloy	A_{Am} ($g^2cm^{-4}s^{-1}$)	Q_m ($kJmole^{-1}$)	R^2
Grade 91	1.12×10^{8}	-372	0.92
VM12	2.67×10^{-2}	-190	0.86
Crofer 22	1.39×10^{-8}	-80	0.55
TP304H	1.87×10^{-6}	-136	1.00
HR3C*	2.14×10^{-13}	-30	1
IN740H	NA	NA	
IN617	NA	NA	

* two data points only, at 650 and 750°C.

2.3.7.B.2 - Scale Thickness-Based Data

Table 2.3.7-3 summarizes thickness-based parabolic oxidation rate constants (k_{pt}) reported in Sections 2.3.5 and 2.3.6. The values for the ferritic steels and TP304H are plotted on Arrhenius coordinates in Figure 2.3.7-2, and the activation energies determined from the slopes of the curves are listed in Table 2.3.7-4. The inability to measure accurately the thin scales formed on the high-temperature alloys until late in this project (after considerable research) resulted in the calculation of k_{pt} values at 700°C only, which are insufficient to provide activation energies. Hence the need to consider other sources.

Table 2.3.7-3
Summary of thickness-based parabolic rate constants (k_{pt}) for exposure at 650-750°C in CO_2 containing 3.6 vol.% O_2 and 5.3 vol.% H_2O at 200 bar.

Alloy	650°C		700°C		750°C	
	k_{pt} (μm^2h^{-1})	R^2	k_{pt} (μm^2h^{-1})	R^2	k_{pt} (μm^2h^{-1})	R^2
Grade 91	9.8×10^{-3}	0.99	6.3×10^{-1}	0.96	1.1	0.78
VM12	2.8×10^{-2}	0.99	$-(2.9 \times 10^{-2})$	0.88	2.2×10^{-1}	0.90
Crofer 22	1.9×10^{-1}	0.97	7.7×10^{-3}	0.63	2.3×10^{-1}	0.99
TP304H	3.3×10^{-3}	0.99	6.7×10^{-3}	0.71	2.2×10^{-2}	0.89
HR3C*	NA		NA		NA	
IN617	NA		5.3×10^{-6}	0.22	NA	
IN740H	NA		2.2×10^{-6}	0.96	NA	

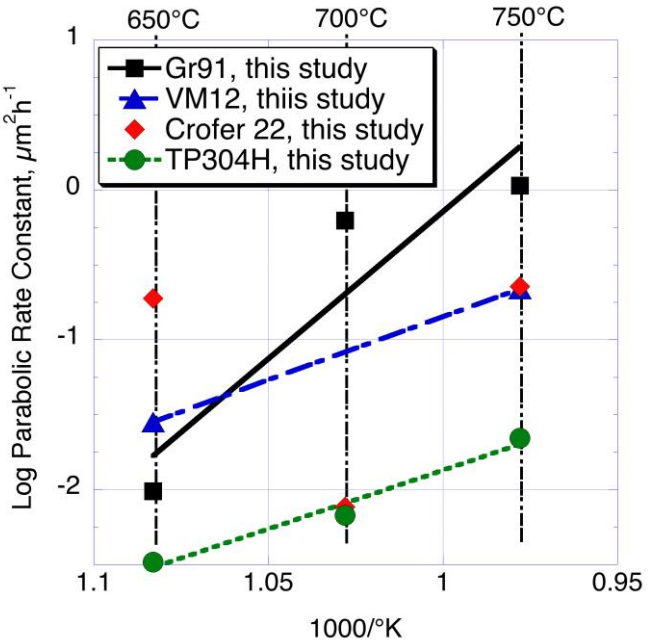

Figure 2.3.7-2 – Arrhenius plots for scale thickness-based kinetics measured for the candidate alloys after exposure at 650-750°C.to CO_2 containing 3.6 vol.% O_2 and 5.3 vol.% H_2O at 200 bar.

Table 2.3.7-4
Activation energies from scale thickness-based kinetics for exposure at 650-750°C to CO_2 containing 3.6 vol.% O_2 and 5.3 vol.% H_2O at 200 bar.

Alloy	A_{At} (μm²/h)	Q_t (kJ/mole)	R^2
Grade 91	2.8×10^{19}	-376	0.88
VM12	4.1×10^{7}	-162	1*
Crofer 22		NA	
TP304H	1.1×10^{6}	-151	1.00
HR3C		NA	
IN740H		NA	
IN617		NA	

*Two data points only, at 650 and 750°C.

2.3.7.B.3 - Alternative Data From Other Sources

In the absence of data from this work from which the required oxidation algorithms for high-temperature alloys such as IN740H could be calculated, results from other studies were examined. The most consistent results for *mass-based* oxidation kinetics in CO_2 were considered to be those of Brese et al [14] for IN740H exposed in industrial grade purity CO_2 at 1 bar (tests run in 10-h cycles). These are compared in Table 2.3.7-5 with those for alloys IN740, PMCr, and 310HCbN exposed in steam at 17 bar (tests run in 500h cycles) [4]. Upon oxidation in steam the latter two alloys formed a scale consisting of a single layer of chromium oxide with minimal internal oxide penetrations into the alloy, especially for

PMCr (Cr-4 wt% Fe). Arrhenius constants calculated from these kinetic data are compared in Table 2.3.7-6, which indicates a good match between those from Brese et al. and those for IN740 and 310HCbN in 17 bar steam. As a result, it is recommended that an oxidation algorithm based on the IN740 steam data (which cover a larger temperature range than the Brese data) be used in the model for calculations involving mass gain of alloy IN740H.

Table 2.3.7-5
Comparison of mass-based parabolic rate constants for chromia-forming alloys in sCO_2 and HP steam.

Temperature °C	k_{pm}, g^2/cm^4s				
	sCO_2	CO_2, 1 bar[C]	Steam, 17 bar[D]	Steam, 17 bar[E]	Steam, 17 bar[F]
650	4.0×10^{-15} (A)		2.8×10^{-16}	1.2×10^{-15}	8.0×10^{-16}
700	2.2×10^{-16} (B)	7.4×10^{-16}	1.2×10^{-15}	2.0×10^{-15}	3.0×10^{-15}
750	6.0×10^{-15} (A)	4.9×10^{-15}	5.9×10^{-15}	1.2×10^{-14}	3.5×10^{-15}
800		3.0×10^{-14}	4.5×10^{-14}	1.7×10^{-14}	3.3×10^{-15}

A: This work: data for HR3C.
B: This work: average for alloys IN740H, IN625, and HA230.
C: Data for IN740H [14].
D: Data for IN740 [4].
E: Data for PMCr [4].
F: Data for 310HCbN [4].

Table 2.3.7-6
Recommended mass gain-based Arrhenius constants for chromia-forming alloys.

Alloy	Environment	T Range (°C)	A_{Am} (g^2/cm^4s)	Q_m (kJ/mole)	Sources
IN740H	CO_2 at 1 bar	700-800	8.45×10^{2}	-340	[14]
IN740	Steam at 17 bar	600-800	3.2×10^{-3}	-229	[4]
PMCr	Steam at 17 bar	600-800	6.1×10^{-4}	-213	[4]
310HCbN	Steam at 17 bar	600-800	6.0×10^{3}	-338	[4]

Since no consistent results were found for scale thickness-based oxidation kinetics in CO_2 for high-temperature alloys such as IN740H, resort again was made to comparisons with results from HP steam. The sole thickness-based parabolic rate constant derived for IN740H from this work is compared in Table 2.3.7-7 with data for alloys IN740, PMCr, and 310HCbN oxidized in steam at 17 bar. The indicated slower scale growth rate at 700°C in sCO_2 may be associated with differences between the measurement techniques used, especially difficulties associated with optical microscopy (employed for the steam data) for examining such thin scales. Nevertheless, given such caveats concerning the measurement difficulties with these very thin scales, it is recommended that the oxidation algorithm based on the IN740 steam data, listed in Table 2.3.7-8, be used in the model for calculations involving scale thicknesses on alloy IN740H.

Table 2.3.7-7
Comparison of thickness-based parabolic rate constants for chromia-forming alloys in sCO_2 and HP steam

Temperature °C	k_{pt}, µm²/h			
	sCO_2	HP steam[B]	HP steam[C]	HP steam[D]
650	NA	6.2×10^{-5}	9.5×10^{-3}	9.8×10^{-5}
700	2.2×10^{-6} (A)	1.4×10^{-4}	7.4×10^{-3}	2.0×10^{-4}
750	NA	3.5×10^{-4}	NA	5.1×10^{-4}
800	NA	1.4×10^{-3}	1.8×10^{-1}	6.8×10^{-4}

A: This work, data for IN740H.
B: IN740 in 17 bar steam [4].
C: PMCr in 17 bar steam [4].
D: 310HCbN in 17 bar steam [4].

Table 2.3.7-8
Recommended thickness-based Arrhenius constants for chromia-forming alloys

Environment	T Range (°C)	A_{At} (µm²/h)	Q_t (kJ/mole)	Source
sCO_2	650-750	NA	NA	This work
HP Steam[A]	650-800	1.4×10^5	-166	[4]
HP Steam[B]	650-800	2.3×10^2	-112	[4]

A: Data for IN740.
B: Data for 310HCbN.

2.3.8 - References Cited in Section 2.3

1. I.G. Wright and R.B. Dooley, "Morphologies of oxide growth and exfoliation in superheater and reheater tubing of steam boilers," *Materials at High Temperatures*, 28 (10), 40-57 (2011).
2. R.D. Springer, Z. Wang, A. Anderko, P. Wang, A.R. Felmy, "A thermodynamic model for predicting mineral reactivity in supercritical carbon dioxide: I. Phase behavior of carbon dioxide–water–chloride salt systems across the H_2O-rich to the CO_2-rich regions", *Chemical Geology*, 322-323, 151-171 (2012).
3. S. Takenouchi, and G.C. Kennedy, "The binary system H_2O–CO_2 at high temperatures and pressures," *American Journal of Science*, 262, 1055-1074 (1964).
4. I.G. Wright, DOE FWP No. FEAA061: *Oxidation of Candidate Alloys in Steam at 17 bar—Final Report on Phase 1 Efforts in Support of the U.S. Consortium Program on Boiler Materials for Ultra-Supercritical Coal Power Plants*, ORNL/TM-2009/232, Nov 2009.
5. *CRC Handbook of Chemistry and Physics*, 98th Edition, J.R. Rumble, Editor in Chief, CRC Press (2017).
6. R. Knodler and P.J. Ennis, "Oxidation of high-strength ferritic steels in steam at 650°C," pp. 355-364 in Vol. 1 of *Proc. Baltica V Conference 2001: Condition Assessment of Power Plant*, June 6-8, 2001, Porvoo, Finland.
7. A.S. Sabau, I.G. Wright, and J.P. Shingledecker, "Oxide scale exfoliation and regrowth in TP347H superheater tubes," *Materials and Corrosion*, 63 (10), 896-908 (2012).
8. J.P. Shingledecker, A.T. Fry, and I.G. Wright, "Managing steam-side oxidation and exfoliation in USC boiler tubes," *Advanced Materials and Processes*, 171, (1) pp. (2013).
9. A.S. Sabau, I.G. Wright, J.P. Shingledecker, and P.F. Tortorelli, "Managing oxide scale exfoliation In boilers with TP347h superheater tubes," *Proc. 7th International Conference on Advances in Materials Technology for Fossil Power Plants*, Waikoloa, Hawaii. EPRI 2014.
10. *Proc. International Conference on Corrosion of Steels in CO_2*, D.R. Holmes, Ed., British Nuclear Energy Society, Reading University (1974).
11. P.L. Harrison, R.B. Dooley, S.K. Lister, D.B. Meadowcroft, P.J. Nolan, R.E. Pendlebury, P.L. Surman, and M.R. Wootton, "The oxidation of 9Cr-1Mo steels in carbon dioxide--a discussion of possible mechanisms," Paper No. 18 in *Proc. B.N.E.S. Intl. Conf. on Corrosion of Steels in CO_2* (1974).
12. G.B. Gibbs, R.E. Pendlebury and M.R. Wootton, "Protective and breakaway corrosion of mild steel in CO_2," Paper No. 6 in *Proc. B.N.E.S. Intl. Conf. on Corrosion of Steels in CO_2* (1974).
13. Y. Gong, D.J. Young, P. Kontis, Y.L. Chiu, H. Larsson, A. Shin, J.M. Pearson, M.P. Moody, and R.C. Reed, "On the breakaway oxidation of Fe-9Cr-1Mo steel in high-pressure CO_2," *Act Met*., 130, 361-374 (2017).
14. R.G. Brese, J.R. Keiser, and B.A. Pint, "Effect of thermal cycling on compatibility in CO_2 for concentrated solar power applications," *Oxidation of Metals*, 87, 631-642 (2017).

2.4: Evaluation of Available Oxidation Kinetics & Comparison with Exposures in Steam

One of the assumptions made at the outset of this project was that, based on preliminary observations of similarities between the oxide kinetics and scale morphologies formed on several classes of alloys after exposure in high-pressure (HP) steam and in sCO_2, the extensive available data on oxidation behavior in HP steam could be viewed as a viable starting point for evaluating oxidation behavior in sCO_2.

2.4.1 — Evaluation of Oxidation Kinetics

Research projects that have generated corrosion kinetics data for structural alloys in CO_2-based environments and the test conditions used are summarized in Table 2.4.1-1. These research efforts span the past 47 years, and initially were in support of commercial gas-cooled nuclear reactors. More recently, the focus has been on simulating conditions expected for supercritical CO_2 (sCO_2) closed cycles applied to nuclear heat and concentrated solar power. Essentially all the data were generated from laboratory tests.

Table 2.4.1-1
Summary of sCO_2 Test Conditions Reported.

Reference	CO_2	Impurities				T (°C)	P (bar)	t (kh)
		CO	H_2	H_2O	O_2			
[1] Roman 2013	99.9998					450-650	200	0.2-1.0
[2] Furukawa 2010	99.995			15ppm*		400-600	200	1.99
[3] Holmes 1974	Bal	1.5v/o		5ppm		500	28.5	0.5-8.4
[4] Pritchard 1974	Bal			8-1000ppm		550	1, 40	0.5-9.0
[5] Rouillard 2010	Bal			6ppm		550	250	0.3
[6] Saari 2014	RG					550-700	150-250	0.25-1.5
[7] Mahaffey 2014	RG			<3-33 ppm		550-650	200	0.2-1.0
[8] Lee 2014	99.999					550-650	200	1.00
[9] Lee 2015	99.999					550-650	200	3.00
[10] Lim 2008	RG					650	120-220	0.2-1.0
[11] Garrett 1974	Bal	2v/o	10v/o	300ppm		650	41.4	0.5-5.0
[12] Pint 2014	Bal	**		±10v/o		650-750	1, 200	0.5
[13] Board 1969	Bal	1v/o		200ppm		650-700	28, 41	0.5-5.0
[14] Antill 1974	Bal			8ppm-3v/o		660	1-40.5	4.00
[15] Mahaffey 2016	RG				±100 ppm	650-750	20	1
[16] Hayashi 2014	>99.5			<0.012v/o	0.6-3v/o	700	1	0.1
[17] This Study	Bal			5.3 v/o	3.6 v/o	700	200	3
[18] Pint 2017	CG					700-800	1-300	4
[19] Brese 2017	CG					700-800	1	1.5

RG = research grade purity

CG = commercial grade purity

*max

**±0.15v/o O_2

Pertinent corrosion data are summarized in the following figures. Since there was little consistency among the test conditions used, Larson-Miller plots are employed as a convenient way of simply comparing the data sets and assessing relative trends. The original reporting of the corrosion data shown was in terms of mass gain and since, as discussed earlier [17] there is no accepted analytical procedure for converting corrosion rates expressed in mass change to scale thickness (or loss of metal thickness), the corrosion rates are expressed in mass gain in these diagrams. No loss of scale by exfoliation was assumed.

Separate figures are used for each group of alloys, and in each figure the legend indicates the source of the data shown for each data set, as well as the test pressure (in bar) and whether the gas was dry (d) or contained specifically-added impurities. For example, a legend of Gr91 (250d) indicates data for Grade 91 ferritic steel exposed to dry CO_2 at 250 bar. The gas purity/impurity level otherwise is not stated (but mostly is available and typically is summarized in Table 2.4.1-1 for each data source). Each Figure has flags to indicate values of the Larson-Miller parameter *P* that correspond to 10^5h at specific temperatures, as a means of facilitating comparison among the data sets for a given alloy, and among alloys. Alloy compositions (where given) are listed in Tables 2.4.1-2 - 2.4.1-6.

Table 2.4.1-2
Compositions of Ferritic Steels Studied.

Alloy	Composition (wt%)								Ref
	Ni	Cr	Si	S	Mn	Mo	C	Other	
T91	0.1	8.3	0.1	—	0.3	1	—		[12]
T91	0.13	8.39	0.24	0.001	0.44	0.93	0.08	0.09Cu; 0.06Nb; 0.18V	[17]
STBA26	—	8.6	0.45	0.003	0.42	0.93	0.12	0.013P	[16]
9Cr-1Mo	0.23	8.63	0.31	0.006	0.43	0.95	0.1	0.046Cu; 0.09Nb; 0.21V	[5]
NF616	0.17	8.82	0.10	—	0.45	0.46	0.11	0.19V; 1.87W	[1]
SAVE12	0.3	9.6	0.1	—	0.4	—	—	3W; 2.6Co	[12,20]
T122	0.35	10.58	0.12	<0.001	0.67	0.36	0.11	0.83Cu; 0.04Nb; 0.22V; 1.9W	[20]
HCM12A	0.39	10.83	0.27	—	0.64	0.30	0.11	1.02Cu; 1.89W; 0.19V	[1]
12Cr	0.39	10.87	0.26	0.002	0.64	0.31	—	1.03Cu; 0.2V; 1.86W	[2]
VM12	0.36	11.2	0.41	0.001	0.39	0.36	0.12	0.08Cu; 0.03Nb; 0.2V; 1.6W; 1.47Co	[17]
TP410	0.1	11.8	0.4	—	0.5	0.5	—		[12,20]
Crofer 22H	0.26	22.71	0.29	0.002	0.43	0.01	0.004	0.5Nb; 1.9W; 0.06La	[17]
EBrite	0.1	25.8	0.2	—	—	1	—	0.1V	[12]

Table 2.4.1-3
Compositions of Austenitic Steels Studied.

Alloy	Composition (wt%)								Ref
	Ni	Cr	Si	S	Mn	Mo	C	Other	
TP304H	8.13	18.42	0.48	0.002	1.8	0.22	0.043	0.18Cu; 0.22Co	[17]
TP316	13.1	17.2	0.60	0.011	1.59	2.69	0.04	<0.01Nb; <0.02Ti; 0.014P	[13]
TP316FR	11.2	16.9	0.59	0.003	0.84	2.23	0.01	0.08V; 0.06Co	[2]
TP316L	12.0	17.0	1.0		2.0	2.0	0.02		[12]
TP316L	11.1	17.4	0.63	0.001	1.39	2.05	0.02	0.22Co	[5]
TP347	13.3	17.5	0.24	0.017	1.35	0.36	0.04	0.86Nb; 0.10Ti; 0.017P	[13]
TP347	9.53	17.9	0.8	—	1.7	0.4	0.06	0.7Nb; 0.4Cu	[7]
TP347HFG	11.8	18.6	0.4	—	1.5	0.2	—	0.2Co	[12,20]
IN800	30.9	19.95	0.39	0.004	0.71	—	0.04	0.34Al; 0.46Ti; 0.08Cu	[5]
IN800H	33.2	19.6	0.29	—	0.77	—	0.06	0.46Al; 0.53Ti; 0.2Cu	[1,7]
SAVE25	20.0	22.3	0.20	—	0.66	0.12	0.07	1w; 0.19Co	[20]
NF709	25.0	22.3	0.42	—	1.02	1.46	0.02	0.04Ti	[20]
HR120	37.6	24.7	0.24	—	0.73	0.28	0.06	0.5W; 0.09Al	[20]
HR3C	19.9	25.1	0.4	0.001	1.19	0.1	0.066	0.44Nb; 0.238N	[17]
310HCbN	20.3	25.5	0.31	—	1.22	0.1	0.05	0.4Nb; 0.27N; 0.34Co; 0.07Cu	[20]

Table 2.4.1-4
Compositions of Wrought, Chromia-Forming Ni-Base Alloys Studied.

Alloy	Composition (wt%)								Ref
	Ni	Cr	Al	Ti	Nb	Mo	C	Other	
IN718	52.5	19	0.5	0.9	5.1	3	0.08	18.5Fe; Cu	[6]
HR282	58	19.3	1.5	2.2	—	8.3	—	10.3Co	[12]
IN625	61	21.5	0.2	0.2	3.6	9	0.05	2.5Fe	[6]
HA617	53.3	22.19	1.13	0.35	0.06	9.5	0.09	1.55Fe; 11.44Co; 0.13W	[17]
CCA617	55.9	21.6	1.3	0.4	—	8.6	0.05	11.3Co; 0.63Fe; 0.09W	[12,20]
HR230	60.1	21.9	0.33	<0.01	0.02	1.15	0.09	14.1W; 1.21 Fe	[20]
HR230	60.5	22.6	0.3	—	—	1.4	—	12.3W	[12]
IN740	48.2	23.4	0.8	2.0	2.1	—	—	20.2Co	[6,16]
IN740H	50.0	24.53	1.33	1.36	1.49	0.32	0.024	0.12Fe; 20.28Co; 0.02Zr	[17]

Table 2.4.1-5
Compositions of Cast, Alumina-Forming Ni-Base Alloys Studied

Alloy	Composition (wt%)							Ref
	Ni	Cr	Al	Ti	Nb	Mo	Other	
IN713LC	74.2	12.1	6.2	0.7	2.1	4.5	0.0Zr	[12]
CM247	59.5	8.5	5.7	1.0	—	0.7	9.8Co; 9.9W; 3.1Ta; 1.4Hf	[12]
PWA1483	60.6	12.0	3.4	4.0	—	1.9	4.1W; 5.2Ta	[12]
Nim105	53.0	15.5	4.9	1.4	—	4.7	19Co; 0.1Zr	[12]
IN738	61.5	16	3.4	3.4	2	1.75	08.5Co; Zr; B; W	[6]

Table 2.4.1-6
Compositions of Specialty Alumina-Forming Alloys Studied.

Alloy	Composition (wt%)								Ref
	Fe	Ni	Cr	Al	Ti	Nb	Mo	Other	
PM2000	74.1	0.02	19.1	5.5	0.5	—	—	0.4Y; 0.25O	[12]
APMT	69.2	0.2	21.1	5.0	—	—	2.8	0.3Y; 0.2Hf; 0.1Zr	[12]
HR214	3.5	75.9	15.8	4.3	—	—	—	0.02Zr	[12]

2.4.1.A - Oxidation of 9-12Cr Ferritic Steels

These alloys are of interest for application in sCO_2 up to temperatures determined by their rate of oxide growth, rather than the strength-based temperature limit recommended in Section 1 of the ASME Boiler and Pressure Vessel Code [21]. Based on experience of the scale growth and failure behavior of Grade 91 steel in steam boilers, EPRI recently recommended that in high heat-flux applications (such as conventional superheater tubing) the temperature limit should be reduced to 560-580°C (compared to the ASME Code limit of 650°C) [22]. For applications with a relatively small temperature differential across the heat exchanger wall (such as heat-recovery steam generators and some locations in sCO_2 recuperators) the recommended limit is raised to 580-600°C.

Figure 2.4.1-1 compares data sets for ferritic steels. The figure illustrates considerable scatter among recent studies for 'advanced' 9Cr steels [4,11,12,13,16,23]. Nevertheless, a majority of the data points provides a reasonable trend line for alloys T91 and STBA26 in sCO_2 containing oxidizing impurities. Comparison with corrosion measurements for T91 and T92 in 17 bar steam [20]) suggests higher mass gains (greater scale thicknesses?) than in sCO_2, especially at lower values of the L-M Parameter *P*. Nevertheless, the mass gains for sCO_2 and steam are reasonably similar at conditions for which *P* = 21-22, and this leads to an expectation that the scale morphologies formed in sCO_2 for those conditions would be similar to those formed in steam.

Systematic data for 9Cr ferritic steels from the earlier studies in support of sCO_2-cooled nuclear reactors [4] indicated that Increasing alloy Si content had the largest effect on decreasing the oxidation rate in both dry and impure sCO_2. Optimization of Si content as well as Cr and S contents resulted in reduction of overall oxidation rates by an order of magnitude or more.

Data for the higher-Cr ferritic steels are compared in Figure 2.4.1-2. The data points for the 12Cr steels (for instance, NF616, SAVE12, HMC12A) in dry sCO_2 appear to be consistent. Surprisingly, the trend line for these data suggests faster corrosion rates than those for the 9Cr alloys up to 10^5h at 550°C. The high-Cr ferritics TP410 and MA957, which are capable of forming more protective (chromia) scales, showed unusual apparent trends of decreasing mass gains with increasing values of *P* in dry sCO_2. This trend may reflect an increasing ability to form chromia scales at higher temperatures due to faster diffusion rates; the smallest mass gains reported for these alloys approach those reported for Ebrite (24 wt% Cr), which is a strong chromia former.

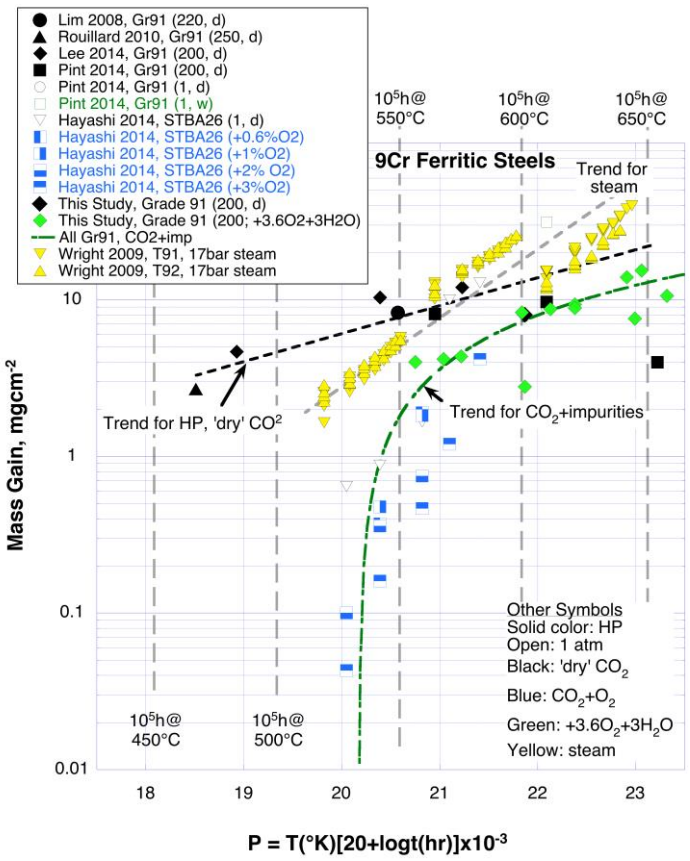

Figure 2.4.1-1 - Compilation of available corrosion data for ferritic steels in CO_2 from recent studies, compared to corrosion in 17 bar steam (green data points [20]).

The data points for corrosion of alloys T122, SAVE12 and TP410 in 17 bar steam (yellow symbols) included for comparison in Figure 2.4.1-2 show trends that appear consistent with that suggested for these alloys in dry sCO_2, but indicate mass gains that are possibly two orders of magnitude lower than those for the 12Cr steels in dry sCO_2. The apparent ranking in terms of decreasing corrosion rate for the nominally 12Cr alloys in 17 bar steam corresponds roughly with increasing Cr content:

SAVE12 (9.6Cr-0.08 Si<10 ppm S) > *T122* (10.6 Cr-0.12 Si<10 ppm S) ≈ *TP410* (12Cr-1Si-300 ppm S)

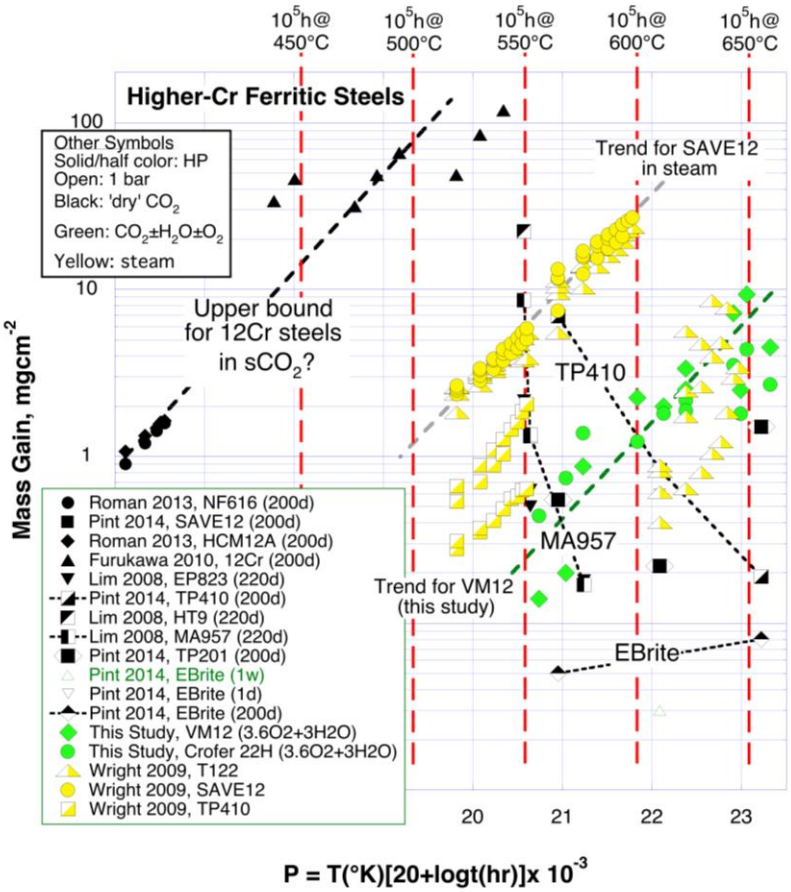

Figure 2.4.1-2 – Compilation of available corrosion data for high-Cr ferritic steels in CO_2.

Data points from this project [17] for alloys VM12 (11 wt% Cr) and Crofer22 (23 wt% Cr) exposed in sCO_2 containing 3.6 vol% O_2 and 5.3 vol% H_2O at 700°C and 200 bar indicate corrosion rates similar to the 10.6 wt% alloy (T122) in 17 bar steam. A point of considerable importance is that for this class of alloys contributions from minor alloying additions (such as Si and S) can be very significant, so that knowledge of the actual composition of the samples used is crucial. Further, any reduction in availability of Cr in the alloy surface to participate in the scale-forming process (possibly by being tied up as carbides) could significantly alter the morphology of the scale formed, and oxidation kinetics.

2.4.1.B - Oxidation of Austenitic Steels

Figure 2.4.1-3 compares the corrosion data of various austenitic steels in 'dry' and 'impure' sCO_2. The results for the standard austenitic steels (TP304H, 321, 347) in Figure 2.4.1-3(a) show considerable scatter; the dashed line suggests a possible upper bound in 'dry' sCO_2. The influence of water vapor impurities on TP321 appeared to be inconclusive, but shot peening was beneficial for this alloy.

Data for the 'oxidation-resistant' austenitic steels TP347HFG and TP310/HR3C in CO_2 are relatively sparse, as shown in Figure 2.4.1-3(b). Nevertheless, the upper bound line in 'dry' sCO_2 for these alloys

suggests a considerable reduction in mass gain compared to the 'standard' austenitics. For TP310 there appears to be an accelerating effect on mass gain of 300 ppmw water vapor [11].

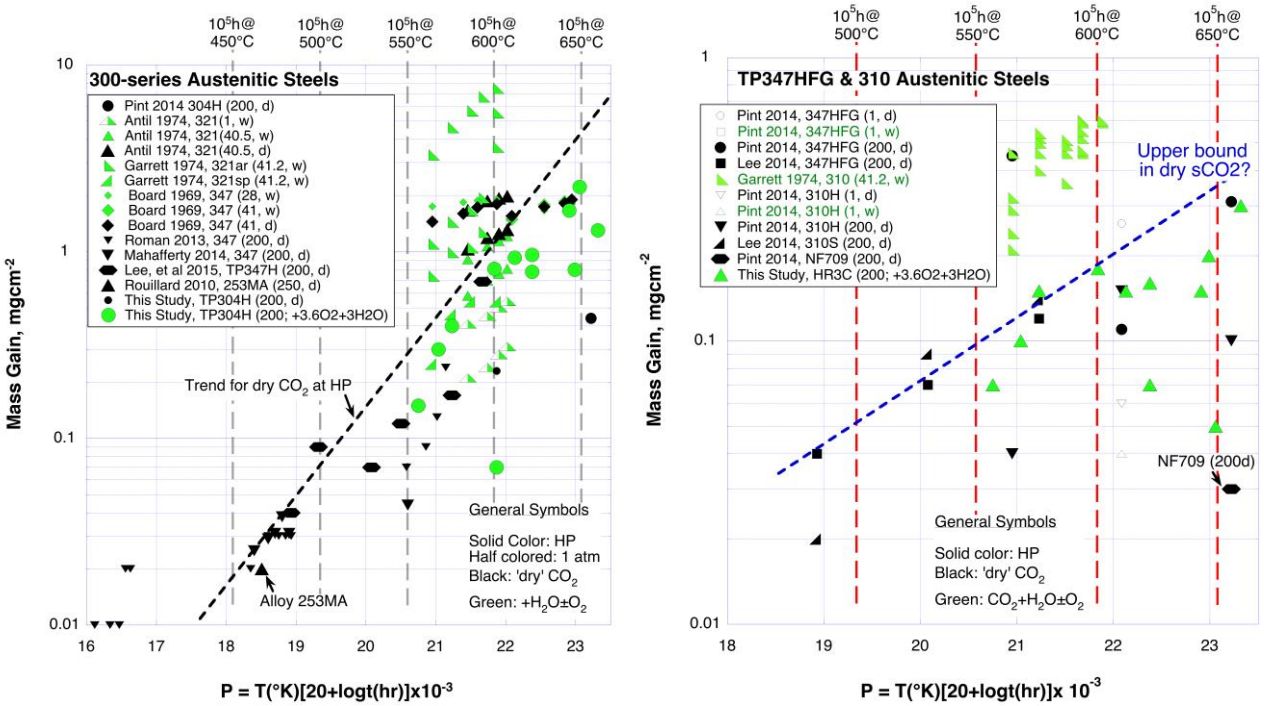

Figure 2.4.1-3 - Compilation of available corrosion data for austenitic steels in CO_2: (a) 'conventional' austenitics; and (b) advanced 'oxidation-resistant' austenitics.

Comparison of the suggested upper bound trend line for TP310 in 'dry' sCO_2 with its oxidation rates in HP steam, Figure 2.4.1-4, suggest that the mass gains in each environment are very similar, in fact, the trend line essentially also represents the upper bound of the steam data. In contrast, steam data for two heats of TP347HFG suggest substantially higher mass gains in steam (though there are relatively few results for 'dry' sCO_2).

Figure 2.4.1-5 presents oxidation results in sCO_2 for two well-established 'higher-strength' austenitic steels, TP316 and variants of Incoloy 800. There was no obvious effect of an addition of 300 ppmw water vapor to sCO_2 on the mass gain of TP316, Figure 2.4.1-5(a); however, there was an apparent trend to increased mass gain with increasing total pressure. The data for Alloy 800H in 'dry' sCO_2 (Figure 2.4.1-5(b)) appear to be consistent over the temperature range ≈450 to 650°C. The upper bound for these data for Incoloy 800 indicated mass gains that were significantly lower than those for TP316, and essentially the same as for TP310.

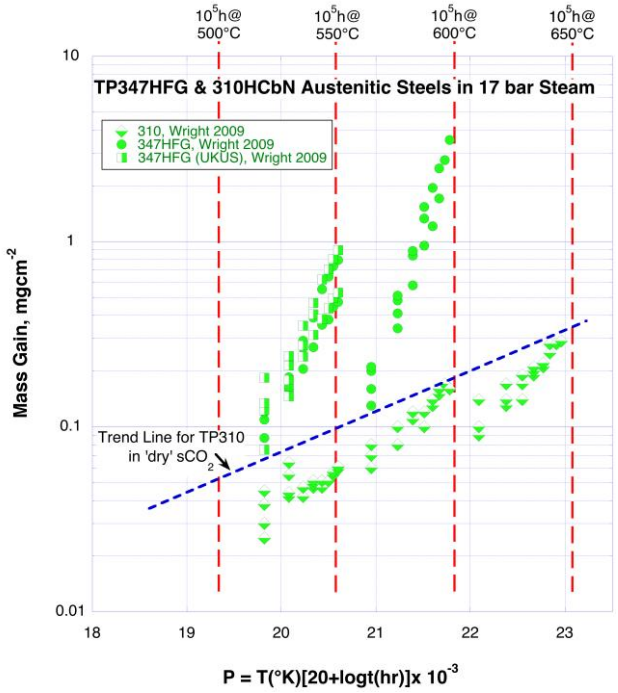

Figure 2.4.1-4 - Comparison of corrosion (mass gain) of advanced 'oxidation-resistant' austenitic steels in 'dry' sCO_2 and in 17 bar steam.

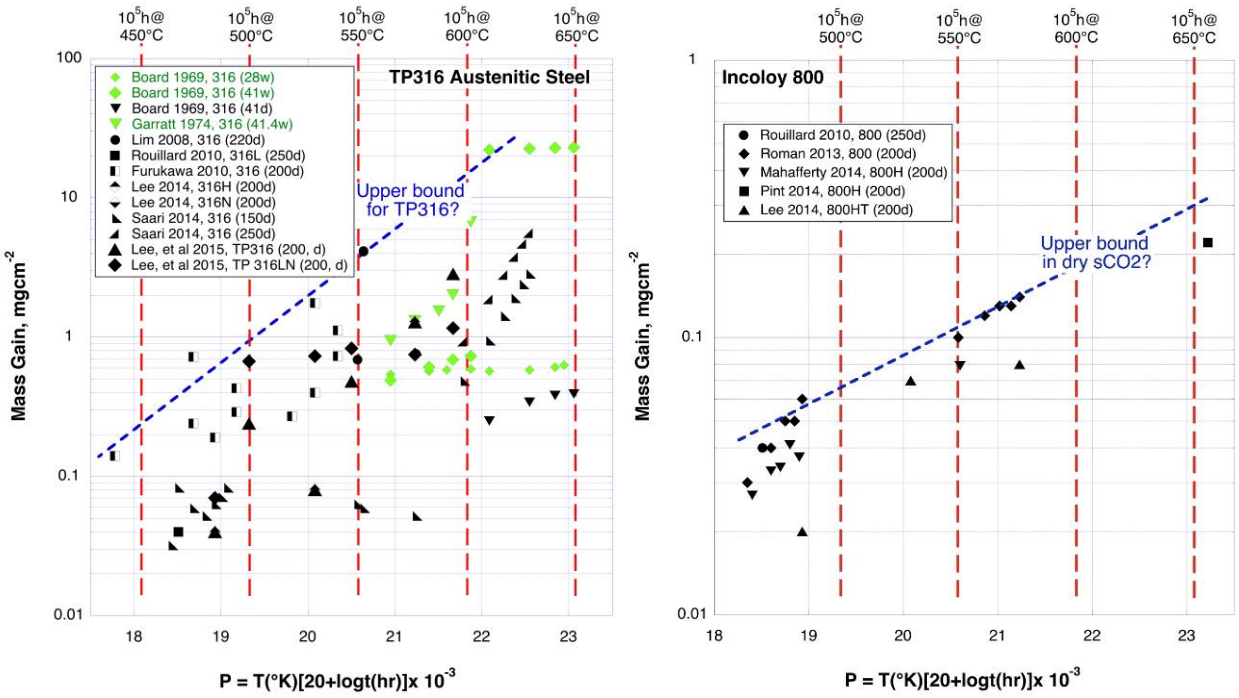

(a) **(b)**

Figure 2.4.1-5 - Compilation of available corrosion data for 'higher-strength' austenitic steels in CO_2: (a) TP316; and (b) Inconel 800 variants.

2.4.1.C - Oxidation of Ni-Based Alloys

Corrosion data in sCO_2 for a range of wrought, chromia-forming Ni-based alloys (i.e., IN600, 617, 625, 690, 718, 740; Haynes 230, 282 and Hastelloy X) are shown in Figure 2.4.1-6(a) [6,8,9,12,17,18,24]. There were too few data points for sCO_2 containing controlled impurities to provide definite indications of any effect of, for instance, water vapor. The upper bound for all these data points occurs at very similar mass gains to that for TP310, though some alloys (notably IN625 and IN740) exhibited significantly lower mass gains. The data for alloy IN740/IN740H [12,17,24] are revisited in Figure 2.4.1-6(b), and an extrapolation to 10^5h at 700°C is suggested; data from the current study [17] for IN740H exposed at 700°C and 200 bar in pure sCO_2 and in sCO_2 containing 3.6 vol% O_2 plus 5.3 vol% H_2O suggest a possible sharp reduction in corrosion when oxidizing impurities are present.

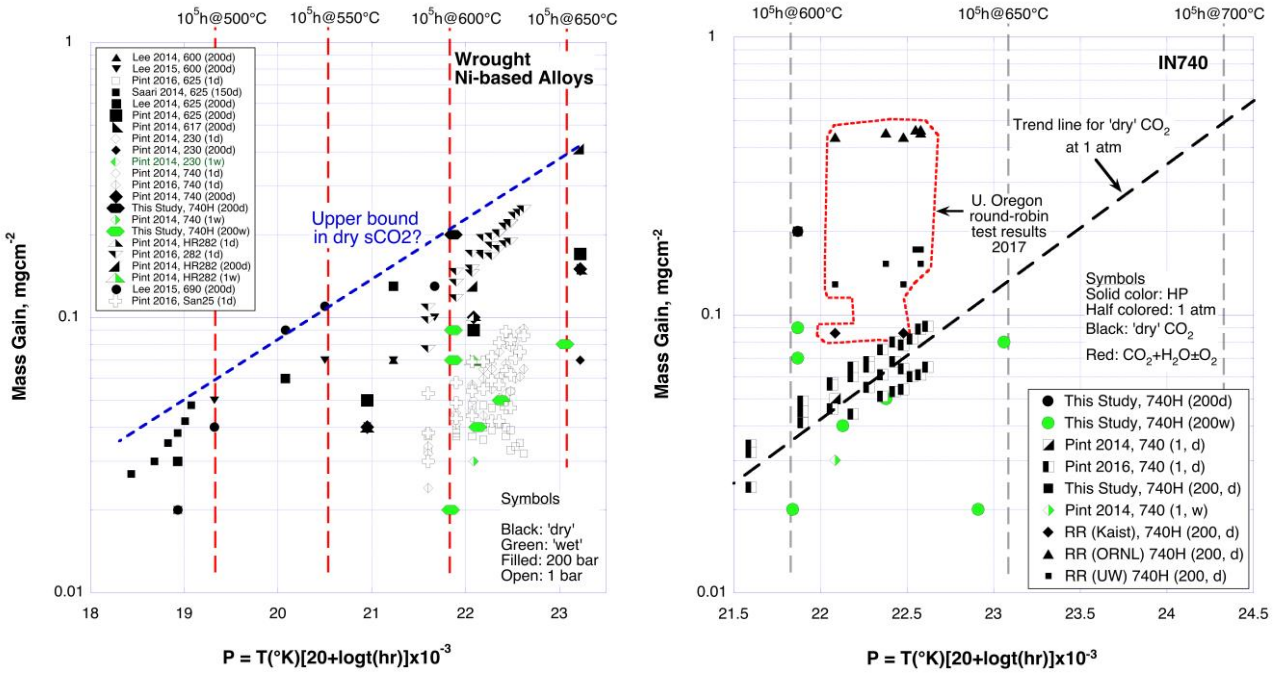

Figure 2.4.1-6 - Compilation of available corrosion data for wrought Ni-based alloys in CO_2: (a) all alloys; and (b) data for IN740 with extrapolation to 700°C ('RR' signifies results from Oregon State University sCO_2 Round Robin group, J. Tucker, Aug 2017).

The steam data used for comparison purposes [20] for these alloys are shown separately in Figure 2.4.1-7. These show a consistent trend with time and temperature for most alloys, the trend extending to considerably higher values of the LM parameter *P* than attained so far by the available test results from sCO_2--maximum steam test conditions reported were 4,000h at 800°C. This consistency in behavior is thought to indicate that no change occurs in the corrosion mechanism (hence oxide scale morphology) in steam over the entire range of test conditions employed. For both the oxidation-resistant austenitic steels and wrought Ni-based alloys the suggested upper bound trend

lines for 'dry' sCO_2 are similarly a good fit for the steam data. This result suggests that for these alloy classes very similar scale morphologies would be expected in both environments.

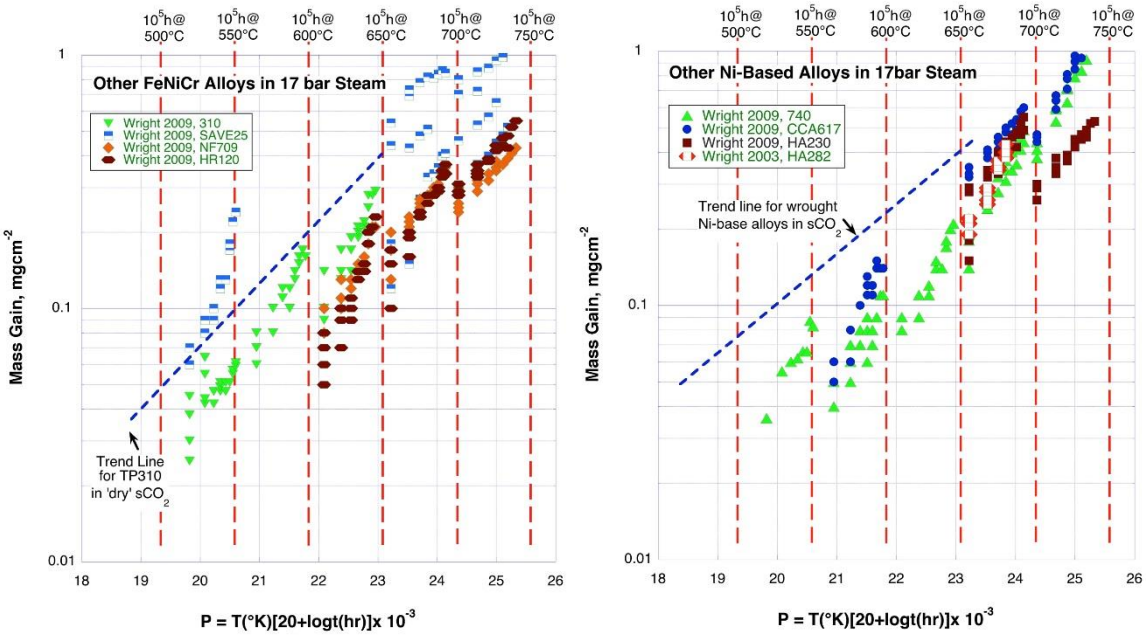

(a) **(b)**

Figure 2.4.1-7 - Corrosion rates in 17 bar steam as a basis for comparison with sCO_2 corrosion data (shown as representative trend line): (a) austenitic FeNiCr alloys; and (b) wrought Ni-based alloys [20].

2.4.1.D - Oxidation of Alumina-Forming Alloys

Alloys with the capability of forming protective alumina (Al_2O_3) scales, rather than the chromia (Cr_2O_3) scales formed on the 'corrosion-resistant' austenitic steels and HT wrought Ni-based alloys, can exhibit extremely high levels of corrosion resistance (low mass gains). An issue is that this exceptional performance requires that the *alpha* form of the protective alumina scale be formed; typically, this occurs at relatively high temperatures (≥900°C). At lower temperatures the more rapidly-growing gamma-Al_2O_3 usually is formed. Nevertheless, this oxide also is considered protective, and would result in mass gains of the same order as those when chromia scales are formed, although at the expense of alloy fabrication difficulties due to the Al content of the alloy.

Available corrosion data for several such alumina-forming Ni-base alloys are summarized in Figure 2.4.1-8 [6,12]. The data for alloy IN738 [6] appear to correspond to approximately the same upper bound suggested for wrought, chromia-forming Ni-base alloys, and also suggest a trend to increasing oxidation rate with increasing sCO_2 pressure from 150 to 200 bar in 'dry' gas. Most of the specialty alumina-forming alloys (HR214, which is a wrought Ni-Cr-Al alloy containing reactive element additions; PWA1483, which is a single crystal, Ni-base superalloy; and APMT which is an oxide dispersion-strengthened Fe-based alloy made by a powder metallurgical route) exhibited mass gains considerably below the suggested upper bound for chromia-forming alloys, possibly demonstrating

superior oxidation resistance provided by alumina scales. The data in Figure 2.4.1-8 also suggest a possible overall trend to lower mass gains with increasing temperature, which would be expected if higher temperatures promoted the formation of alpha alumina scales (though the maximum temperature in any of the tests was 750°C).

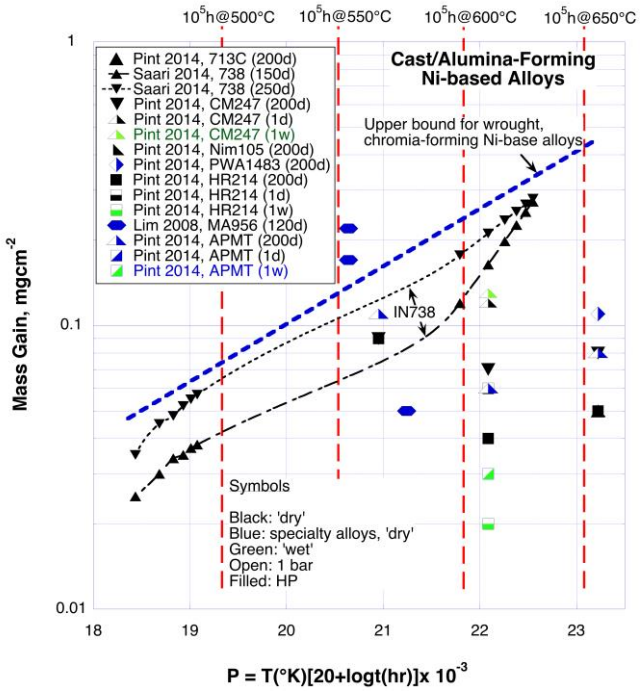

Figure 2.4.1-8 - Compilation of available data for corrosion in CO_2 of alloys capable of forming alumina scales.

An overall observation from the preceding Larson-Miller plots for a wide range of alloys is that the use of CO_2 with different purity levels in some research work, and the inclusion of specific (oxidizing or reducing) additions to CO_2 in others, did not result in definitive conclusions concerning effects of impurities. However, a program in which this issue was addressed specifically (K. Sridharan and M. Anderson [25]) indicated no statistical difference in the rate and mode of oxidation of chromia-forming alloys IN625 and HA230 in research-grade and industrial-grade CO_2 (99.5% purity) at 200 bar and 650-750°C. However, intentional additions of 10 and 100 ppm O_2 resulted in a dramatic *increase* in corrosion rate, suggesting that such additions dominated the oxidation behavior of these alloys, and dissociation of CO_2 played a minor role.

In addition, the preceding Larson-Miller comparison plots do not appear to suggest a clear or major trend for the effect of total pressure on oxidation rates, which may be unsurprising given the competing considerations that:

i) increasing pressure will decrease the tendency for CO_2 to dissociate (for instance, $CO_2 = CO + ½O_2$ will be driven to the left); and
ii) increasing pressure will increase the rate of the oxidation reaction (for instance, $M_2 + 1½O_2 = M_2O_3$ will be driven to the right).

Of the few studies where the effect of pressure has been investigated explicitly, Lee, et al. [26] reported that the oxide morphologies grown on chromia-forming alloys IN600, IN690, and Alloy 800HT at 550-650°C were very similar after oxidation in CO_2 at 1, 100, and 200 bar, but that for each alloy the increase in oxide layer thickness was less than factor of 2 with increasing pressure from 1 to 200 bar. Similar relatively small increases in oxidation rate with large increases in total pressure can be inferred from other studies [e.g. 12]. Possibly more importantly, Lee et al. [26] measured an increase by a factor of less than 2 in C ingress into the alloy with increasing pressure from 1 to 200 bar.

2.4.2 — Comparison with Scale Morphologies Formed in Steam

Relevant experience of scale morphologies formed on ferritic steels after oxidation in sCO_2 from work associated with the British CO_2-cooled nuclear reactors is presented in Appendix D. The exposure conditions were somewhat different from those of interest for current sCO_2 power-generation cycles, with most effort focused on CO_2 containing additions of CO and H_2 at pressures up to 40 bar, and temperatures up to 700°C. While a major emphasis was to predict the time to onset of rapid ('breakaway') oxidation of ferritic steels resulting from C uptake, some informative morphological observations were made during those studies.

2.4.2.A - Oxidation of Ferritic Steels

Initial observations suggest that the external scales formed on ferritic steels in sCO_2 resemble those grown in steam: they are double-layered with an inner layer (L1) of Fe-Cr spinel (essentially magnetite containing Cr) and an outer layer (L2) of columnar-grained magnetite, as illustrated in Figure 2.4.2-1. Oxygen tracer studies suggest that L1 grows predominantly by inward transport of gaseous CO_2 through L2, and that new oxide forms throughout the thickness of L1, rather than solely at the L1-alloy interface [27]. The growth of L2 involves outward transport of iron ions and formation of new magnetite at the L2-gas interface, as summarized in Appendix E. The ratio of thicknesses of L1:L2 typically is in the range 1.1 to 1.4. Assuming that growth of L1 involves oxygen from the dissociation of CO_2 via, for instance, $CO_2 = CO + O$ or $CO^{2+} + O^{2-}$ at various locations in L1, then continued transport of the remaining CO species to the L1-alloy interface is assumed to account for the observed alloy carburization. Apparently, C is immobile in magnetite [27], but nevertheless enters the alloy surface to form internal carbides. If CO_2, CO or CO^{2+} take part in the oxidation process, then (simplistically) if L1 grows predominantly by reaction with gaseous CO_2 or its constituents an amount of C equal to 12/32 of the mass gain associated with the formation of L1 will become available to take part in carburization reactions. This assumption leads to the expectation of significant potential for alloy carburization when double-layered scales of this type are formed. Even given this difference between the reactions occurring in steam and sCO_2, there are examples (Appendix E) of scales from the latter environment exhibiting identical features to steam-formed scales up to the point where the alloy is saturated with C and accelerated oxidation is imminent [28].

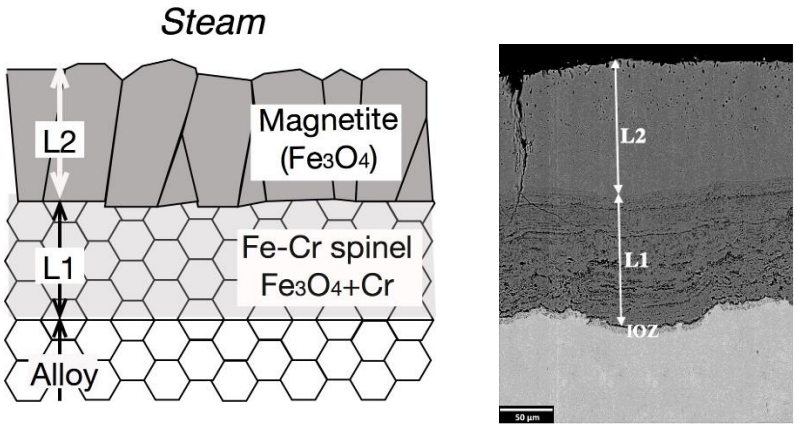

(a) (b)

Figure 2.4.2-1 – Scales formed on ferritic steel (a) schematic representation of a simple, duplex scale formed in steam; and (b) scale on 9Cr steel after 20,000h at 600°C in 42 bar CO_2 (containing 1 vol% CO-300 vppm H_2O-300vppm CH_4-100 vppm H_2) (after Gong, et al. [28]).

2.4.2.B - Oxidation of Austenitic Steels

These alloys can have Cr contents ranging from 16 to 25 wt%, and those containing ≥20 wt% Cr typically are capable of forming Cr-rich protective oxide scales. The morphologies of the protective scales formed in steam basically rely on the same oxides as those formed on the 9 wt% Cr ferritics, but the scale morphologies are significantly influenced by increasing alloy Cr content [29,30]. The first manifestation is a corresponding rise in Cr level in the inner (Fe-Cr spinel) layer (L1) and the progressive slowing of outward transport of Fe ions so that the outer layer (L2) transforms from magnetite to hematite, beginning at the L2-steam interface. At a certain level of Cr availability at the alloy surface (due to an inherent high Cr content, or to enhanced Cr diffusion due to a fine alloy grain size from processing or surface cold working) a Cr-rich scale (essentially chromia) can form at the base of a Fe-Cr spinel L1 or directly on the surface at the start of exposure. This event results in a significant change in scale morphology (and oxidation rate).

The capability of developing thin protective scales on austenitic steels with compositions at the lower end of the Cr range (typically 18Cr-8Ni, wt%) is marginal at temperatures higher than 600°C. More usually, even where such thin scales are formed initially, local disruption of the scale quickly results in the formation of double-layered nodules with structures very similar to the layers formed on the 9-Cr ferritics in steam and in commercial-grade (CG) purity sCO_2 (Figure 2.4.2-2). With time, such nodules spread laterally until the whole scale is double layered. For scales that remain predominantly thin, single-layers of chromia with few double-layered nodules, the thickness of L1 in the double-layered structures can be very variable (a function of the Cr level in L1).

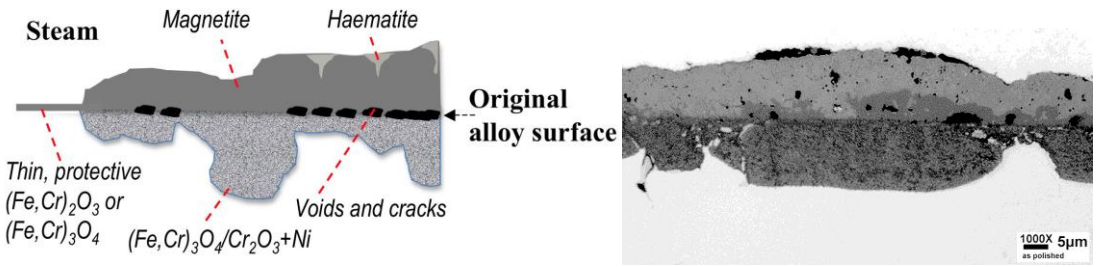

Figure 2.4.2-2 – Scales formed on austenitic steels (a) schematic representation of the main features of scale formed in HP steam [30]; and (b) optical micrograph of a metallographically-polished cross section of scale formed on TP347HFG after 500h at 700°C in CG purity CO_2 at 200 bar [12].

The relatively high Cr content of these alloys renders them increasingly susceptible to carbon uptake during oxidation in sCO_2, provided that C can penetrate the external scales. Studies with model binary Fe-Cr alloys showed a minimum in C uptake for alloy Cr levels of 12-20 wt% [32], that is, for alloys capable for forming single-layered chromia scales. Nevertheless, isotope measurements have indicated inward transport of both C and O through chromia scales [32,33], apparently occurring predominantly along oxide grain boundaries. The major elements added for strengthening these alloys usually are not strong carbide formers (with the exceptions of, for instance, of Nb or Ti), so that the tendency for C uptake reasonably can be correlated with the alloy Cr content. Since the mode of scale growth is analogous to that proposed for the ferritic steels, there is a stronger tendency for C uptake where double-layered scales are formed. Although carburization also has been observed beneath single-layered chromia scales, it occurs at a much slower rate [32].

Observations using a model Fe-20 wt% Cr (chromia-forming) alloy indicated that the rate of scale thickening in an Ar-20 vol% CO_2 gas mixture was 24% faster than in Ar-20 vol% O_2 [31]. Since other results suggested that significant catalysis of carbon deposition from CO_2 is not supported on chromia, it appears likely that the oxidants involved in the formation of such single-layered scales is oxygen derived from dissociation of CO_2 on the outer surface of the scale via $CO_2 = CO + ½O_2$, rather than via $CO_2 = O_2 + C$. This might also suggest that carburization may result from inward transport of CO through these chromia scales.

2.4.2.C - Oxidation of Alloys That Reliably Form Chromia Scales

Upon high-temperature oxidation in steam, Fe-Ni-based alloys with Cr levels greater than 25 wt% and Ni-based alloys with Cr levels greater than 22-25 wt% form single-layered, protective layers of essentially chromia that typically are uniform in thickness upon exposure to HP steam [29]. Additions of, for instance, Co, W, or Mo employed for solid-solution strengthening typically do not significantly modify the scale growth rates or morphologies.

Increased strength at higher temperatures can be achieved in these alloys through incorporation of precipitation strengthening by intermetallic phases such as TiAl (γ') and (Ti,Nb)Al (γ''). However, additions of Al and Ti at the levels commensurate with precipitation strengthening lead to the formation

in steam of a notable subscale of internal oxide particles (primarily of Al_2O_3) directly beneath the main external scale, as illustrated in Figures 2.4.2-3 and 2.4.2-4 [20]. Such precipitates often penetrate a significant distance into the alloy along grain boundaries that intersect the surface. This subscale complicates attempts to estimate the fraction of measured mass gain attributable to formation of the protective outer chromia layer.

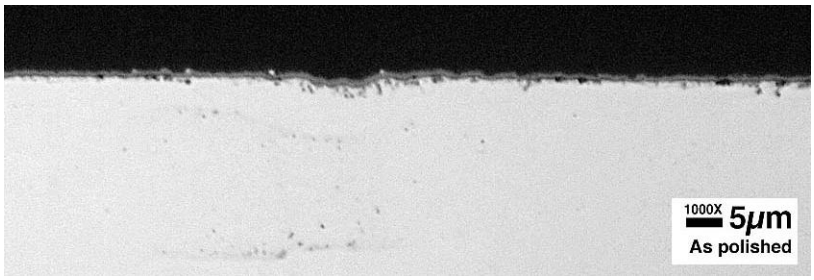

Figure 2.4.2-3 - Alloy CCA617 after 4kh at 650°C in 17 bar steam [20].

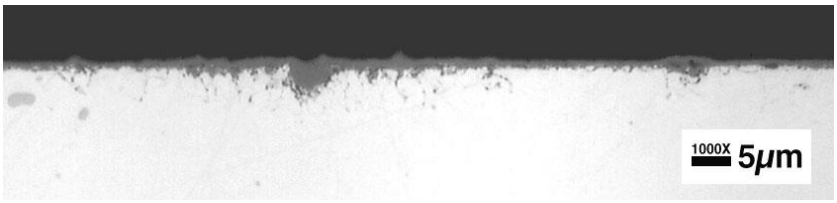

Figure 2.4.2-4 - Alloy IN740 after 4kh at 700°C in 17 bar steam [20].

The alloys of interest for application at the highest temperatures in sCO_2 recuperators are IN617 and IN740H, both of which incorporate precipitation-strengthening elements. While the inherently thin nature of these protective scales renders thickness measurement and characterization more difficult than for the thicker scales formed on ferritic and lower-Cr austenitic steels, initial observations suggest that the morphologies in sCO_2 are similar to those observed in steam. However, since Ti and Nb in particular are strong carbide formers there are expectations of some differences in scale morphologies, and probably in mass gains compared to those observed in HP steam. It appears likely that the subscale formed in sCO_2 initially will consist of carbides of Ti and Nb due to C penetration of the 'protective' chromia scales [32]. With time, as the oxidation front advances into the alloy and encroaches on these carbides they will be converted to oxides, and the carbon released will migrate deeper into the alloy to form further carbides at locations where the oxygen partial pressure is sufficiently low. At this time, it is not clear if this change in mechanism from that apparently operating in HP steam will affect significantly the oxidation kinetics (or alloy strength). Confirmation (or otherwise) of current speculation about the detailed scale morphologies formed on these alloys in sCO_2 (or steam) awaits further research.

2.4.3 — References Cited in Section 2.4

1. P.J. Roman, J.J. Jelinek, K. Sridharan, G. Cao, T.R. Allen, and M. Anderson, "Corrosion study of candidate alloys in HT, HP sCO2 for Brayton Cycle applications," Paper no. 51313, *International NACE Corrosion Conference and Expo, 2013*.
2. T. Furukawa, Y. Inagaki, and M. Aritomi, "Corrosion behavior of FBR structural materials in high-temperature supercritical carbon dioxide," *J. Power and Energy Systems*, 4 (1), 252-261 (2010).
3. D.R. Holmes, D. Mortimer, and J. Newell, "Discovery and assessment of accelerated corrosion in Fe-9Cr alloys and steels," Paper No. 13 in *Proc. B.N.E.S. Intl. Conf. on Corrosion of Steels in CO_2* (1974).
4. A.M. Pritchard and A.E. Truswell, "Mechanistic experiments on the oxidation of 9% Cr steels in CO_2 at 550°C," Paper No. 19 in *Proc. B.N.E.S. Intl. Conf. on Corrosion of Steels in CO_2* (1974).
5. F. Rouillard, F. Charton and G. Moine "Corrosion Behavior of Different Metallic Materials in Supercritical CO_2 at 550°C and 250 bar," Paper no. 10195, *International NACE Corrosion Conference and Expo, 2010*.
6. H. Saari, C. Parks, R. Petruskeno, B. Maybee, and K. Zanganeh, "Corrosion testing of high-temperature materials in supercritical CO_2," Paper no. 32 presented at the *4th International Symposium - Supercritical CO_2 Power Cycles*, September 9-10, 2014, Pittsburgh, Pennsylvania.
7. J. Mahaffey, A. Kalra, M. Anderson, K. Sridharan, "Materials corrosion in HT sCO_2," Paper No. 2, presented at the *4th International Symposium - Supercritical CO_2 Power Cycles*, September 9-10, 2014, Pittsburgh, Pennsylvania.
8. H.J. Lee, H. Kim, and C. Jang, "Compatibility of candidate structural materials in high-temperature S-CO_2 environment," Paper no. 32 presented at the *4th International Symposium - Supercritical CO_2 Power Cycles*, September 9-10, 2014, Pittsburgh, Pennsylvania.
9. H.J. Lee, H. Kim, S.H. Kim, and C. Jang, "Comparison of the corrosion behaviors of Fe-base and Ni-base austenitic alloys in high-temperature S-CO_2 environment," Section 3, Session 1A-Supercritical CO_2 Oxidation/Corrosion, Proc. EPRI International Conference on Corrosion in Power Plants (San Diego, Oct 13-15, 2015), EPRI Report No. 3002006972, Nov. 2015.
10. J.Y. Lim, T.J. McKrell, G. Eastwick, and R.G. Ballinger, "Corrosion of materials in supercritical carbon dioxide environments," Paper no. 08430, *NACE International Corrosion Conference and Expo, 2008.*
11. J.C.P. 11, S.K. Lister, P.J. Nolan and J.T. Crook, "Some factors in the oxidation of austenitic stainless steels," Paper No. 23 in *Proc. B.N.E.S. Intl. Conf. on Corrosion of Steels in CO_2* (1974).
12. B.A. Pint and J.R. Keiser, "The effect of temperature on the sCO_2 compatibility of conventional structural alloys," Paper no. 61 presented at the *4th International Symposium - Supercritical CO_2 Power Cycles*, September 9-10, 2014, Pittsburgh, Pennsylvania.
13. J. Board and R. Winterborne, "Oxidation of Austenitic Stainless Steel Boiler Tubing in Carbon Dioxide," *British Corrosion Journal* 4 (2), 86-93 (1969).
14. J.E. Antill and A.E. Trusswell, "Mechanistic aspects of the reactions of austenitic stainless steel with carbon dioxide at high temperatures," Paper No. 26 in *Proc. B.N.E.S. Intl. Conf. on Corrosion of Steels in CO_2* (1974).
15. J. Mahaffey, D. Adam, M. Anderson, and K. Sridharan, "Effect of oxygen impurity on corrosion in supercritical CO_2 environments," Proc. *5th International Supercritical CO_2 Power Cycles Symposium*, Mar 29-31, 2014, San Antonio, Texas.
16. K. Kaya, S. Hayashi, and S. Ukai, "High-temperature oxidation behavior of Fe-9Cr steel in CO_2-O_2 gas mixture," *ISIJ International*, 54 (6), 1379-1385 (2014).

17. J.P. Shingledecker, *Predicting the Oxidation/Corrosion Performance of Structural Alloys in Supercritical CO_2,* Research Performance Progress Report on Contract DE-FE0024120, Jan 30, 2015.
18. B.A. Pint, R.G. Brese, and J.R. Keiser, "Effect of pressure and thermal cycling on compatibility in CO_2 for concentrated solar power applications," paper No. GT2017-65066, Proc. ASME Turbo Expo 2017, Charlotte, North Carolina (2017).
19. R.G. Brese, J.R. Keiser, and B.A. Pint, "Effect of thermal cycling on compatibility in CO_2 for concentrated solar power applications," *Oxidation of Metals*, 87, 631-642 (2017).
20. I.G. Wright, DOE FWP No. FEAA061: *Oxidation of Candidate Alloys in Steam at 17 bar: Final Report on Phase 1 efforts in support of the US Consortium Program on Boiler Materials for Ultra-Supercritical Coal Power Plants*, ORNL/TM-2009/232 (Nov. 2009).
21. ASME Boiler and Pressure Vessel Code, Section I: *Rules for Construction of Power Boilers*, ASME, Three Park Avenue, New York, New York, (2015).
22. "Grade 91 Use Temperature Limits," *EPRI Proposed User Guideline*, May 2016.
23. G.B. Gibbs, R.E. Pendlebury and M.R. Wootton, "Protective and breakaway corrosion of mild steel in CO_2," Paper No. 6 in *Proc. B.N.E.S. Intl. Conf. on Corrosion of Steels in CO_2* (1974).
24. A.S. Sabau and I.G. Wright, "Influence of oxide growth and metal creep on strain development in the steam-side oxide in boiler tubes," *Oxidation of Metals*, 73, 467-492 (2010).
25. K. Sridharan and M. Anderson, *Corrosion of Structural Materials for Advanced Supercritical Carbon-Dioxide Brayton Cycle*, Final Report on US DOE-NERI Grant No. DE-NE0000677 (NEUP Ref: 13-4900), May 13, 2017.
26. H.J. Lee, G.O. Subramanian, S.H. Kim, and C. Jang, "Effect of pressure on the corrosion and carburization behavior of chromia-forming heat-resistant alloys in high-temperature carbon dioxide environments," *Corrosion Science*, 111, 649-658 (2016).
27. M.R. Taylor, J.M. Calvert, D.G. Lees, and D.B. Meadowcroft, "The mechanism of corrosion of Fe-9%Cr alloys in carbon dioxide," *Oxidation of Metals*, 14 (6), 499-516 (1980).
28. Y. Gong, D.J. Young, K. Kontis, Y.L. Chiu, H. Larsson, A. Shin, J.M. Pearson, M.P. Moody, and R.C. Reed, "On the breakaway of Fe-9Cr-1Mo steel in high-pressure CO_2," *Acta Materialia*, 130, 361-374, (2017).
29. I.G. Wright and R.B. Dooley, "A review of the oxidation behavior of structural alloys in steam," *International Materials Reviews*, 55 (3), 129-167 (2010).
30. I.G. Wright and R.B. Dooley, "Morphologies of oxide growth and exfoliation in superheater and reheater tubing of steam boilers," *Materials at High Temperatures*, 28 (10), 40-57 (2011).
31. D.J. Young and J. Zhang, "Carbon corrosion of alloys at high temperature," *J. S. Afr. Inst. Min. Metall.*, 113 (2), Johannesburg, Feb 2013. *On-line version* ISSN 2411-9717.
32. D.J. Young, *High-Temperature Oxidation and Corrosion of Metals*, Elsevier (2016), pp. 522.
33. I. Wolf, H.J. Grabke, and P. Schmidt, "Carbon transport through oxide scales on Fe-Cr alloys," *Oxidation of Metals*, 29 (3), 289-306 (1988).

2.5: Computational Model of Oxidation/Corrosion in sCO_2

The EPRI-ORNL model for predicting growth and exfoliation of oxide scales [1] is based on thermo-mechanical simulation of the evolution of stresses and strains in those scales during operation of a heat exchanger. The model originally addressed the scales formed inside superheater and reheater tubes in steam boilers. It includes two comprehensive modules: 'SpallMap' and 'SpalLoop.' *SpallMap* solves the stress-strain equations in a growing oxide scale at a specific location along a tube during boiler operation, and tracks stress/strain evolution in the scales, including the influence of scale morphological features, effects of axi-symmetric geometry, and boiler operating parameters such as load changes and outages. The resulting strains are compared with scale damage criteria suggested originally by Armitt et al. [2] and subsequently updated [3], and typically represented by the type of diagram shown in Figure 2.5.1. *SpalLoop* uses this information to estimate the amount of scale lost during an exfoliation event by calculating the stress/strain evolution in the scale along an entire heat exchanger channel, taking into account the temperature changes in the fluid and metal along the channel.

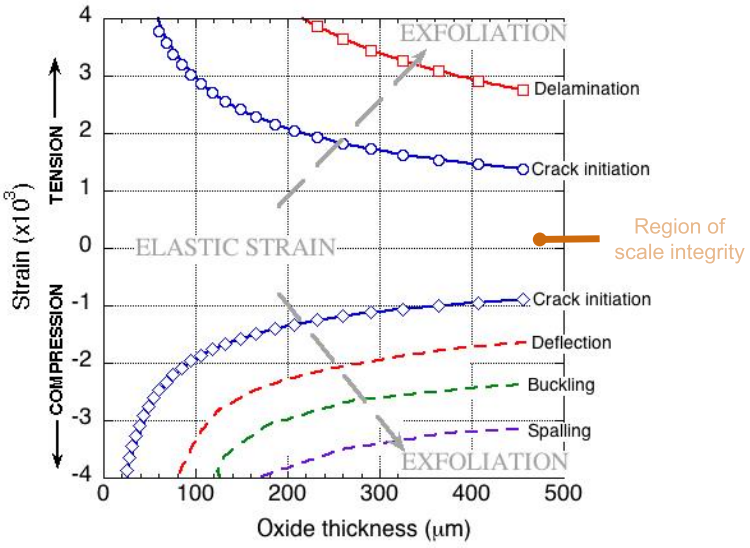

Figure 2.5.1. Example of an 'Armitt diagram' equating scale failure modes with oxide thickness and accumulated strain [2].

Both *SpallMap* and *SpalLoop* include the capabilities of handling: (a) scales consisting of several layers of oxides with different properties (such as Fe-Cr spinel, magnetite, and/or hematite formed in steam); (b) a temperature gradient through the channel wall, including different growth temperatures for each oxide layer; (c) creep in the alloy and oxide scale; and (d) load cycling, including shut-down events. The *SpalLoop* module includes a model for estimating blockage resulting from accumulation of exfoliated scale. One or two tube bends typical of hairpin loops in steam boilers successfully have been addressed, typically with differentiation between blockage in the inlet loop bend and outlet loop bend. The overall model has been tested against published data for steam boilers as well as a limited number of field failures of tubes, and has shown good agreement with observations for onset of oxide scale failure as well as area blockage fraction.

For the current application the model has been extended to incorporate the properties of supercritical CO_2, as well as generic design information for sCO_2 recuperators.

2.5.1 — Overall Approach

In this Task the EPRI Exfoliation Model [1] will be used to provide rigorous approaches for the calculation of oxide growth rates under realistic heat-flux conditions. In particular, the current model includes modules that take account of the fluid properties and design characteristics of the heat exchanger, and so considers the effects of thermal gradients created by the heat flux through the heat-transfer wall (hence influence of alloy type and wall thickness) on growth of the oxide scales. When considering propensity for exfoliation, knowledge of the morphologies of the oxide scales is an important factor in calculating the time to reach the critical strain in the oxide at which exfoliation becomes possible. The model examines the possible sources from which strain can originate, which include (i) thermal expansion mismatch between the alloy(s) and oxides that comprise the scales; (ii) mechanical constraints due to the configuration of the heat exchanger surfaces; and (iii) load-related cycling in heat exchanger operation.

Overall, it is anticipated that when applied to the fluid properties, component configurations and operating parameters, and the oxidation behavior of the alloy candidates in sCO_2, the considerations embodied in various scenarios for possible effects of oxide growth on service lifetime may lead to different relative dependencies than suggested in Figure 2.5.1-1. In order to generate such diagrams for projected lifetimes of compact heat exchangers proposed for use in sCO_2, it is necessary to develop algorithms that relate oxide thicknesses grown in sCO_2 as a function of time and temperature. Such algorithms derived from the experimental program, summarized in Tables 2.3.7-2, 2.3.7-4, 2.3.7-6 and 2.3.7-8 in Section 2.3.7, are repeated below as Tables 2.5.1-1 (mass gain-based) and 2.5.1-2 (scale thickness-based).

These tables show mass gain-based data for all the ferritic steels and austenitic steel TP304H. However, because of difficulties in satisfactory measurement of the very small mass gains for the HT alloys HR3C, IN617, and IN740H, it is recommended that alternative data from steam studies listed in Tables 2.5.1-1 and 2.5.1-2 be used for HR3C (310HCbN) and IN740H. Scale thickness-based data are available for ferritic steels Grade 91 and VM12, and for austenitic steel TP304H. Again, because of practical difficulties in making satisfactory measurements of the very thin scales associated with oxidation in sCO_2 of HT alloys HR3C, IN617, and IN740H, it is recommended that oxidation algorithms for HR3C (310HCbN) and IN740 derived from steam data be used in the model for calculations involving scale thicknesses on those two alloys.

Table 2.5.1-1
Recommended mass gain-based Arrhenius constants for alloys of interest.

Alloy	Environment	T Range (°C)	A_{Am} (g^2/cm^4s)	Q_m (kJ/mole)	R^2	Source
Grade 91	CO_2 at 200 bar	650-750	1.12×10^{8}	-372	0.92	This work
VM12	CO_2 at 200 bar	650-750	2.67×10^{-2}	-190	0.86	This work
Crofer 22	CO_2 at 200 bar	650-750	1.39×10^{-8}	-80	0.55	This work
TP304H	CO_2 at 200 bar	650-750	1.87×10^{-6}	-136	1.00	This work
HR3C*	CO_2 at 200 bar	650, 750	2.14×10^{-13}	-30	1	This work
IN617	CO_2 at 200 bar	650-750	NA	NA	—	—
IN740H	CO_2 at 200 bar	650-750	NA	NA	—	—
IN740H	CO_2 at 1 bar	700-800	8.45×10^{2}	-340	0.82	[4]
IN740	Steam at 17 bar	600-800	3.2×10^{-3}	-229	0.98	[5]
PMCr	Steam at 17 bar	600-800	6.1×10^{-4}	-213	0.97	[5]
310HCbN	Steam at 17 bar	650-800	6.0×10^{3}	-338	0.87	[5]

*Two data points only, at 650 and 750°C.

Table 2.5.1-2
Recommended thickness-based Arrhenius constants for alloys of interest.

Alloy	Environment	T Range (°C)	A_{At} ($\mu m^2/h$)	Q_t (kJ/mole)	R^2	Source
Grade 91	CO_2 at 200 bar	650-750	2.8×10^{19}	-376	0.88	This work
VM12	CO_2 at 200 bar	650, 750	4.1×10^{7}	-162	1*	This work
Crofer 22	CO_2 at 200 bar	650-750	NA	NA	—	—
TP304H	CO_2 at 200 bar	650-750	1.1×10^{6}	-151	0.99	This work
HR3C	CO_2 at 200 bar	650-750	NA	NA	—	—
IN617	CO_2 at 200 bar	650-750	NA	NA	—	—
IN740H	CO_2 at 200 bar	650-750	NA	NA	—	—
IN740	Steam at 17 bar	650-800	1.4×10^{5}	-166	0.97	[5]
310HCbN	Steam at 17 bar	650-800	2.3×10^{2}	-112	0.98	[5]

*Two data points only, at 650 and 750°C.

2.5.2 — Thermodynamic and Fluid Properties of Working Fluid

Thermodynamic and fluid properties of sCO_2 and steam were calculated from the REFPROP database [6]. Those shown for steam are intended for use as a reference, since most the scale exfoliation studies on which the model was based were conducted for conventional steam boiler tubes. The REFPROP database provides accurate properties for specific heat, density, viscosity, and thermal conductivity, which are key parameters required in heat transfer calculations. For the sake of simplicity, the Prandtl Number (*Pr*) in Equation 2.5.2-1, which a dimensionless variable used in heat transfer correlations, also is shown for both sCO_2 and steam:

$$Pr = \frac{C_p \mu}{k} \tag{2.5.2-1}$$

where C_p is the specific heat, μ is the dynamic viscosity, and k is the thermal conductivity. As shown in Tables 2.5.2-1 and 2.5.2-2, the major differences between the properties of sCO_2 and steam are:

1. The specific heat of sCO_2 is approximately 30-50% that of steam.
2. The density of sCO_2 is approximately 1.5-1.7 times that of steam.
3. The thermal conductivity of sCO_2 is approximately 60% that of steam and, as a result,
4. The Pr for sCO_2 is approximately 60-80% that of steam.

The properties of steam and sCO_2 were compared at operational pressures relevant to modern steam cycles (250 bar) and proposed sCO_2 power cycles (200 bar), and were used in analysis of the impact of the different properties of the two fluids, and of different heat exchanger geometries on scale exfoliation parameters. The fluid flow rates associated with the two types of power cycle, and the thermophysical properties of the working fluids were used to calculate the local heat transfer coefficient (*h*) in Equation 2.5.2-2 for different heat exchanger geometries, using correlations for Nusselt Number (*Nu*), as:

$$h = \frac{Nu_D(Re_D, Pr)\, k}{D} \tag{2.5.2-2}$$

where D is the diameter of the flow channel, and Re_D is the Reynolds Number.

Table 2.5.2-1
Properties of supercritical steam at 250 bar (typical for supercritical steam boilers).

Temperature (°C)	Specific heat (kJ/kg K)	Density (kg/m^3)	Viscosity*10^5 (Pa s)	Thermal conductivity (W/m K)	Pr
500	3.764	89.7	3.064	0.100	1.15
510	3.623	87.1	3.101	0.0999	1.13
520	3.503	84.7	3.139	0.0997	1.10
530	3.400	82.5	3.177	0.0998	1.08
540	3.311	80.4	3.216	0.100	1.06
550	3.234	78.5	3.255	0.101	1.05
560	3.166	76.8	3.294	0.101	1.03
570	3.106	75.1	3.332	0.102	1.02
580	3.054	73.6	3.371	0.102	1.01
590	3.007	72.1	3.410	0.103	0.993
600	2.965	70.7	3.449	0.104	0.982
610	2.928	69.4	3.488	0.105	0.972
620	2.895	68.2	3.527	0.106	0.963
630	2.865	67.0	3.565	0.107	0.955
640	2.839	65.9	3.604	0.108	0.947
650	2.815	64.8	3.642	0.109	0.940
660	2.793	63.8	3.680	0.110	0.933
670	2.773	62.8	3.718	0.111	0.927
680	2.756	61.9	3.756	0.112	0.921
690	2.740	61.0	3.794	0.113	0.916
700	2.726	60.1	3.832	0.115	0.911
710	2.713	59.2	3.870	0.116	0.907
720	2.702	58.4	3.907	0.117	0.903
730	2.692	57.7	3.944	0.118	0.899
740	2.682	56.9	3.981	0.119	0.896
750	2.674	56.2	4.018	0.120	0.893

Table 2.5.2-2
Properties of supercritical CO_2 at 200 bar.

Temperature (°C)	Specific heat (kJ/kg K)	Density (kg/m^3)	Viscosity*10^5 (Pa s)	Thermal conductivity (W/m K)	Pr
500	1.233	133.28	3.601	0.0594	0.747
510	1.234	131.39	3.630	0.0601	0.746
520	1.236	129.56	3.660	0.0607	0.745
530	1.238	127.78	3.688	0.0614	0.744
540	1.239	126.06	3.717	0.0620	0.743
550	1.241	124.40	3.746	0.0626	0.742
560	1.243	122.78	3.775	0.0633	0.741
570	1.244	121.20	3.804	0.0639	0.740
580	1.246	119.67	3.832	0.0646	0.739
590	1.248	118.19	3.861	0.0652	0.739
600	1.250	116.74	3.889	0.0659	0.738
610	1.251	115.33	3.918	0.0665	0.737
620	1.253	113.96	3.946	0.0671	0.737
630	1.255	112.63	3.974	0.0678	0.736
640	1.257	111.33	4.002	0.0684	0.735
650	1.259	110.06	4.030	0.0691	0.735
660	1.261	108.82	4.058	0.0697	0.734
670	1.262	107.61	4.085	0.0703	0.734
680	1.264	106.43	4.113	0.0709	0.733
690	1.266	105.28	4.141	0.0716	0.732
700	1.268	104.16	4.168	0.0722	0.732
710	1.270	103.06	4.195	0.0728	0.731
720	1.271	101.99	4.222	0.0734	0.731
730	1.273	100.94	4.250	0.0741	0.731
740	1.275	99.911	4.276	0.0747	0.730
750	1.277	98.907	4.303	0.0753	0.730

2.5.3 — Design Consideration for sCO_2 Heat Exchangers

In order to set up numerical simulations, the proposed designs and operating conditions for sCO_2 recuperators were surveyed, and the results are summarized in Table 2.5.3-1. The two most advanced concepts for sCO_2 recuperators are the *Formed Plate Heat Exchanger* (FPHE) [7] and the *Printed Circuit Heat Exchanger* (PCHE) [8]. Generic dimensions are summarized in Table 2.5.3-2. The sCO_2 channels in the FPHE design are quite different in shape than used in the PCHE: in the FPHE they are semi-circular in cross section, whereas the geometries of the PCHE flow passages result in sCO_2 contacting both convex and concave shapes. Typically, the sCO_2 channels in both high-pressure and low-pressure circuits may be bundled together in layers, resulting in little pressure differential or temperature gradient across the wall thickness between two adjacent channels.

Table 2.5.3-1
Comparison of Proposed operating conditions for sCO_2 recuperators and steam boiler superheaters

Fluid/Size/Property	High-Pressure Side sCO_2	Low-Pressure Side sCO_2	Steam tubes
ID pressure (bar)	200-300	30	250
OD pressure (bar)	200-300	30	10
Differential P across the metal wall	none	none	24
ID temperature (°C)	50-750	700-	600
OD temperature	50-750	700-	1,200
Differential T across the metal wall	none	none	600
Cycles full-load to low-load	-	-	weekly
Cycles full-load to room temperature	180 per year	180 per year	2 per year

Table 2.5.3-2
Typical dimensions and geometries of flow paths for sCO_2 recuperators

Size/Property	PCHE Channels	FCHE Channels
Channel shape	Variable curvature	Semicircular
Oxide growth location	Inside channel (concave) Outside channel (convex)	Inside channel (concave)
Metal thickness (mm)	0.2	0.9
Internal hydraulic diameter (mm)	*0.2 to 0.4	1
Channel length (mm)	500 to 1,000	500 to 1,000
Ratio channel length to ID	1,200 to 5,000	500 to 1,000

*ID radius of curvature 0.2 to 0.6 mm

Because of the differences in size and shape of sCO_2 recuperator flow channels compared to standard superheater tubes in steam boilers, further consideration of potential sites where exfoliated oxide scales might cause blockage was required. The main issues were:

1) Blockage typically occurs in regions of significant geometrical change in the flow path, such as 90° or 180° bends in steam boiler tubes. The individual channels in a sCO_2 FPHE are straight, while those for a PCHE usually are wavy, with a very small bend angle (15°).
2) Based solely on this channel shape (straight or wavy with small angles), blockage in individual channels normally would be ruled out. However, these channels are very long with respect to the internal tube diameter (ID), which offers a higher probability for deposits on the internal tube surfaces. Thus, it was considered that individual tube blockage *must* be considered (Table 2.5.3-3).
3) A possible blockage site would be the exit manifold (Table 2.5.3-3) after which the flow path experiences a sharp turn. Figure 2.5.3-1 illustrates this scenario.

Table 2.5.3-3
Blockage at each channel exit for PCHE and FCHE channels.

Blockage Site Variables	FCHE Channels	PCHE Channels
Number of 90°-180° bends per channel	None (straight channels)	None (wavy channels with small bends)
Number of 15° bends per channel	None	60
Location of possible blockage	Tube exit	Tube exit
Length of blockage	5-10x ID	5-10x ID
Shape of blockage	Horizontal	Horizontal

Table 2.5.3-4
Blockage at the exit manifold for PCHE and FCHE channels.

Blockage Site Variables	sCO_2 Channels
Number of bends in the flow path	One bend at channel exit
Location of possible blockage	Manifold (where channel flow merge)
Length of blockage	According to manifold dead spaces due to change in flow path shape
Shape of blockage	Horizontal

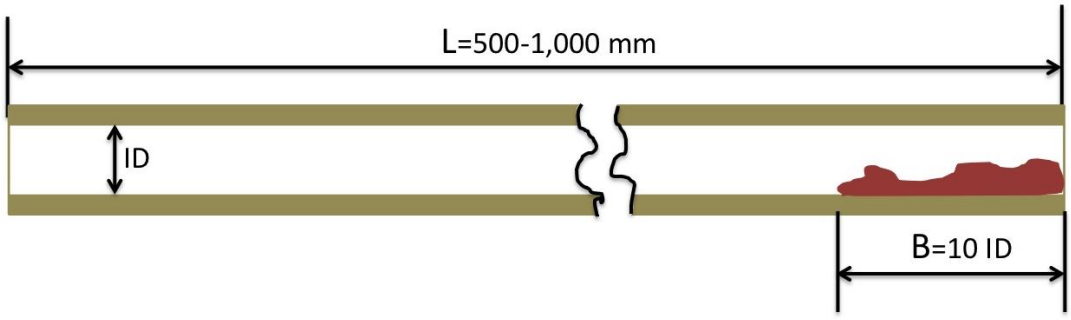

Figure 2.5.3-1 - Examples of blockage locations within individual channels, showing a blockage length (*B*) of 5 to 10 internal diameters (ID).

Table 2.5.3-5 is an overall summary of generic data for geometries of the key features of heat exchanger designs proposed for sCO_2 cycles compared to the parameters used by the model for steam tubes. Based on typical cross-sectional geometries of flow passages that involve flow of sCO_2 through both convex and concave shapes, the existing computer code for predicting blockage from scale growth only on the inside (concave) surfaces of tubes was changed to include blockage due to scale exfoliation from an outside (convex) surface. This is illustrated schematically in Figure 2.5.3-2, where cross-sections of tubes having 200 μm-thick metal walls are drawn to scale. The revised blockage module of the model can handle the growth of scale on the inside of the tube (Figure 2.5.3-1b) and on the outside (Figure 2.5.3-1(c)).

Table 2.5.3-5
Typical dimensions and geometries of flow paths for sCO_2 recuperators as compared to those in a superheater steam boiler tube

Fluid/Size/Property	sCO_2 channels	Steam tubes
Channel shape	Variable curvature	Circular
Oxide growth location	Inside channel (concave) Outside channel (convex)	Inside channel (concave)
Metal thickness (mm)	0.2	7 to 10
Internal Hydraulic Diameter (mm)	*0.2 to 0.4	20 to 30
Channel length (mm)	500 to 1,000	20,000 to 25,000
Ratio channel length to ID radius	1,200 to 5,000	600 to 1,200
Number of 90^o or 180^o bends per channel	**none	1
Location of possible blockage	Tube exit	Bends
Shape of blockage	Horizontal, or in the bend at channel exit	Horizontal, or inclined in bends

*ID radius of curvature 0.2 to 0.6 (mm);
**Bend at channel exit in the current design.

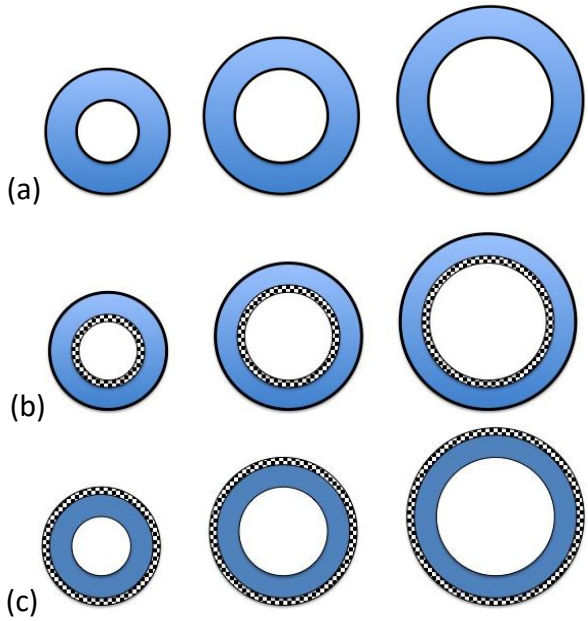

Figure 2.5.3-2 - Schematic representation of simple flow path cross sections for sCO_2 recuperators: (a) before any oxide scale formation; (b) after growth of a 50 µm-thick scale on the *internal* tube surface; and (c) after growth of a 50 µm-thick scale on the *external* tube surface. The metal thickness is considered to be 200 µm (tube dimensions and oxide scale thickness are drawn to scale).

2.5.4 — Initial Results of Numerical Simulation Using the Exfoliation Model

As indicated earlier, the results from the *SpalLoop* blockage module are very sensitive to the parameters used to specify the geometric features describing the heat exchanger, in particular the expected blockage length and number of bends per channel, as well operating parameters such as frequency of temperature cycles [9]. While for this project the blockage length was arbitrarily set at 5x channel ID (as typically used in steam oxidation/exfoliation considerations), the appropriate length of sCO_2 flow channels and location of blockage sites (especially for oxide grown on the outside surfaces of channels) will be specific to each recuperator design. Preliminary data from the manufacturers of sCO_2 recuperators indicated that more frequent load cycling is expected than for the superheaters in steam power plants.

While oxide scales grown on the surfaces of the flow channels are stress-free at high temperatures, during excursions to low temperatures stresses are generated from differences in coefficients of thermal expansion between the alloy and various layers in the scales, changes in system pressure, and mechanical constrains from geometric features. Once the scales are sufficiently thick that the stress developed exceeds some critical value (during a shut-down event, for instance, that typically represents the largest temperature swing experienced by a heat exchanger), failure of the scale by one of several possible modes [3] is expected, and exfoliation becomes likely. In the simulations conducted it was considered that regular shut-down events occurred at 3-month intervals.

Some initial results from use of upgraded versions of the *Spallmap* and *SpalLoop* modules of the EPRI/ORNL exfoliation code [1] to generate the mass of exfoliated scale are presented in Figure 2.5.4-1 for an austenitic steel (TP347H) for cases S2 and S3 listed in Table 2.5.4-1.

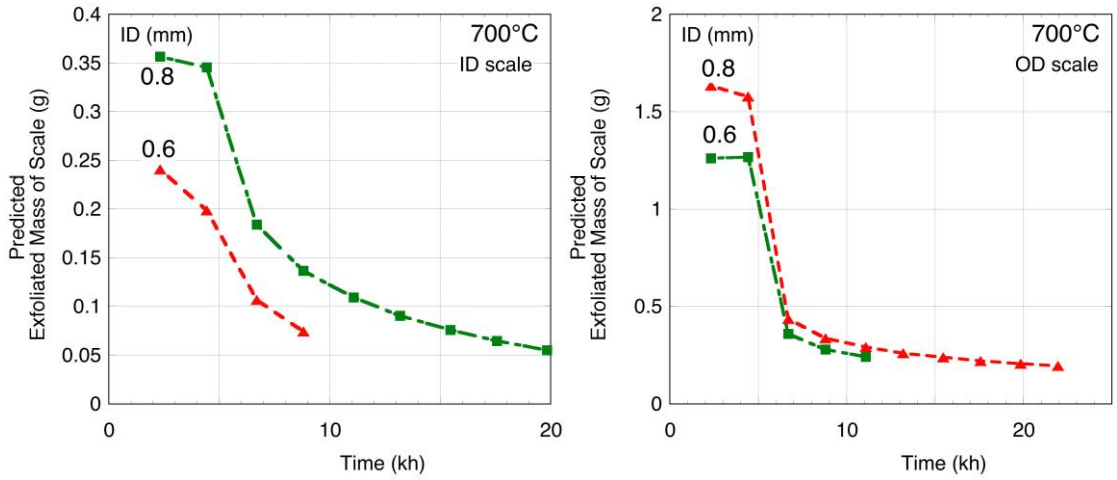

(a) (b)

Figure 2.5.4-1 – Examples of the predicted mass loss with time of magnetite exfoliated from a circular section flow channel of TP347H (2mm-thick walls, 0.5m total length), using a pure elastic model for calculating the stress and strains, for: (a) scale grown on the inner surface; and (b) scale grown on the outer surface.

Table 2.5.4-1
Cases considered for blockage simulations
for 0.5m-long channels with 0.2mm-thick walls.

Case	Alloy	Location of scale	ID (mm)	OD (mm)
*S1	SS347	inside	0.4	0.8
*S1o	SS347	outside	0.4	0.8
S2	SS347	inside	0.6	1
S2o	SS347	outside	0.6	1
S3	SS347	inside	0.8	1.2
S3o	SS347	outside	0.8	1.2
In1	IN740H	inside	0.4	0.8
In1o	IN740H	outside	0.4	0.8
In2	IN740H	inside	0.6	1
In2o	IN740H	outside	0.6	1
In3	IN740H	inside	0.8	1.2
In3o	IN740H	outside	0.8	1.2

*Code converged only at very small scale thicknesses

The examples used were 0.5m-long flow channels of circular cross section and wall thickness 0.2mm, and major thermal excursions (shut-down events) were assumed at 3-month (2.2kh) intervals, and at each shut down the exfoliated scale was removed. Only an outer (magnetite) layer was considered to exfoliate from the scale formed on TP347H. The results indicate that a larger amount of scale would exfoliate as the tube diameter increased and, in addition, a significantly larger amount of scale (approximately 5x) would exfoliate from the outside (convex) surfaces than from the inside (concave) surfaces. The main differences are that during cool down a tensile component of stress would be imposed of the scale formed on the (larger) outer surface by the retreating alloy, whereas the scale on the inner surface would experience a net compressive stress.

For TP347H transport of oxidants through the inner, adherent Fe-Cr spinel layer controls the overall rate of scale growth so that, following the exfoliation event, the oxidation rate in areas from which the outer (magnetite) layer has been lost is essentially unchanged from that before the exfoliation event. Thus, while the exfoliated mass is predicted to be relatively high during the first two or three shut-down events, because the exfoliated scale is replaced at a slower rate than that at which the original scale was grown, mass loss decreases during subsequent events, as suggested in Figure 2.5.4-1.

For IN740H, in the absence of detailed observations it was assumed that exfoliation involves the full scale thickness. Assuming a scale of uniform thickness, all the scale grown at a given temperature should attain a thickness commensurate with the critical strain for failure at approximately the same time, and would be lost at the first exfoliation event. Subsequently, essentially no further exfoliation would be expected until sufficient time had elapsed that the scale has been regrown to the critical thickness/strain. If the full scale thickness were removed, the rate of re-oxidation of the exposed alloy surface would be the same as that following the original exposure. In practice, since the scale may not be totally uniform in thickness, all the scale would exfoliate in a single event and a mass loss-time curve probably would consist of spikes of major (but possibly not total) loss, interspersed with periods of no loss where the scale had not reached the thickness commensurate with critical strain.

The patterns of exfoliated mass loss with time initially predicted by the model for IN740H are shown in Figure 2.5.4-2. The exfoliated mass from the inside (concave) surface was found to increase steadily with time (and with increased channel diameter), with no indication of a major exfoliation event even after the total exposure assumed (Fig. 2.5.4-2a). The plot for the scale formed on the outer (convex) surface exhibited only one major exfoliation event that occurred after two shut-down events, with a loss of scale some 8-11x the amount lost from the inner surface after the same time. As expected because of the disparity in actual surface areas, the mass lost from the inside surface was smaller than from the outside surface, and the amount of scale lost increased with increasing channel diameter.

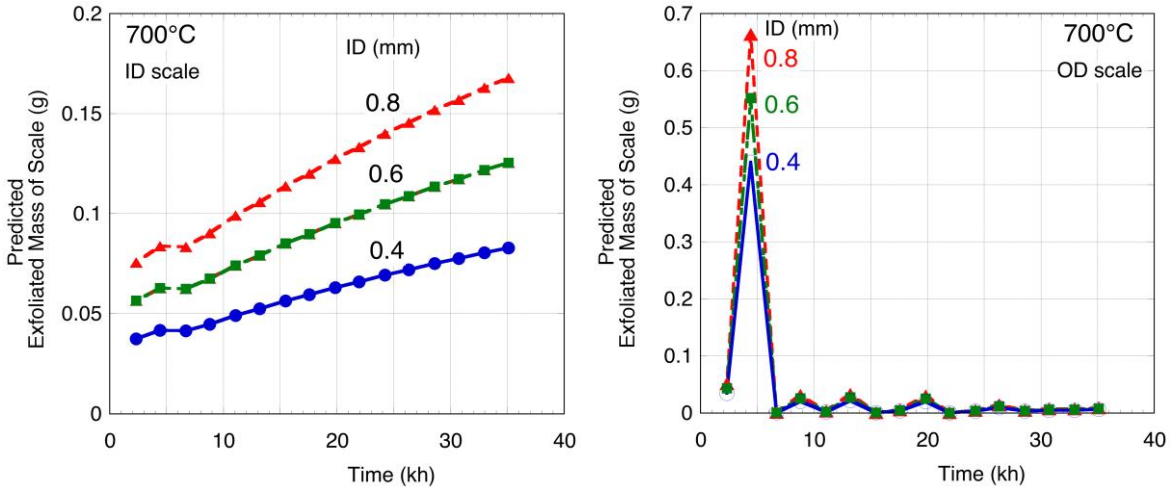

(a) (b)

Figure 2.5.4-2 – Examples of predicted mass loss of scale from a circular section flow channel of IN740H, using a pure elastic model for calculating the stress and strains, for: (a) scale grown on inside surface; and (b) scale grown on the outside surface.

Overall, the predicted behavior of TP347H was entirely in keeping with practical observations and current understanding, whereas the predictions for IN740H were difficult to interpret, and led to re-examination of the procedures used by the model to treat the apparently different exfoliation characteristics of alloys such as IN740H. The main differences between the modeling inputs for TP347H and IN740H were a large difference in rates of oxide growth, and the assumptions associated with a two-layered scale losing only the outer layer compared to a single-layered scale that exfoliated completely. Clearly, further detailed morphological understanding of this area is needed to ensure that the correct sequence of events is incorporated into the model.

2.5.5 — Potential Effects of Thickening Oxide Scales on Heat Exchanger Lifetime

Since the formation of surface oxide scales is inevitable in high-temperature heat exchangers, it is important to recognize how they can affect operation and performance. Here, three scenarios are considered whereby the growth of an adherent, protective oxide scale on the walls of a heat exchanger can affect its service life:

1. Reduction in available flow area (RFA_{ox}) as the oxide scale on the surfaces of the flow passages thickens with time.
2. Depletion of Cr in the tube wall surface (due to the formation of a Cr-rich protective scale) to a level where faster-growing, less protective oxide could develop; and
3. Exfoliation of scale when some critical level of accumulated strain is reached, leading to release of flakes of oxide into the flow stream and potential blockage of flow passages. This scenario involves two connected considerations: (a) the time to attain the critical oxide strain at which scale failure or exfoliation becomes possible, and (b) the acceptable threshold for blockage (% open area).

In order to demonstrate the potential for these three scenarios to modify the lifetime of heat exchangers, their effects were calculated for a typical superheater tube used in utility steam boilers, as described in Appendix F. Note that these calculations were intended only to suggest the relative importance of different failure mechanisms resulting from the increase of scale thickness, rather than providing absolute differences in time-to-failure for a specific configuration of the superheater pendant in a steam boiler. In addition, these comparisons involved first-order approximations by assuming oxide growth under isothermal conditions, and a time-to-failure by scale exfoliation based simply on the oxide growth to attain a specific critical scale thickness.

For Scenarios 1 and 3, the overall model requires algorithms to describe the rate of oxide scale growth in terms of time and local metal temperature. As summarized in Section 2.3.7.B, acceptable algorithms were developed from exposures at 650-750°C in CO_2-3.6 vol% O_2-5.3 vol% H_2O at 200 bar only for Grade 91 and TP304H. These alloys exhibited consistent scale morphologies that permitted extrapolation to the lower temperatures (550-600°C) at which they are likely to be employed. Ferritic alloys VM12 and Crofer 22H exhibited oxidation kinetics that were essentially intermediate between Grade 91 and TP304H but the trend with temperature was inconsistent, possibly indicating a transition in scale morphologies with temperature (increasing Cr diffusion rates). The very thin scales formed on the HT alloys HR3C, IN617, and IN740H presented practical difficulties in obtaining satisfactory thickness measurements; a technique trialed late in the project produced more details of the scale morphologies as well as thickness measurements, but only for specimens exposed at 700°C. In order to include these alloys in subsequent calculations, thickness-based kinetics data from exposure of IN740 in HP steam (650-800°C) were substituted. The recommended scale thickness-based oxidation parameters were listed in Table 2.5.1-2.

Plots of total scale thickness as a function of time and temperature, based on these recommended oxidation algorithms, are shown in Figure 2.5.5-1 for the isothermal oxidation of alloys Grade 91, TP304H, and IN740H. These plots illustrate the large increase in rate of scale growth for Grade 91 at 650°C compared to 600°C, and suggest an oxidation-based temperature limit for this alloy commensurate with recently-recommended temperature limits for steam boilers of 580-600°C [10]. Similarly, the rate of scale growth on TP304H appears to accelerate significantly above 650°C, suggesting that it be restricted to use at or below that temperature. While the rate of scale growth on IN740H also appears to begin to accelerate above 700°C, the actual rates are sufficiently low that the application of this alloy (in terms of oxidation rate) up to 750°C appears to be justified.

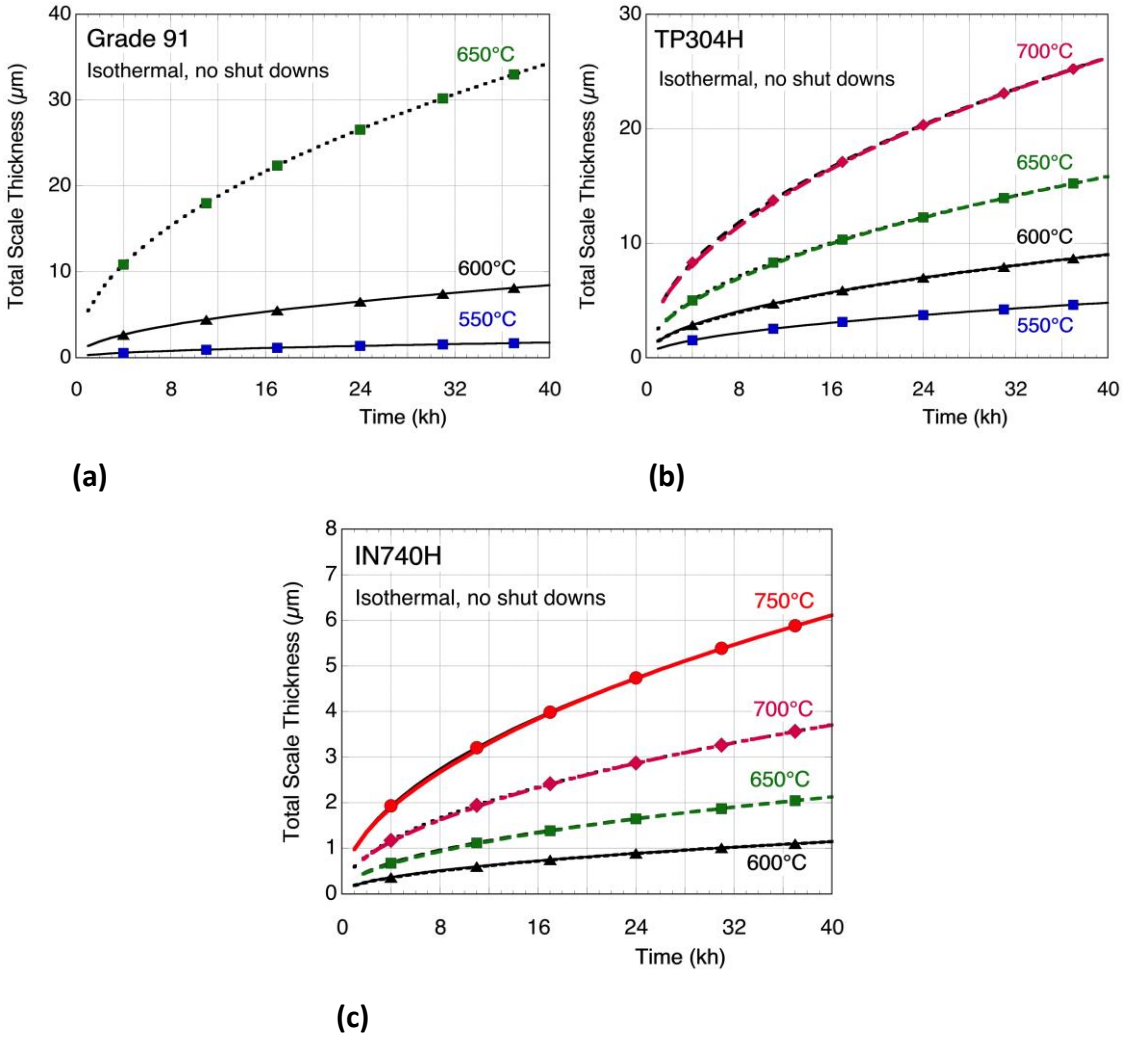

Figure 2.5.5-1 – Thickness-based oxidation kinetics from algorithms derived for use in the model. Note that the data for alloys (a) Grade 91 and (b) TP304H are from exposures in CO_2-3.6 vol% O_2-5.3 vol% H_2O at 200 bar, measured at 650-750°C. Those for (c) IN740H were taken from exposures in 17 bar steam at 650-800°C.

Figure 2.5.5-2 illustrates the influence of the temperature-dependence of oxidation rates on the scale thicknesses formed along a 0.5m-long heat exchanger channel made of Grade 91 after 1 and 2kh for two different thermal gradients: where the gas inlet and outlet temperatures are 550 and 700°C, and 600 and 750°C, respectively. Clearly, channel exit temperatures of 700°C and above should be avoided with this alloy.

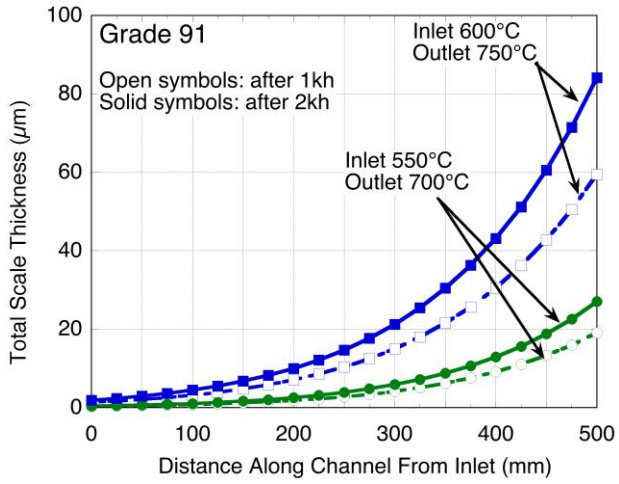

Figure 2.5.5-2 – Variation in scale thickness along a heat exchanger channel for Grade 91 in CO_2-3.6 vol% O_2-5.3 vol% H_2O at 200 bar.

The data plotted in Figure 2.5.5-3 make a similar point for TP304H, reinforcing the suggestion of a temperature limit closer to 600°C than 650°C. The scales formed on IN740H are sufficiently slow-growing that the relatively thin scales formed will not exceed 5 µm after 20kh operation with channel exit temperatures of 750°C (Figure 2.5.5-4a). Figure 2.5.5-4b illustrates that while the same maximum oxide thickness (i.e. potential for increased pressure drop) will be attained in shorter channel lengths under the same operating conditions, the total amount of scale formed (hence amount of scale potentially available to exfoliate) will be reduced.

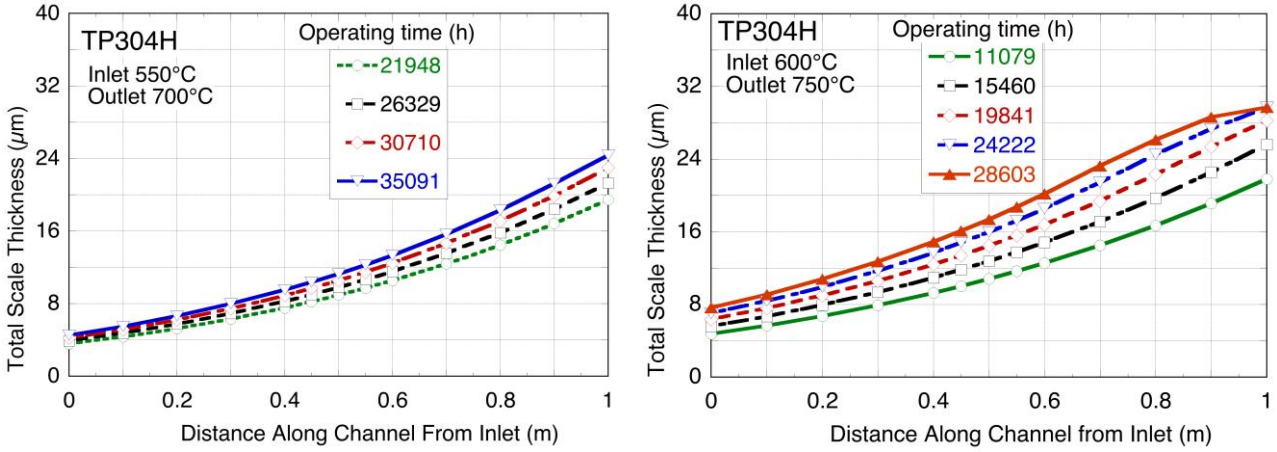

(a) **(b)**

Figure 2.5.5-3 – Variation in scale thickness along a heat exchanger channel for TP304H in CO_2-3.6 vol% O_2-5.3 vol% H_2O at 200 bar for (a) inlet at 500°C, outlet 700°C; and (b) inlet at 600°C, outlet 750°C.

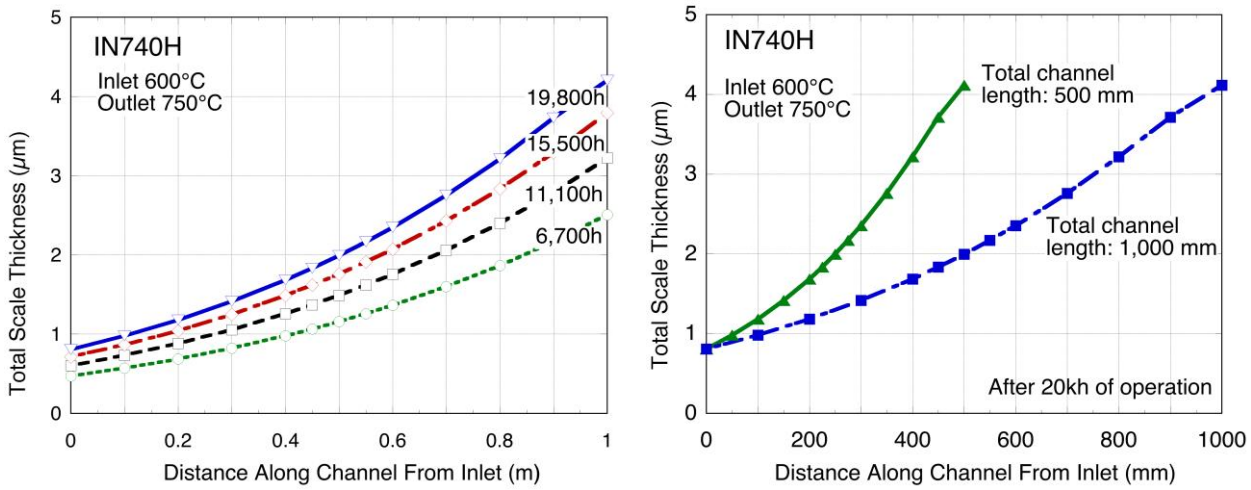

(a) **(b)**

Figure 2.5.5-4 – Scale thickness formed on IN740H in CO_2-3.6 vol% O_2-5.3 vol% H_2O at 200 bar: (a) along a 1m-long channel as a function of time; and (b) after 20kh in heat exchanger channels having the same overall temperature gradients but different lengths.

2.5.5.A - Scenario 1: Reduction in Flow Area From Oxide Growth (RFA_{ox})

A feature of recuperators intended for use in sCO_2 power systems is the use of small flow channels and high flow rates. Thus, avoiding any significant increase in pressure drop is an important criterion for maintaining system efficiency. Inevitably, oxide scales will grow on the surfaces of the metallic channels in contact with the hot fluid, so that the rate of thickening of such scales and its influence on pressure drop becomes an important consideration. Figure 2.5.5-5 illustrates the relationship between increase in pressure drop and reduction in flow area (%RFA).

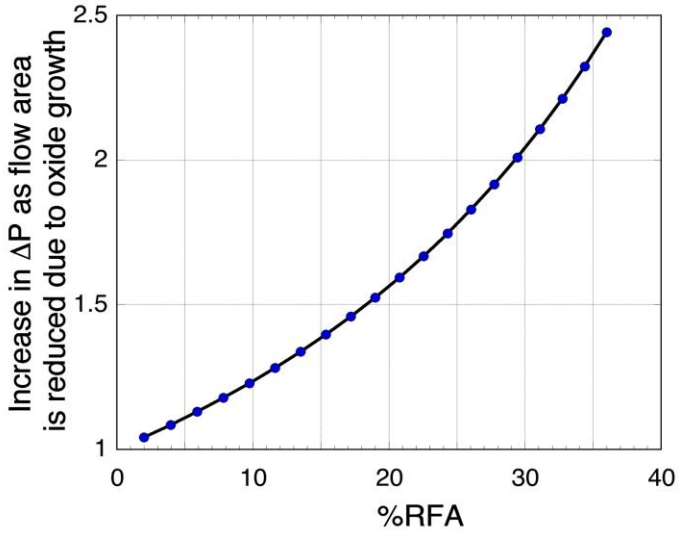

Figure 2.5.5-5 – Relationship of reduction in flow area (%RFA) to increase in pressure drop for laminar flow through a tube.

As shown in Appendix F, the extent of reduction in flow area due to the growth of an adherent oxide scale on the surfaces of a circular cross-section flow passage (RFA_{ox}) is given simply by:

RFA_{ox} = [(cross sectional area corresponding to the original tube bore) – (cross sectional area corresponding to the oxidized tube bore)]/(cross sectional area corresponding to the original tube bore)

i.e. $$RFA_{ox}\ (\%) = [1-(D_b-2d_{ox})^2/D_b^2]*100 \qquad (2.5.5\text{-}1)$$

where:
D_b is the cross sectional area corresponding to the original tube bore; and
d_{ox} is the thickness of the oxide scale

Oxide thicknesses corresponding to specific values of %RFA are listed in Table 2.5.5-3 for different flow channel diameters. For most such flow systems, a reduction in flow area of up to 5% usually is considered acceptable. As an example, for a channel with a 0.6 mm diameter circular cross section, this equates to a uniform scale thickness of 7.6 µm.

Table 2.5.5-3
Calculated values of d_{ox} for specified values of RFA_{ox}.

%RFA_{ox}	**Oxide thickness (d_{ox}) µm**		
Tube ID:	***0.3mm***	***0.6mm***	***0.9mm***
1	0.75	1.5	2.3
2	1.5	3.0	4.5
5	3.8	**7.6**	11.4
10	7.7	15.4	23.1
20	15.8	31.7	47.5
50	43.9	87.9	131.8

Based on the algorithms in Table 2.5.1-2, Figures 2.5.5-6 and 2.5.5-7 compare the times to achieve 1%, 2%, and 5% RFA for 0.3mm diam. channels of alloys Grade 91, TP304H, and IN740H over the temperature range 550 to 750°C, as well as the time for 0.6mm and 0.9mm channels to achieve 5% RFA. Note that these plots required some extrapolation of the oxidation algorithms since actual oxidation kinetics were measured only for 650-750°C. In terms of time to reach a scale thickness of 7.6 µm/5%RFA in a 0.6mm diam. channel, this would be attained in 32,400h (3.7yr) by Grade 91 at 600°C, 9,216h (1.1yr) by TP304H at 650°C, and 61,711h (7.1yr) by IN740H at 750°C (168,236h/19.3yr at 700°C). Some other examples are shown in Table 2.5.5-4, and indicate that the use of 0.3mm diam. channels would lead to unacceptably short lives, even for IN740H at 700°C. Limiting RFA to 1% would reduce the lifetime of 6mm channels of IN740H to 6,641h at 700°C, and 9mm channels to 14,678h at 700°C.

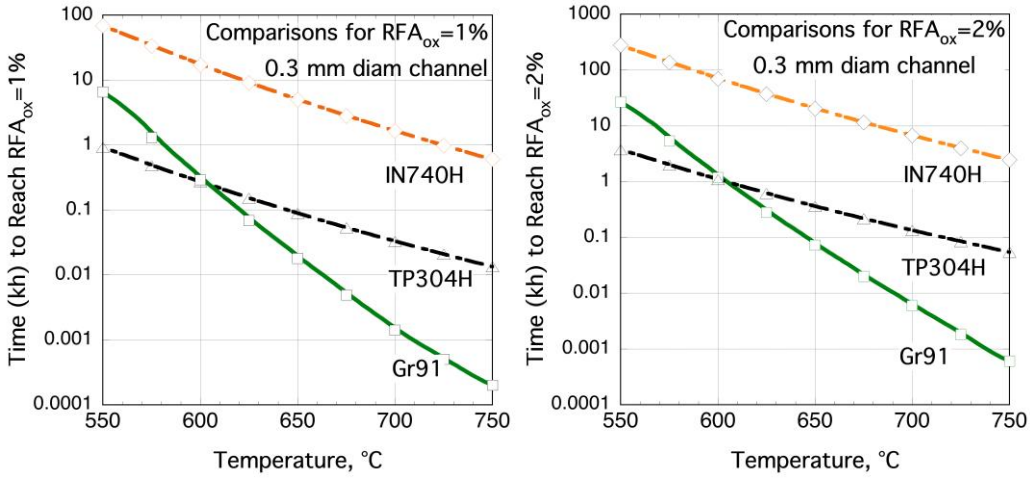

Figure 2.5.5-6 – Comparison of times for 0.3mm diam. channels of Grade 91, TP304H, and IN740H to attain 1 and 2% RFA at 550-750°C in CO_2-3.6 vol% O_2-5.3 vol% H_2O at 200 bar.

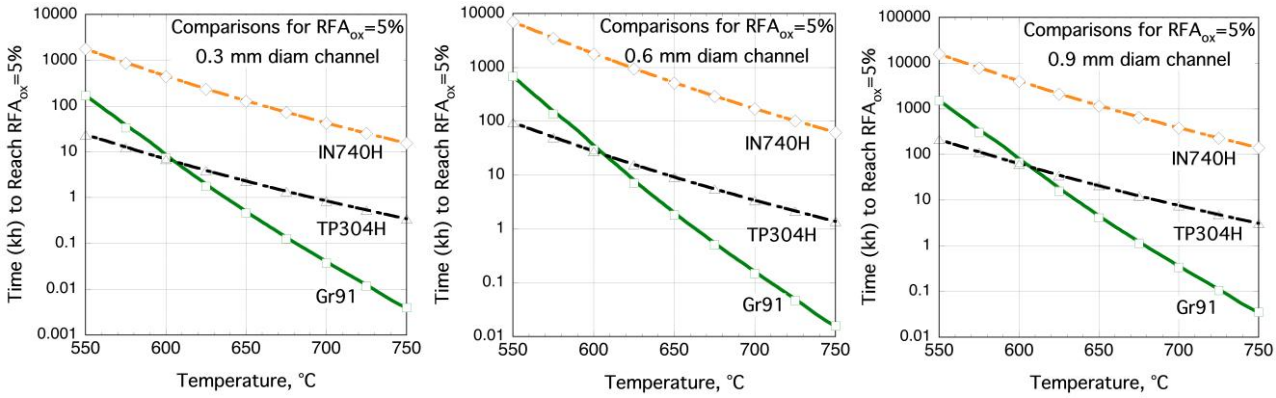

Figure 2.5.5-7 – Comparison of times for 0.3, 0.5, and 0.9mm diam. channels of Grade 91, TP304H, and IN740H to attain 5% RFA at 550-750°C in CO_2-3.6 vol% O_2-5.3 vol% H_2O at 200 bar.

Table 2.5.5-4
Examples of times (in hours) to reach specified values of RFA_{ox} in CO_2-3.6 vol% O_2-5.3 vol% H_2O at 200 bar.

Alloy	T°C	Time (h) to Reach Stated %RFA				
		0.3 mm Channel			0.6mm	0.9mm
	RFA_{ox}:	*1%*	*2%*	*5%*	*5%*	*5%*
Grade 91	**600**	320	1,280	8,100	32,400	72,700
VM12	**600**	30	140	870	3,470	7,800
TP304H	**650**	90	364	2,304	9,216	20,699
IN740H	**700**	1,638	6,641	42,059	168,236	377,867

2.5.5.B - Scenario 2: Exhaustion of Cr Reservoir

The ability of an alloy to form a protective outer oxide scale (usually chromia or a Cr-rich spinel for the alloys considered) requires the presence of a minimum (critical) level of Cr (C_B) at the alloy-environment interface. Since growth of the desired oxide consumes Cr, it is important that the level of Cr at the alloy-oxide interface is maintained above C_B to ensure that predictable, protective oxidation behavior continues. Ideally, during the course of exposure the gradient in Cr concentration that develops from the alloy-oxide interface inward will remain small, so that essentially all of the original Cr content of the alloy (C_0) in excess of the value of C_B will be available to support maintenance of the protective scale. This is generally the case for ferritic alloys at higher temperatures, but for austenitic Fe-Ni-Cr and Ni-base alloys at temperatures in the range of interest it is more usual for a noticeable Cr gradient to develop, so that the available 'reservoir' of Cr in the alloy is less than C_0-C_B.

An approach for modeling the length of time taken for oxide growth to lower the level of the scale-forming element at the alloy surface to C_B has been demonstrated successfully [11,12], as discussed in Appendix F, but only for alumina-forming ferritic alloys operating at temperatures above 1000°C. Under those conditions there is a negligible depletion gradient of Al, which simplifies the calculation. Work to develop a similar approach for calculating reservoir depletion-controlled lifetimes for thin-walled components of chromia-forming Ni-base alloys [13] is at a preliminary stage and was not available for use here. As a result, despite reservations concerning its neglect of Cr depletion gradients, the earlier approach was applied to provide some indications of the potential importance of this Scenario. The time (t_B) for the critical depletion of Cr to C_B to be reached was taken to be (Appendix F):

$$t_B = 2.663\text{x}10^{-6}*[(C_0\text{-}C_B)*w*\rho]^2/k_{pm} \qquad (2.5.5\text{-}2)$$

where:
C_0 the initial Cr concentration (wt%) in the alloy,
C_B the Cr concentration (wt%) in the alloy at transition to less-protective oxide formation,
w is the initial tube wall thickness,
ρ is the alloy density, and
k_{pm} is the mass-based parabolic rate constant for the oxidation process.
Note also that the wall thickness equated to the Cr reservoir was taken to be $w/2$, since Cr loss by oxidation is assumed to be occurring on both inside and outside walls of the heat exchanger channel.

Algorithms that describe the rate of mass gain in CO_2-3.6 vol% O_2-5.3 vol% H_2O at 200 bar in terms of time and local metal temperature were generated in this project for austenitic steel TP304H at 650-750°C. The consistency of the measured mass change data for the HT alloys was considered unacceptable so that, as with the thickness-based kinetics data, results for IN740 (and HR3C) oxidized in HP steam at 600-800°C were substituted. The recommended values were listed in Table 2.5.1-1. The values used for C_B were loosely-based on experimental results for model (binary) alloys [14].

Results of calculations for alloys TP347H, HR3C, and IN740H with wall thicknesses of 0.2 mm exposed in CO_2-3.6 vol% O_2-5.3 vol% H_2O over the temperature range 550-750°C are shown in Figure 2.5.5-8. These data indicate that, for the assumptions made, the lifetimes for HR3C and IN740 at 750°C would

exceed 10 yr. In contrast, TP304H would reach C_B after only 2.2 yr at 650°C. Further results for wall thicknesses of 0.3, 0.5, and 1.2 mm (shown in Table 2.5.5-5) suggest that this Scenario would be life-limiting only for TP304H.

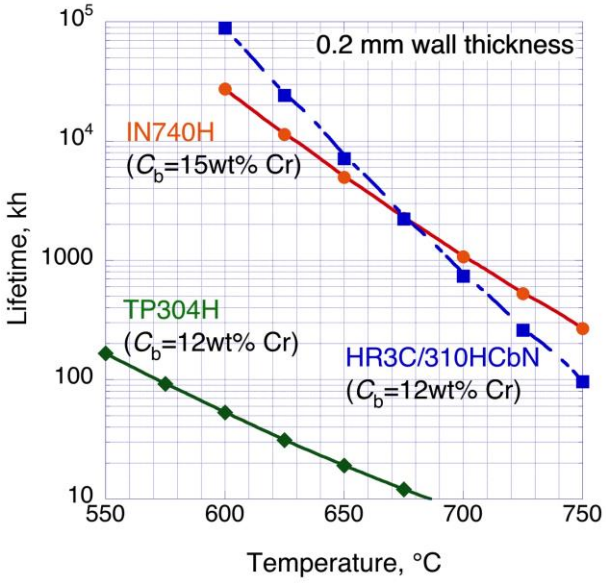

Figure 2.5.5-8 – Comparison of Cr depletion-governed lifetimes times for a 2mm-thick channel wall made from alloys TP304H, HR3C, and IN740H at 550-750°C in CO_2-3.6 vol% O_2-5.3 vol% H_2O at 200 bar.

Table 2.5.5-5
Examples of times (in hours) to reach critical Cr levels for onset of rapid oxide growth (end of service life) in CO_2-3.6 vol% O_2-5.3 vol% H_2O for different channel wall thicknesses.

Alloy	Temp. (°C)	Lifetime (kh)			
Wall Thickness (mm):		***0.2***	***0.3***	***0.5***	***1.2***
TP304H	**650**	19	43	120	692
HR3C	**700**	739	1,663	4,619	26,605
IN740H	**750**	1,070	2,407	6,686	38,509

Note that three unaccounted factors would seriously these projected lifetimes:

1) More severe Cr depletion due to formation of scale on the outer surface of the channel (depending on the temperature),
2) The extent to which the arbitrarily-chosen values of C_B are in error, and
3) The actual Cr depletion gradient in the alloy surface that would decrease the effective Cr reservoir.

2.5.5.C - Scenario 3: Scale Exfoliation

The operating time until scale failure and exfoliation would be expected, and the amount of scale then expected to accumulate in the channels were calculated using the SpallMap and SpalLoop modules of the EPRI-ORNL model [1]. Assumptions concerning the heat exchanger were that it would employ channel lengths of 0.5 or 1m, and would be operated in three-month cycles between shut down events to allow any exfoliated scale to be cleaned out. Based on experience from steam boilers, it was assumed that the deposits formed would have a porosity of 25%, and that the length of deposits of accumulated exfoliant could be approximated as 10x the channel diameter. Deposition is expected to occur immediately upstream of any major change in the flow stream, such as a right-angled bend.

Results for 0.5 and 1.0m-long channels of diameters 0.3 and 0.6mm of alloy TP304H, expressed in terms of area fraction blocked by exfoliated scale as a function of operating time, are shown in Figure 2.5.5-9 for channel inlet and outlet temperatures of (a) 550 and 700°C, and (b) 600 and 750°C. In all cases, exfoliation initiated earliest in the smallest diameter channel, and the amount of deposit (predicted blockage fraction) was greatest in the longest channels (greater length of tube providing exfoliated scale). The large effect of increasing temperature is evident from comparison of the two plots: since each data point indicates the mass exfoliated at 3-month intervals it is evident that for the lower-temperature case that exfoliation in the 3mm diameter starts after approx. 26kh (36 months) compared to approx. 11kh (15 months) in the higher-temperature case. These results suggest that the heat exchanger need not be shut down for cleaning for at least 39 and 18 months (28 and 13kh), respectively. The predicted blockage fraction for a 1m-long, 0.3mm diam. channel attained a value of 0.05 (RFA_B = 5%) after 30.8kh for the conditions of 550°C inlet and 700°C outlet, compared to only 12.2kh for 600°C inlet and 750°C outlet. Nevertheless, these times are significantly longer for the conditions of 550°C inlet and 700°C outlet than the time to reach a value of RFA_{ox} = 5% (2.3kh) due to simple oxide thickening at 650°C

Sufficient exfoliation from alloy IN740H to lead to blockage (RFA_B) equivalent to 5% RFA in 1m-long, 3mm diam channel was predicted after 18.7kh, and after 22.4kh for a 0.5m-long channel, both operated at 600°C inlet and 750°C outlet (Figure 2.5.5-10). This compares to 42kh to attain RFA_{ox} = 5% in a 3mm diam. channel of IN740H from oxide thickening at 700°C. These and examples for 6mm diam. channels also are shown in Table 2.5.5-6.

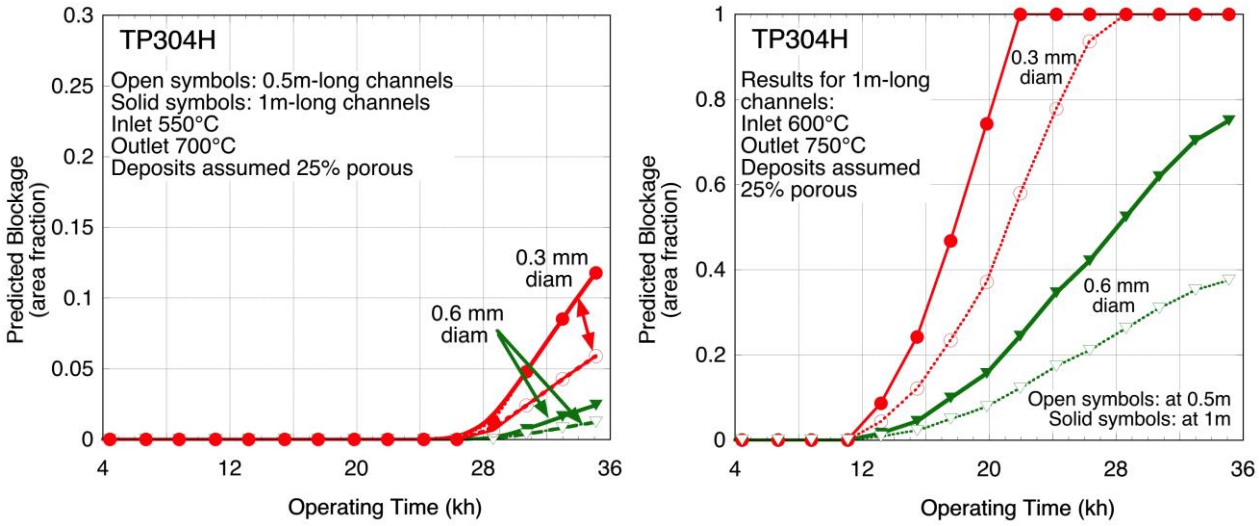

(a) **(b)**

Figure 2.5.5-9 – Comparison of times for the onset of blockage due to exfoliation from channels made from Alloy TP304H operated in CO_2-3.6 vol% O_2-5.3 vol% H_2O at 200 bar at (a) 550°C inlet-700°C outlet; and (b) 600°C inlet-750°C outlet.

Table 2.5.5-6

Examples of times to reach specified values of RFA_B = 5% in CO_2-3.6 vol% O_2-5.3 vol% H_2O.

Alloy	Temp. (°C)	Lifetime (kh)			
Channel Length (m):		***0.5***		***1.0***	
Channel diam (mm):		***0.3***	***0.6***	***0.3***	***0.6***
TP304H	***550-700***	33.9	>>40	30.8	>40
	600-750	13.2	17.5	12.2	15.6
IN740H	***600-750***	22.4	>40	18.7	28.6

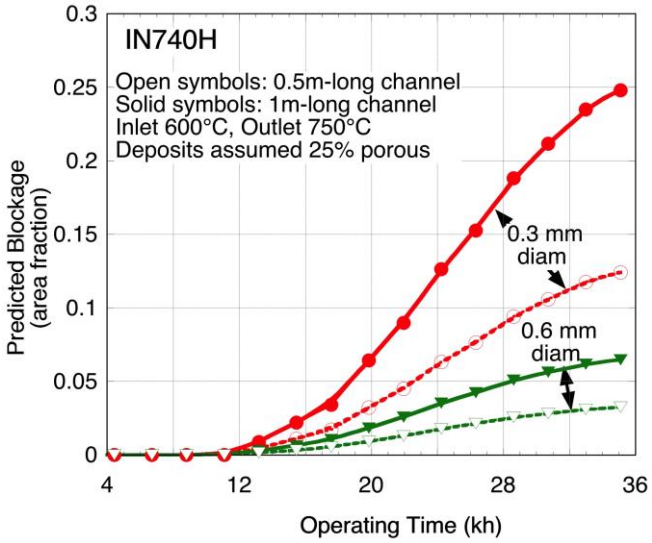

Figure 2.5.5-10 – Comparison times for the onset of blockage due to exfoliation from channels made from Alloy IN740H operated at 600°C inlet-750°C outlet in CO_2-3.6 vol% O_2-5.3 vol% H_2O at 200 bar.

2.5.5.D - Summary of Relative Importance of Scenarios Considered

Because of the high temperatures at which it is planned to operate sCO_2 recuperators, the rate at which oxide scales grow and thicken on alloys in contact with the gas is an important consideration. The two scenarios that explicitly consider reduction in flow area due to oxide growth (and exfoliation) are connected, since while protective oxidation behavior contributes to progressive increase in RFA_{ox}, reduction in flow area by exfoliation (RFA_B) usually is a singular occurrence that occurs at specific intervals (associated with thermal shocks such as heat exchanger shut-down events). Depending on the detailed morphology of the oxide scales, the material lost by exfoliation may constitute part or all of the thickness of the initially-protective scale that contributed to RFA_{ox}. Upon restarting the heat exchanger when the exfoliant contributing to the RFA_B has been removed, the value of RFA_{ox} associated with the affected length of channel will be reset (reduced), and the effective value of the RFA_{ox} then will be set by the thickest adherent scale remaining in that channel.

Experience of scales grown in HP steam is that exfoliation from ferritic steels such as Grade 91 and austenitic steels such as TP304H typically involves an outer layer of scale (magnetite), and that the remaining adherent scale continues to grow at a similar rate as immediately prior to the exfoliation event. For some HT alloys that form scales that are essentially single layers it is expected that the full scale thickness will be lost upon exfoliation, but understanding of such cases is lacking.

For the examples considered there appear to be sets of conditions (for TP304H, for instance) where protective scale growth will attain values of $RFA_{ox} \geq 5\%$ before any exfoliation is likely, complication the setting of criteria for channel life or refurbishment by removing the scale by mechanical or chemical means. Such considerations emphasize the importance of accurate knowledge of the rates and modes of scale growth and failure.

The scenario where consumption of the reservoir of Cr in the channel wall by continued growth of protective scale reduces the Cr level at the alloy-oxide interface to a value where the protective layer no longer can be supported, leading to much faster rates of scale growth, appears to be life-limiting only for alloy TP304H (for the conditions of temperature and wall thickness considered). Obvious remedies would be to reduce the temperature and/or increase the thickness of the channel wall, or to use a more oxidation-resistant alloy. For IN740H (and presumably HT alloys with similar oxidation behavior) this scenario appears to lead to lifetimes somewhat longer than those directly causing reduction in flow area (for the conditions considered).

2.5.6 — References Cited in Section 2.5

1. A.S. Sabau, I.G. Wright, J.P. Shingledecker, and P.F. Tortorelli, "Managing oxide scale exfoliation In boilers with TP347H superheater tubes," *Proc. 7th International Conference on Advances in Materials Technology for Fossil Power Plants*, Waikoloa, Hawaii. EPRI 2014.
2. J. Armitt, D.R. Holmes, M.I. Manning, D.B. Meadowcroft, and E. Metcalfe, *The Spalling of Steam-Grown Oxide From Superheater and Reheater Tube Steels,* EPRI Report No. FP-686, Feb 1978.
3. M. Shütze, M. Malessa, D. Renusch, P.F. Tortorelli, I.G. Wright, and R.B. Dooley, "Mechanical properties and adherence of oxide scales," *Materials Science Forum*, 522, 393-400 (2006).
4. R.G. Brese, J.R. Keiser, and B.A. Pint, "Effect of thermal cycling on compatibility in CO_2 for concentrated solar power applications," *Oxidation of Metals*, 87, 631-642 (2017).
5. I.G. Wright, DOE FWP No. FEAA061: *Oxidation of Candidate Alloys in Steam at 17 bar—Final Report on Phase 1 Efforts in Support of the U.S. Consortium Program on Boiler Materials for Ultra-Supercritical Coal Power Plants*, ORNL/TM-2009/232, Nov 2009.
6. E.W. Lemmon, M.L. Huber, and M.O. McLinden, *NIST Standard Reference Database 23: Reference Fluid Thermodynamic and Transport Properties-REFPROP version 8.0*, National Institute of Standards and Technology, Standard Reference Data Program, Gaithersburg (2007).
7. X. Li, R. Le Pierres and S. Dewson, "Heat exchangers for the next generation of nuclear reactors," *Proc. ICAPP*, 6, 4-8 (2006).
8. I.H. Kim, H.C. No, J.I. Lee, and B.G. Jeon, "Thermal hydraulic performance analysis of the printed-circuit heat exchanger using a helium test facility and CFD simulations," *Nuclear Engineering and Design*, 239, 2399-2408 (2009).
9. A.S. Sabau and I.G. Wright, "Influence of oxide growth and metal creep on strain development in the steam-side oxide in boiler tubes," *Oxidation of Metals*, 73, 467-492 (2010).
10. "Grade 91 Use Temperature Limits," *EPRI Proposed User Guideline*, May 2016.
11. W.J. Quadakkers and K. Bongartz, "The prediction of breakaway oxidation for alumina-forming alloys using oxidation diagrams," *Werkstoffe u Korrosion*, 45, 232-241 (1994).
12. W.J. Quadakkers and M.J. Bennett, "Oxidation-induced lifetime limits of thin-walled, iron-based, alumina-forming, oxide dispersion-strengthened alloy components," *Mat. Sci & Techn.,* 10, 126-131 (1994).
13. R. Duan, A. Jalowicka, K. Unocic, B.A. Pint, P. Huczkowski, A. Chyrkin, D. Grüner, and W.J. Quadakkers: Work in progress at Jülich and Oak Ridge National Laboratories on *Predicting Oxidation-Limited Lifetime of Thin Walled Components of NiCrW Alloy 230* (2016).
14. G.C. Wood, I.G. Wright, T. Hodgkiess, and D.P. Whittle, "A Comparison of the Oxidation of Fe-Cr and Co-Cr Alloys in Oxygen and Water Vapor," *Werkstoffe und Korrosion*, 21, 900 (1970).

3 Products

3.1 - Conference papers, or other public releases of results

- Presentation to a DOE Peer Review Panel.
- Presentation at the International Conference on Corrosion in Power Plants
- Presentation at the *2016 Crosscutting Research & Rare Earth Elements Portfolios Review Meeting,* Pittsburgh, Pennsylvania, 2016.
- J.P. Shingledecker, S.C. Kung, D. Thimson, I.G. Wright, B.M. Tossey, and A.S. Sabau, "Oxidation/Corrosion in materials for supercritical CO_2 power cycles," presented at the *5th International sCO2 Power Cycle Symposium*, San Antonio, Texas, Mar 29-31, 2016.
- A.S. Sabau, J.P. Shingledecker, S.C. Kung, I.G. Wright, and J. Nash, "Exfoliation propensity of oxide scales in heat exchangers used for supercritical CO_2 power cycles," presented at the *5th International sCO2 Power Cycle Symposium*, San Antonio, Texas, Mar 29-31, 2016.
- "Materials degradation in supercritical CO_2 power cycle," presented at the *Materials Science & Technology 2016 Conference,* Salt Lake City, Utah, October 2016.
- Presentation at the *2017 Project Review Meeting for Crosscutting Research and Analysis, Gasification Technologies, and Rare Earth Element Research Portfolios Review Meeting,* Pittsburgh, Pennsylvania, March 20, 2017.
- S.C. Kung, J.P. Shingledecker, I.G. Wright, T. Lolla, and A.S. Sabau, "Corrosion of heat exchanger alloys in open-fired sCO_2 power cycles," *6th International Supercritical CO2 Power Cycles Symposium*, Pittsburgh, Pennsylvania, March 27-29, 2018.
- T. Lolla, S.C. Kung, J.P. Shingledecker, I.G. Wright, and A.S. Sabau, "Characterization of Oxide Scale Structures on Alloys exposed to Open-Fired sCO_2 Power Cycles," *6th International Supercritical CO2 Power Cycles Symposium*, Pittsburgh, Pennsylvania, March 27-29, 2018.

3.2 - Networks or collaborations fostered

- Participation in a joint *NETL-EPRI Workshop on Heat Exchangers for sCO2 Power Cycles*, San Diego, California, Oct 15, 2015.
- S.C. Kung, J.P. Shingledecker, T. Lolla, A.S. Sabau, and I.G. Wright, "Predicting the Oxidation/Corrosion Performance of Structural Alloys in Supercritical CO_2," presentation at the *2017 University Turbine Systems Research Project Review*, Pittsburgh, Pennsylvania, Nov 2, 2017.
- J.P. Shingledecker, "Predicting the Oxidation/Corrosion Performance of Structural Alloys in Supercritical CO_2," WebEx presentation, December 18, 2017

3.3 - Technologies/Techniques developed

N/A

3.4 - Other products, such as data or databases, models, instruments or equipment

N/A

4 Recommendations

A significant amount of new information has been generated from this project, which leads to improved understanding of the oxidation and corrosion behaviors of structural alloys exposed to high-temperature, high-pressure sCO_2. Additional research is recommended to further advance the corrosion knowledge so that suitable selection of materials can be made to ensure reliable and safe operation of the sCO_2 power systems under design. Specifically, the following areas of research are proposed.

1. Perform additional characterization on samples that had been exposed to the test conditions of this project:
   - Samples of various alloys and HX subcomponents had been subjected to the 1,000-5,000h tests at700^{o}C. These materials were outside the scope of the current study but were added to the tests when space became available. Due to budget constraints, performing detailed characterization of these samples was not possible. It is believed that analysis of these samples, especially the exposed HX subcomponents, would produce invaluable information to benefit the design of sCO_2 power systems.
   - The potential of carburization for alloys exposed to sCO_2 was demonstrated in this study by means of micro-hardness measurements. Validation of carburization should be further performed using other advanced analytical techniques on selected samples, such as SIMS and GDOES.
2. Perform additional oxidation and corrosion testing
   - 'Static' test systems implemented in laboratories do not allow full understanding of the role of impurities in sCO_2 oxidation and corrosion. Therefore, more studies with better test system design are desired.
   - The transformational fossil power systems prefer the use of syngas as a fuel. As a result, better understanding of the impact of other impurities, such as sulfur and chlorine species, on the oxidation and corrosion of structural alloys is necessary
   - As demonstrated in this study, long-term corrosion data were critical to generating reliable kinetic data. Therefore, future research should focus on long-term testing at a wide range of temperatures
3. Advanced modeling is essential to the success of sCO_2 power systems
   - Limited long-term data were generated from this study and utilized for the model development. Additional longer-term kinetic data are needed.
   - Results of the current study indicated that RFA (Reduction in Flow Area) in compact heat exchangers could have a major effect on the sCO_2 system performance. It is necessary to validate the impact of RFA on heat exchangers through field testing in a STEP pilot plant under construction.
   - Further understanding of carburization in alloys exposed to sCO_2 must be rigorously pursued.

Appendix A

Optical photomicrographs, SEM/BSE images and EDS maps of alloys exposed at 650°C for 300, 628, and 1,000h in CO_2 containing 3.6 vol.% O_2 and 5.3 vol.% H_2O at 200 bar

GRADE 91

300 hours

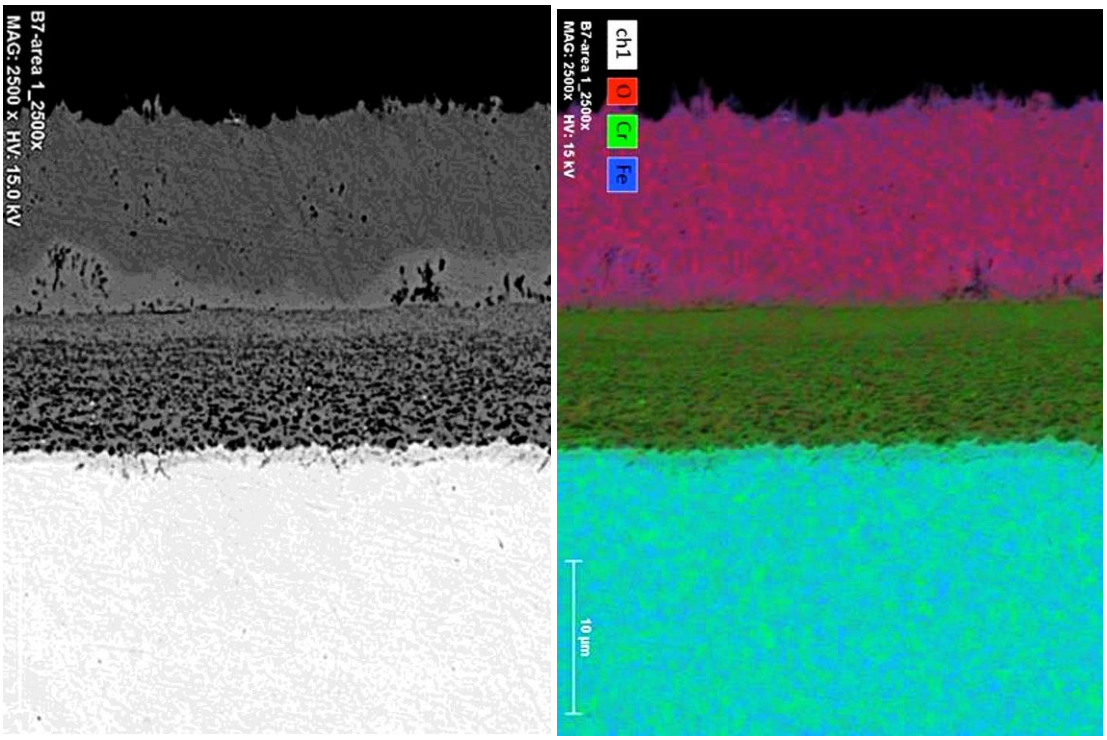

300 hours

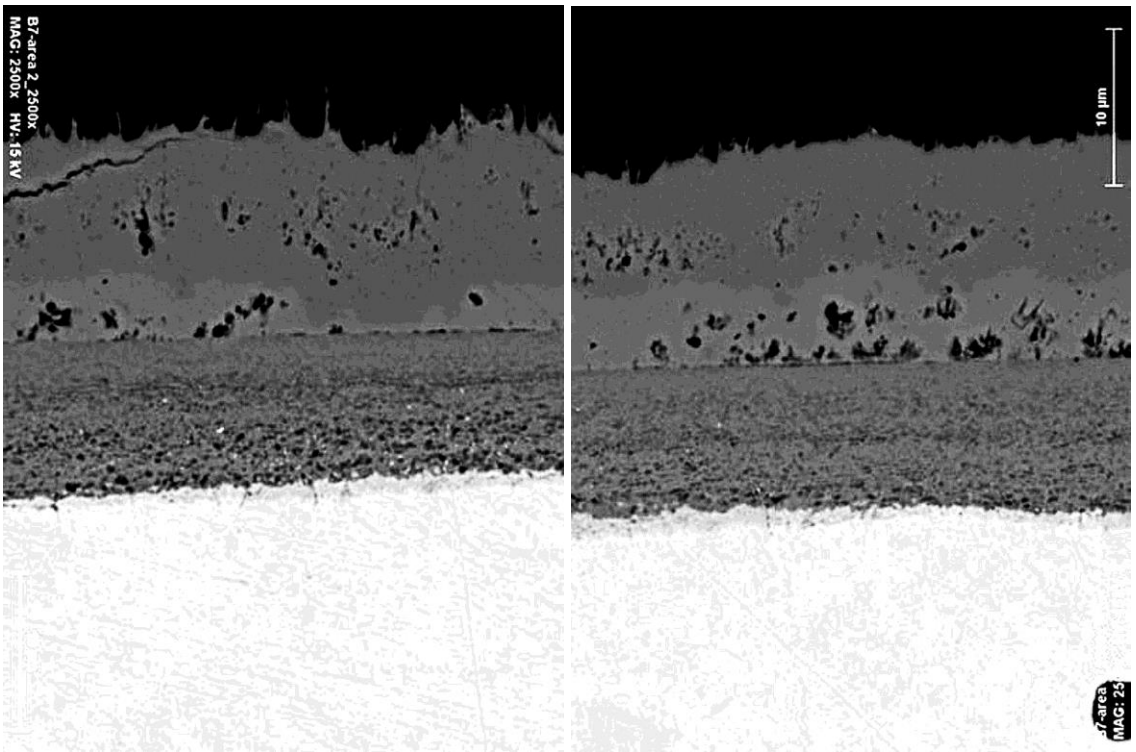

GRADE 91

628 hours

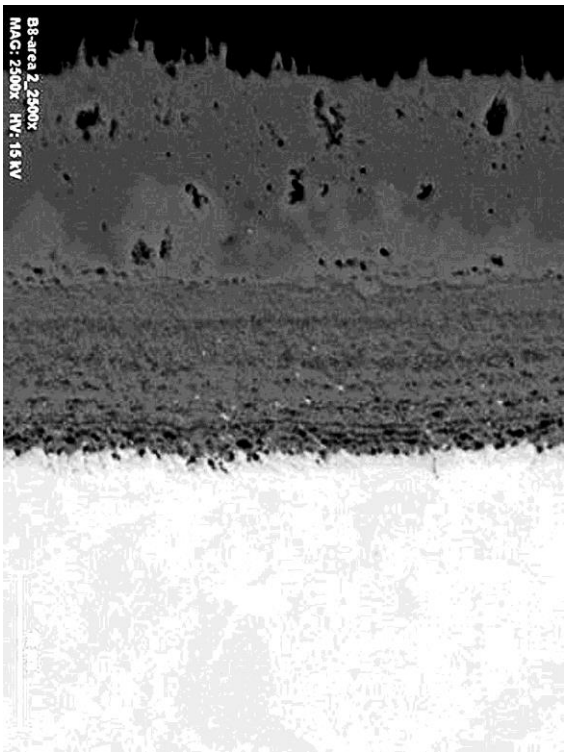

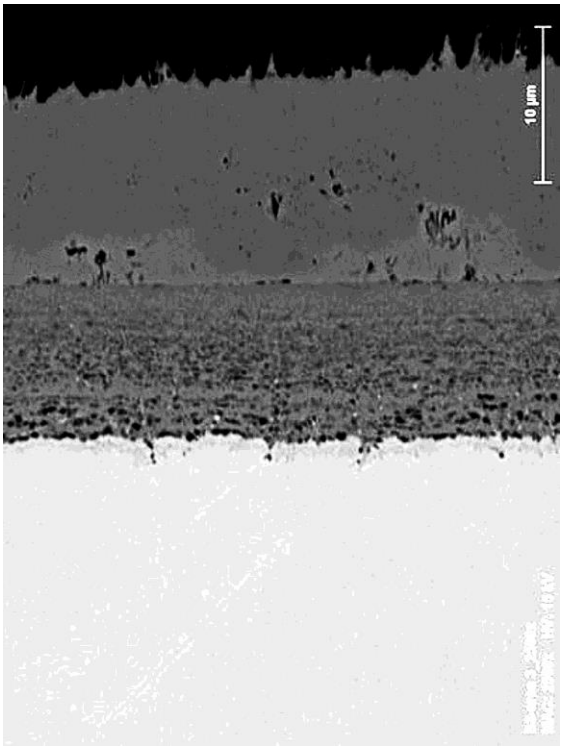

1,000 hours

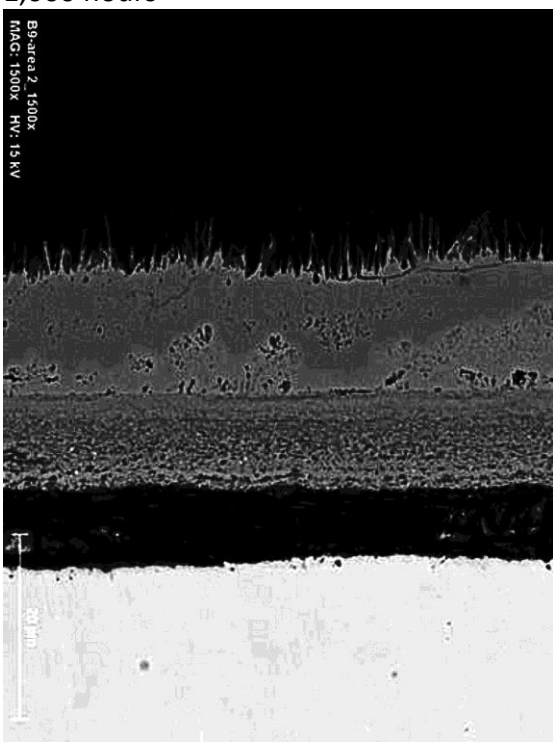

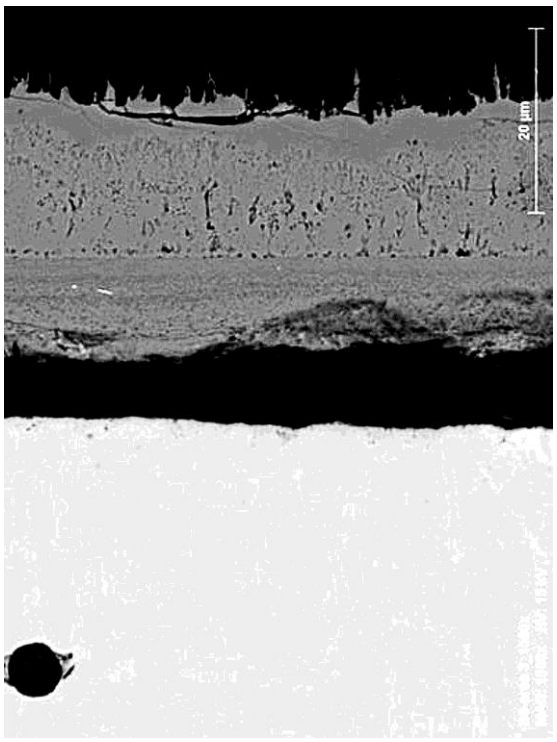

VM 12

628 hours

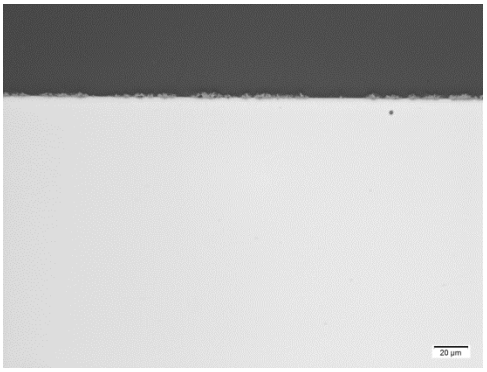

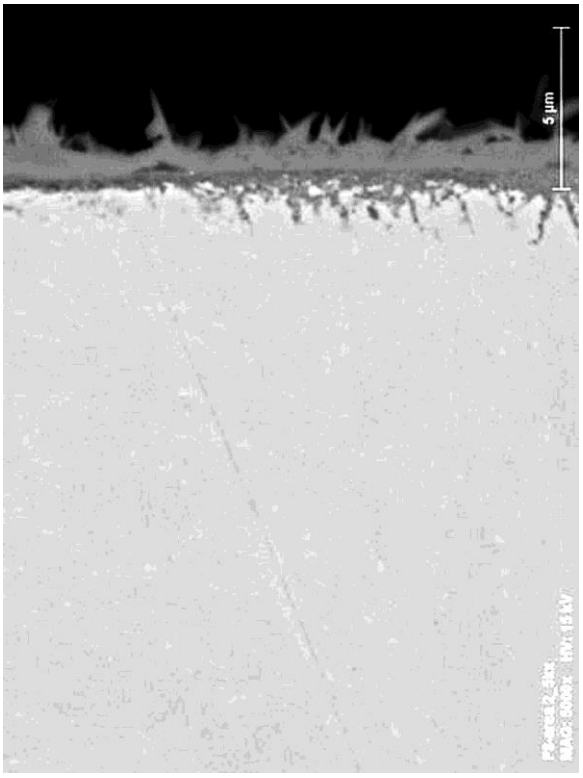

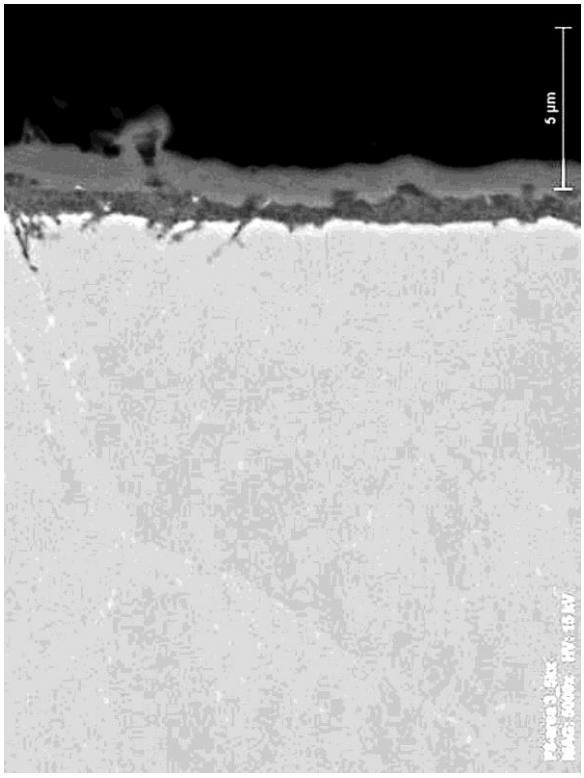

VM 12

1,000 hours

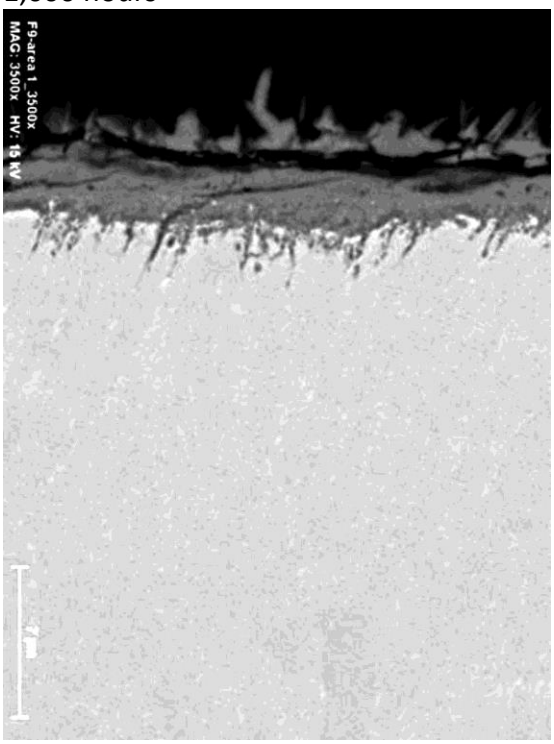

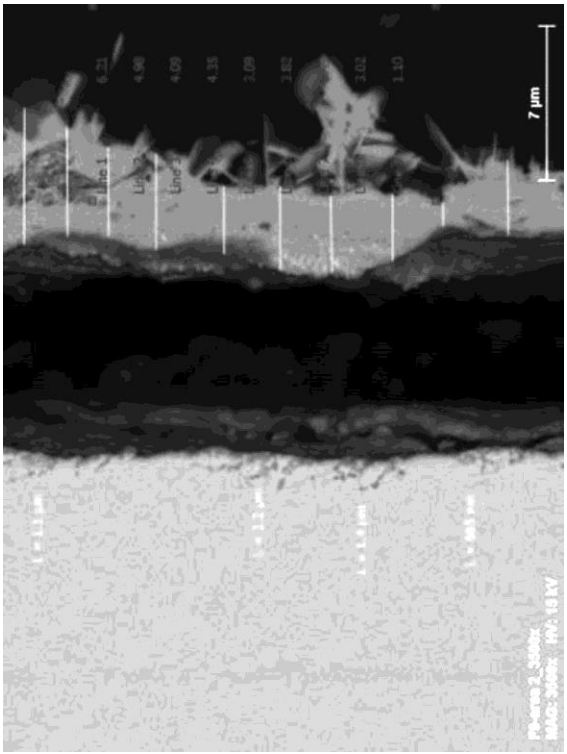

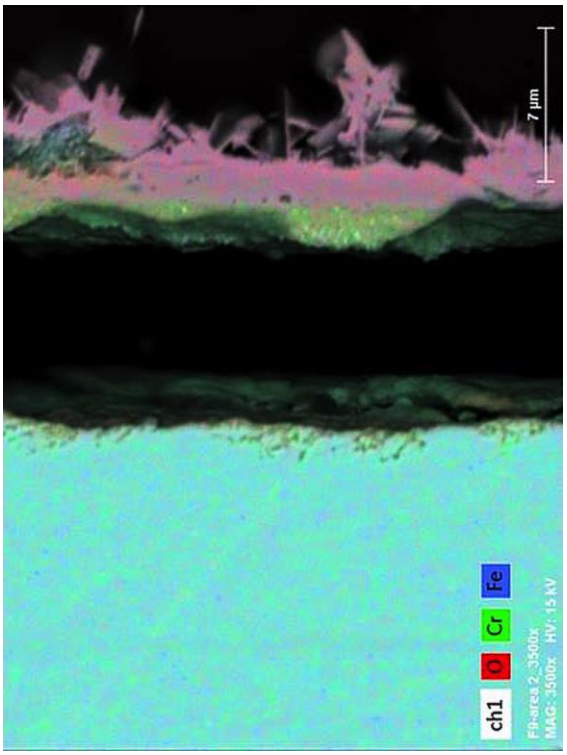

VM 12

1,000 hours

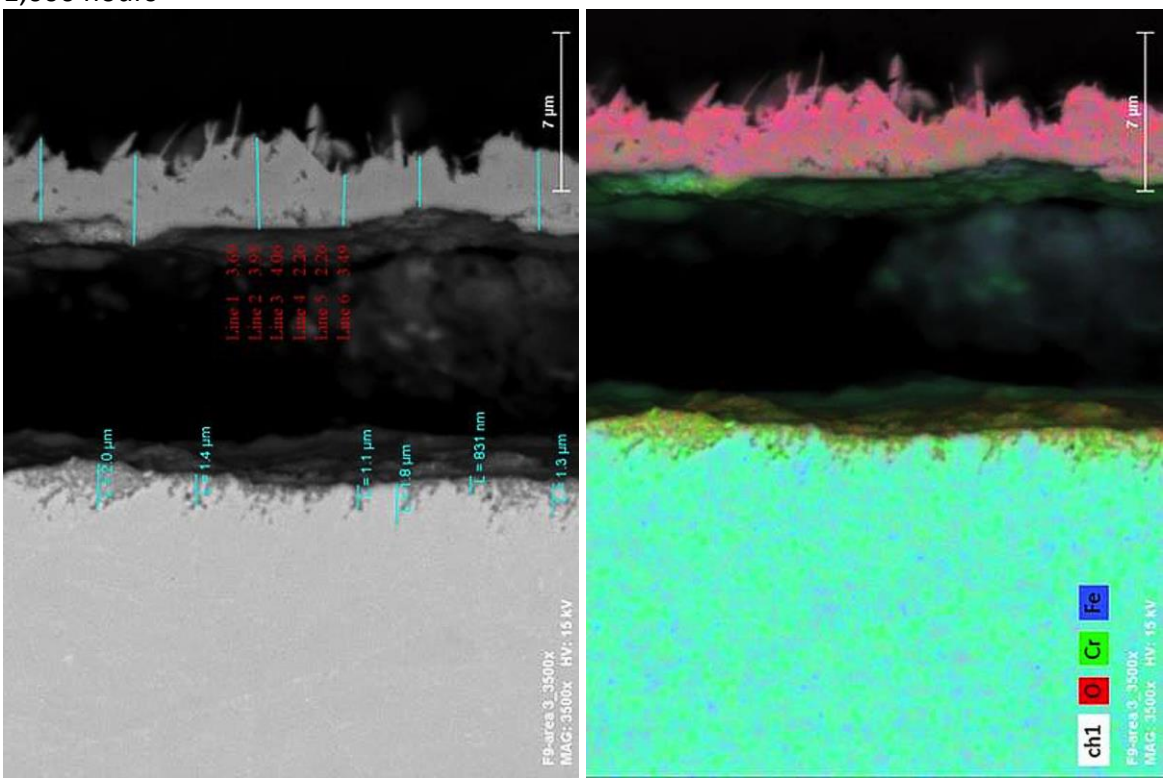

CROFER 22 H

628 hours

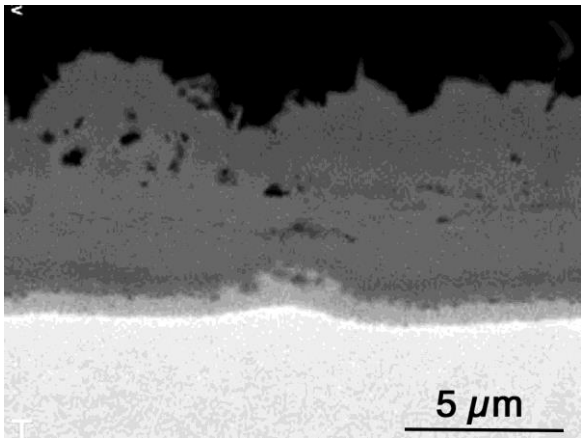

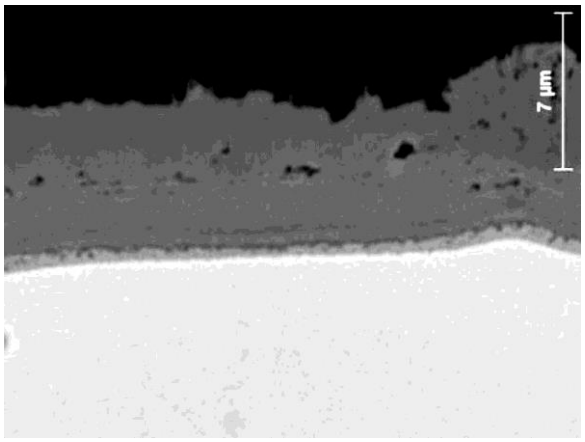

628 hours

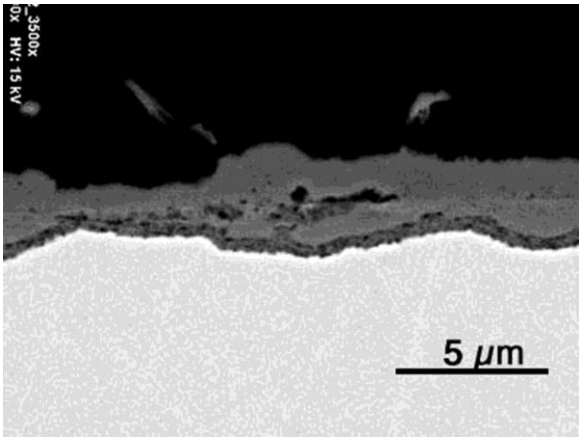

1,000 hours

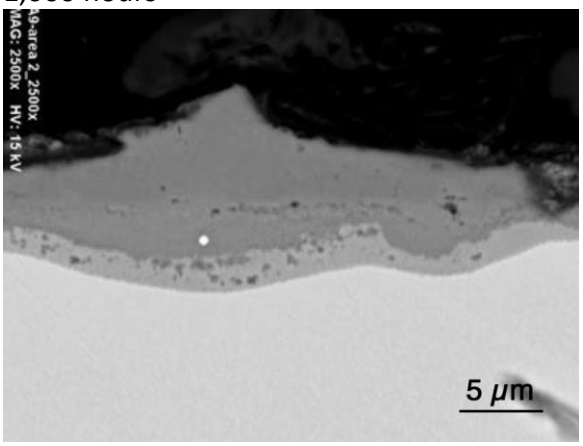

TP304H

300 hours

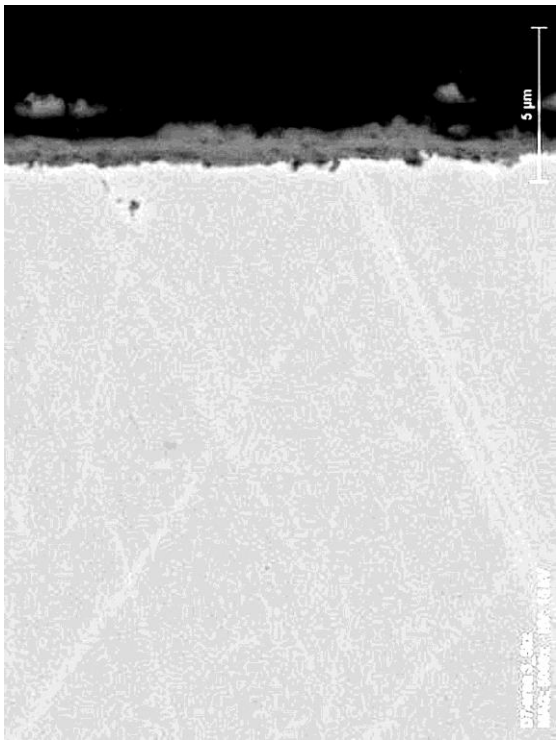

628 hours

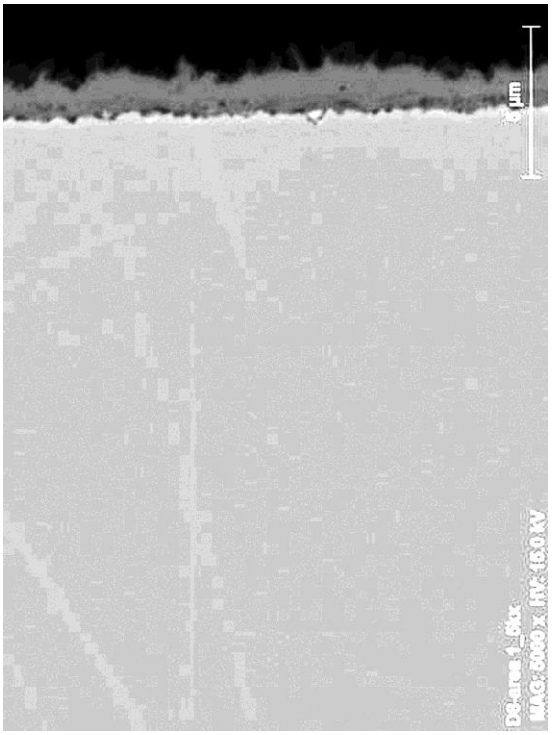

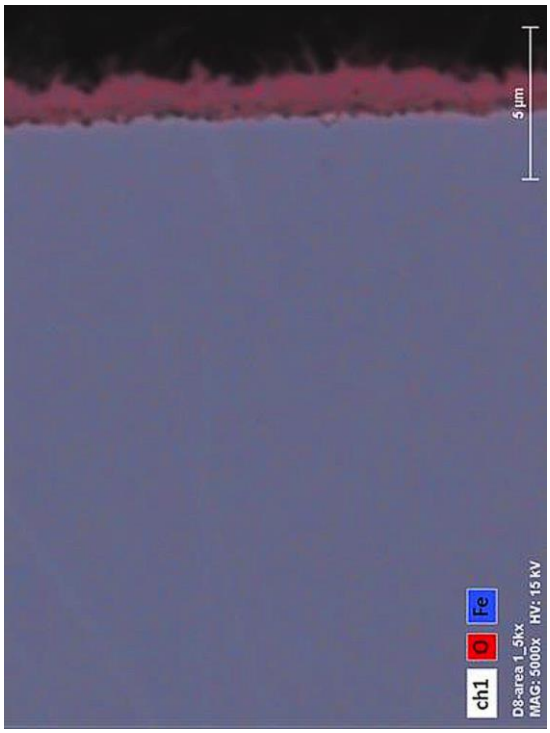

TP304H

628 hours

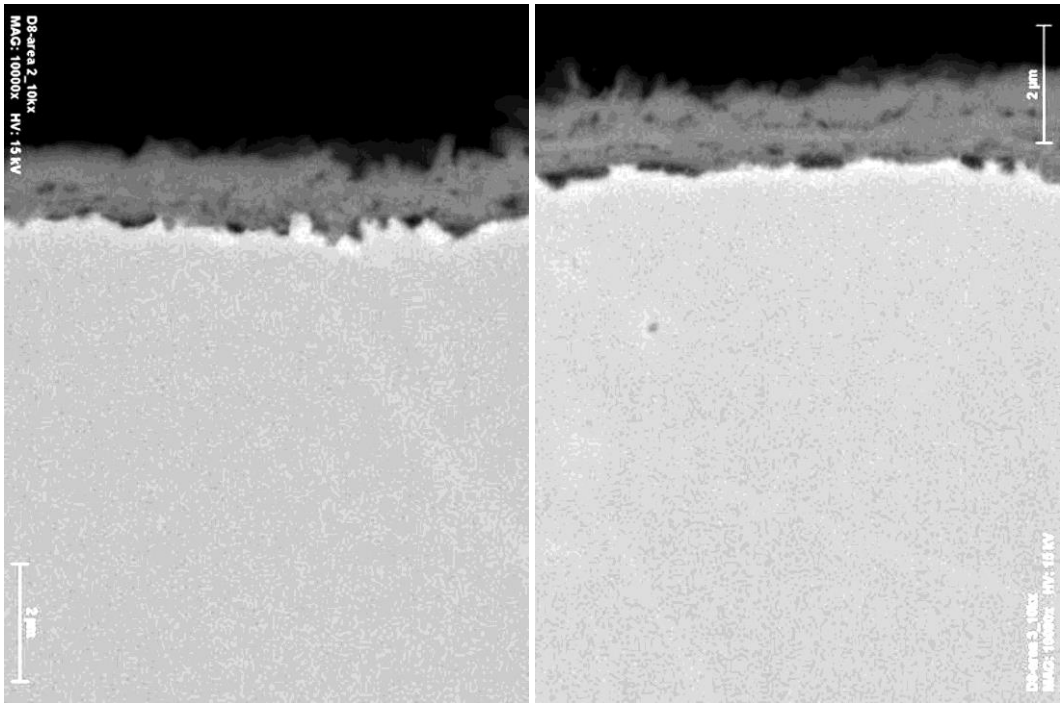

1,000 hours

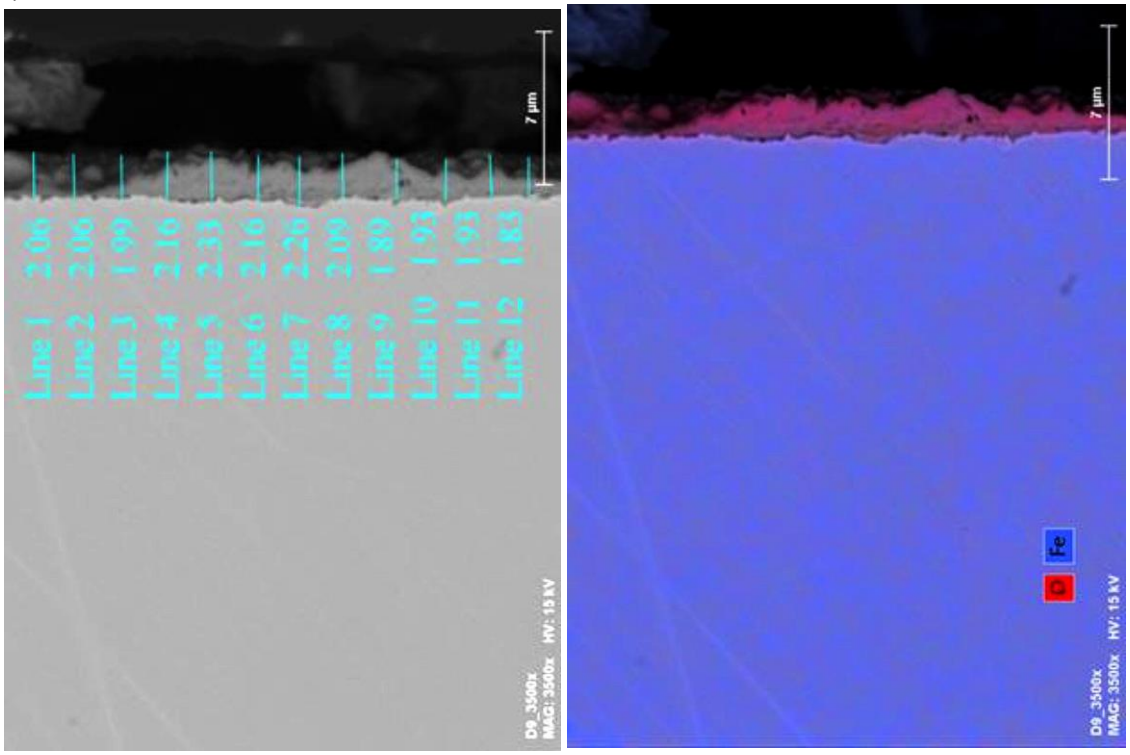

Appendix B

Optical Photomicrographs, SEM/BSE Images and EDS Maps of Alloys Exposed at 750°C for 300, 628, and 1,000h to CO_2 Containing 3.6 vol.% O_2 and 5.3 vol.% H_2O at 200 bar

GRADE 91

300 hours

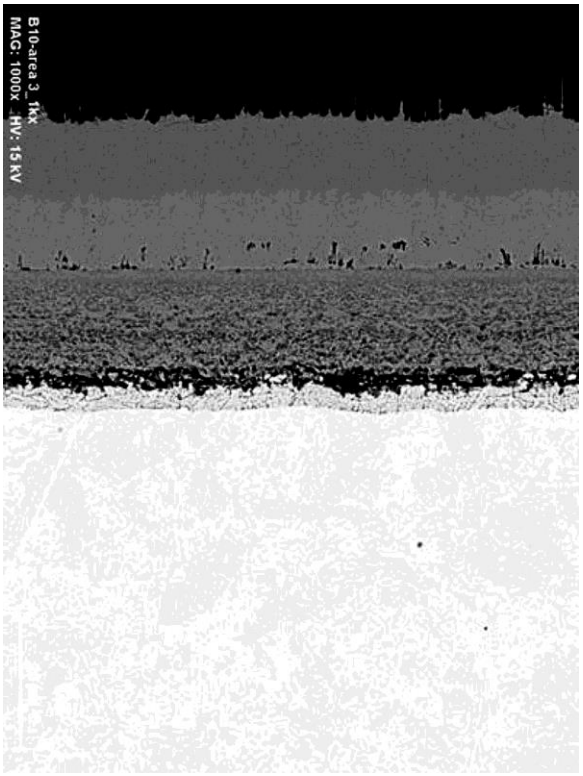

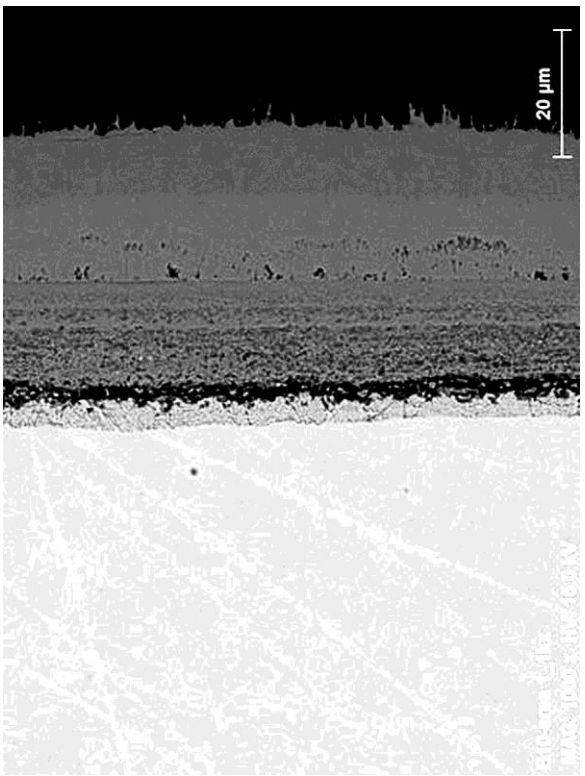

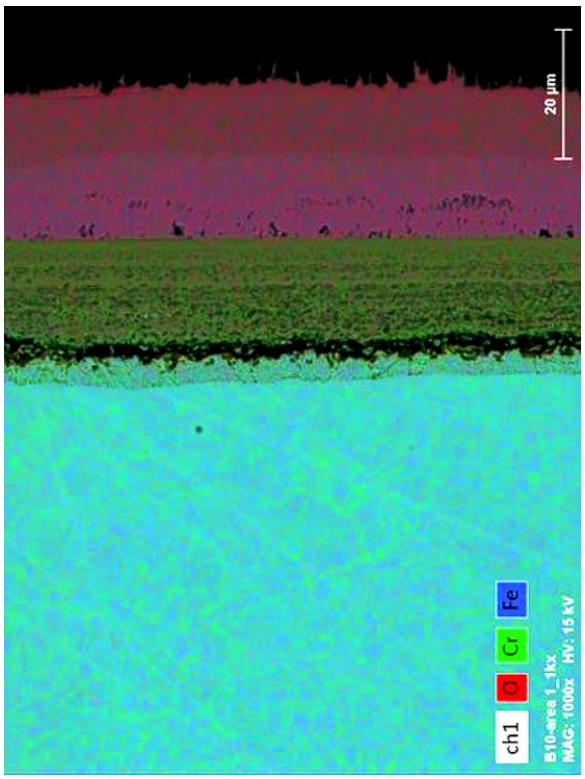

GRADE 91

628 hours

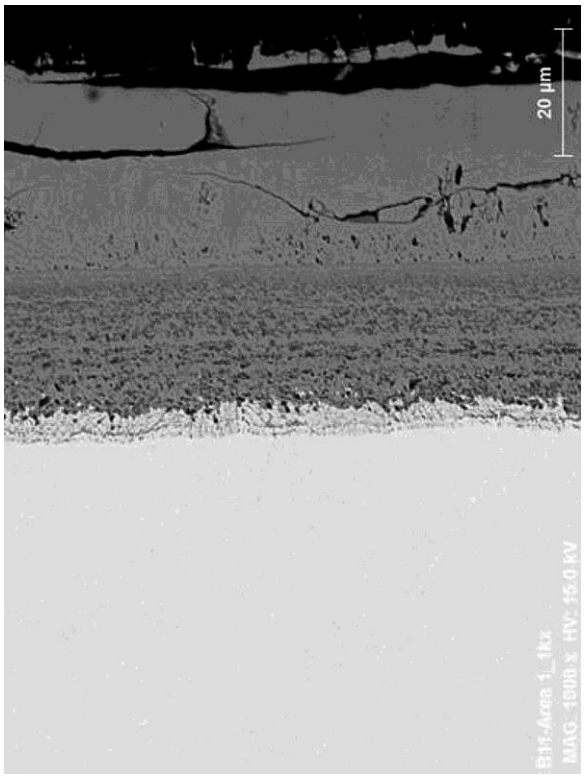

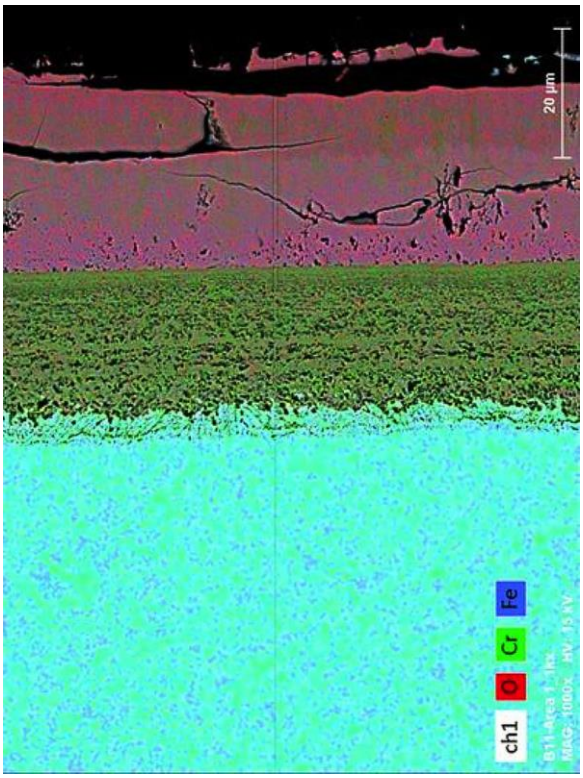

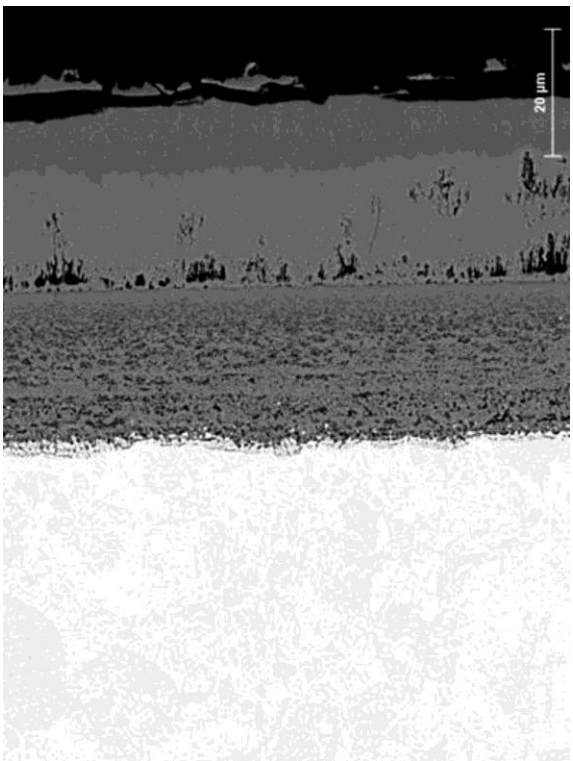

628 hours

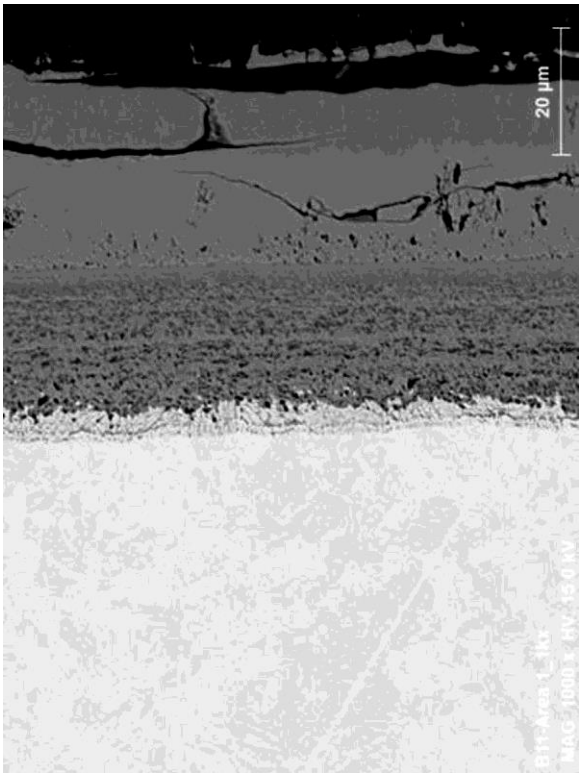

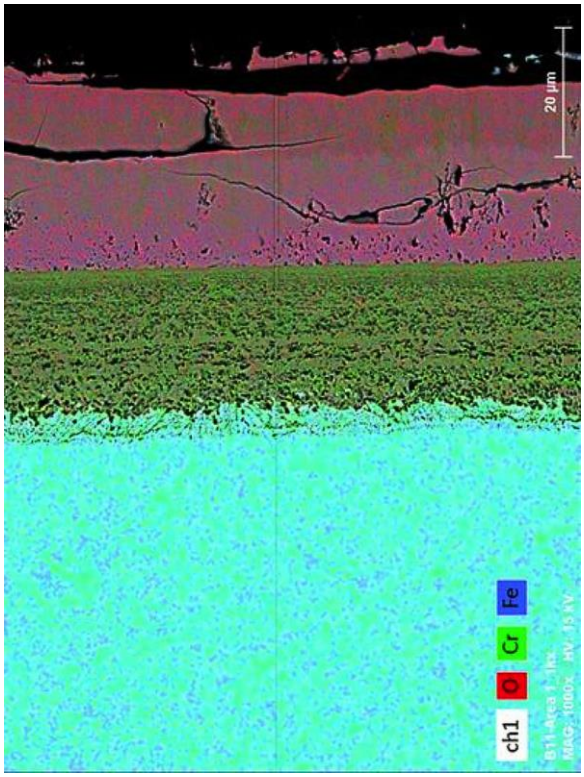

1,000 hours

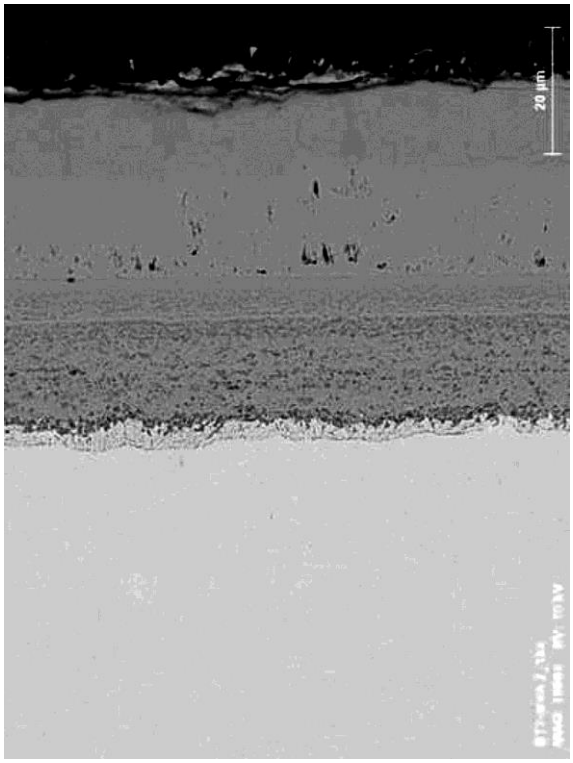

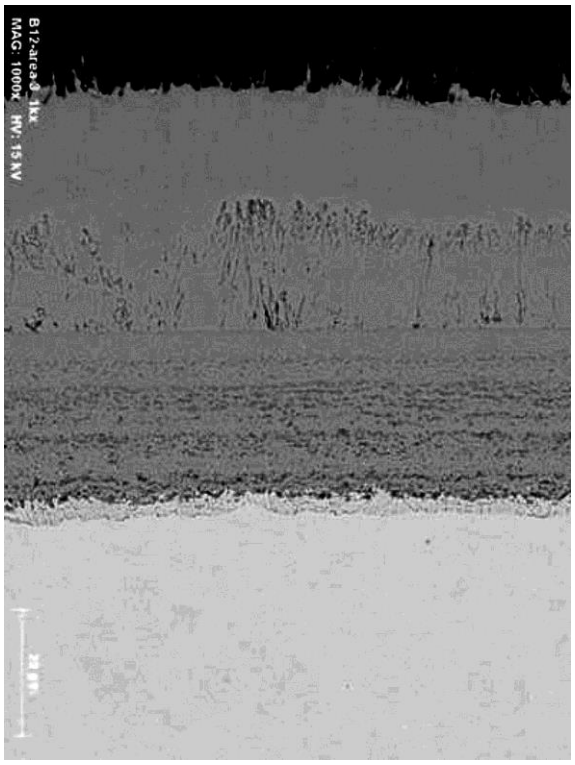

VM 12

300 hours

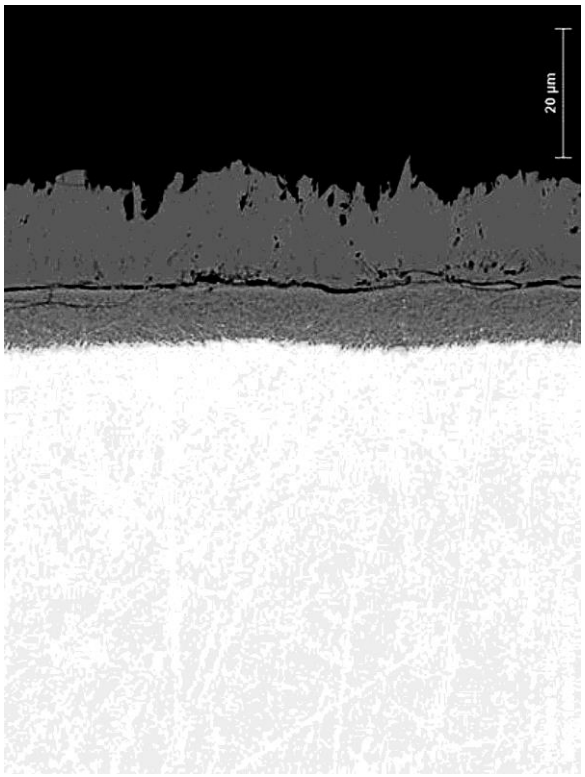

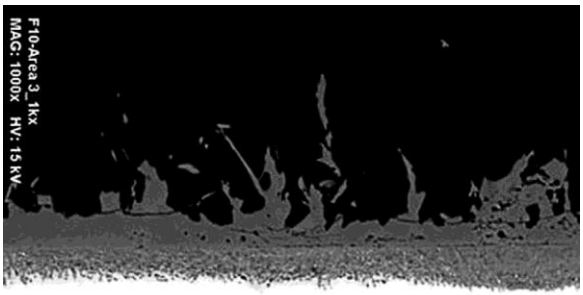

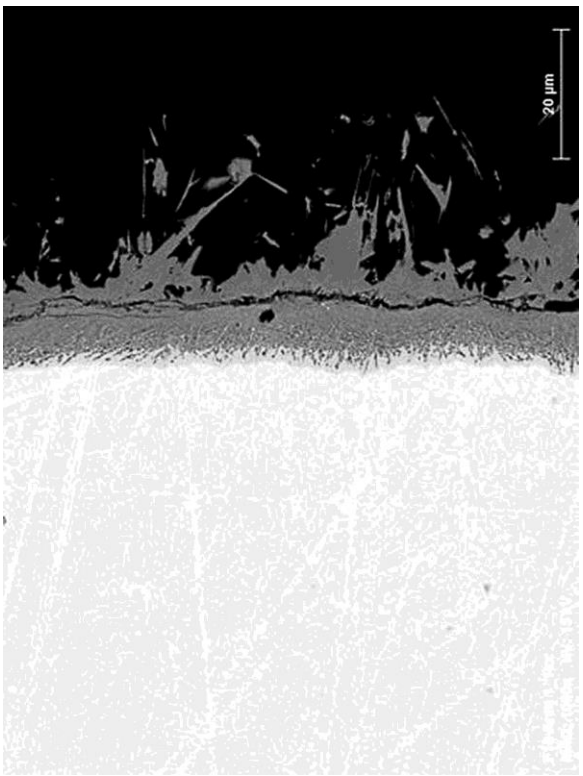

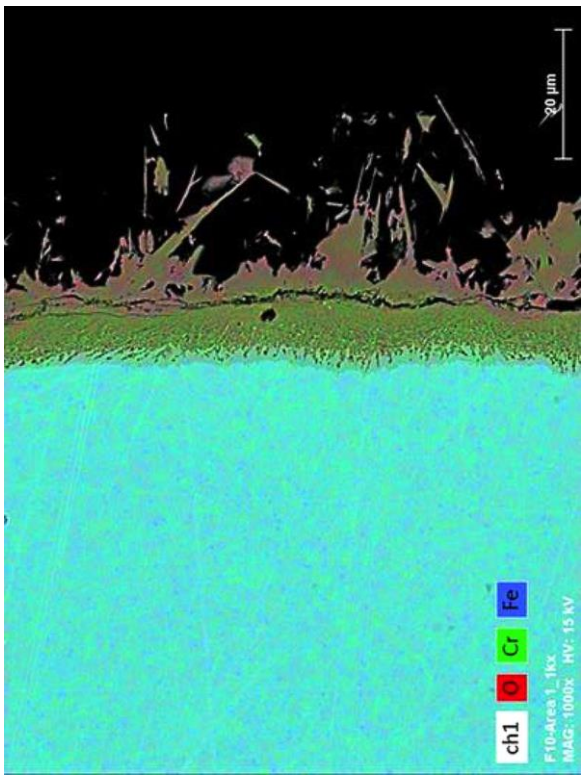

VM 12

628 hours

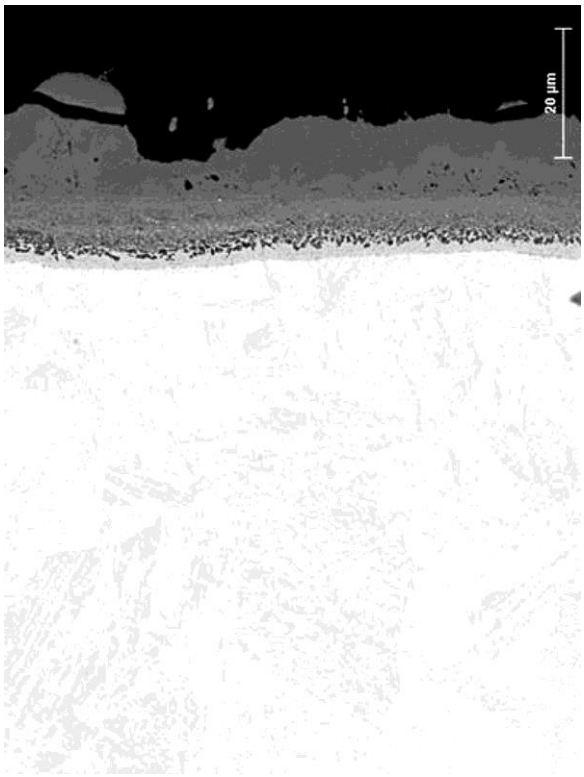

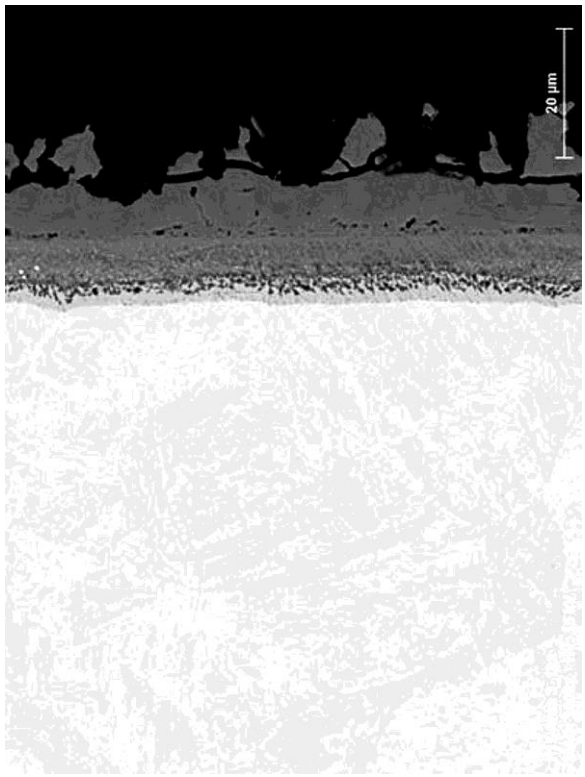

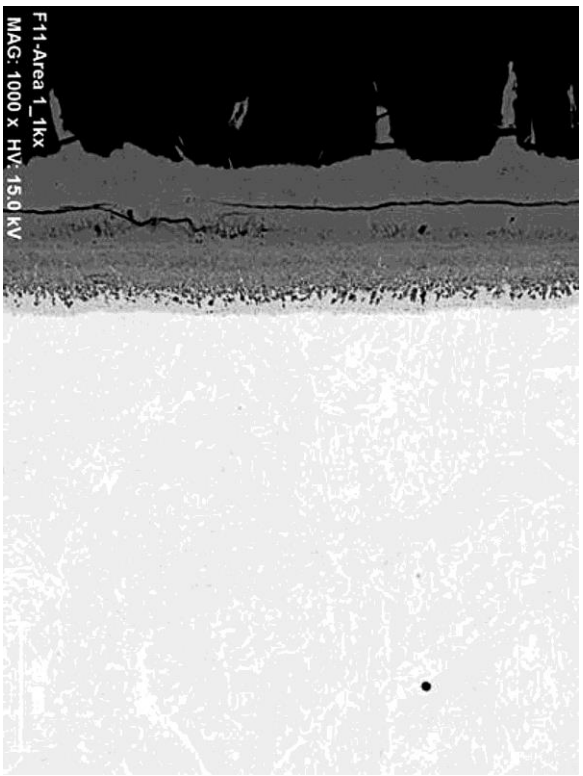

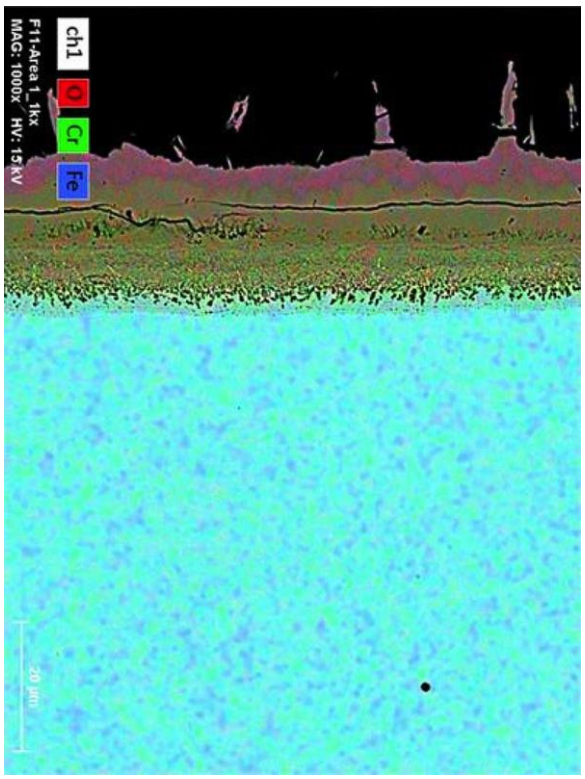

VM 12

1,000 hours

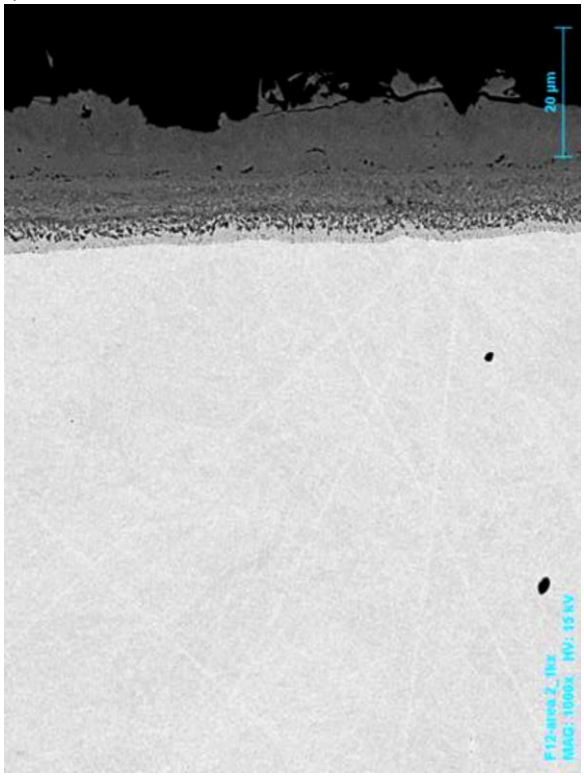

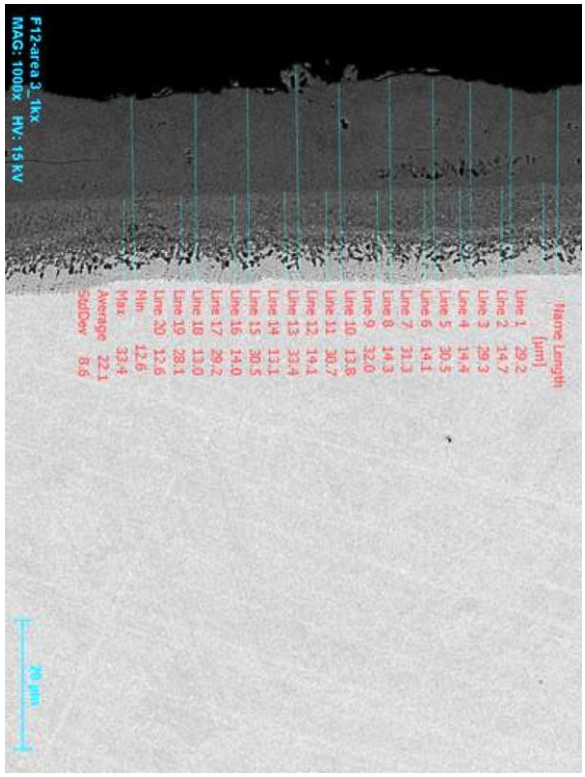

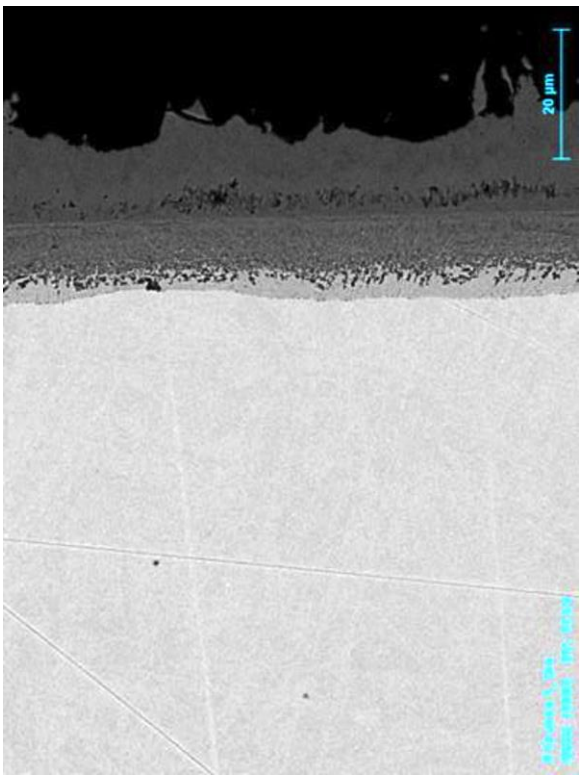

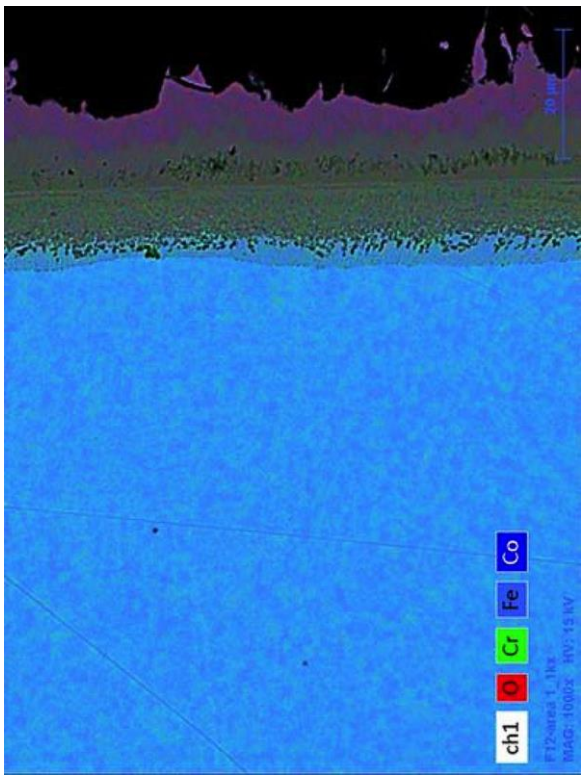

CROFER 22 H

300 hours

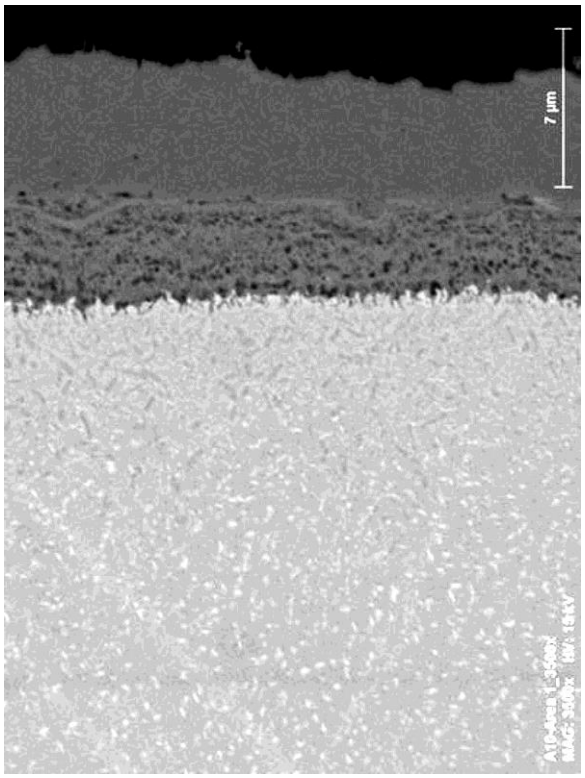

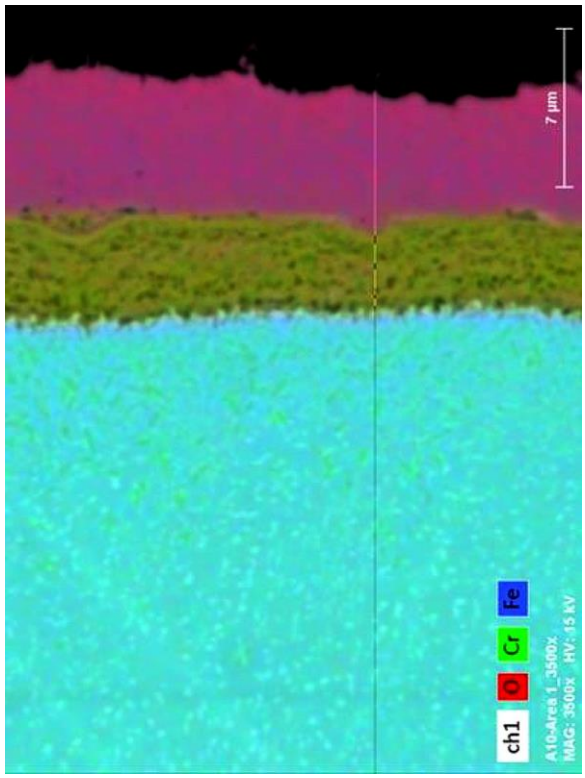

628 hours

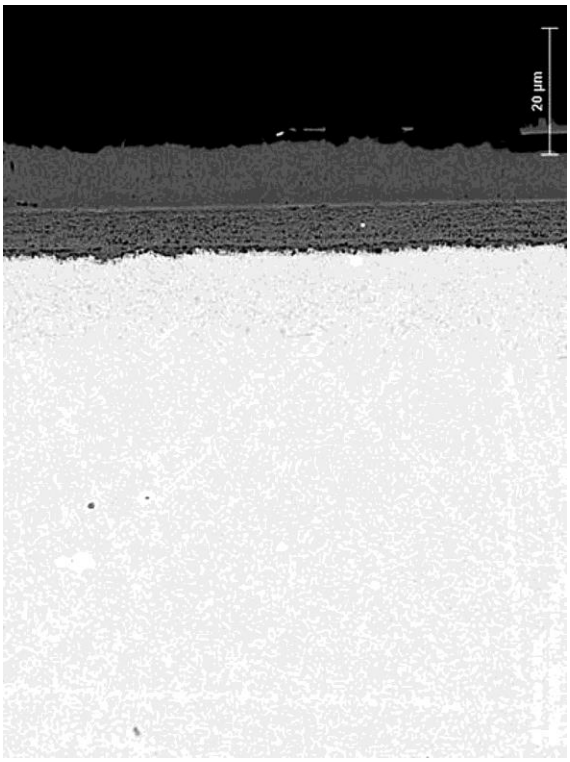

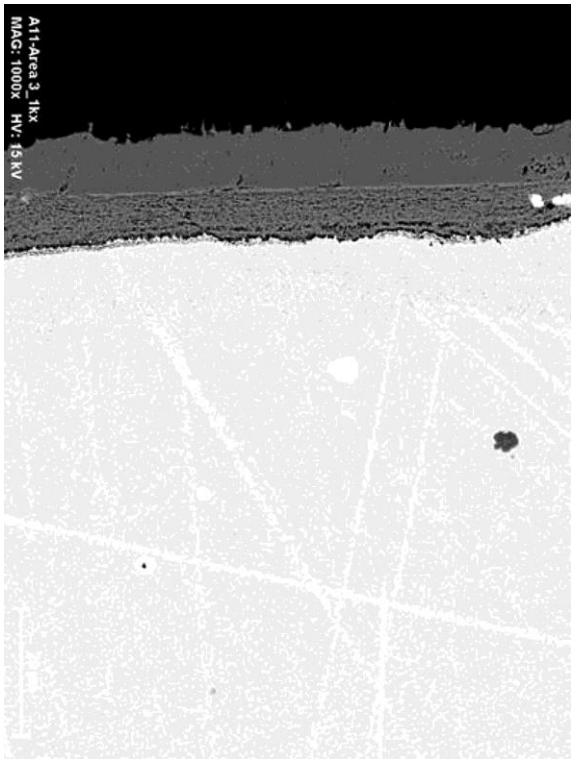

628 hours

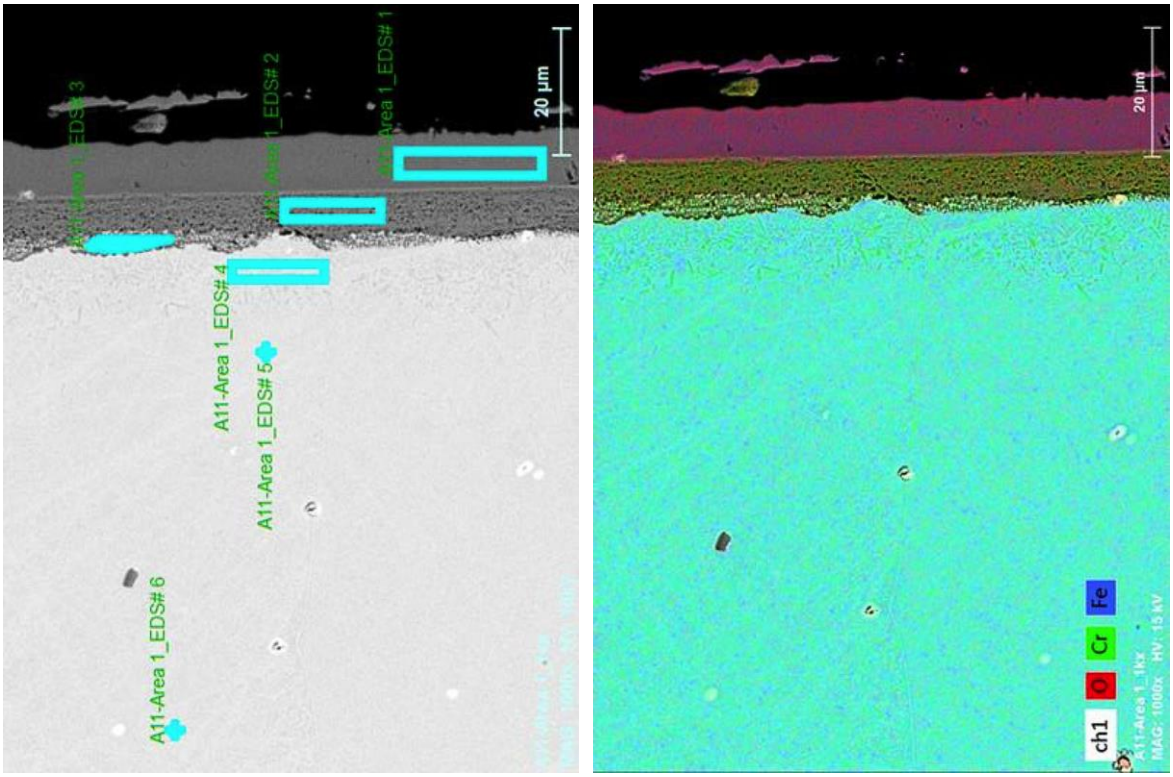

1,000 hours

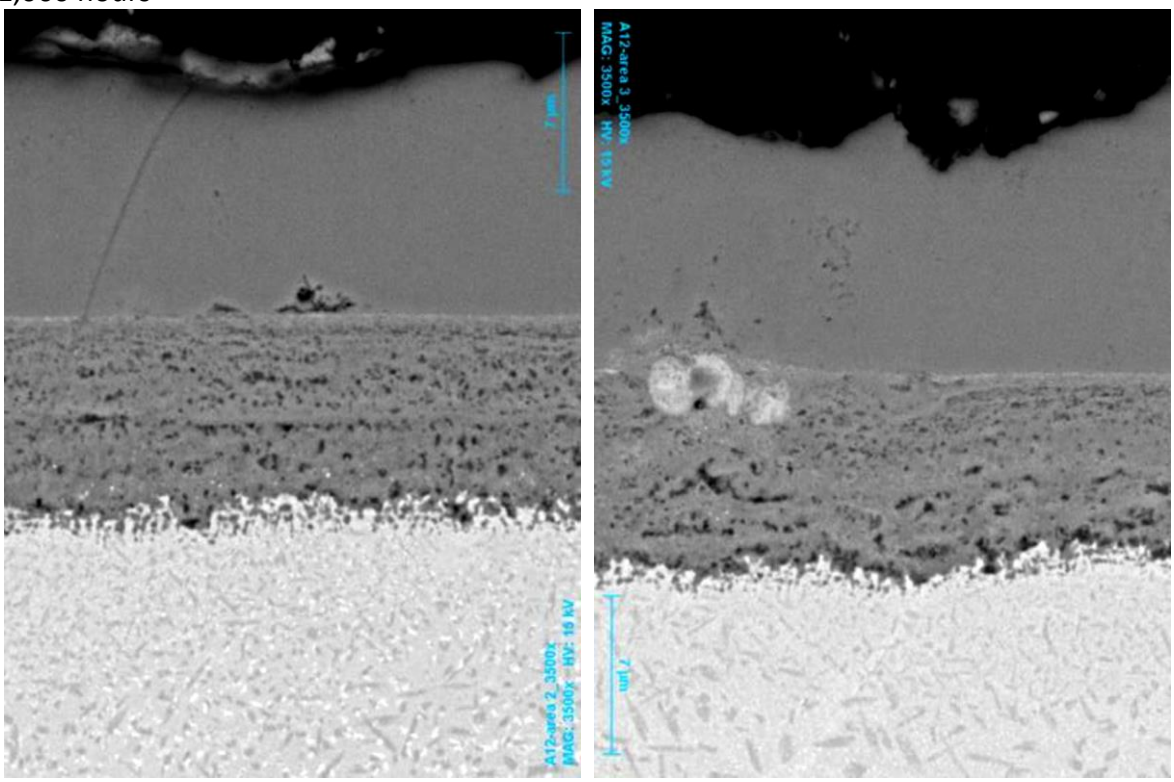

TP304H

300 hours

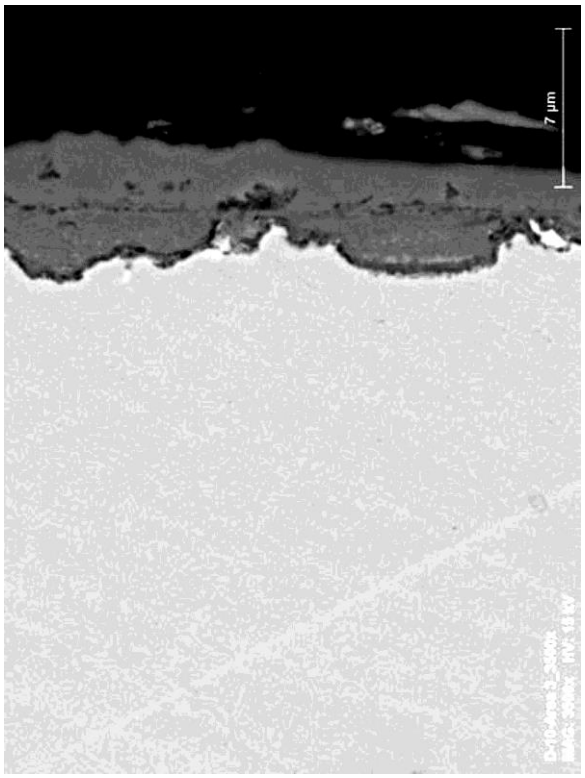

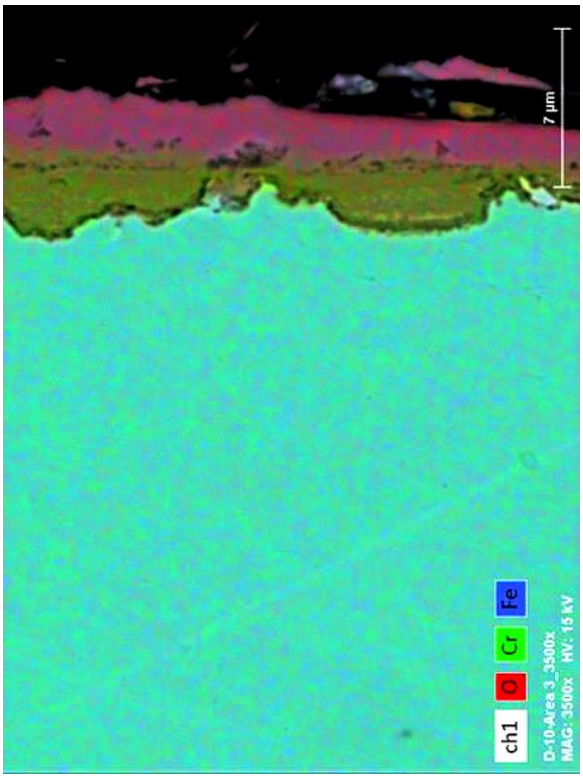

628 hours

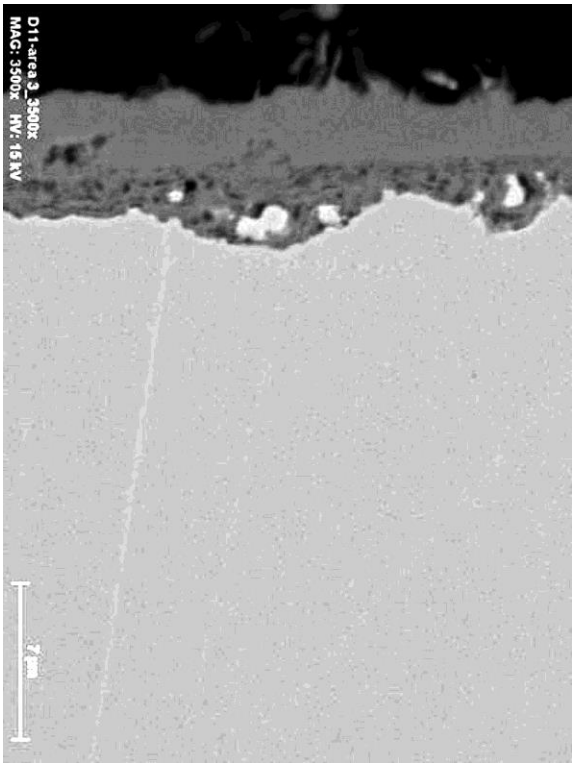

628 hours

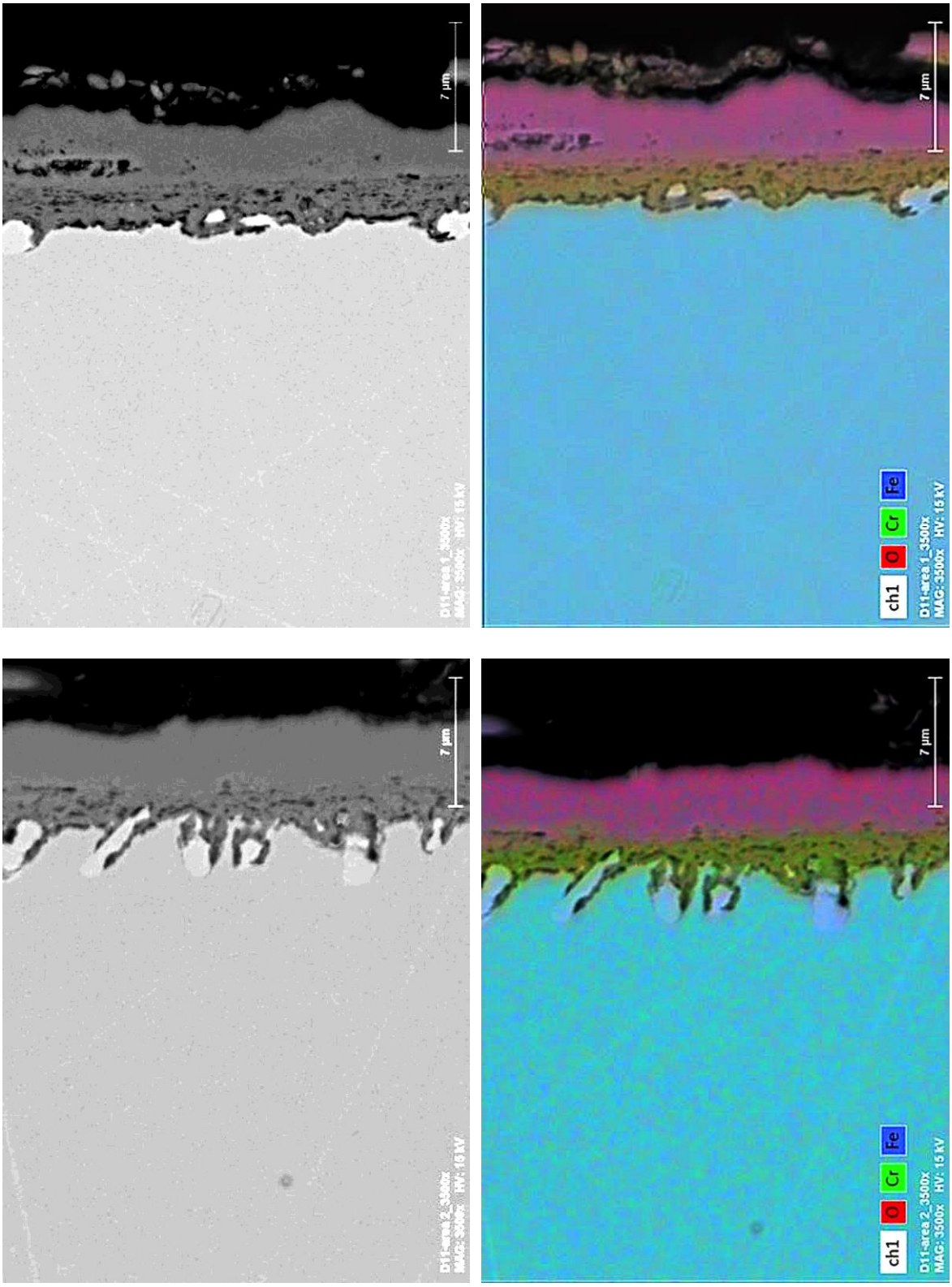
7 µm
D11-area 1_3500x
MAG: 3500x HV: 15 kV
7 µm
ch1 O Cr Fe
D11-area 1_3500x
MAG: 3500x HV: 15 kV
7 µm
D11-area 2_3500x
MAG: 3500x HV: 15 kV
7 µm
ch1 O Cr Fe
D11-area 2_3500x
MAG: 3500x HV: 15 kV

1,000 hours

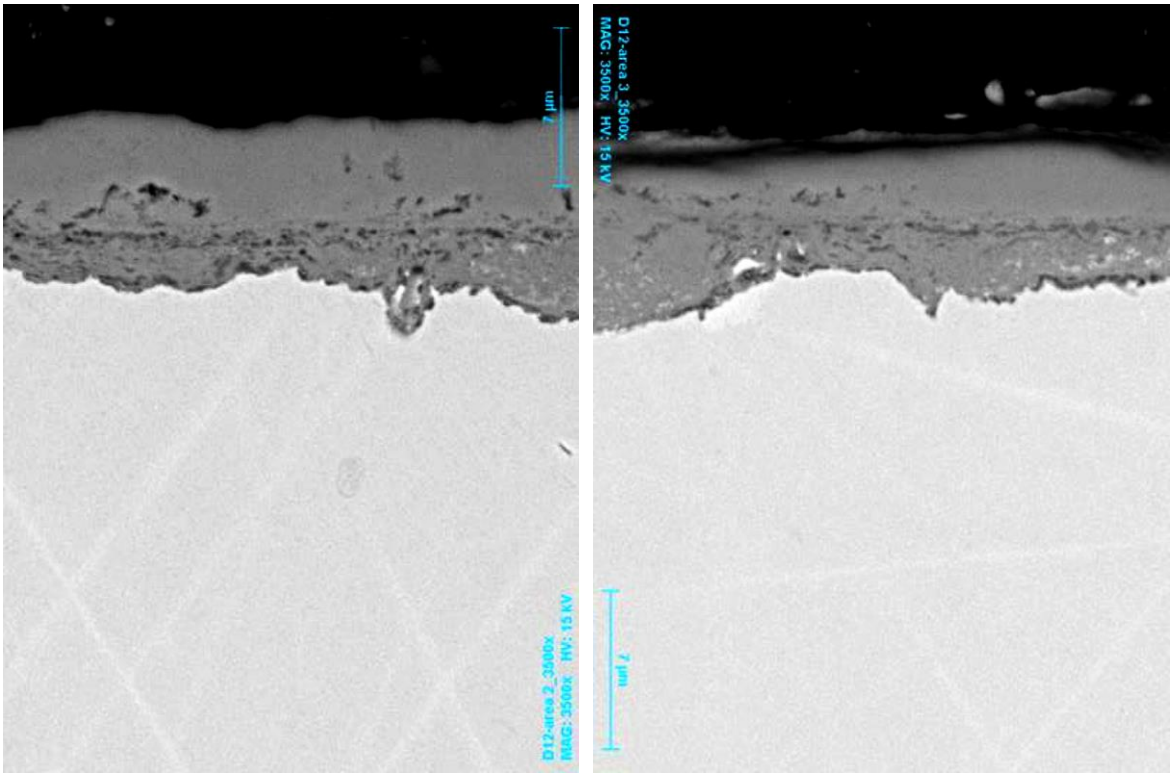
7 µm
D12-area 2_3500x
MAG: 3500x HV: 15 kV
D12-area 3_3500x
MAG: 3500x HV: 15 kV
7 µm

IN617

628 hours

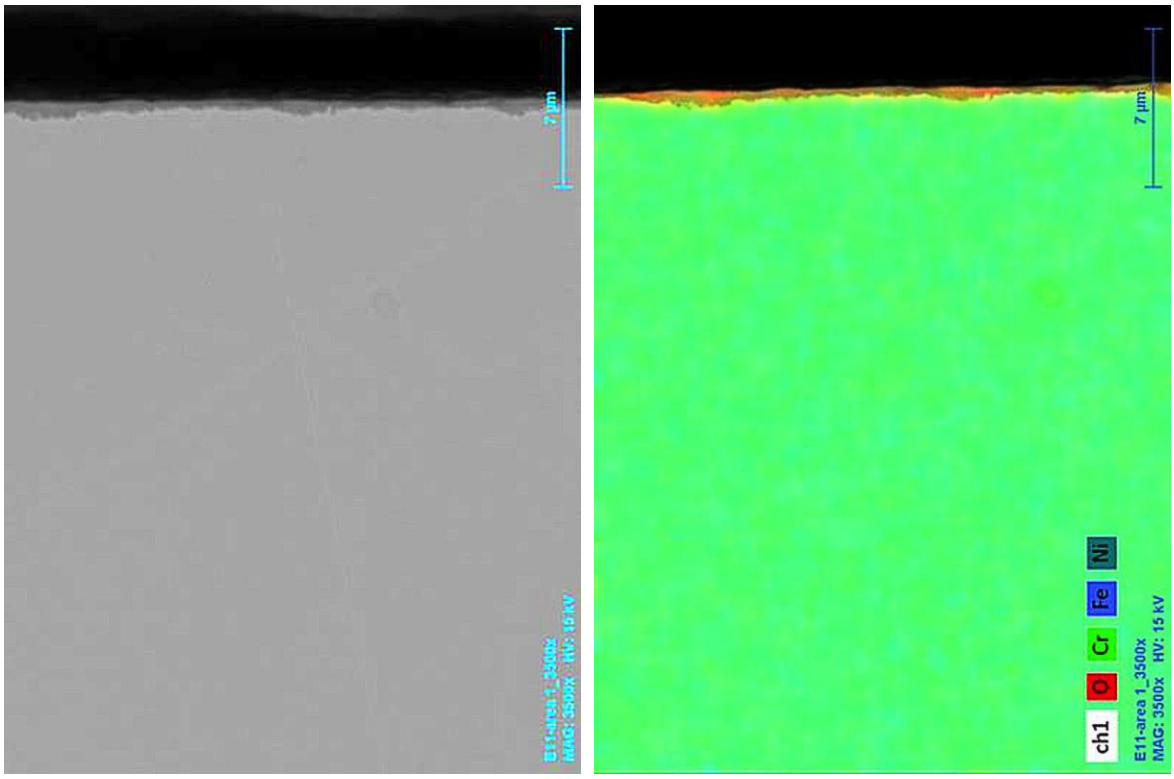

1,000 hours

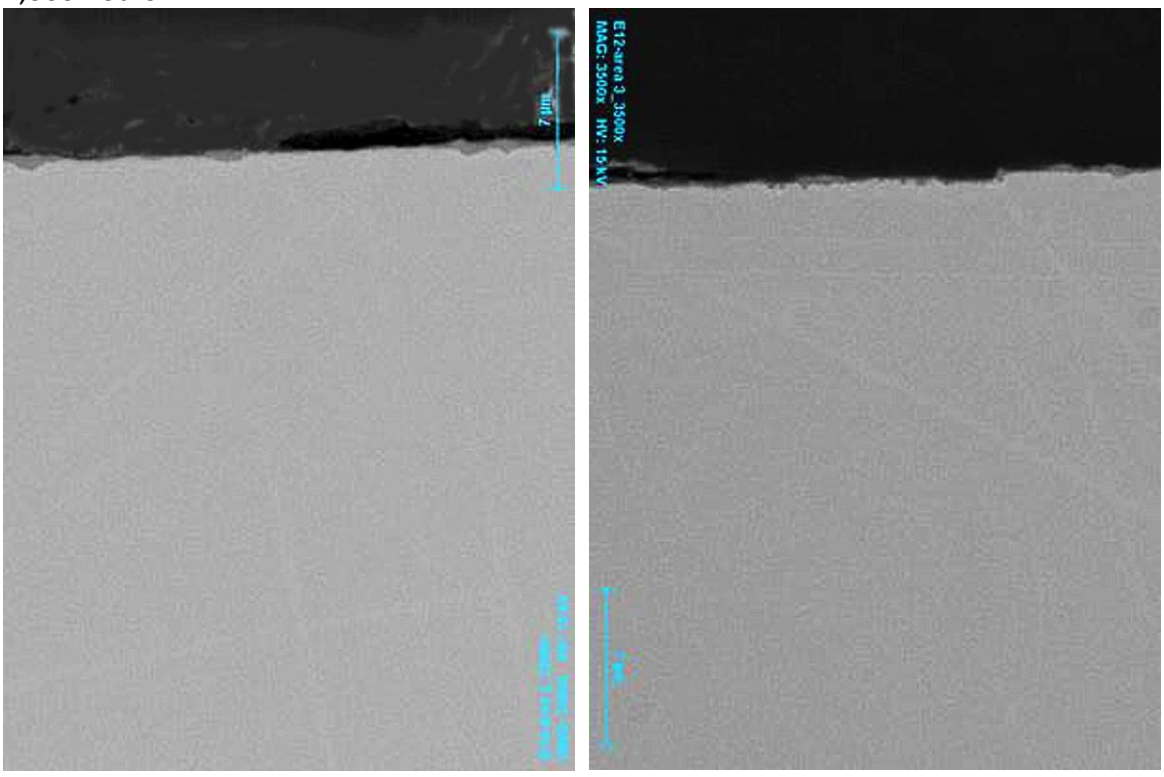

IN740H

300 hours

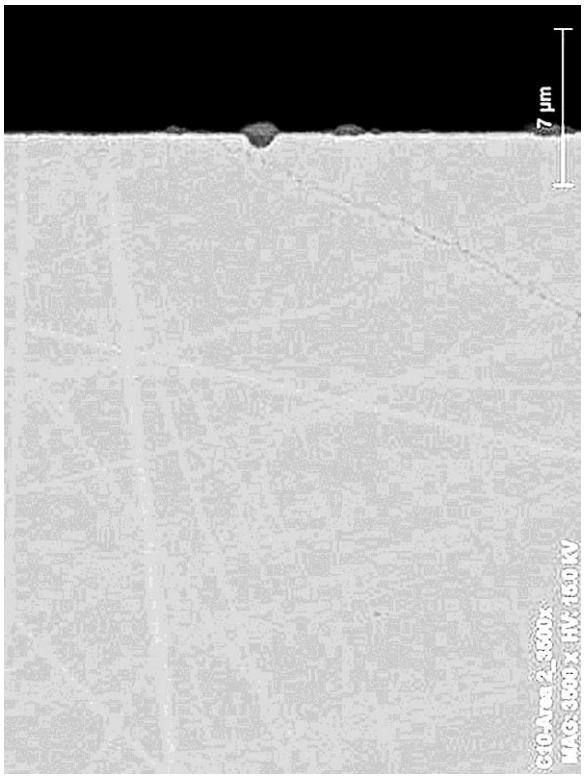

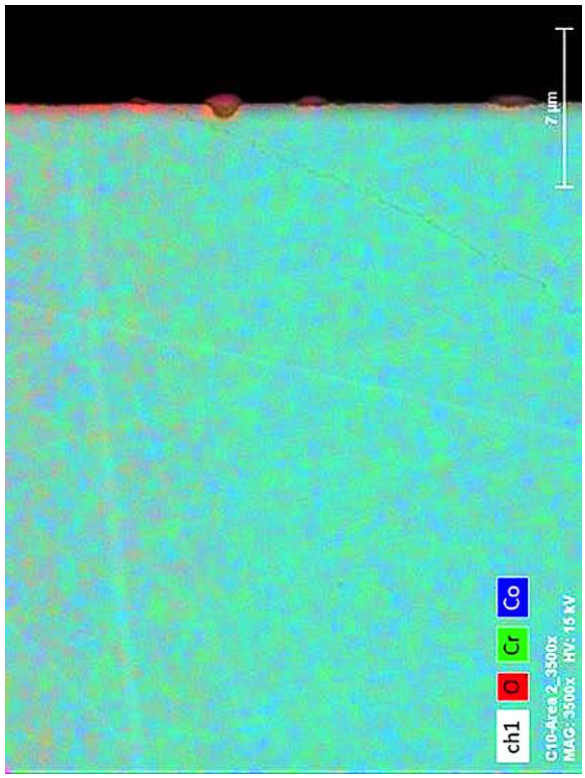

628 hours

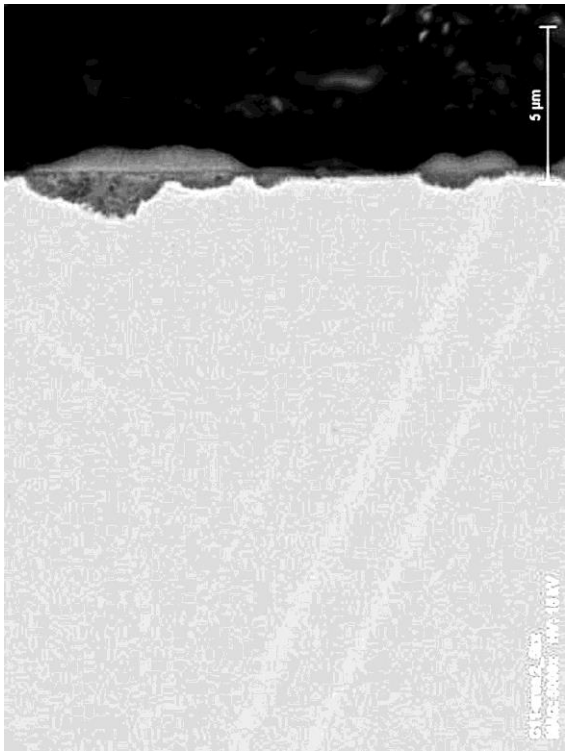

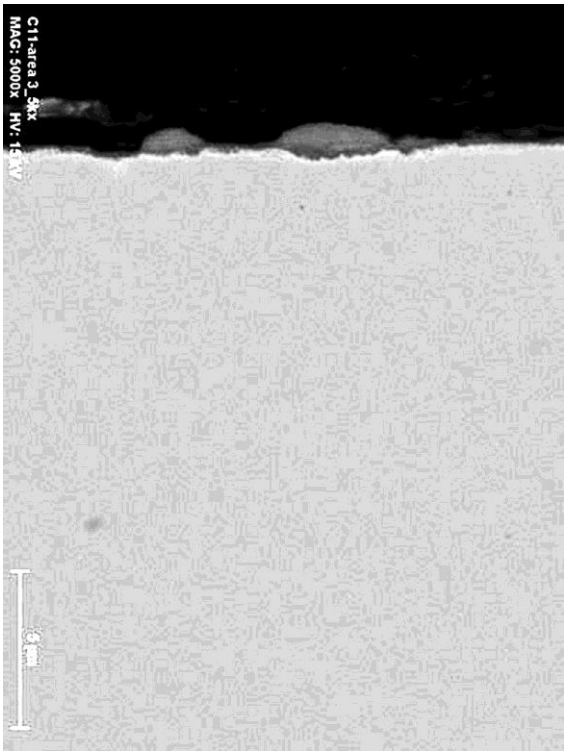

IN740H

1,000 hours

Appendix C

Surface Topographies of as-Tested Specimens After Exposure at 700°C for up to 5,000h in CO_2 Containing 3.6 vol.% O_2 and 5.3 vol.% at 200 bar

Grade 91, standard specimens

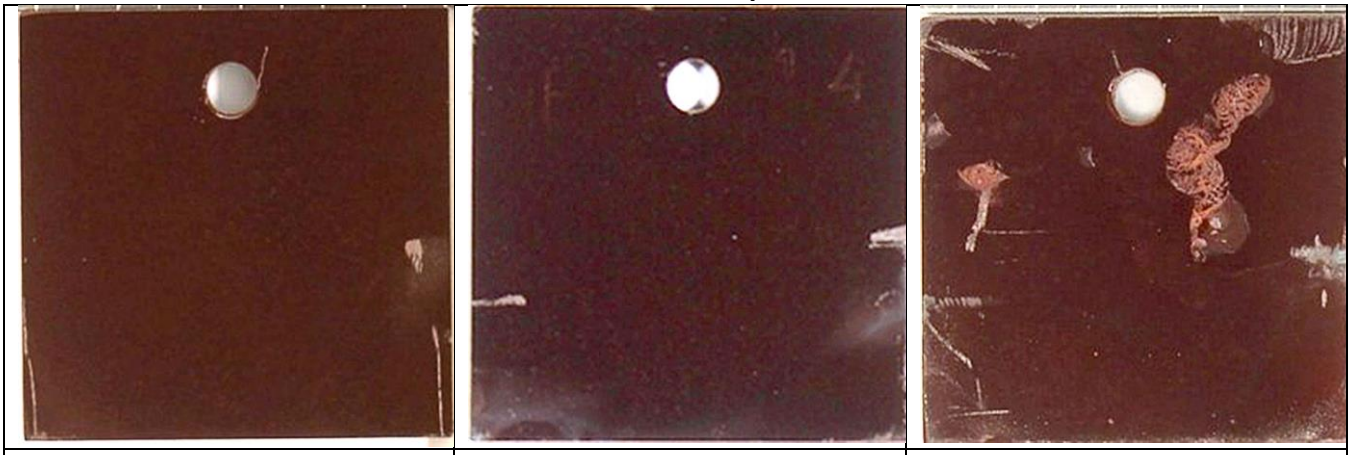

1,000h	3,500h	5,000h

VM12, standard specimens

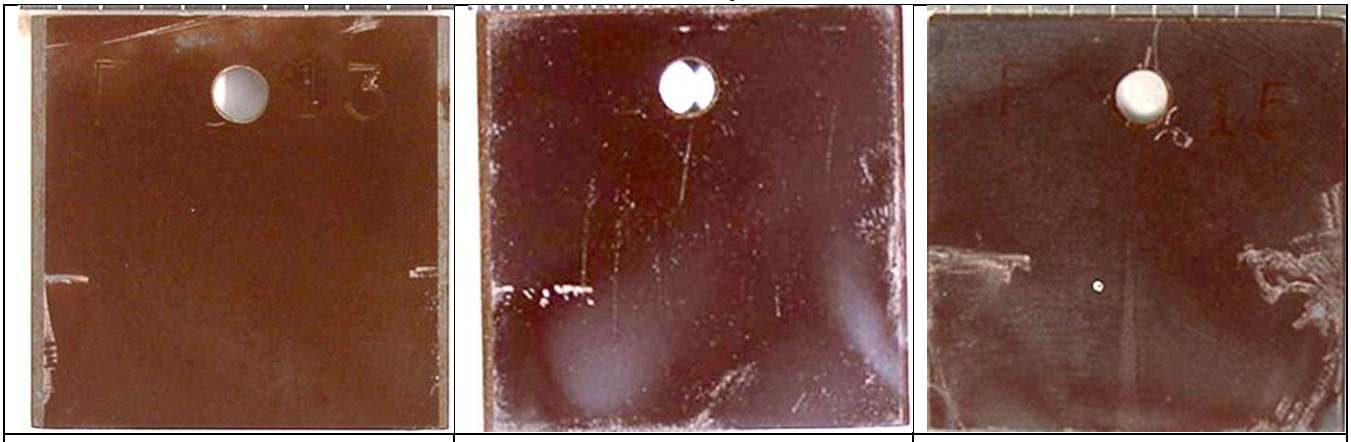

1,000h	3,500h	5,000h

CROFER 22H, standard specimens

1,000h	3,500h	5,000h

TP304H, standard specimens

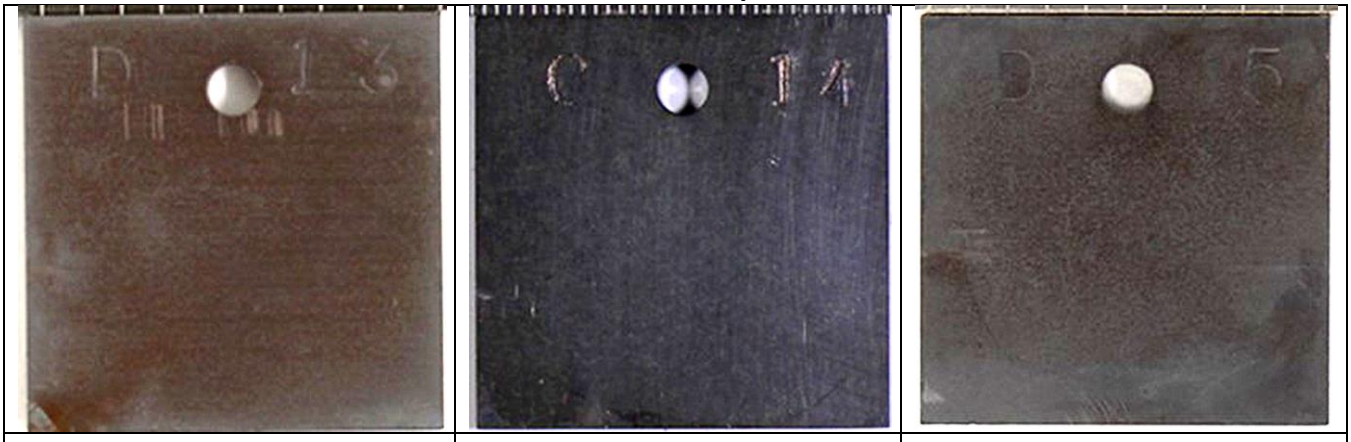

1,000h	3,500h	5,000h

HR3C, specimens cut from ex-service tube

1,000h	3,500h	5,000h

IN740H, standard specimens

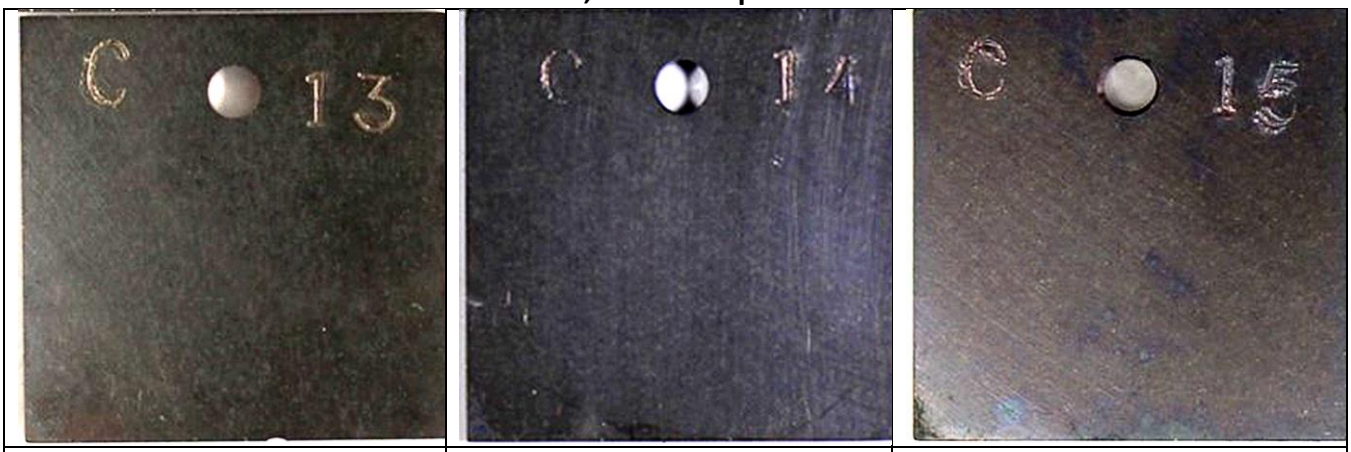

1,000h	3,500h	5,000h

IN617, standard specimens

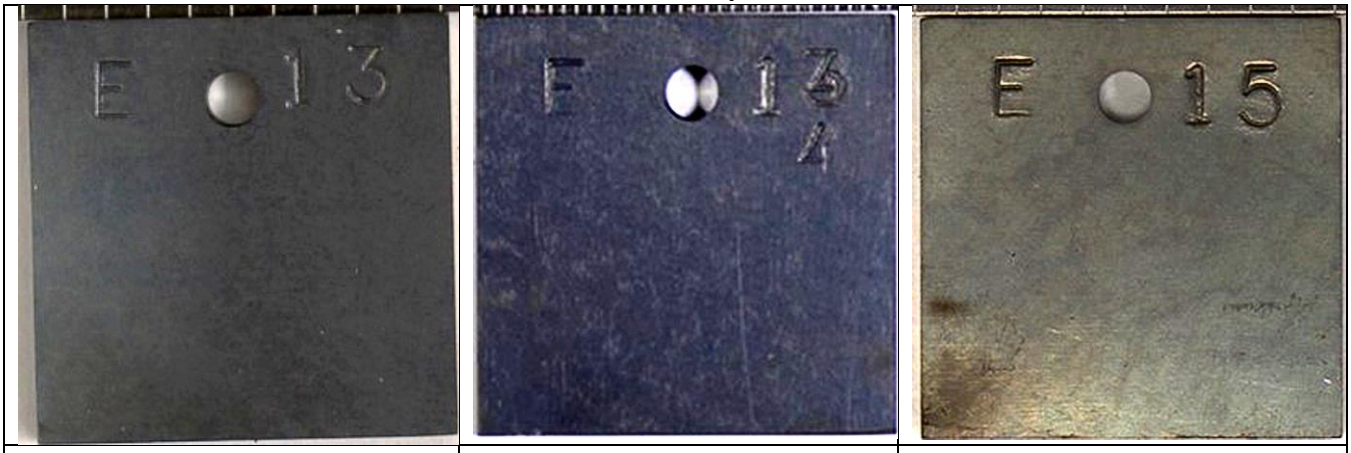

1,000h	3,500h	5,000h

IN625, 'microchannel' specimens

1,000h	3,500h	5,000h

Haynes 230, 'microchannel' specimens

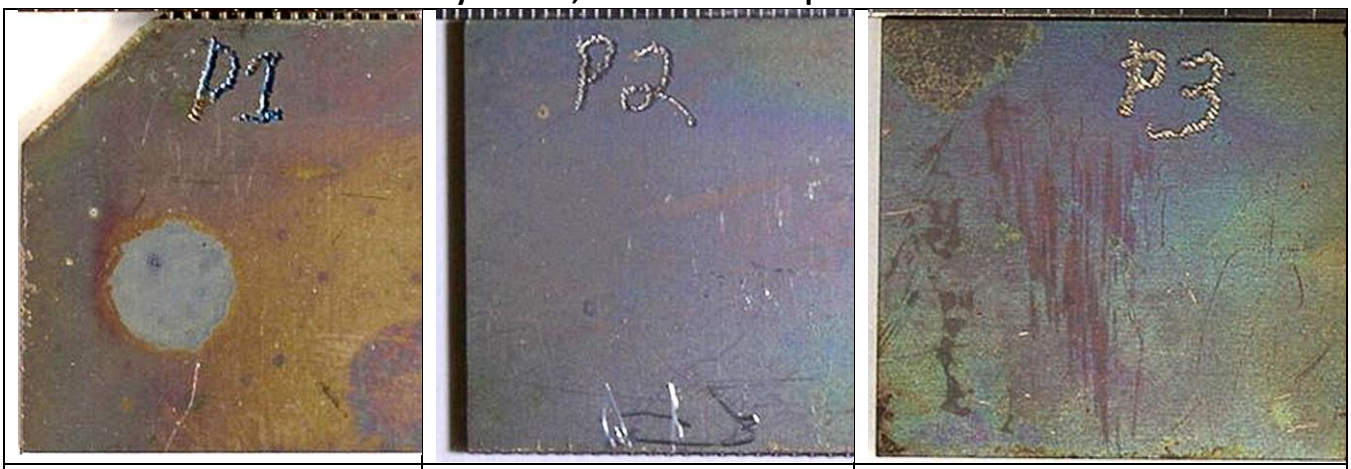

1,000h	3,500h	5,000h

TP347H, 'microchannel' specimens

		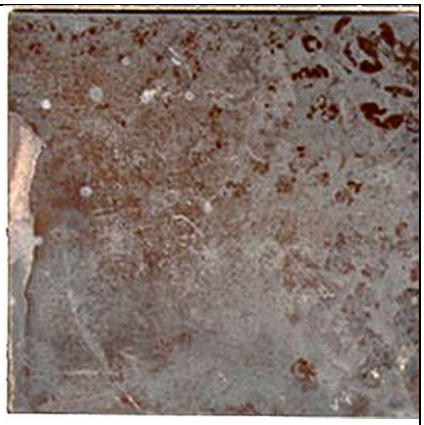
1,000h	**3,500h**	**5,000h**

FeCrAl (Sample #17)

	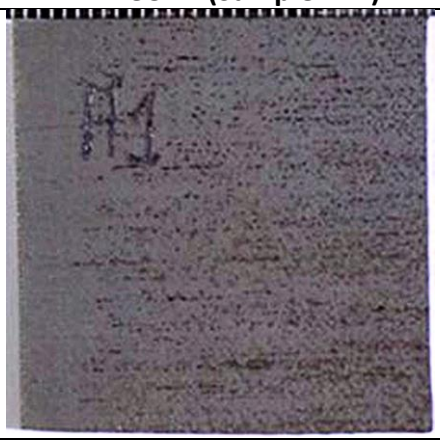	
	2,500h	**4,000h**

Haynes 230, 'microchannel' specimens

	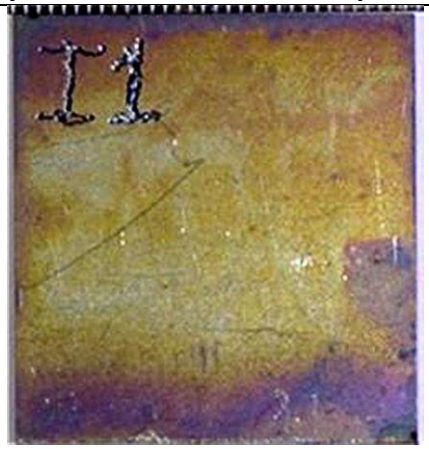	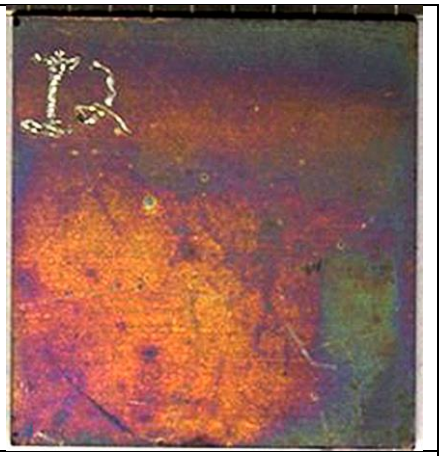
	2,500h	**4,000h**

TP347H, 'microchannel' specimens

		
	2,500h	**4,000h**

IN625 microchannel

		
	3,500h	**5,000h**

FeCrAl (Sample #18)

		
	2,500h	**4,000h**

COMPREX mesh specimens

		
	2,500h	**4,000h**

COMPREX brazed monolithic specimens

		
	2,500h	**4,000h**

TP316 (Sample #95)

		
		1,500h

TP316 (Sample #96)

		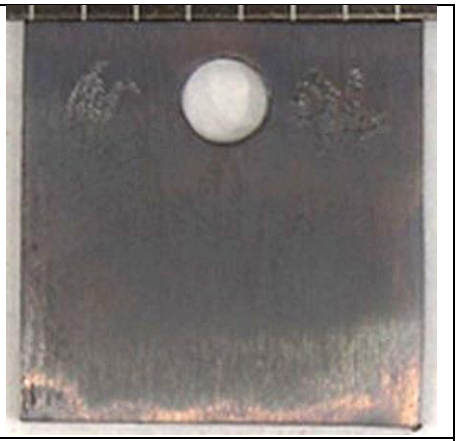
		1,500h

625 (Sample #89)

		
		1,500h

TP625 (Sample #90)

		
		1,500h

120 (Sample #88)

		
		1,500h

120 (Sample #89)

		
		1,500h

APPENDIX D

Relevant Experience from Work Associated with the British CO_2-Cooled Nuclear Reactors of Scale Morphologies Formed on Ferritic Steels after Oxidation in SCO_2

There is relevant experience of oxidation of ferritic steels in sCO_2 from work associated with the British CO_2-cooled reactors [1], though the temperatures and pressures involved (up to 700°C and 40.5 bar) were somewhat lower than envisaged in the present application. Reports from that work suggest that ferritic steels (up to 9 wt% Cr) developed scale structures that initially had similarities with those in high pressure (HP) steam, but that at longer times there was a strong acceleration of the corrosion process not typically observed in HP steam. That accelerated oxidation appeared to be associated with the eventual development of porosity in the inner layers formed on ferritic steels up to 9 wt% Cr (T9).

The proposed mechanism involved ingress of C into the alloy which continued until the alloy was saturated, at which point C started to build up in the inner layer of scale leading to the development of porosity near the alloy-oxide interface, decomposition of CO, and 'breakaway' oxidation. Evolution of the scales formed on 9-Cr steels in sCO_2 was thought to involve four types of scale morphologies [2], characterized as follows:

Type 1--Initial thin, protective, two-layered scale: this type of scale formed over small areas of the surface at temperatures >547°C. In such scales, the thickness of the inner layer (L1) was very irregular (Figure D.1). The Cr content of L1 reached up to 40 wt%, while the alloy beneath L1 was significantly depleted in Cr. The presence of this nominally two-layered structure (L1+L2) was often observed on tubes that had been shot blasted. Such scale morphologies are similar to those formed in air oxidation, but the very non-uniform appearance of L1 usually is not seen in HP steam.

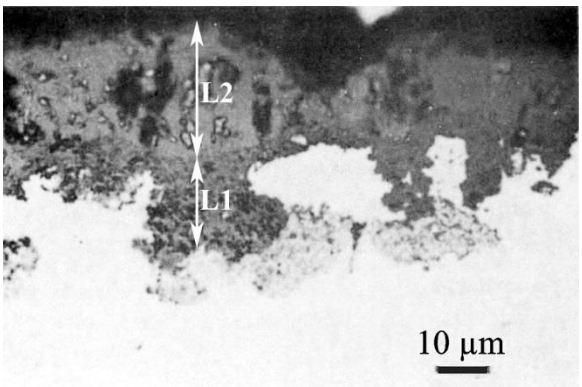

Figure D.1 - Cross section of Type 1 'thin, protective, two-layered scale' formed on Fe-9Cr-1Mo [1].

Type 2--Protective two-layered scale: such scales with layer thicknesses where L1 ≈ L2 (Figure D.2) were reported to form by inward movement of CO_2. This morphology was very similar to that formed in HP

steam (Appendix E), with the exception that L1 often contained unoxidized C particles. An internal oxidation zone was present (as on some 9Cr ferritics in HP steam). Unfortunately, the quality of the original micrographs was insufficient to provide much information on the structures of L1 and L2. An increase in the C content of the alloy after exposure was measured to depths up to 5x the scale thickness.

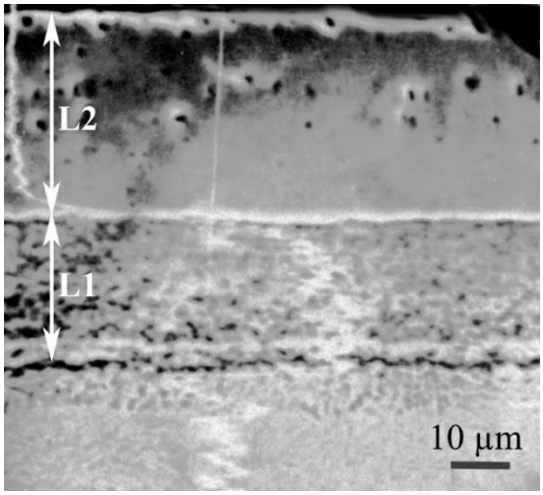

Figure D.2 - Cross section of Type 2 'protective, two-layered scale' formed on Fe-9Cr-1Mo [1].

Type 3--Protective multilayered scale: as shown in Figure D.3, this was similar to the multi-laminated scale morphology formed in HP steam (Appendix F). In sCO_2 it appeared that only the original L2 and the spinel layer of the innermost lamination in L1 (adjacent to the alloy) continued to grow. These morphologies were mostly associated with corners and edges of specimens where cracking of outer layers was most likely to occur because of mechanical constraints. The multilayers developed much sooner on shot blasted vs ground (600 grit) surfaces. Transition from duplex to multilayered structures apparently did not affect the overall oxidation kinetics. The microstructure of the spinel layers (L1) was reported to 'ghost' the alloy microstructure.

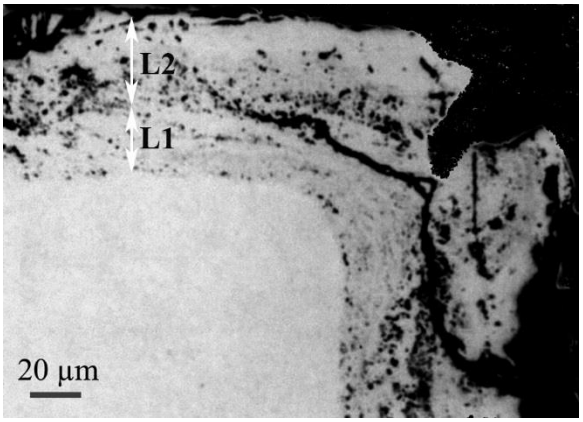

Figure D.3 - Cross section of Type 3 'protective, multilayered scale' formed on Fe-9Cr-1Mo [1].

Type 4--Non-protective scales: typically were associated with islands of highly-porous scale, and with very heavy enhancement of the carbide structure of the metal. Large platelets or globules of C often were present at the alloy-L1 interface. Figure D.4(a) illustrates an area where a double-layered protective scale has experienced breakaway oxidation with the formation of voluminous porous oxide. Nodules of breakaway oxide spread over the alloy surface and eventually coalesced (Figure D.4(b)). In these areas there was no ghosting of alloy grains or any presence of unoxidized C particles. No zone of internal oxidation was observed. Type 4 morphologies apparently developed more often from Type 3 scales than from Type 2. Such non-protective scale formation also most often occurred at sharp edges, and at higher temperatures.

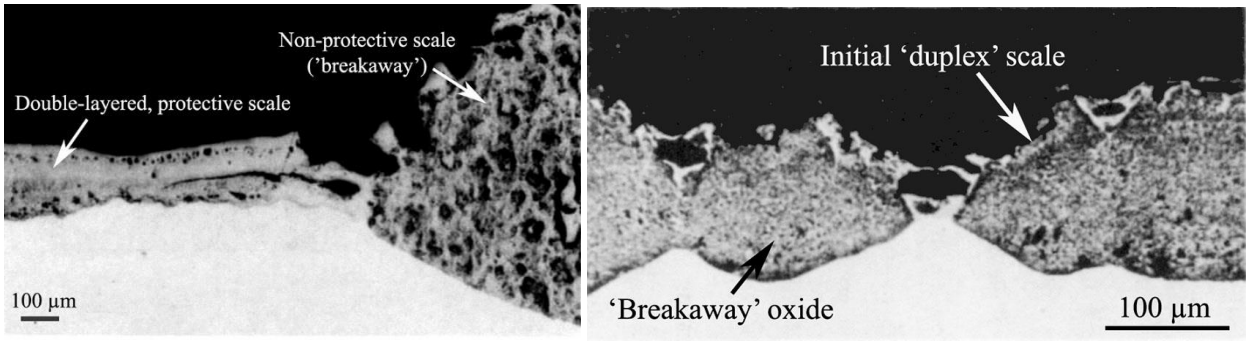

(a) **(b)**

Figure D.4 - Cross sections of scales that have experienced breakaway oxidation (Type 4): (a) on Fe-9Cr-1Mo [1]; and on mild steel [2].

It appeared that disruption of the initially protective scales resulted from accelerated oxidation of the alloy *beneath* a protective duplex scale, close to the alloy-L1 interface. The topographical appearance of an initial disruption of such a protective duplex scale by the protrusion of an excrescence of breakaway oxide is shown in Figure D.5(a). A corresponding cross section (Figure D.5(b)) suggests that the disruptive breakaway oxide originates from the base of the original protective scale.

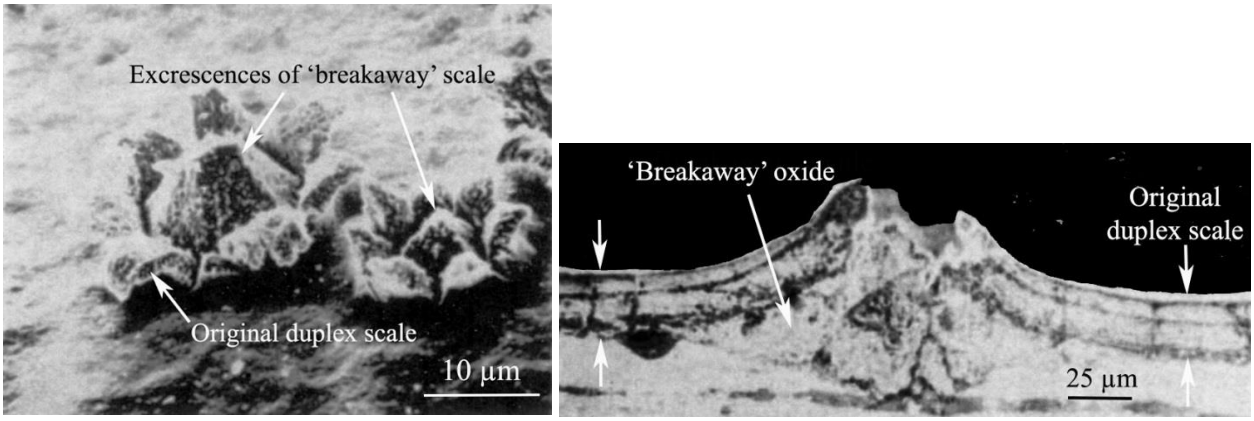

(a) **(b)**

Figure D.5 - Topographical view of scale formed on mild steel showing disruption of original duplex scale by excrescences of 'breakaway' oxide formed beneath: (a) topographical view (Scanning Electron Microscopy); and (b) cross section of a similar area [2].

A model of the breakaway oxidation process intended to draw together the common observations made in the materials support work for CO_2-cooled reactors was suggested by Gibbs [3]. This model was based mainly on observations for mild steel, but may have wider application since similar morphologies were formed on ferritic steels up to 9Cr-1Mo. The steps involved in the transition from protective to breakaway oxidation in CO_2 were summarized as indicated in Figure D.6. According to this model, the process of scale breakdown of ferritic steels in sCO_2 involves the following steps:

(i) The initial scale grows by outward cation diffusion to form mostly magnetite); on mild steel, typically L2 (magnetite)>>L1, the difference decreasing with increasing level of elements such as Cr, Mo, Si, etc.).

(ii) Vacancies are injected into the alloy-magnetite interface and lead to loss of scale adhesion. This results in the formation of an inner layer of oxide (L1) that contains impurities such as indicated above, and the original magnetite becomes L2. On the Cr-containing ferritics the scale always consists of L1+L2.

(iii) Micro-channels develop in the 'protective' scale by cracking or dissociation along oxide grain boundaries, allowing ingress of CO_2.

(iv) Reaction beneath L1 between CO_2 and the alloy produces oxide and CO, such as via:

$$4CO_2\ (g) + 3Fe = Fe_3O_4 + 4CO(g) \qquad \text{(D-1)}$$

The CO released accumulates beneath the scale and restricts crystal growth locally, so that a microporous structure is perpetuated in L1.

(v) Eventually, a Boudouard catalyst is generated at the alloy-L1 interface, and CO is rapidly consumed via:

$$2CO\ (g) = CO_2\ (g) + C\ (s) \qquad \text{(D-2)}$$

The C released is deposited in the structure of L1 and prevents sintering of the scale, maintaining a high level of porosity. The fall in CO level leads to rapid growth of the crystal structure of L1.

Overall, morphologies such as Type 4 are not seen in HP steam, so that a mechanistic description of this mode of scale failure currently is not available for use by the EPRI-ORNL model for scale exfoliation.

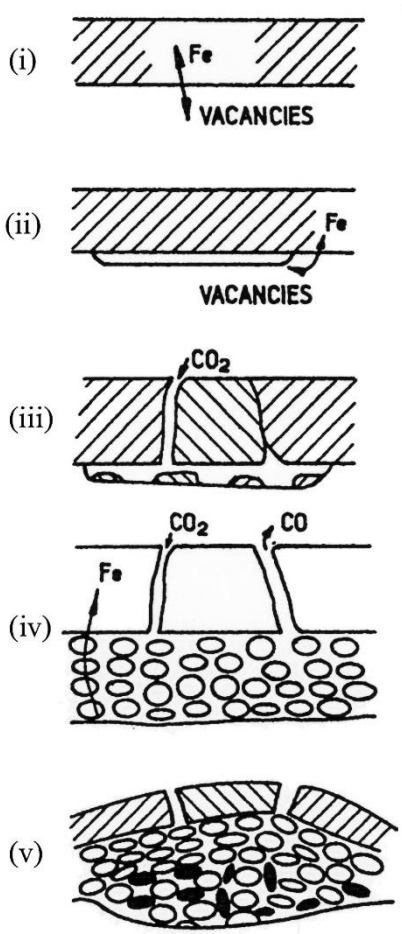

Figure D.6 - Suggested model for the oxidation of mild steel in CO_2 [3].

References Cited in Appendix D

1. *Proc. International Conference on Corrosion of Steels in CO_2*, D.R. Holmes, Ed., British Nuclear Energy Society, Reading University (1974).
2. P.L. Harrison, R.B. Dooley, S.K. Lister, D.B. Meadowcroft, P.J. Nolan, R.E. Pendlebury, P.L. Surman, and M.R. Wootton, "The oxidation of 9Cr-1Mo steels in carbon dioxide--a discussion of possible mechanisms," Paper No. 18 in *Proc. B.N.E.S. Intl. Conf. on Corrosion of Steels in CO_2* (1974).
3. G.B. Gibbs, R.E. Pendlebury, and M.R. Wooton, "Protective and breakaway corrosion of mild steel in CO_2," Paper No. 6 in *Proc. B.N.E.S. Intl. Conf. on Corrosion of Steels in CO_2* (1974).

APPENDIX E

Scale Morphologies Formed in High-Pressure Steam

There are numerous examples available of scale morphologies formed on some of the most widely-used alloys used in high-pressure (HP) steam service as a function of time and operating conditions, though not for all alloys for which ASME B&PV code approval is available. In an effort to summarize current understanding of the scale morphologies associated with alloys typically employed in steam boilers, EPRI recently published an atlas of such morphologies, with emphasis on describing the evolution of scale structures and the recognized steps leading to failure by the exfoliation process of [1].

Comparison of those morphologies with scales grown on similar alloys in sCO_2 is expected to provide a reasonable basis for identifying similarities and differences that would provide guidance on changes required to adapt the EPRI-ORNL scale exfoliation model for application to scales formed in sCO_2. In the following a brief discussion is presented of current understanding of the evolution and failure of oxide scales formed on the classes of alloys employed as superheater and reheater tubes in steam boilers: ferritic and austenitic steels.

E.1. Scale Morphologies on Ferritic Steels in HP Steam

When ferritic steels are oxidized in HP steam, the Cr in the alloy is oxidized in situ and so serves to demarcate the original alloy-steam interface [2]. Current understanding is that the scales developed in HP steam consist of a distinct 'inner' layer (L1) of magnetite (Fe_3O_4) surrounding fixed-in-place Cr-rich oxide precipitates and an outer layer (L2) of Cr-free magnetite that grows by outward transport of Fe ions. Such a scale structure is shown schematically in Figure E.1(a). The effective growth fronts are held to be the alloy-L1 interface (net inward oxidant transport) and the L2-steam interface (net outward Fe ion transport). Subsequent growth of the overall scale is governed by a complex interplay among inward transport of oxidizing species, outward transport of Fe ions, reaction between magnetite and the Cr-rich precipitates in L1, and dissociation of magnetite (typically near the L1-L2 interface) to release O and Fe ions [3]. All of these processes are influenced by time, temperature, and the level of Cr (and elements such as Si, S, Nb, and W) in the alloy. As a result, the morphologies of L1 and L2 evolve with continued service.

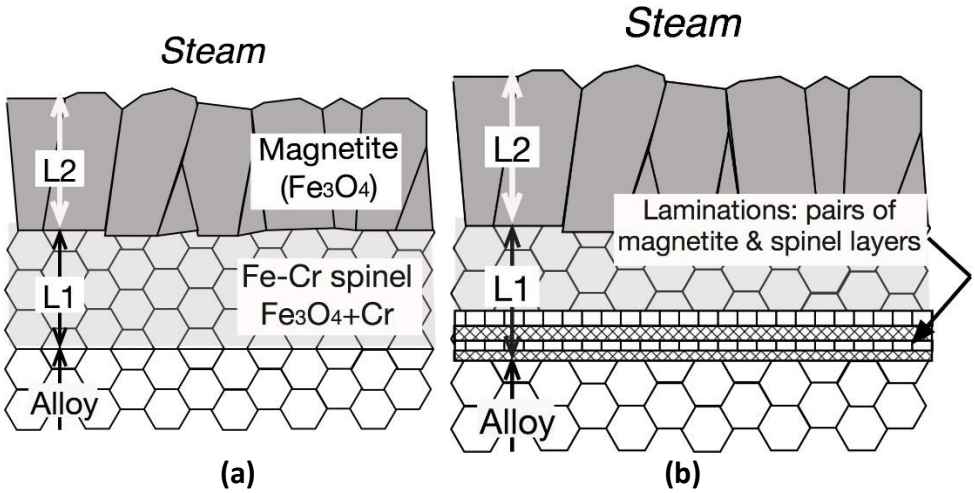

Figure E.1 - Suggested sequence of events in the development and failure (leading to exfoliation) of the oxide scale formed on ferritic steels in HP steam: (a) simple, duplex scale formed initially; and (b) development of laminated structure starting at the L1-alloy interface.

Morphological changes identified as precursors to scale failure and exfoliation in the standard ferritic steels containing up to 5 wt% Cr (and possibly 9 wt% Cr, though alloy T91 exhibits somewhat different behavior) involve the development of a laminated structure in L1 near the L1-alloy interface (Figure E.1(b)). These laminations consist of pairs of very thin layers of magnetite and spinel oriented parallel to the L1-alloy interface. Each lamination can be continuous over a significant distance, and is relatively uniform in thickness. The reason for the formation of these laminated structures and the mechanism by which they grow is not known [4-6], though a typical observation for T22 is that usually laminations are present after long service times at a point where some creep of the tubes has occurred [7].

Exfoliation from these steels typically does not begin until the full thickness of L1 is occupied by laminations. Exfoliating flakes consist of a few laminations from L1 and the whole of the thickness of the original L2 (Figure E.2) [6]. Such flakes typically are relatively small and, since they separate during normal plant operation, usually are entrained in the steam and carried out of the tube. Exfoliation from T91 is somewhat different, typically involving separation along the L1-L2 interface and loss of the complete thickness of L2. However, in some cases, apparently where severe thermal shocking of the tube is experienced, exfoliation from T91 can involve the total scale thickness (L1+L2).

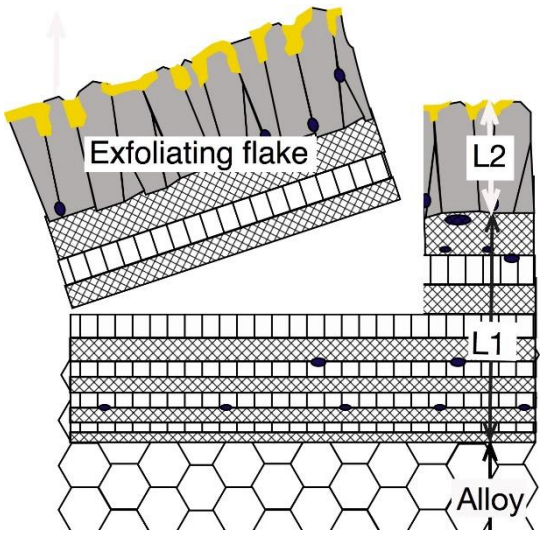

Figure E.2 - Separation of a flake of scale that comprises the original L2 + several laminations of L1.

E.2. Scale Morphologies of Austenitic Steels in HP Steam

The scales formed on austenitic steels in HP steam consist of essentially the same oxides as formed on the higher-Cr ferritic steels. Nevertheless, the resulting scale morphologies differ since the Fe-Cr spinel layer (L1) formed on austenitic steels typically contains higher Cr levels than on the ferritic steels of interest, and this leads to reduced transport of reactants through L1. Typical features of the morphologies of scales grown on austenitic steels in HP steam are:

i) The composition of the initially-formed L1 may correspond to $FeCr_2O_4$ (46 at% Cr) or even Cr_2O_3 (68 at% Cr), depending on the availability of Cr from the alloy (a function of alloy Cr content and grain size/degree of cold work). As a result, the rate of growth of L1 may be significantly slowed that the initial scale consists of a uniformly-thin, single layer with little or no outer L2 (magnetite).
ii) Where the availability of Cr at the alloy-L1 interface is reduced with time (usually on lower-Cr austenitics), or in locations where the original L1 is damaged or disrupted, nodules consisting of a lower-Cr version of L1 and an outer layer of magnetite (L2) form.
iii) Where these nodules can extend laterally with time, an overall double-layered scale structure develops in which the thickness of L1 may be very non-uniform, whereas L2 usually is quite uniform.
iv) With time, on some alloys the L1-alloy interface may become enriched with Cr (most often by transport along alloy grain boundaries) so that the overall transport of reactants again slows, and the reduced outward flow of iron ions allows hematite to develop at the L2-steam interface. In the extreme, all of the L2 may be converted to hematite, and the increased difference in coefficient of thermal expansion with L1 increases the tendency for exfoliation.

Figure E.3 illustrates the development of the scale morphology on austenitic stainless steels

according to the illustrated sequence. Note that exfoliation most typically involves only L2 once the scale has accumulated sufficient strain during a boiler shutdown, leaving the L1 intact on the tube. It is not uncommon for the complete L2 layer in a given location of a superheater tube to exfoliate during a high stress event

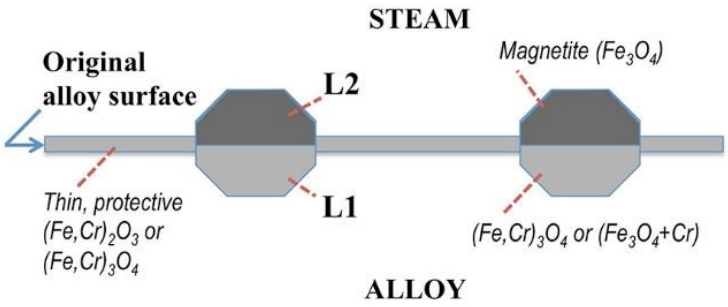

(a) Thin protective initial oxide layer with nodules of duplex (L1+L2) scale (stage ii).

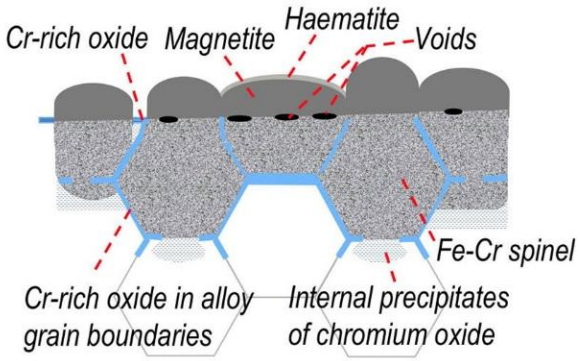

(b) Complete transformation to a duplex oxide scale (stage iii).

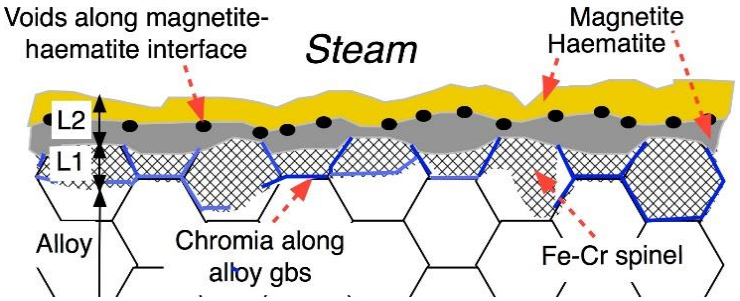

(c) Fully-developed, nominally protective scale with progressive conversion of L2 from magnetite to hematite (stage iv).

Figure E.3 – Schematic diagrams of cross section of the scale formed on an austenitic steel oxidized in HP steam depicting typical stages in its development [2].

The higher-Cr austenitic steels and Ni-based alloys intended for use up to the maximum temperature of interest in sCO_2 typically form Cr-rich protective scales (often single-layered) in HP steam, usually with a subscale of particles of oxides of alloying additions such as Al and Ti. So far there is little indication (from laboratory studies) that these internal oxide precipitates are detrimental to the long-term oxidation behavior of the alloys, though their consumption of key alloying additions presumably changes the mechanical properties in the surface regions.

References Cited in Appendix E

1. J.P. Shingledecker, R.B. Dooley, S. J. Kung, B.A. Pint, A.S. Sabau, and I.G. Wright, *Atlas of Steam-Side Oxide Scales Formed on Superheater and Reheater Tubes*, EPRI project in progress, 2015.
2. I.G. Wright and R.B. Dooley, "Morphologies of oxide growth and exfoliation in superheater and reheater tubing of steam boilers," *Materials at High Temperatures*, 28(1), 40-57 (2011).
3. I.G. Wright and R.B. Dooley, "A review of the oxidation behavior of structural alloys in steam," *International Materials Reviews*, 55 (3), 129-167 (2010).
4. M.I. Manning and D.B. Meadowcroft, "Effects of tube creep strains on laminated scale formation in ferritic pressure tubing," CERL Report No. RD/L/R2012 (1980).
5. P. Mayer and A.V. Manolescu, "The role of structural and compositional factors in corrosion of ferritic steels in steam," pp. 368-379 in *High-Temperature Corrosion*, R.A. Rapp, Ed., Intl. Corrosion Conf. Series NACE-6, NACE, Houston, Texas (1983).
6. I.G. Wright and R.B. Dooley, "Steam-side scale morphologies associated with scale exfoliation from ferritic steel T22," *Materials at High Temperatures*, 30 (3), 168-182 (2013).
7. Private communication from P.J. James, E.ON New Build & Technology, Ltd., to I.G. Wright, Sep. 2013.

Appendix F

Summary of Potential Effects of Thermal Oxide Growth on Heat Exchanger Service Life

Three scenarios whereby the growth of an adherent, protective oxide scale on the internal walls of a heat exchanger can affect its service life are considered:

1. Reduction in flow area (RFA);
2. Depletion of Cr in the tube wall surface to a level where less protective oxide could develop; and
3. Scale exfoliation leading to blockage of flow passages.

1. Reduction in Available Flow Area From Growth of Adherent Oxide Scale

The extent of reduction in flow area (RFA) due to the growth of an adherent oxide scale on the surfaces of a circular cross-section flow passage is given by:

RFA_{ox} = [(cross sectional area corresponding to the original tube bore) – (cross sectional area corresponding to the oxidized tube bore)]/(cross sectional area corresponding to the original tube bore)

i.e. $$RFA_{ox}\ (\%) = \{\pi/4*[D_b^2 - (D_b-2d_{ox})^2]*100\}/(\pi*D_b^2/4) \quad \text{(F-1)}$$

i.e. $$RFA_{ox}\ (\%) = [1-(D_b-2d_{ox})^2/D_b^2]*100 \quad \text{(F-2)}$$

where:
D_b is the cross sectional area corresponding to the original tube bore; and
d_{ox} is the thickness of the oxide scale.

When expressed in terms of oxide thickness:

$$d_{ox} = \tfrac{1}{2}D_b[1 - (1- RFA_{ox}/100)^{0.5}] \quad \text{(F-3)}$$

The time to grow an oxide thickness corresponding to a given RFA_{ox} (%), t_{RFA}, is readily calculated from available oxidation kinetics data. Where a limiting acceptable value of RFA_{ox} can be defined, t_{RFA} becomes the effective service lifetime of the heat exchanger. The relationship between d_{ox} and t_{RFA} (and temperature, T) for protective oxide scales that grow according to a parabolic rate law is:

$$d_{ox}^2 = 2*A_t*e^{-Qt/RT}*t_{RFA} \quad \text{(F-4)}$$

or: $t_{RFA} = d_{ox}^2/(2*A_t*e^{-Qt/RT})$ (F-5)

where:

A_t is the Arrhenius Constant for the oxidation process,

Q_t is the activation energy for oxidation, and

subscript 't' indicates kinetic data derived from oxide thickness measurements.

An example of an alloy typically used in this service is austenitic steel TP347H, while the fine-grained version of this alloy, TP347HFG, intended to form a slower-growing oxide scale (chromia) is used where scale exfoliation is a problem. Table F-1 lists values of A_t and Q_t for these alloys for oxidation in high-pressure steam derived from measurements made in steam boiler service. In addition, oxidation parameters are listed for Ni-based alloy IN740. This alloy has not yet been used in steam boilers, so that reliance is placed on laboratory data taken from Task 3.7. It is assumed that this alloy forms a single-layered (chromia) scale in HP steam, so the parameters listed are taken to refer to the thickness of that single layer.

Table F-1
Scale Thickness-Based Oxidation Parameters.

Alloy	A_t ($\mu m^2/h$)	Q_t (kJ/mole)	Source
TP347H*	5.0×10^9	-171	[1]
TP347HFG*	2.6×10^7	-154	[1]
IN740	1.4×10^5	-166	[2]

*These alloys form double-layered oxide scales; the oxidation parameters refer to the growth of the inner (L1, rate-controlling) layer only. Total scale thickness usually is assumed to be x2.

Using as an example a superheater tube used in a utility boiler operating with steam at 550-700°C, with a typical tube outside diameter of 25.4 mm (1 in), and wall thicknesses (w) ranging from 1.25 to 3.1 mm (0.049 to 0.12 in), then D_b ranges from 19.2 to 22.9 mm. Table F-2 gives a list of values of d_{ox} calculated to correspond to defined values of RFA_{ox}.

Table F-2
Calculated values of d_{ox} for specified values of RFA_{ox}.

Tube ID (D_b) mm	RFA_{ox}, %	Oxide thickness (d_{ox}) µm
19.2	1	48
19.2	2	96
19.2	5	243
22.9	1	57
22.9	2	115
22.9	5	290

Using the values of d_{ox} in Table F-2, the effective lifetimes (i.e., time to reach specified values of RFA_{ox}) as a function of T were calculated for steam superheater tubes using Equation (F-5) and oxidation kinetic data from Table F-1. Results for TP347 and TP347HFG are compared in Figure F-1, and clearly illustrate that the times required for scale growth on alloy TP347H sufficient to reduce the flow area by 1% are relatively short, even at 550°C (4 kh). The sharp decrease with increasing temperature simply reflects the rapid scale growth on this alloy. The time for the same RFA_{ox} for the fine-grained alloy TP347HFG at 550°C is 66kh, some 16+ times longer, illustrating the large effect of scale type and morphology.

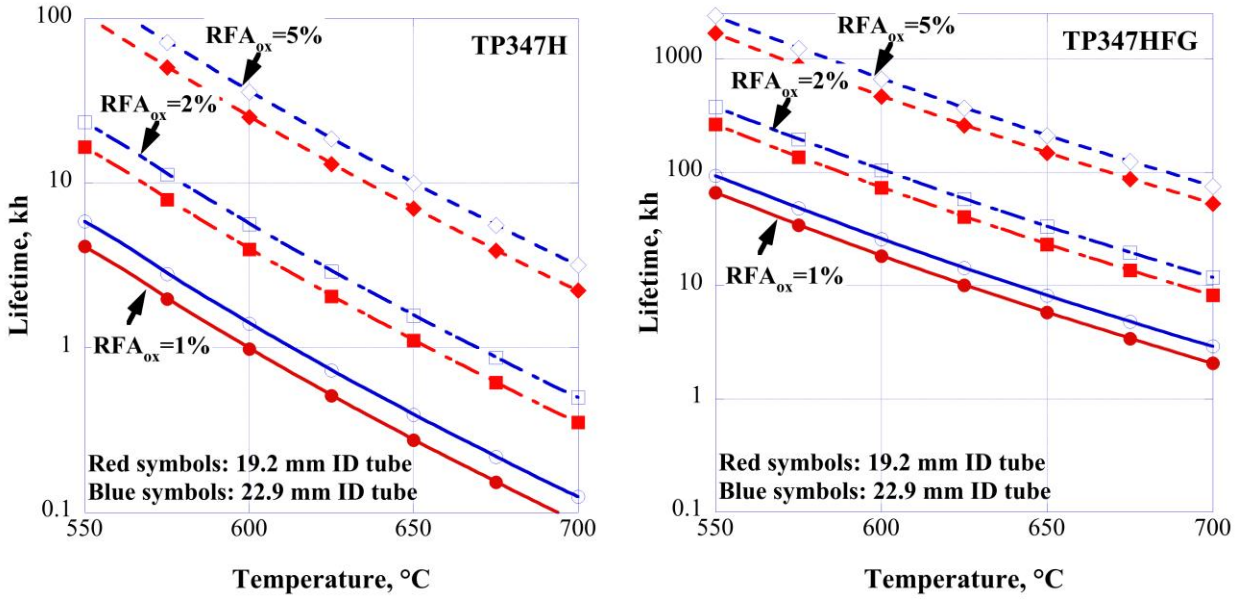

Figure F-1 - Effective lifetimes based on times to reach specified values of RFA_{ox} for superheater tubes using alloys TP347H and TP347HFG.

2. Time for Alloy Cr Reservoir to Become Depleted to a Level Where Formation of an Adherent Protective Scale No Longer is Supported.

The ability of an alloy to form a protective outer oxide scale (usually chromia or a Cr-rich spinel) requires the presence of a minimum level of Cr (C_B) at the alloy-environment interface. Since growth of the desired oxide consumes Cr, the ability to maintain C_B at the alloy-oxide interface is an important factor in determining the service life of the component. Typically, Cr removed from the alloy-oxide interface is replenished by diffusion from the interior of the component. At moderate temperatures for austenitic alloys, such diffusion gives rise to a depletion gradient in Cr concentration from the alloy-oxide interface inward. This can result in C_B being reached at the alloy-oxide interface while the Cr content in the bulk alloy remains much higher. At higher temperatures, diffusion may be much faster so that the Cr concentration profile through the alloy is much flatter, and more of the total Cr available can be used for scale formation.

A further consideration is that of the 'total available Cr reservoir,' which also has a bearing on the length of time that the Cr level at the alloy-oxide interface can be maintained above C_B. Usually this is determined by the starting Cr level in the alloy and the thickness of the component (and sometimes its shape). Also, when both sides of a heat transfer tube (e.g., 'steamside' and 'fireside' in the case of a superheater tube) are subject to oxidation/corrosion, the maximum effective Cr reservoir becomes essentially one half the thickness of the tube wall.

Once the critical Cr level (C_B) is reached at which a protective scale no longer can be maintained, less protective, base-metal oxides form that thicken more rapidly and often are less adherent, both features having implications for tube blockage. Rigorous calculation of the time to attain C_B involves detailed knowledge of diffusion behavior in each specific alloy, which often is not available. Theoretical treatments are available for addressing this issue, and in some cases experimental measurements of C_B have been made.

The calculations shown here represent a first estimation of the time to reach C_B, based on the simplifying assumption of flat Cr profiles and experimentally-inferred values of C_B. These undoubtedly lead to predictions of longer Cr depletion lifetimes than would actually occur; however, a mitigating consideration is that, in the case of the thin tube walls and higher temperatures considered for recuperators in sCO_2 cycles, the influence of these assumptions will be reduced. Quadakkers et al. [3,4] used a similar approach for calculating the lifetimes of ferritic alloys that formed alumina scales, allowing their operation at very high temperatures. Higher diffusion rates in ferritic compared to austenitic alloys, and the high temperatures involved meant that the assumptions discussed above were quite reasonable for those alloys. Work currently is in progress to develop similar concepts for use with thin-walled components of chromia-forming Ni-base alloys [5].

The mass gain (M_{ox}) due to oxide grown during a period of protective (parabolic) oxidation can be calculated from an algorithm analogous to that in Equation (F-4) for calculating oxide thickness:

$$M_{ox}^2 = 2*A_m*e^{-Qm/RT}*t \qquad \text{(F-6)}$$

where subscript *m* indicates oxidation kinetic data derived from mass change measurements.

Alternatively: $$M_{ox} = (2*k_{pm}*t)^{1/2} \qquad \text{(F-7)}$$

where: $$k_{pm} = A_m*e^{-Qm/RT} \qquad \text{(F-8)}$$

M_{ox} is in fact a measure of the oxygen reacted with the alloy; where the oxide formed is chromia (Cr_2O_3), and the amount of chromium consumed to form oxide is $M_{ox}*(2*52)/(3*16)$, i.e. $2.1667*M_{ox}$.

The amount of chromium consumed per unit area also can be represented as:

$$(C_0-C_B)*w*\rho/100 \qquad \text{(F-9)}$$

where:

C_0 the initial Cr concentration (wt%) in the alloy,
C_B the Cr concentration (wt%) in the alloy at transition to less-protective oxide formation,
w is the initial tube wall thickness, and
ρ is the alloy density.

Combining Equations (F-10) and (F-11) and considering the amount of Cr consumed, and where the thickness of metal taken to be the reservoir for Cr is $w/2$ (since Cr loss by oxidation is occurring on both inside and outside walls of the heat exchanger tube), and $t = t_B$ to represent the time to develop a critical depletion of Cr, gives:

$$2.1667 * M_{ox} = 2.1667 * (2 * k_{pm} * t_B)^{1/2} = [(C_0 - C_B)/100] * (w/2) * \rho \qquad \text{(F-10)}$$

Rearranging to give the time until critical depletion (t_B), i.e. the duration over which the tube will oxidize in a protective manner:

$$t_B = [(C_0 - C_B) * (w/2) * \rho / 216.67]^2 / (2 * k_{pm}) = 2.663 \times 10^{-6} * [(C_0 - C_B) * w * \rho]^2 / k_{pm} \qquad \text{(F-11)}$$

The example used here is a superheater tube in a utility boiler operating with steam at 550-700°C, with a typical tube outside diameter of 25.4 mm (1 in), and wall thicknesses (w) ranging from 3 to 0.2 mm (0.008 to 0.12 in). Values of the oxidation parameters used to calculate k_{pm} are listed in Table F-3.

Table F-3
Mass-Based Oxidation Parameters in HP Steam.

Alloy	A_m ($g^2cm^{-4}s^{-1}$)	Q_m (kJ/mole)	Source
300-series austenitic steels	1.6×10^2	-229	[2]
Super304H	0.21	-219	[2]
310HCbN	6.0×10^3	-338	[2]
IN740	3.2×10^{-3}	-229	[2]

Results of calculations for alloy TP347H with wall thicknesses of 3, 1.2, 0.5, 0.3, and 0.2 mm are shown in Figure F-2. Values of C_b were set arbitrarily at 10wt% Cr for alloys TP347H, TP347HFG, and 310HCbN, and at 16 wt% Cr for IN740. This plot illustrates that for alloy TP347H (18.55 wt% Cr) with wall thickness of 1.25 mm, the lifetime as limited by Cr depletion is of the order of 54 to 107 kh (6 to 12 yr) at 550°C (depending if inner and outer tube surfaces oxidize at the same rate), rising to 308 to 617 kh (35 to 71 yr) for a wall thickness of 3 mm. For operation at 650°C, for which the assumption of a flat Cr profile may be more reasonable, a 1.25 mm wall would result in a maximum lifetime of only 2,850 h (4 months).

Figure F-2 also indicates that alloy 310HCbN (25.5 wt% Cr), with its significantly larger reservoir of Cr and a much lower rate of oxide growth than TP347H, has an almost infinite estimated lifetime for a 1.25 mm wall at 650°C—386,800 kh (Figure F-2, given the assumptions used here).

For the thinnest wall envisioned in published recuperator designs for use in sCO_2 (200 µm), the expected service life for Ni-based alloy IN740 (24 wt% Cr) at 750°C, based on this Cr depletion criterion, would be 120-239 kh (14 to 27 yr).

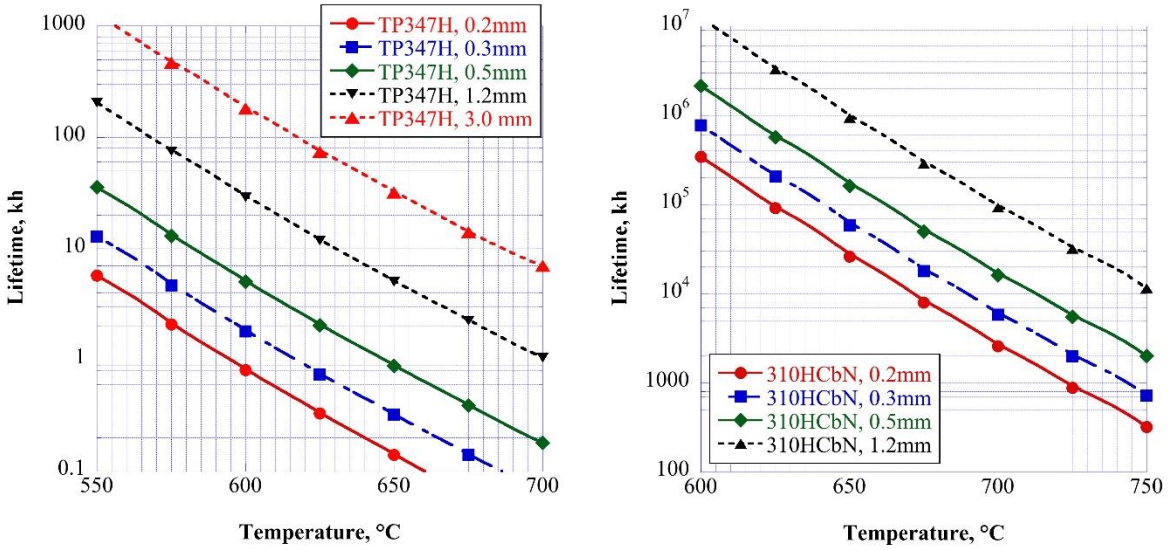

Figure F-2 - Effective lifetimes based on time to reach critical Cr depletion (t_B) for superheater tubes with wall thicknesses of 0.2 mm to 3.0 mm.

3. Time to Reach Critical Scale Thickness for Exfoliation.

A recently-developed mathematical model for predicting the onset of exfoliation of oxide scales grown on the steam side of superheater and reheater tubes in conventional steam boilers [1,6-9] indicates that for standard austenitic steels such as TP347H scale failure followed by exfoliation is expected at total scale thicknesses of the order of 45 µm. This model is dependent on understanding the role played not only by the operating parameters of the superheater tube, but also the influences of the modes of scale evolution and failure, which can vary significantly among nominally similar alloys. The scales grown on TP347H in high-pressure steam consist essentially of two layers of oxide that nominally are of equal thickness. Upon exfoliation, the outer layer is lost, while the inner layer remains essentially intact.

Although the scales formed on higher-Cr austenitic steels such as 310HCbN have similar morphologies, the two oxide layers usually are not of equal thickness (the outer layer typically is much thinner), and the mode of exfoliation is not well documented, largely because these alloys are not widely used in utility boilers. There is a similar lack of information for high-temperature N-based alloys such as IN740H. Lack of pertinent information limits the demonstration of this scenario to the standard austenitic steel TP347H.

Values of the time to reach the critical scale thickness (d_{exf}) for exfoliation are readily calculated from Equation (D-12), which is a variation of Equations (F-4) and (F-5):

$$d_{exf}^2 = 2*k_{pt}*t_{exf} \quad \text{(F-12)}$$

Rearranging for t_{exf}:

$$t_{exf} = d_{exf}^2/(2*k_{pt}) \quad \text{(F-13)}$$

Figure F-3 illustrates results for alloy TP347H assuming that d_{exf} = 45 µm. The projected times until exfoliation is expected decrease rapidly from approximately 6.3kh at 550°C, to approximately 1.5kh at 600°C, and only 395h at 650°C. In practice this alloy is not normally operated intentionally at temperatures higher than 650°C.

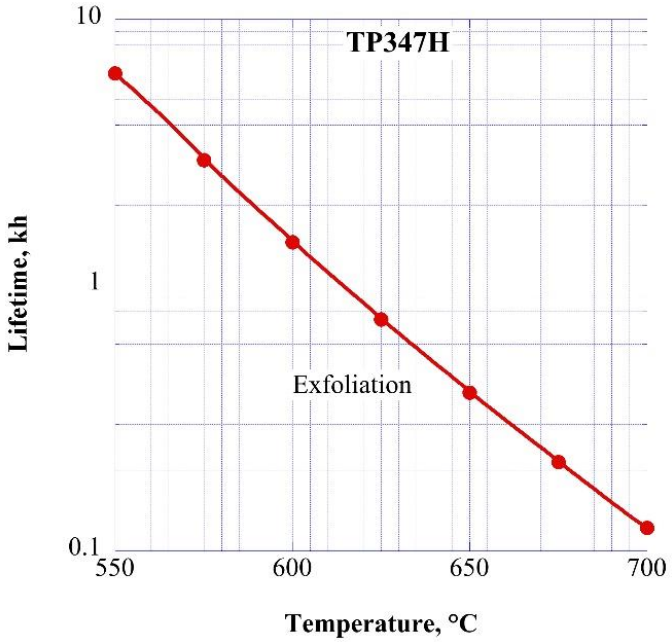

Figure F-3 - Effective lifetimes for austenitic steel TP347H based on time to reach critical scale thickness for exfoliation (t_{exf}).

References Cited in Appendix F

1. J.P. Shingledecker, et al., *Development of an Integrated Model to Predict and Control Oxide Scale Exfoliation, 2010 Progress - Industry Experience & Model Refinement*, EPRI 1019793 (Sep 2010).
2. I.G. Wright, DOE FWP No. FEAA061: *Oxidation of Candidate Alloys in Steam at 17 bar: Final Report on Phase 1 efforts in support of the US Consortium Program on Boiler Materials for Ultra-Supercritical Coal Power Plants*, ORNL/TM-2009/232 (Nov. 2009).
3. W.J. Quadakkers and K. Bongartz, "The prediction of breakaway oxidation for alumina-forming alloys using oxidation diagrams," *Werkstoffe u Korrosion*, 45, 232-241 (1994).
4. W.J. Quadakkers and M.J. Bennett, "Oxidation-induced lifetime limits of thin-walled, iron-based, alumina-forming, oxide dispersion-strengthened alloy components," *Mat. Sci & Techn.,* 10, 126-131 (1994).
5. R. Duan, A. Jalowicka, K. Unocic, B. Pint, P. Huczkowski, A. Chyrkin, D. Grüner, and W.J. Quadakkers: Work in progress at Jülich and Oak Ridge National Laboratories on *Predicting Oxidation-Limited Lifetime of Thin Walled Components of NiCrW Alloy 230* (2016).
6. J.P. Shingledecker, et al., *Development of an Integrated Model to Predict and Control Oxide Scale Exfoliation, 2011 Progress—Blockage Model Development and Initial Evaluation of Shot-Peened Field Exposed Tubes*, EPRI 1022128 (Dec 2011).
7. A.S. Sabau, I.G. Wright, and J.P. Shingledecker, "Oxide scale exfoliation and regrowth in TP347H superheater tubes," *Materials and Corrosion*, 63 (10), 896-908 (2012).
8. J.P. Shingledecker, A.T. Fry, and I.G. Wright, "Managing Steam-Side Oxidation and Exfoliation in USC Boiler Tubes," *Advanced Materials and Processes*, 171, (1) pp. (2013).
9. A.S. Sabau, I.G. Wright, J.P. Shingledecker, and P.F. Tortorelli, "Managing oxide scale exfoliation In boilers with TP347H superheater tubes," *Proc. 7th International Conference on Advances in Materials Technology for Fossil Power Plants*, Waikoloa, Hawaii. EPRI 2014.